UNIVERSITÉ D'ORLÉANS

ÉCOLE DOCTORALE
Énergie - Matériaux - Sciences de la Terre et de l'Univers

CEMHTI : Conditions Extrêmes et Matériaux : Haute Température et Irradiation
UPR3079

THÈSE présentée par :

Zhiwei HU

Soutenue le : **31 Mai 2022**

Pour obtenir le grade de : **Docteur de l'Université d'Orléans**

Discipline/ Spécialité : Physique des matériaux

The effect of purity on the microstructural evolution of tungsten under irradiation

L'effet de la pureté sur l'évolution de la microstructure du tungstène sous irradiation

THÈSE dirigée par :	
M.-F. BARTHE	Directrice de recherche, CEMHTI, CNRS
RAPPORTEURS :	
C. BECQUART	Professeure, École Centrale de Lille
A. DEBELLE	Maître de conférences, Université Paris-Saclay
PRESIDENT :	
C. HUGENSCHMIDT	Professeur des universités, TUM, Munich
JURY :	
M-A. PINAULT	Chargée de Recherche, GeMAC, CNRS, Versailles
P. DESGARDIN	Chargé de Recherche, CEMHTI, CNRS, Orléans
INVITEES :	
C. GENEVOIS	Ingénieure de recherche, CEMHTI, CNRS, Orléans

Remerciements

Dans un premier temps, je souhaite adresser mes sincères remerciements à Marie-France BARTHE, qui a supervisé cette thèse de près et a toujours consacré du temps à discuter et à comprendre les résultats en donnant toujours des idées constructives et fructueuses.

Je remercie également Charlotte BECQUART, Aurélien DEBELLE, d'avoir accepté d'être rapporteurs, et Christophe Hugenschmidt et Marie-Amandine Pinault d'avoir accepté d'être membres du jury.

Je tiens également à remercier Pierre DESGARDIN pour sa disponibilité, son partage de connaissances et expérience en science des matériaux surtout sur la spectroscopie d'annihilation de positons (PAS). Je remercie Cécile GENEVOIS pour son soutien et son encadrement sur la microscopie électronique en transmission (MET) et le traitement des images.

Je remercie aussi François Jomard. Ses connaissances sur la spectrométrie de masse des ions secondaires (SIMS) et son expertise sur les aspects expérimentaux et de traitement des données ont été essentielles pour réaliser cette thèse. Je remercie Brigitte Decamps et Robin Schäublin pour leurs soutiens sur les expériences de MET in situ. Je tiens à remercier tous les collègues de la plateforme JANNuS, et du LSI pour la réalisation des expériences d'irradiation. Je remercie Marco Minissale et Laurent Gallais pour leurs disponibilités et les expériences partagées sur la pyrométrie.

Je tiens à remercier Qigui Yang, Ilja Makkonen et Pär Olsson, pour leurs disponibilités et soutiens en simulation, ce qui nous a permis de mieux comprendre les résultats expérimentaux.

Je remercie spécialement Jérôme JOSEPH pour le support technique qu'il a pu apporter durant cette thèse, également pour tout ce qu'ils m'ont appris (avec Pierre D), et pour leur aide et conseil pour mieux vivre en France. Je remercie également Thierry Sauvage**,** Olivier Wendling et Aurélien Bellamy pour le support des expériences de NRA.

Je remercie aussi Hélène Lecoq et Emmanuel Véron pour le soutien sur le microscope électronique à balayage, Séverine Brassamin et Emmanuel de Bilbao qui a permis de réaliser les observations au microscope optique.

Je n'oublie pas tous les collègues du CEMHTI pour leur gentillesse et enthousiasme. Spécialement, Marie-lyne Amany et Ahmad Chehade, tous nos échanges pendant ces années de thèse ont été très enrichissants.

A la fin, je voudrais remercier infiniment mes parents et mes grands-parents, qui m'ont soutenu pour poursuivre mes études en France, je culpabilise souvent pour n'avoir pas pu rester à leur côté, et avoir décidé de partir loin dans un pays de l'autre côté de la terre.

Contents

List of acronyms

DEMO	Demonstration power plant
ELM	Edge Localised Mode
FIM	Field Ion Microscope
HF	High Fluence
IFMIF	International Fusion Material Irradiation Facility
ITER	International Thermonuclear Experimental Reactor
JANNuS	Joint Accelerators for Nanosciences and Nuclear Simulation
JET	Joint European Torus
LEs	Light-Element Impurities
LF	Low Fluence
LSI	Laboratoire des Solides Irradiés
NRA	Nuclear Reaction Analysis OKMC Object Kinetic Monte Carlo
PALS	Positron Annihilation Lifetime Spectroscopy
PAS	Positon Annihilation Spectroscopy
PFC	Plasmas-Facing Components
PFM	Plasma Facing Materials
PKA	Primary Knock-on Atom
RID	Radiation-Induced Defects
SEM	Scanning Electron Microscope
SIA	Self-Interstitial Atom
SIMS	Secondary Ion Mass Spectroscopy
SPB-DB	SPB-DB Slow Positron Beam- Doppler Broadening
SRIM	Stopping and Ranging of Ion in Matter
TDE	Threshold Displacement Energy
TEM	Transmission Electron Microscope
TOKAMAK	тороидальная камера с магнитными катушками (chambre toroïdale à bobines magnétiques)

Introduction

Nowadays, energy need is growing and fossil fuels are running out giving rise to origin of the global warming. Thus, the production of greener and more sustainable energy is the main issue for the future. Compared to the potential less polluting energy production, such as solar and wind energy, thermonuclear fusion could be expected as a stable and permanent source.

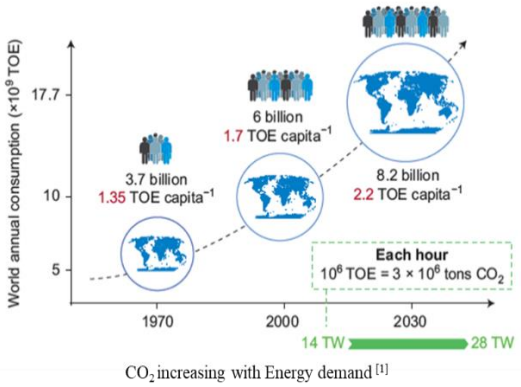

Figure 1: Annual consumption of the energy of the past until the estimated value in the future [1]

The assembly of the TOKAMAK of the International Thermonuclear Experimental Reactor (ITER) started on 28 July 2020. However, to realize the dream of energy production by thermonuclear fusion, more technological development and material investigations are needed. The mastery of thermonuclear fusion must be demonstrated before the first industrial power prototype, a transition to DEMOstration power plant (DEMO) can be considered. To achieve this goal, a large number of technological obstacles will have to be overcome, including problems related to the behavior and resistance of materials in the fusion reactor harsh environment.

In this context, tungsten, the most promising material for dealing with plasma, has been selected to cover the ITER divertor and possibly the first inner wall of the TOKAMAK of the DEMO. The divertor is a critical component of the future fusion reactor, it allows the evacuation of plasma dust and energetic particles generated during fusion. Tungsten will be subjected to high heat flux, intense neutron irradiation and plasma exposure. These will lead to the creation of defects that will cause the microstructural evolution of the material and, degrading its macroscopic properties, affecting even the normal operation of the reactor. It is therefore important to be able to predict the behavior of this material in the reactor and thus to determine its lifetime under operational conditions. Numerous studies aim to determine irradiation-induced defects and their properties in order to develop models for calculating the microstructural evolution of tungsten in the reactor. Apart from these major extreme conditions, low atomic mass impurities - such as carbon and oxygen - cannot be ignored. Such impurities are present in the material itself and also in the plasma during normal reactor operation, energetic particle bombardment and high-flux thermal loading can promote their penetration into the tungsten. Theoretical

studies indicate that these atoms can interact with irradiation-induced defects, which can impact the microstructural evolution of tungsten. The aim of this thesis is to carry out several experimental studies to better understand these potential interactions and their consequences on the microstructure of irradiated tungsten. Tungsten samples of different purities (99.95 to 99.9999 wt.%) were irradiated under different conditions: **(1)** electron irradiations to introduce countable point defects, **(2)** self-irradiations to create similar defects to those induced by neutrons. The nature and distribution of radiation-induced defects (RIDs) were characterized by positron annihilation spectroscopy (PAS) and transmission electron microscopy (TEM). In addition, quantitative chemical analysis techniques (secondary ion mass spectrometry –SIMS-, nuclear reaction analysis –NRA-) were used to access the distribution of the light-elements atoms (C and O), and correlate them with the defect results obtained by PAS and TEM. The present work is separated into four parts.

The ***first chapter*** describes the concept and material issues of thermonuclear fusion reactors, especially, those of tungsten. A variety of discovered macroscopic degradations are presented. The consequences of plasma exposure and irradiation are detailed. In particular, the formation of defects is summarized and their fundamental properties as well as the theoretical data on the properties of light elements are also reported. Finally, known data on positron annihilation spectroscopy in tungsten are listed.

The ***second chapter*** presents the experimental techniques used in this study. The sample preparation procedure and irradiation conditions are listed. The principles of positron annihilation spectroscopy which allows to probe small vacancy defects are described. The implementation of both techniques (Doppler Broadening –DB- and Lifetime –PALS-) allowing to measure both annihilation characteristics: the electron positron momentum distribution and the positron lifetime and the way to identify and quantify defects are explained. Meanwhile, the conditions for observation and quantification of cavities (or cluster of vacancies) by transmission electron microscopy (TEM) are summarized. In addition, quantitative chemical analysis techniques used to determine the concentration profiles of light elements (carbon and oxygen) i.e. Secondary Ion Mass Spectroscopy (SIMS) and Nuclear Reaction Analysis (NRA) are also explained.

The ***third chapter*** is focused on the verification of the quality of the pristine samples prepared from various batches of different purities. On the one hand, the prepared samples contain a low defect density, as confirmed by the two types of PAS measurements (DB and PALS). On the other hand, the purity of the materials is analyzed by SIMS and depends on the batches. We mention also the difficulties that were encountered during this work on the preparation of some samples. The presence of a carbon-enriched layer has been demonstrated and its origin is discussed.

In the ***fourth chapter***, the distribution of defects in samples irradiated with electrons and self-ions was characterized and correlated to chemical analysis to highlight the effect of irradiation conditions

and sample purity on induced defects. This chapter is subdivided in three sections. First, DB and positron lifetime measurements were used to show that individual vacancies were induced by electron irradiations. The positron annihilation characteristics obtained were compared to carbon and oxygen concentration versus depth profiles measured using SIMS. The combination of these results suggests that a large fraction of vacancies is decorated with atoms of oxygen. Second, the saturation of the defect distribution has been demonstrated in self-ion irradiated tungsten with different energies at room temperature (RT) using PAS. Third, the effect of irradiation temperature and sample purity was also investigated in self-ion irradiated samples by combining PAS (DB), TEM and SIMS analyses. DB shows the formation of vacancy clusters when the irradiation is carried out at a temperature above or equal to 500 °C. Their size distribution depends on the purity as indicated by PAS and TEM. The origin of this difference is discussed in correlation with SIMS results.

At the end, a general conclusion allows to sum up the results of the study and is followed by a perspective.

Chapter I: Bibliography

In this chapter, the concept, significance and the challenges of the thermonuclear fusion reactors is introduced. The behavior of the material under extreme conditions is one of the most important issue, in particular, the investigations were carried out on tungsten. And then, according to the recent decades researches, the collected experimental and theoretical results point out the shortage of experimental results on the interaction between the radiation induced defects and light-element impurity atoms and its effect on the microstructure.

I.1 Nuclear fusion and the TOKAMAK

I.1.1 Fusion energy

The nuclear fusion consists of approaching sufficiently two light nuclei. When the total kinetic energy of the two light nuclei goes beyond the Coulomb repulsive force, they fuse to form firstly a larger nucleus at an instable energy state before splitting to at less two particles with stable configuration. As shown in Figure 2.a, the fusion reactions occur between the elements with a mass inferior to the one of the 56 (Fe). The cross section of various fusion reaction are shown in Figure 2.b. Among of them, the reaction between the Deuterium (D) and the Tritium (T) is the most probable. Therefore, D and T (eq. 1) are the most important fuel for future fusion reactors. Their fusion releases an amount of energy of about 17.6 MeV distributed to the products, i.e. the alpha particle with 3.5 MeV and neutron of 14.1 MeV.

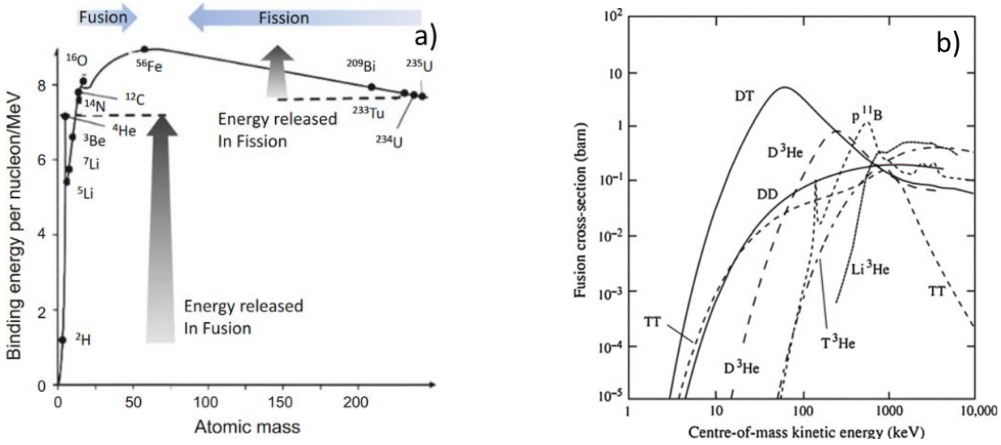

Figure 2: a) Binding energy as a function of atomic mass and b) Cross section of various fusion reactions [2].

$$^{2}_{1}H + ^{3}_{1}H = ^{4}_{2}He\ (3.6\ MeV) + ^{1}_{0}n(14\ MeV) \qquad eq.\ 1$$

In general, to trigger the fusion reaction between D and T, the energy state of the reactants (D and T) must be higher than the Coulomb repulsion between them. It requires to heat the reactants to a temperature of a few hundred times hotter than the core of the sun, at about 25 keV or 300 000 000 °C [2], that is why the fusion occurs often in stellar bodies and becomes their energy source. Such conditions, can be created with D and T particles plasma. According to the Lawson criterion, for the D-T fusion reaction, the product of plasma density and confinement time should be minimized to about 10^{20} m^{-3}.s [3] to maintain the fusion reactions.

Furthermore, since the tritium is a very valuable element with a natural abundance of only 3.5 kg in the world, its current price is over 30,000 $ US per gram, and a relatively short radioactive half-life (~12.3 years). The source of tritium could be from the detritiation of the heavy water (D_2O) in the Canada Deuterium Uranium (CANDU) reactor. However, the quantity of the tritium produced from the CANDU is insufficient to offset the ITER consumption. Consequently, an idea to produce in situ the tritium with

the nuclear reaction (eq. 2) between the fusion-products was conceived i.e. neutron and lithium (Li). Lithium is one of the most used element in daily applications. The natural abundance of two isotopes is 92.41 % and 7.59 % for 7-Li and 6-Li, respectively [4]. So that, it is reasonable to envisage the application of self-sufficient tritium in the fusion reactors. It has to be noticed that this self-production is challenging due to safety requirements [5].

$$\begin{cases} {}^{6}_{3}Li + {}^{1}_{0}n\_slow = {}^{4}_{2}He + {}^{3}_{1}H + 4.78\ MeV \\ {}^{7}_{3}Li + {}^{1}_{0}n\_fast = {}^{4}_{2}He + {}^{3}_{1}H + {}^{1}_{0}n\_slow - 2.47\ MeV \end{cases} \qquad \text{eq. 2}$$

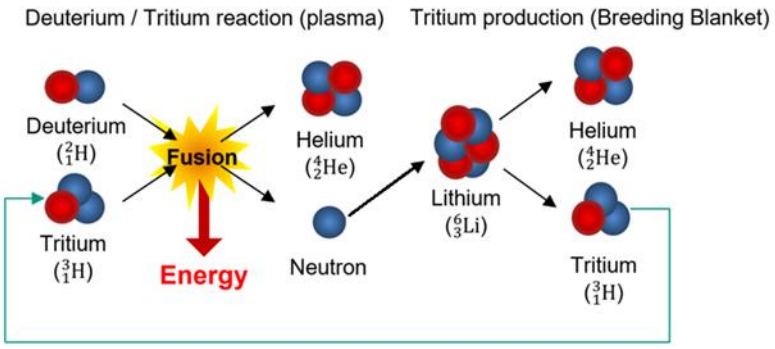

Figure 3: Sketch of D-T fusion reaction with an in situ production of the tritium

I.1.2 The TOKAMAK

I.1.2.1 Magnetic confinement

The magnetic confinement is the most popular method to control the fuel particle in plasma. For instance, the TOKAMAK (acronym of toroidal magnetic coil chamber from Russian) is the most developed configuration for in-building experimental fusion reactors. Figure 4 shows a design of different components in a tokamak. The several magnetic field coils confine fuel particles (D and T) plasma to continue the fusion reactions. A series of coils (in bleu) generates 'toroidal' magnetic field, along the toroidal direction. A central solenoid (a magnet that carries electric current) creates a second magnetic field directed along the poloidal direction, the short way around the torus. These two field components induce a helical magnetic field which confines the plasma as a donut-shape (in pink) with a top view. A third set of field coils (in grey) allow to better control the shape and position of the plasmas by the generated outer poloidal field (in green).

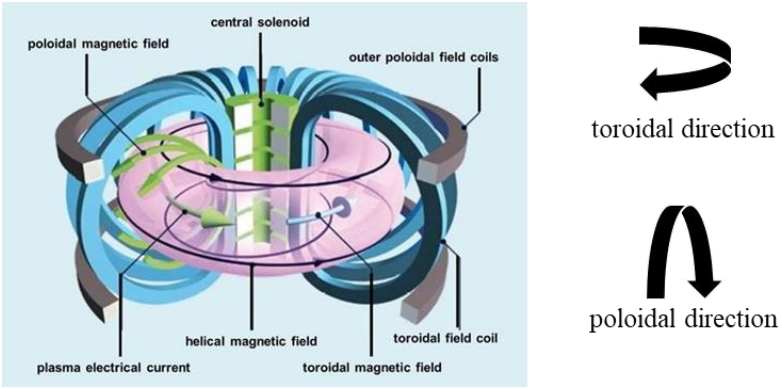

Figure 4: Magnetic coils of the TOKAMAK

I.1.2.2 Experimental fusion reactor ITER

The project of the International Thermonuclear Experimental Reactor, i.e. ITER, which means 'The Way' in Latin, is one of the most established equipment for testing the energy production via the fusion reaction. It has been launched in 1985 with the support of 35 nations. The objective of the project is to produce energy with nuclear fusion to obtain an energetic gain - i.e. the ratio of power production over the consumption or Q factor - superior to ten: for instance, a power of 500 MW generated from the fusion with 50 MW power for heating the plasma. Up to now, the optimal value of about Q = 0.67 was recorded in the Joint European Torus (JET) based at the Culham Centre for Fusion Energy (CCFE) in 1997, with a power of 16 MW produced from a heating power of 24 MW. However, to withstand the extreme conditions in the fusion reactor –tokamak-, the performance of the material is one of several key issues, in particular, the material of the 'vacuum vessel' in which the fusion reactions occur: The inner wall of the tokamak, namely 'blanket' aims to protect other components placed behind such as the superconducting toroidal field magnets. It is made of a first wall that is directly in contact with the fusion

fuel i.e. plasmas hydrogen isotopes and the high energy particles originated from the fusion. One of the critical components is the divertor. Located at the bottom of the reactor in ITER facility (Figure 5), it allows the evacuation of heat and particles produced during the fusion. It enables not only to purify the plasma, but also to reduce the bombardment of the particles on other plasmas-facing components (PFC).

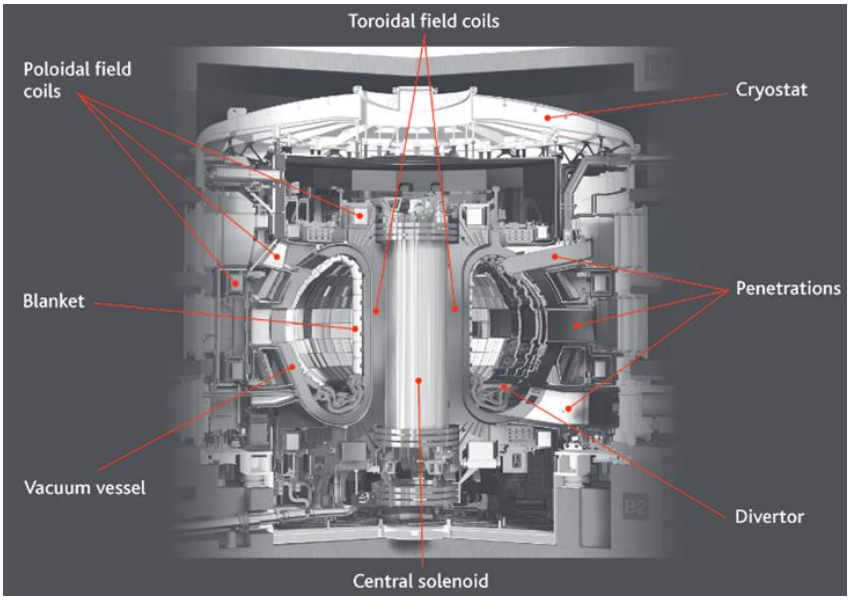

Figure 5: Schema of the main components of the ITER facility [5]

Figure 6.a shows a sectional drawing of the ITER with highlighted configuration of the divertor. It is composed of 54 cassettes assemblies (CAs) with a weight of ten tons. Each CA compounds (Figure 6.b) contains an inner, outer vertical target (IVT and OVT), and a dome. This system is developed to transform the energetic energy of the fusion products guided to the divertor by a special configuration of the magnetic field which create open field lines crossing at the X-point (red area in Figure 6.c) in heat flux that have to be evacuated. The surface of these components is composed of a large number of tungsten monoblocks, cooled by water circulation in an internal CuCrZr tube. From 2013-2018, for testing the feasibility of the full-tungsten coated divertor, the project WEST (W Environment Steady-state Tokamak) was launched (where W is the chemical symbol of the tungsten). The idea is to transform the TOKAMAK facility, Tore Supra established in the same period as JET (~1960) in Cadarache (south of France) into a full tungsten-coated TOKAMAK.

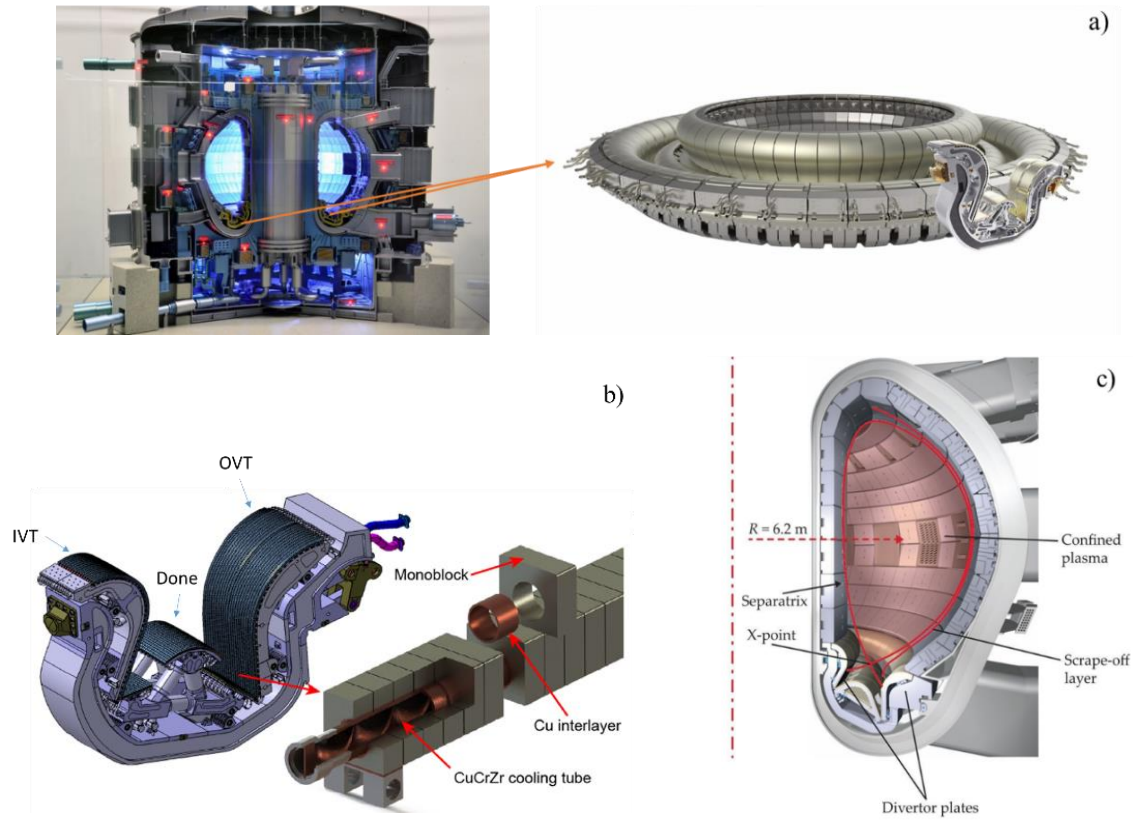

Figure 6: a) Aspect of the ITER divertor b) the components of a cassette and c) the cross-configuration of the inner-chamber of the ITER TOKAMAK [6–8]

I.2 Plasma-facing material: tungsten

Tungsten, a metallic element with body-centered cubic (BCC) crystalline structure (lattice parameter, a =0.317 nm), is localized in the sixth column with an atomic number of 74 in the periodic table. It was first discovered in 1783 in the mineral wolframite, from where its element symbol was chosen, W. Its name comes from the Swedish words *'tung-sten'*, which means 'heavy stone'. As its name suggests, its modulus of elasticity (Young's module) is about 400 GPa, one of the hardest pure metals, and its density is 19.3 $g.cm^{-3}$. In addition, tungsten is characterized by high melting (T_{melt} = 3422 °C), boiling (T_{melt} = 5700 °C) point, low coefficient of thermal expansion (4.4×10^{-6} m. mK^{-1}), high electrical (18.2×10^{6} S. m^{-1}), and thermal conductivity (160 W. m^{-1}. K^{-1}) [9].

a) b)

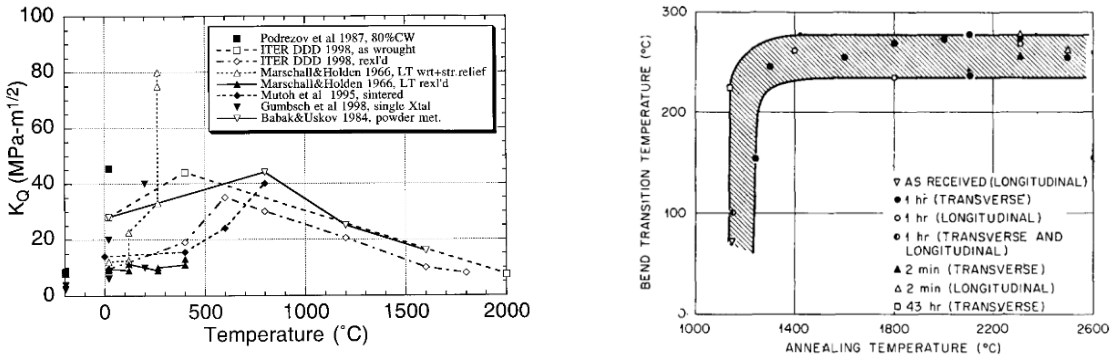

Figure 7: a) Experimental value of fracture toughness of pure tungsten versus various temperatures [10] b)DBTT of pure tungsten annealed at different temperatures [11]

Given its suitable mechanical and thermal properties, tungsten was considered as the most reliable PFM (Plasma Facing Materials) for fusion reactor construction due to its low sputtering rate, high melting point and, thermal conductivity which ensures efficient heat removal in contrast to other PFMs candidates like beryllium-based materials and carbon fiber composites (CFCs), which have a major drawback due to their relatively low melting point (T_{melt} = 1287 °C [12]). However, the inherent high ductile-to-brittle transition temperature (DBTT), and a low fracture toughness temperature are still potential drawbacks for tungsten. Figure 7.a shows the experimental value of the fracture toughness as a function of temperature, with the most common rupture occurring between 500-700 °C [12]. Figure 7.b shows the DBTT measured in pure tungsten as a function of the annealing temperature in the range from 200 to 300 °C [13]. Recently, the DBTT of tungsten is demonstrated [11] depending on the grain direction, a DBTT variation could attain around 50 % for samples from the same batch. In addition, the incorporation of particles (potassium, TiC, and ZrC) could also change the DBTT, thus, the manufacturing optimization might decrease the DBTT.

Overall, under the extreme conditions in the TOKAMAK, the PFCs made of tungsten or tungsten-based materials must be able to withstand high temperature thermal loads, intense plasmas exposure (^{2}H,

^{3}H, ^{4}He) and energetic particle irradiation (3.5 MeV-^{4}He and 14.1 MeV-^{1}n), these major issues impacting on the performance and even the lifetime of the fusion reactors.

I.2.1 Thermal loads

For optimal operation of the TOKAMAK, the PFCs must withstand a heat flux of 5000 cycles at 10 $MW.m^{-2}$ and 300 cycles at 20 $MW.m^{-2}$ [14,15] which is equivalent to an energy density of about 1 $MJ.m^{-2}$, which is well-known as the Edge-Localized mode (ELM) transition heat load. First of all, to resist the heat from the plasmas exposure, the PFCs must have a melting point well above the temperature ~2000 °C [8,9]. The high flux of the heat could lead to drastic degradation of the material. For instance, Nogami et *al.* [15] irradiated the monoblocks with electrons (70 kV, 3 A and 1 KHz) to simulate the conditions in TOKAMAK (5000 cycles at 10 $MW.m^{-2}$ and 300 cycles at 20 $MW.m^{-2}$) with a heating and cooling time of 10 s and 20 s for one cycle, which is also close to the ITER facility (10 s /10 s) [15]. As shown in Figure 8, after heat loading, scanning electron microscope (SEM) observation showed a clear degradation of the monoblock. Especially, in the center of the exposed surface, the cracks were clearly observed, in contrast to the microscopic cracks in other parts.

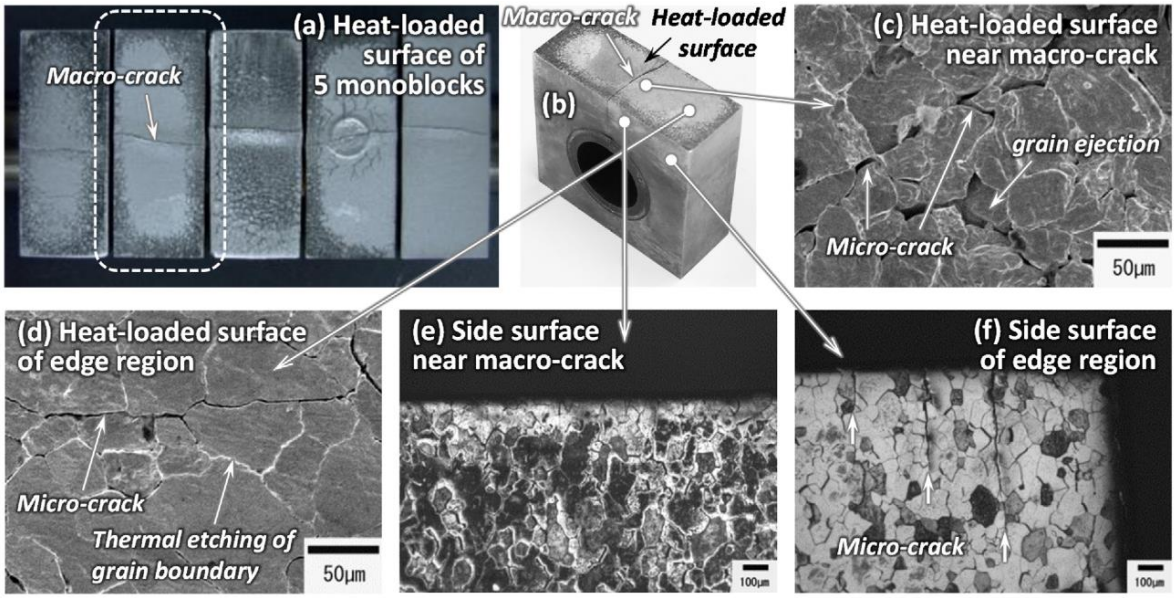

Figure 8: Observed cracks of one monoblock after the heat loading condition referred to the ones of the TOKAMAK [16]

I.2.2 Plasma exposure

In the TOKAMAK, along with thermal loading, PFCs mainly also undergo bombardment of the neutralized fuel particles, i.e. hydrogen isotopes (D and T) and helium (He), with an intense flux. Numerous experiments [17–19] have systematically investigated this issue. It was reported that for pure tungsten exposed to a high fluence D-flux ($10^{20}\ m^{-2}.\ s^{-1}$, $>10^{23}\ H.m^{-2}$ [20]) and helium ($>10^{21}$ He $.m^{-2}$ [20]) with a low-energy (< 100 eV) at below ~950 K [21–23], the blistering surface was observed using SEM. Ye et *al.*[18] and Luo et *al.*[23] determined that the size and density of the H-blisters increase not only

with increasing of the flux (as show in Figure 9. a-c), but also with the plasma incident energy. In addition, Ueda et *al.* [24] demonstrated that the density of the blistering increase with the concentration of carbon in the sample and also incident energy of the hydrogen ions.

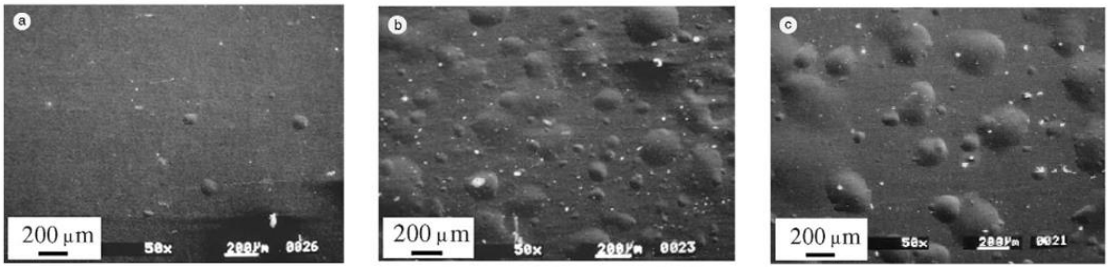

Figure 9: SEM image of pure tungsten after hydrogen plasma irradiation at 920 K for an fluence of a) 1.4 × 10^{25} m^{-2}, b) 2.8 × 10^{25} m^{-2} and c) 4.7 × 10^{25} m^{-2} [18]

When the temperature is above 1000 K during plasma exposure, and the incident plasma energy is above a critical value (~20-30 eV) [25], special nanotendril-like structure, namely 'fuzz' has been observed [26–28] on tungsten surface. Figure 10.a-e show cross-sectional SEM images of the pure tungsten after exposure to low-energy (~60 eV) He plasma with a flux of about 5 × 10^{22} $m^{-2}.s^{-1}$ at 1120 K. It is evident that the thickness of the 'fuzz' increases with increasing exposure time. Moreover, when the energy of He ion reached 12 keV (with a fluence > 4 × 10^{24} m^{-2} at ~1300 K), Wang et *al.* [29] observed using SEM the growth of nanotendrils (~180 nm) with a factor of ~nine compared to those induced by low-energy ions (~50 eV). In addition, Ni et *al.*[30] indicated a nearly linear mass loss of the tungsten and tungsten-based alloys (Re-W, La_2O_3-W, and Y_2O_3-W) with increasing the thickness of the nanotendril, leading to a reduction of the thermal and electrical conductivity of tungsten [25].

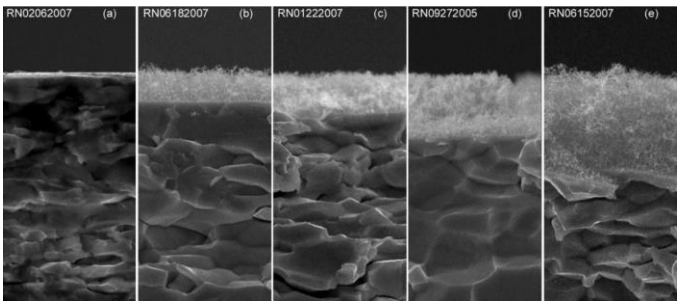

Figure 10: Growth of the fuzzy surface with increasing exposition time of plasmas He with a density of 4 × 10^{18} m^{-3} from a) 300 s , b)2000 s , C) 4300 s, d)9300 s, and e)22000 s at a fixed temperature of 1120 K [27]

Furthermore, when the sample surface was exposed to He plasmas at temperatures above 1200 K, the formation of holes and bubbles was revealed. As shown in Figure 11, after exposure to a low energy (≤30 eV) plasma with a high flux (10^{23} He. $m^{-2}.s^{-1}$) in the hot steady state (> 2000 K), the holes formed when the plasma energy is greater or equal to 5 eV [31], which is close to the calculated energy barrier (5.5-5.9 eV [32]) for a He atom to occupy an interstitial site in tungsten. Furthermore, the growth of holes, and bubbles with increasing of plasma temperature was observed using SEM and transmission

electron microscope TEM [31]. At the same magnification, the observed bubble size increased from 5 nm at 1300 K to 500 nm at 1950 K.

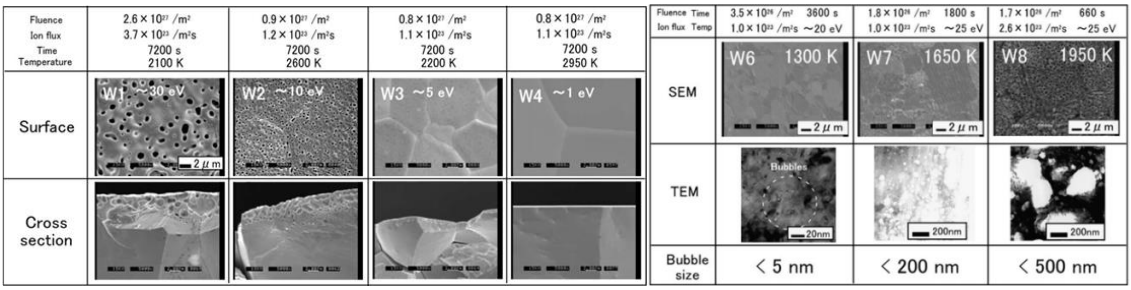

Figure 11: SEM and TEM images of the energy, temperature dependence of the hole and bubble formation in the pure tungsten after He-exposition with various conditions [31].

The condition of the formation of blisters and/or bubbles was proposed as follows: first, the thermal vacancies are considered as traps for H and He atoms, and second the high mobility at high temperature leads to rapid agglomeration for both atoms. At low temperature, the diffusion of He atom is relatively hindered, in contrast to the case of H atoms, which could be the reason for which the H-blistering formed only below 950 K, and the formation of He bubbles occurs above 1000 K, when mobility of He atoms becomes high enough. This assumption is consistent with the simulation work reported by Sun et *al.*[33], at 300 K, 6.5 atoms of hydrogen can be trapped at a single vacancy of the tungsten, while at 900 K the number of trapped H-atom decreases to 5. In addition, Figure 12 illustrates a simulation result of H-trapping in the void, the trapped H-atoms tend to form a screen layer at the periphery of the void instead of staying at its center. Once the screen layer formed, the further trapped atoms were prevented from interacting with the matrix atoms and they enter into the void. Then, H_2 molecules could be formed at the void center, which is considered as the origin of the H-blistering [33]. Regarding the He-bubble, Iwakiri et *al.* [34] used in situ TEM to study the microstructure of the tungsten after He irradiation (with 0.25, and 8 keV) at different temperatures (293, 873, and 1073K). They found that at low energy, no PKA (primary knocked-on atom) atoms are formed and the impurities act as the trap for He atoms giving rise to the nucleation and formation of the bubbles. At high energy, He atoms can bind to the radiation-induced vacancies, forming the He_nV_1 vacancy-complexes. In addition, according to simulation work by Wilson et *al.* [35], when the number of helium atoms is high enough (> 5), they could also create a lattice Frenkel pairs. Once the He_nV_1 vacancy-complexes are formed, they could grow up by absorbing other He atoms. In P.E. Lhuillier' thesis, the behavior of the helium in tungsten was discussed [36].

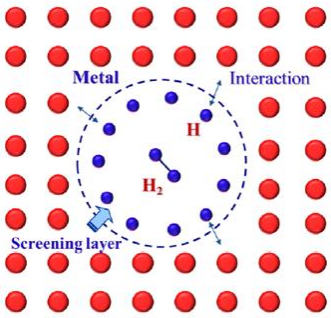

Figure 12: Simulation work on the H-trapping in a BCC metal [33].

Therefore, the blisters and/or bubbles formation has been demonstrated to affect the movement of dislocations resulting in embrittlement [37,38] of tungsten. Moreover, the swelling caused by He-bubble in ferrite steel [39] and nickel-chromium-iron-based alloy [40] should not be ignored for tungsten, nor hardening due to He-bubble which has been observed in tungsten [41].

I.2.3 Neutron bombardements

Apart from the plasmas and heat load, the surface of the PFCs is expected to withstand the neutron yield produced by D-T fusion reactions. For ITER facility, the 14 MeV neutrons induced a damage level in the PFMs of about 2 to 3 dpa (displacement per atom) for its full operation time [5] which means the number of times one atom can be displaced from its origin crystallographic site. After fast-neutron irradiation with fluence of 10^{22} cm^{-2} at 550 °C, Sikka and Moteff [42] observed void lattice with a lattice parameter of about 19.5 nm and the void size ranging from 1 to 6 nm (Figure 13). Similar results were also obtained by Tanno et *al.* [43] in pure tungsten irradiated by fast neutrons (>0.1 MeV) with fluence of 10^{21} $n.cm^{-2}$ corresponding to ~1.54 dpa at 750 °C. Hasegawa et *al.*[44] studied the microstructural evolutions after neutron irradiations (Figure 14).

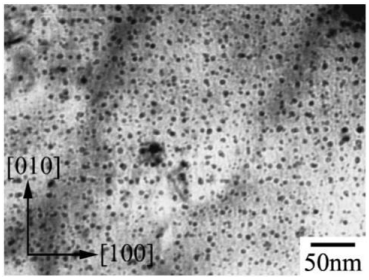

Figure 13: TEM image of 'void- lattice' in neutron-irradiated pure to 1.54 dpa (~10^{21} cm^{-2}) at 750 °C, the lattice spacing is about 20 nm and the averaged void diameter is around 5 nm. [43]

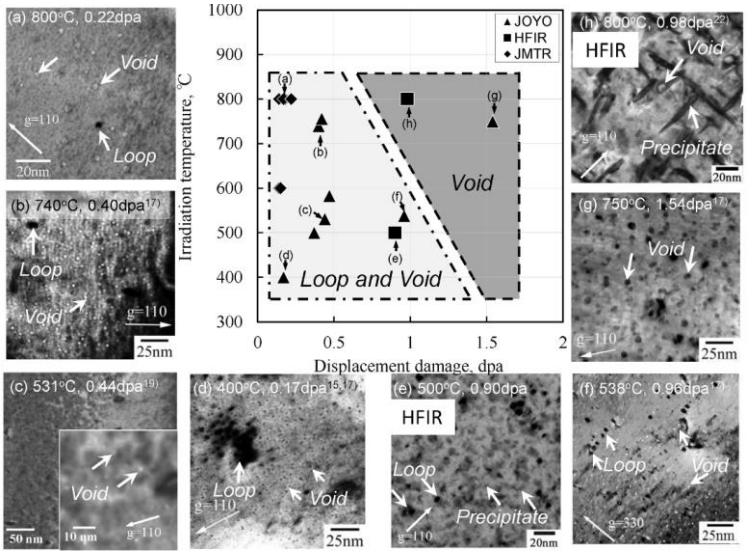

Figure 14: Neutron-induced microstructural defects in tungsten [44]

Figure 14 summarizes their results for irradiations performed in different experimental reactors (HFIR, JOYO and JMTR). Various defects (voids, dislocation loops, and precipitates) were induced by neutron irradiations in pure tungsten. The microstructural behaviors of these radiation-induced defects (RIDs) play an important role on the degradation of tungsten properties. For instance, based on the scattering mechanism of heat transport, the simulation of Wang et *al.* [45] showed a decrease in thermal conductivity in tungsten if the temperature is less than 400 K and the density of the dislocation exceeds 10^{14} m^{-2}. The measurement of the thermal diffusivity and electrical resistivity was performed by Akiyoshi et *al.* [46] and Hasegawa et *al.* [44], respectively, who indicated a degradation of about 20 % on thermal diffusivity, and 10 % on electrical conductivity in pure tungsten after neutron irradiation (10^{25} $n.m^{-2}.s^{-1}$, E > 0.1 MeV, ~0.4 dpa). Moreover, Matolich et *al.* [47] estimated the swelling (Figure 15.b) of pure tungsten after fast neutron irradiation, as observed at the macroscopic scale in the case of 316-steel [48] (Figure 15.a).

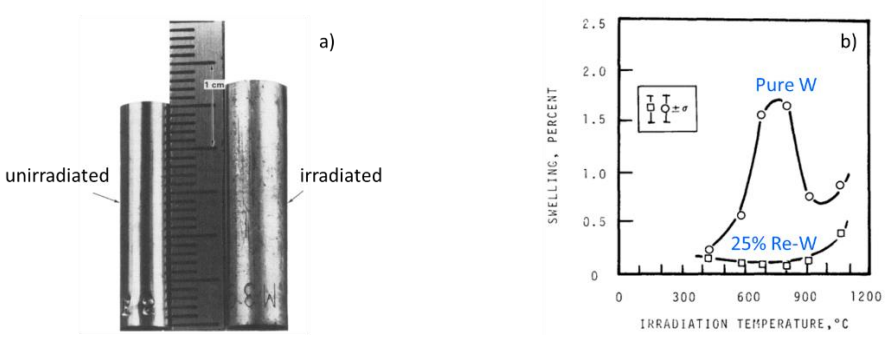

Figure 15: Swelling of a) 316 L cladding tube at 1.5 × 10^{23} $n.cm^{-2}$ (E > 0.1 MeV) or 75 dpa at 510 °C in EBR-II experimental reactor) [48] and b) in tungsten the after fast neutron irradiation (> 1 MeV, of about 1 × 10^{22} n cm^{-2}) [47]

The neutron being a special particle, it can be captured by the atoms of irradiated materials. After its capture, several new elements will be generated by transmutation, such as Rhenium (Re), Osmium (Os), and Tantalum (Ta), which are the main transmuted elements [48]. Figure 16. a-b show the simulation predicted concentration of transmutation products of tungsten after 5 and 14 years of operation. These transmutation products also have an impact on the properties of PFCs. Dürrschnabel et *al.* [49] observed the precipitation of the Re and Os (Figure 17) atoms using STEM in the neutron-irradiated tungsten (1.25 dpa, 800 °C, and ~10^{16} cm^{-2}), in which a large density of the dislocation or voids (~5nm, 4.0 × 10^{23} m^{-3}) was also revealed. The presence of these (Re, Os) precipitates has an impact on the mechanical properties of tungsten. Tanno et *al.* [43] discovered a drastic hardening in the binary alloy W-Os with only 3 mass% Os compared to pure tungsten, while obvious hardening was observed in the case of the binary alloy W-Re when the mass of Re reaches 25 %. The hardening is then close to half of the one observed in the W-Os alloy. These results indicate that the amount of Os plays an important role on the hardening of tungsten.

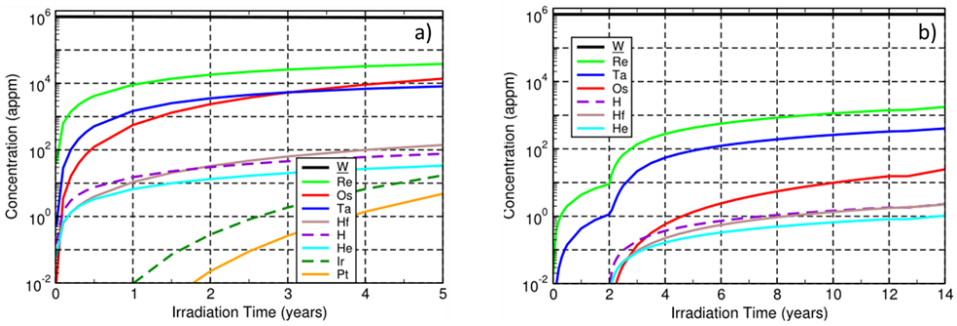

Figure 16: Concentration of the neutron-induced transmutation elements in the ITER facility after a) 5 years and b) 14 years operation [50]

In addition, Hasegawa and Fukuda et *al.* [44,51–55] have extensively studied pure tungsten and tungsten alloys after neutron irradiation under various conditions. Hu et *al.* summarized the results in [51]. Figure 18 shows an estimate of the contribution of various defects (dislocations, voids, precipitates) on hardening calculated using result obtained for various irradiation experiments in different experimental reactors (HEIR and JOYO), of which the precipitates (Re, Os…) are considered as the main factor for radiation-induced hardening at high-dose (> 1.54 dpa).

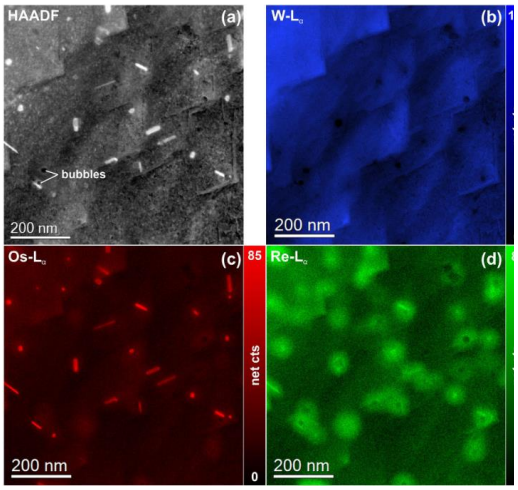

Figure 17: STEM image of the distribution of the a) defects b) tungsten c) Osmium d) Rhenium [49]

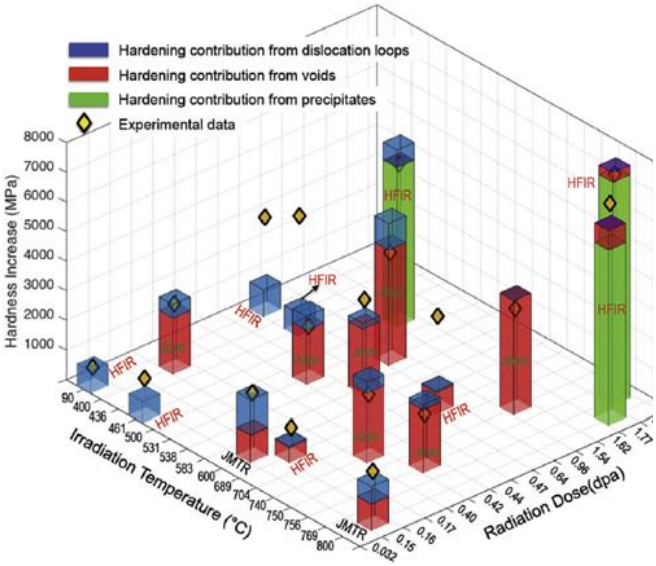

Figure 18: Calculated contribution on the hardening based on of various irradiation experiments in different experimental reactors (HEIR and JOYO) [51]

I.3 Generation of the microstructural defects induced by irradiation

Because of the effect of irradiation on the macroscopic properties of material that we have highlighted in Chap I.2, it is important to better understand the mechanisms that are at the origin of the evolution of the microstructure.

I.3.1 Cascade collisions created under neutron irradiations

First, when a neutron or an energetic particle (atom, ion...) enters a solid, it interacts with the electrons and nuclei of the target and thus loses its incident energy along its path. Some of these interactions are elastic collisions with nuclei in which the impinging particle can transfer kinetic energy to the target atom called the Primary Knock-on Atom (PKA).

The fate of the PKA will depend on the transmitted energy T and on a target property, namely the displacement energy threshold, noted $\boldsymbol{E_d}$.

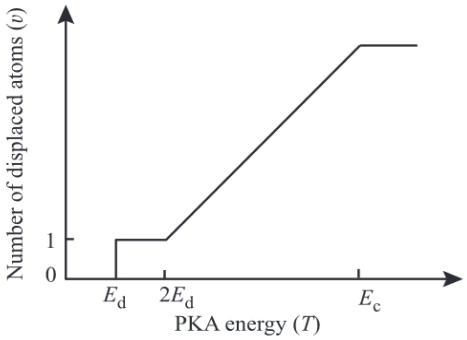

Figure 19: Number of displaced atoms by using Kinchin-Pease (K-P) model [56,57]

$$v(T)\begin{cases} 0 & T < E_d \\ 1 & E_d < T < 2E_d \\ \frac{T}{2E_d} & 2E_d < T < E_c \\ \frac{E_c}{2E_d} & T \geq 2E_c \end{cases} \qquad \textit{eq. 3}$$

According to the Kinchin-Pease (K-P) formalism [57], as shown in Figure 19, if the transferred energy T is lower than E_d, no atom will be displaced; When $E_d < T < 2E_d$, the PKA will be displaced, and exist as an '***interstitial***' atom in the lattice. Meanwhile, its initial site will be vacant, and becomes a '***vacancy***', thus a '***Frenkel pair***' (FPs) has been generated. When the transferred energy is high enough, for instance, in the energy range of $2E_d < T < E_c$, where E_c is the cut-off energy[1], more or less large number of atoms will be displaced. In this case, the PKA has a sufficient energy to displace another lattice atom, giving up an energy T' that could be still sufficient to move a third atom, and further interatomic collisions may be generated until $\frac{T}{2E_d}$ atoms are displaced, thus generating a '***cascade***' of collisions.

[1] Cut-off: the threshold energy above which the energy will not be taken into account in the simulation

Based on the K-P formalism, a simplified model [58] was proposed by M.I. Norgett, M.T. Robinson, and I.M, Torrens, namely NRT model expressed in Figure 20, in which the threshold energy E_d is the unique parameter to quantify the number of displaced atoms and T_D is the available energy to generate the defects. From the NRT model, the displacement per atom (dpa) can be estimated as the ratio of the number of the generated FPs over the number of total atom number of the same volume. This model is also the theoretical base of the 'quick-calculation option' of the Stopping and Range of Ion in Matter (SRIM) software. This method is the most used to estimate the defect distribution for irradiation experiments.

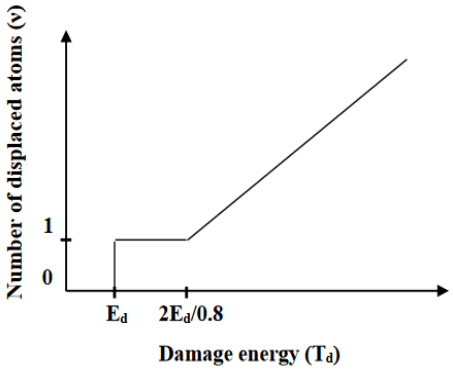

Figure 20: Number of displaced atoms by using NRT model [58,59]

$$v(T)\begin{cases} 0 & T_d < E_d \\ 1 & E_d < T_d < \frac{2E_d}{0.8} \\ \frac{0.8\,T_d}{2E_d} & \frac{2E_d}{0.8} < T_d < \infty \end{cases} \qquad \textit{eq. 4}$$

Concerning the value of the threshold displacement energy E_d also called TDE, the commonly used value is 90 eV for tungsten as recommended by the American Society for Testing and Materials (ASTM). However, Mason et *al.*[60] calculated the average TDE using the experimental values found for different crystalline directions reported by Maury et *al.*[61]. A mean value of 55.3 eV was obtained close to the results (between 45 and 61 eV) calculated using Molecular Dynamics (MD) [62]. This value is the new recommended TDE for tungsten by International Atomic Energy Agency (IAEA) [63] and used in present work. Besides, Banisalman et *al.* [64] have found a value of 85 (4) eV using also MD calculations. It seems that the discrepancy on the estimated TDE value in tungsten is not resolved so far and depends particularly on the empirical potentials that are used for these calculations [65,66]. It is necessary to keep it in mind, because the TDE value is essential for predicting the radiation damage.

A schematic illustration of the various defects (Vacancy, Interstitial, Transmuted atom…) induced by neutron irradiation in tungsten was represented in Figure 21. [67]. After a collision cascade [68], a large number of interstitial atoms were induced in the vicinity of the scattering path of the PKA, resulting in a 'void' (vacancy cluster) which localized in the core of the cascade.

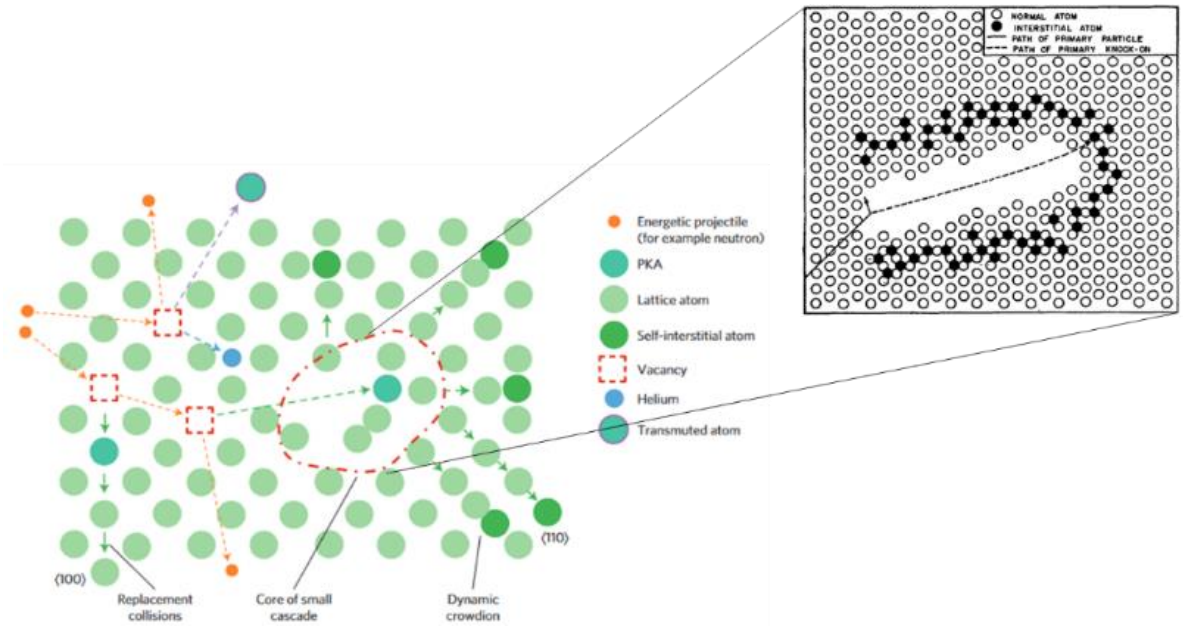

Figure 21: Outline of collision cascade [67,68]

The damage induced in collision cascade triggered by an energetic atom (PKA for example) can be calculated using molecular dynamics [69]. It has been shown that damage production becomes a linear function of recoil energy after the onset of subcascade[2] break-up [70]. More recently, De Baker et *al.*[66] simulated the displacement cascades induced by 50 keV tungsten recoiled atom using various empirical potentials. This energy is expected to be lower than the critical energy to create subcascade in tungsten (i.e. approximately 75 keV [71]). The distributions plotted in Figure 24 show the typical power law which vanishes at the maximum cluster size [72] with a bump which is due to the distribution of the largest defects in each cascade.

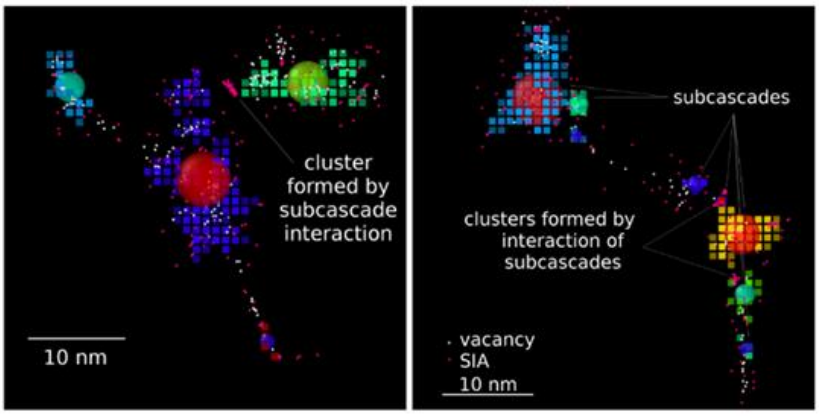

Figure 22: Representative outline of subcascades determined using MD simulation in iron [73]

[2] subcascade: multiple damage region separated in crystal lattice Figure 22

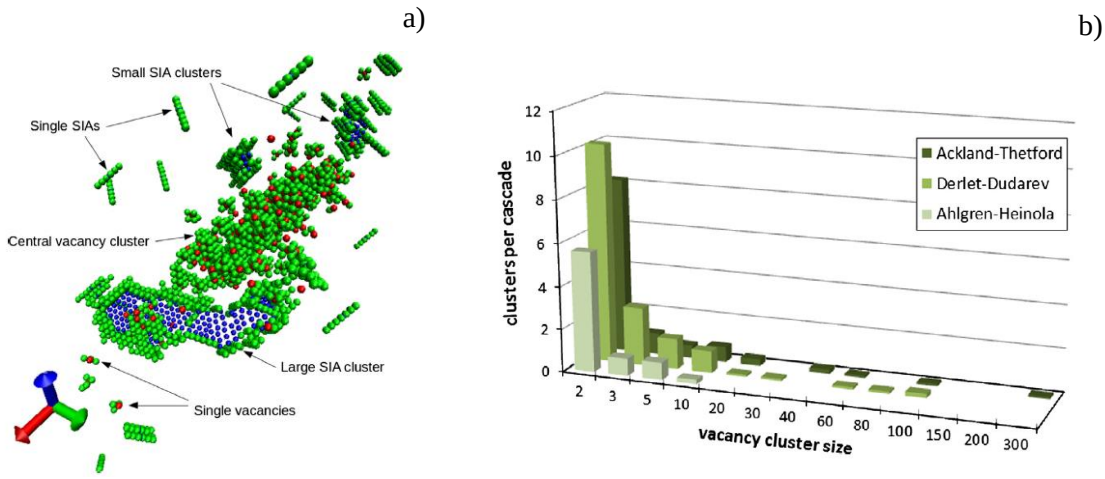

Figure 23 : a) Final damage configuration from a 150 keV PKA in W. (see [69] for details. b) size distribution of vacancy clusters for cascades simulated in random directions, with the A–T (Ackland-Thetford), D–D (Derlet-Dudarev) and A–H – Ahlgren-Heinola) potentials

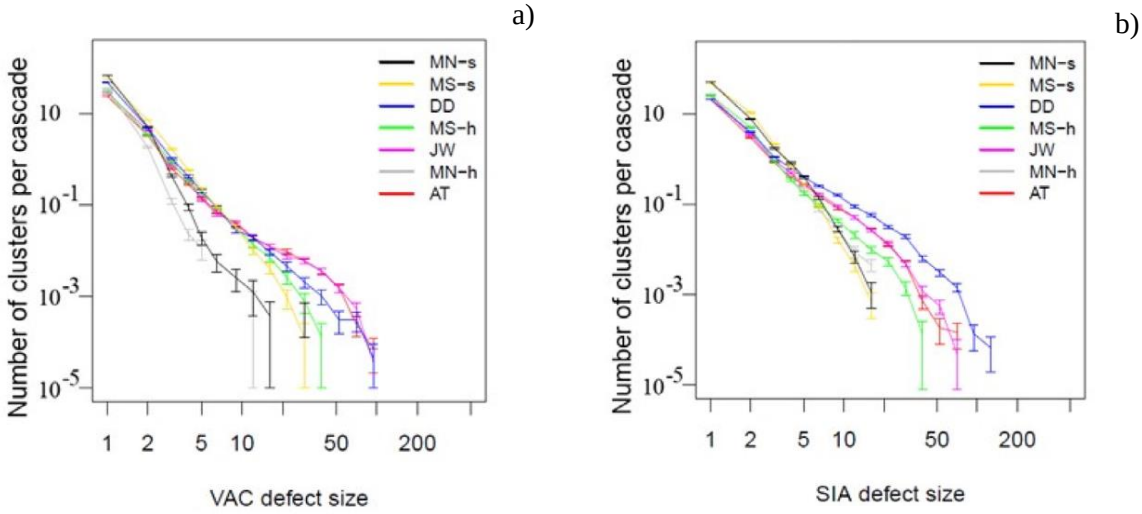

Figure 24 : Point defect cluster size distributions in 50 keV displacement cascades created in W. a) vacancy cluster, b) SIA cluster calculated using various empirical potentials from [66]

Among the radiation-induced defects (RIDs) found in tungsten at the end of the cascade, the point defects (single vacancy, V_1 and self-interstitial atom, SIA) represent the majority about 80 to 90 % for V_1 and between 60 to 80 % for SIA depending on the empirical potential. In addition, some clusters are also created directly in the cascade. Their fraction decreases with their size. The fraction of clusters made of 10 or more vacancies or SIA is less than approximately 0.2 % and 1 % respectively depending on the empirical potential.

In addition, the point defects (PD), i.e. FPs (a single vacancy, V_1 + a self-interstitial atom, SIA), are the predominant defects after light particle irradiations (electron [61], ^{3}He [74], and ^{1}H [75]). PD are the elementary species to form more complex defects, and their fate during irradiation and post-irradiation treatments will rely on their own properties as well as those that control their interactions with each other and with the extrinsic species.

I.3.2 Point defects (PDs) properties in tungsten

The formation and migration energy of V_1 and SIA were determined by both experiments and theoretical calculations. Some reported energies have been summarized in Table 1. For the single vacancy, the mean experimental formation E_f and migration E_m energy is about 3.6 eV, and 1.80 (10) eV, respectively. These values are close to theoretical ones E_f = 3.43 eV and E_m = 1.76 eV. At the same time, the migration energy of SIA in tungsten is very low. The highest reported value is about 0.085 eV from [64,76], which is lower than the lowest one (1.44 eV) [77] for the single vacancy by a factor of 17, suggesting a much greater mobility of the SIA in contrast to the single vacancy in tungsten, even at very low temperature [78].

Single vacancy, V_1				Self -interstitial atom, SIA			
E_f (eV)	E_m (eV)	Methods	Ref	E_f (eV)	E_m (eV)	Methods	Ref
	1.86-2.08	DFT	THE [79]		≤ 0.020	HVEM OKMC	EXP & THE [80]
3.11-3.46	1.66	DFT	THE [81,82]		0.05	DFT	THE [83]
3.6	1.7-1.8	Quenching Annealing TEM Resistivity	EXP [84–88]	8.871-9.557	0.009 - 0.027	MD	THE [89]
3.56-3.63	1.44-2.05	MD	THE [77]		0.054 ± 0.005	Isochronal resistivity recovery	EXP [90]
3.56	1.78	DFT	THE [83]	8.4 - 9.8	0.027- 0.061	MD	THE [77]
3.75	1.80	DFT	THE [91]		0.027	DFT	THE [92]
	1.85 ± 0.05	PALS Annealing	EXP [93]	9.9 9.98	0.002 0.005	DFT	THE [91]
3.6		FIM Resistivity	EXP [94]		0.079-0.085	FIM & Isochronal annealing	EXP [64,76]

Table 1 : Formation E_f, and migration E_m energy of single vacancy and self-interstitial atom in tungsten determined by experiments (EXP) or theoretical calculations (THE)

I.3.3 SIA and vacancy cluster properties

Due to the high mobility of SIA, several complexes of SIA were characterized in tungsten and also in other BCC metals (Mo, Ta, Fe…). Figure 25 illustrates the different structures identified in BCC metals [95]. On the one hand, the split 'Dumbbell' i.e. an SIA correlated with a lattice atom sharing the same crystallographic site (Figure 25.a-c). Except for split dumbbell, the SIAs can also be incorporated at the tetrahedral (TIS, Figure 25.d) or octahedral (OIS, Figure 25.e) lattice site, with a relatively higher

energy of formation. It suggests that the TIS and OIS occupation sites are more difficult to form comparing to dumbbell. On the other hand, the 'crowdion' structure (Figure 25.f) results in the incorporation of one SIA between two near neighbors atoms in the <111> direction giving rise to a unidimensional distortion [96]. The SIAs prefer to align in <111> , <001>, and <110> directions [97–99], according to the Ab initio calculations [81]. The SIA dumbbell along the <111> direction was considered as one of the most stable structure in tungsten, which differs from BCC iron, for which the most stable structure is that of <011> dumbbell [100,101]. Afterwards, Amino et *al.* [80] combined high-voltage electron microscopy (HVEM) and object kinetic Monte Carlo (OKMC) and they demonstrated that the <111> crowdion is the most stable structure in tungsten. These results are in agreement with density functional theory (DFT) calculations [83,102], which is similar to Molybdenum (Mo). Moreover, a new result obtained by using DFT calculation [89] showed that the <111> dumbbell and crowdion have the equivalent formation energy, the fast motion of the SIAS in <111> direction occurs through a series of transformation between the dumbbell and the crowdion.

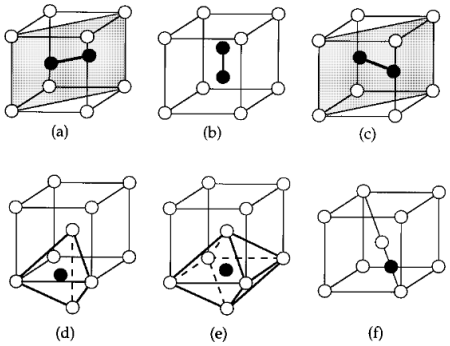

Figure 25: Different interstitial configurations in bcc metals, (a) <110> split dumbbell, (b) <001> split dumbbell, (c) <111> split dumbbell, (d) tetrahedral site, (e) octahedral site, and (f) crowdion site. [95]

Moreover, the motion of the SIAs is considered as the origin of the different microstructural evolutions. They can form larger clusters by agglomeration, such as dislocation loops and dislocation lines. Regarding the vacancy clusters in tungsten, since their tiny size, they are invisible to most of the techniques, thereby, the theoretical calculations are the efficient method for predicting their properties. Becquart et *al.*[81] calculated, using DFT, the binding energy of a single vacancy to a cluster until it contains 7 vacancies. They found that this energy is negative for a cluster made of two vacancies (di-vacancy, V_2), indicating that both vacancies repulse each other even for positions with a distance of the fifth nearest neighbor (NN), suggesting the di-vacancy is an instable structure [72]. In addition, from a cluster containing three V_1 (tri-vacancy, V_3), the binding energy is slightly above zero and it increases with increasing of the number of V_1 in the cluster.

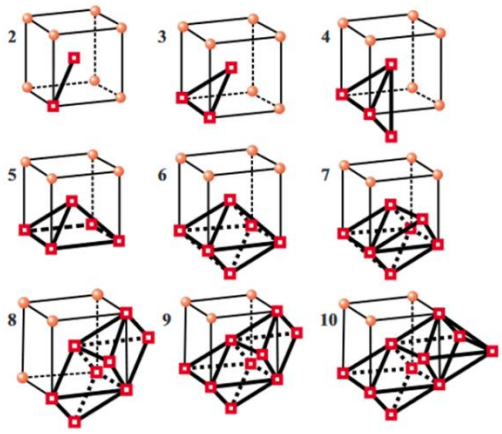

Figure 26: The lowest energy configuration of vacancy clusters containing 2-10 vacancies, calculated by BOP [82]

Number of vacancy in the cluster	Binding energy (eV)	Number of vacancy in the cluster	Binding energy (eV)
2[a]	0.6559	7	1.7459
3	1.1127	8	1.8353
4	1.8942	9	2.2658
5	1.7833	10	2.2686
6	2.2953		

[a]Nearest neighbor configuration

Table 2: the binding energies of a one vacancy to a cluster containing 2-10 vacancies, calculated by BOP [82]

However, Ahlgren et *al.* [91] calculated the binding energies of a vacancy to a cluster containing 2 to 10 vacancies using BOP (Bond Order Potentials), which are summarized in Table 2. The lowest binding energy is that of the di-vacancy, about 0.66 eV. This value is in agreement with the recommended value (0.85 ± 0.15 eV) obtained by experiment [94], in which a migration energy of di-vacancy was estimated to be greater or equal to 0.9 eV (1.65 eV in [103]), and its mobility is expected to be equivalent to that of the single vacancy, with a slight energy deviation less or equal to 0.3 eV [87,94,103]. Nevertheless, the increase in binding energy is not strictly proportional to the number of single vacancies added in the cluster, decreasing slightly from four (V_4) to five vacancies (V_5), and the highest value was found for six vacancies (V_6), which is probably due to a stable structure with an octahedral shape. In addition, the new ab initio calculation performed by Becquart et *al.* [104] for cluster containing from 2 to 8 vacancies also showed the highest binding energy for six vacancies. Compared to the single or di-vacancy, the tri-vacancy was found to have higher mobility in tungsten [105] as well as other BCC metals. For larger vacancy cluster ($>V_{10}$), Hou et *al.* [106] are suggested a new model for BCC metals, by using First-principles density functional theory (DFT), Object kinetic Monte Carlo (OKMC) calculations and Molecular statics simulations, the result match better to the experiments in contrast to the simple spherical model. Due to the relatively lower migration energies, indicated by the theoretical calculations (Fe [64], Mo [107], Nb [64]). However, the relatively high formation energy and lower binding energy of the di- and tri-vacancy predicted by simulations [64,102,105], suggesting unfavorable formation of such defect in the BCC metals. Furthermore, Li et *al.* [108] performed OKMC (Object Kinetic Monte Carlo) simulation to investigate the formation of the void lattice (Figure 13), which is considered as a consequence of the synergy of the fraction of the clustered vacancies in cascades and the 1D <111> SIA motion.

I.3.4 Impurities interactions with defects

In addition, impurities can strongly interact with RIDs. Numerous theoretical works predict the interactions between the Light-Element (LE) impurities with PDs. Castin et *al.* [109] demonstrated the effect of carbon on the evolution of the SIA loops in self-ion irradiated tungsten by combining OKMC simulation and experiments (SIMS and TEM). Table 3 summarizes the properties of LE (H, C, N, O) atoms by using the first-principles calculations in tungsten lattice [22–30]. These results indicated that the LE atoms favor OIS or TIS occupancy near single vacancies (V_1) in the tungsten matrix. Furthermore, the high binding energies between LE atoms and V_1 suggest the LEs tend to be trapped in single vacancies. One V_1 can trap more than one LE atom. For instance, a single vacancy can trap as many as 12 hydrogen atoms [33], 4 carbon atoms [82], 6 nitrogen atoms [110], and 6 oxygen atoms [111]. Becquart et *al.*[104] and Heinola et *al.*[103] demonstrated that the presence of carbon in vacancy stabilize the 2NN di-vacancy in tungsten in agreement with [112], and the presence of H atoms enhances also the stability of the di-vacancy [113] with a binding energy greater than that of the V_1-H [114]. The number of H atoms trapped at a V_1 decreased with increasing temperature, the recommended maximum number is twelve [115]. Meanwhile, LE-vacancy complexes were also studied in other BCC metals. Barouh et *al.* [64] predicted the complex of tri-vacancy (V_3) correlated to one LE atoms (X), i.e.V_3-X, is the most mobile solute in BCC iron [64]. It was also found that the vacancy-oxygen complexes interact with hydrogen atoms in vanadium [116]. Besides, the number of trapped H atoms in a single vacancy decreases with increasing of trapped C atoms in tungsten lattice [112], i.e. one V_1, V_1-C_1, V_1-C_2 and V_1-C_3 could trap 12, 8, 5 and 3 H atoms, respectively.

X	E_f^X *(eV)*	E_m^X *(eV)*	$E_b^{V_1-X_1}$ *(eV)*	$E_b^{V_1-X_n}$ *(eV)*
H	4.05 (SS) 0.93 (TIS) [117] 1.27 (OIS)	0.21 (TIS-TIS) [118] 0.59 (OIS-TIS)	1.24 [112]	0.34 [112] (V_1-H_{12})
C	4.25 (SS) [119] 2.24 – 2.28 (TIS) [112,119] 0.78 (OIS) [119]	1.46 (TIS-OIS) [82] 3.87 (OIS-TIS)	1.93 [82]	1.54 [120] (V_1-C_4)
N	-0.13 (SS) -3.06 (TIS) [121] -3.79 (OIS)	0.73 (TIS-OIS) [121] 3.60 (OIS-TIS)	2.48 [110]	9.66 [110] (V_1-N_6)
O	0.5 (SS) -1.75 (TIS) [111] -1.43 (OIS)	0.17 (TIS-TIS) [111] 0.32 (TIS-OIS)	3.04 [110]	11.21 [110] (V_1-O_6)

Table 3 : Calculated formation energy E_f^X, migration energy E_m^X of element X and its binding energy with a tungsten single vacancy $E_b^{V_1-X_1}$, and the binding energy, $E_b^{V_1-X_n}$ of a tungsten single vacancy with the maximum of LE atoms that can be trapped, n. (SS: substitutional site TIS: tetrahedral interstitial site, OIS: octahedral interstitial site)

Apart from these theoretical results, Vehanen et *al.* [122] demonstrated in carbon-doped electron-irradiated bcc iron, using positron annihilation spectroscopy that carbon-vacancy complexes are formed in stage III (200 K, related to V migration) due to the trapping of vacancies by carbon atoms. These

carbon-vacancy complexes prevent the clustering of vacancies up to about 450 K where dissociation of the V-C complex was observed. They also showed that at about 350 K carbon atoms become mobile, and can be trapped in the V-C complexes. The higher the number of carbon atoms, the more the generated V-C_n complexes hinder the positron trapping. However in tungsten, only Amarendra et *al.* [123] assumed the formation of carbon-vacancy complexes in the annealed tungsten, and Yabuuchi et *al.* [124] evoked the formation of the hydrogen-vacancy complexes in electron-irradiated tungsten, without quantifying the C and H atoms. Therefore, further experiments are necessary to better understand the formation of the LEs vacancy-complexes and their effect on the evolution of the defects.

I.3.5 Diffusivity of single vacancy and LE atoms in tungsten

Comparing the migration energy to that of the aforementioned V_1 (1.80 (10) eV), the single LE atoms have higher mobility against V_1. As the migration of SIAs was confirmed at even cryogenic temperatures, only the diffusivity against the temperature of V_1 was estimated in the following by using the same method as in [124]. The result is compared with that of the LEs diffusivity in tungsten lattice. The diffusion coefficient of the V_1 and LEs could be described by using Arrhenius equation (eq. 5), Using values of D_0 and migration energies reported in Table 4, it allows to roughly estimate of the diffusion length at a given temperature for time (t), i.e. $L_{diff} = \sqrt{D_x t}$.

$$D_x = D_0 e^{\left(-\frac{E_x^m}{k_B T}\right)} \qquad \textit{eq. 5}$$

with D_0: pre-exponential factor acquired from [124]

E_x^m: migration energy of object x (V_1, H, C, N, and O)

k_B: Boltzmann constant 1.38×10^{-23} J.K^{-1}

T: temperature K

Figure 27 illustrates the estimated diffusion length as a function of the temperature for diffusing time ranging from 1 hour to 1 year. A comparable high mobility of the H and O atoms was revealed. They can diffuse on 3.6 nm and 9.5 nm at 20 °C in 1 s, respectively. Whereas carbon atoms and V_1 can only diffuse 0.003 nm and 0.6 nm at 300 °C in 1 s. Thereby, they are expected to be immobile at a temperature lower than ~300 °C.

	D_0 (m^2.s^{-1})	E^m (eV)
V_1	2.91×10^{-9}	1.66 [81]
H	5.2×10^{-8}	0.21 [118]
C	2.56×10^{-7}	1.46 [82]
N	1.66×10^{-7}	0.73 [110]
O	7.57×10^{-8}	0.17 [125]

Table 4: Values of pre-exponential factor D_0 [124] and migration energy E_X^m of single vacancy V_1 and LEs (H, C, N, and O)

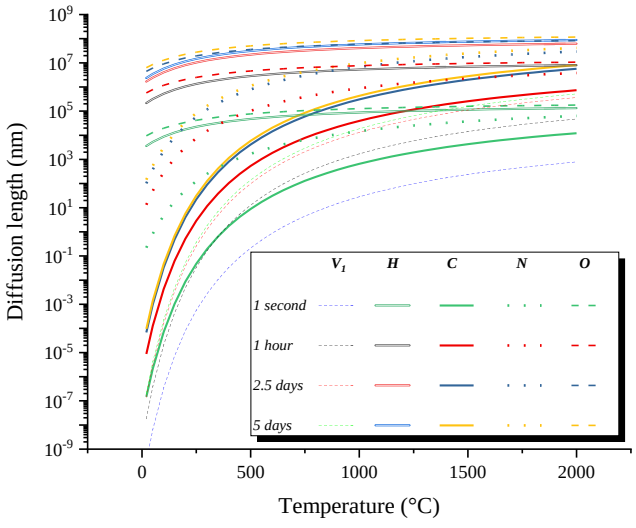

Figure 27: Estimated diffusion length from the eq. 5 with the parameters given in the Table 4 as a function of the temperature of single vacancy V_1 and LEs (H, C, N, and O) in tungsten during several times (1 second, 1 hour, 2.5 days, and 5 days)

I.3.6 Thermal evolution of the defects

Concerning the microstructural evolutions of the RIDs were investigated in fast neutron-irradiated tungsten. G.H. Kinchin and M.W. Thompson [88] carried out electrical resistivity measurement in the neutron-damaged tungsten. A recovery of the resistivity was observed at -193 K and 593 K with activation energy of about 0.48(2), and 1.7(1) eV, respectively. After that, Thompson [85] performed a new resistivity recovery (RR) measurement in neutron-irradiated tungsten (E_n > 1 MeV, 10^{11} to 10^{13} n.cm^{-2}.s^{-1}) at cryogenic temperatures (4 K, 77 K), after which five RR stages were identified, and they are presented in Figure 28.a.

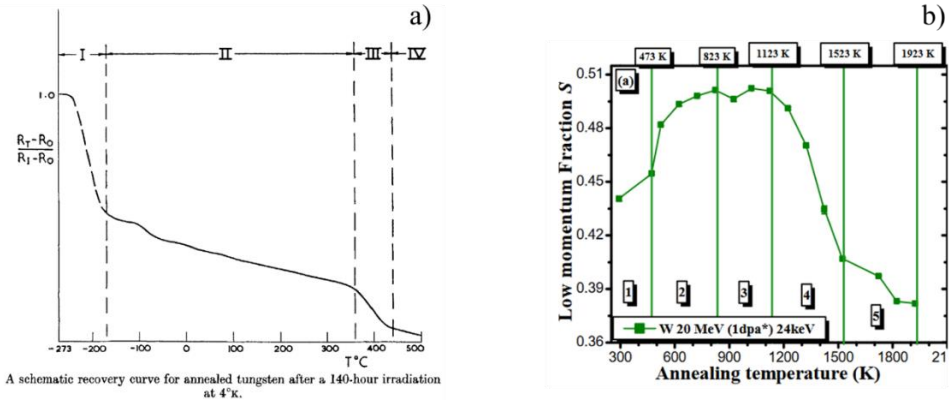

Figure 28: a) RR in the neutron irradiated tungsten as a function of the temperature[85] and b) the evolution of vacancy-type defects as a function of versus annealing temperature [126]

The first recovery was overserved below -100 K (**stage I**), in which the SIAs should be already mobile, on the contrary to V_1. The V_1, grain boundaries (GP), impurity atoms, and dislocations are the potential traps for SIAs. Thus, the **recombination of the FPs** at near positions, due to the migration of the SIAs was considered as the main evolution at this stage. From RT to 623 K (**stage II**), the SIAs are still mobile and the detrapping of the SIA and the recombination of the FPs at farer positions are expected. Yi et *al*. [127,128] observed the highest density of the dislocation loops, with a majority of ½<111> Burgers vector (> 60%), which might be a consequence of the 1D motion of the <111> dumbbells and crowdions, as mentioned in the end of the Chap I.3.3. Between 473 and 723 K (**stage III**), a variety of experimental studies (FIM [129], TEM [127], TDS [130], and PAS [131]) indicated the formation of large vacancy clusters, which probably results of the agglomeration of the single vacancies. Therefore, the **stage III** was attributed to the **migration of the single vacancies**. Another stage was highlighted for higher temperature, ranging from 723 to 1173 K (**stage IV**), according to the previous PAS [126] study results in self-ion irradiated tungsten (Figure 28.b). In this temperature range, whatever the size or density of the vacancy cluster, the positron annihilation characteristics remain constant before the decrease of total vacancy defects. This result is in agreement with a TEM [132] study, in which the density of the dislocation loops decreases abruptly with increasing size from 1073 K and

the density of the vacancy clusters continue to decrease while their size increases at higher temperature range (**stage V**), suggesting the coalescence of the vacancy clusters.

I.3.7 Characterization of the vacancy-type defects - PAS

In the aim of investigating the vacancy-type defects, the PAS is an essential technique which allows the detection of the vacancy-type defects ranging from the single vacancy to vacancy cluster. Both positron annihilation spectroscopy (PALS) and Doppler Broadening (DB) spectroscopy can be used. Both techniques are based on the annihilation of the positron with electrons of solids allows to probe electron density and momentum distribution respectively (the principle and experimental implementation of these techniques are presented in ***Chapter II : MethodologyChapter II : Methodology***). The nature of the annihilation states can be identified by different annihilation characteristics such as positron lifetime and momentum distribution of annihilated positron and electron pairs.

Figure 29 represents the positron annihilation lifetime for perfect lattice, dislocation and the single vacancy in the tungsten, which were determined by experiment (dark symbol) or theoretical calculations (red symbol), the exact values are summarized in Table 5.

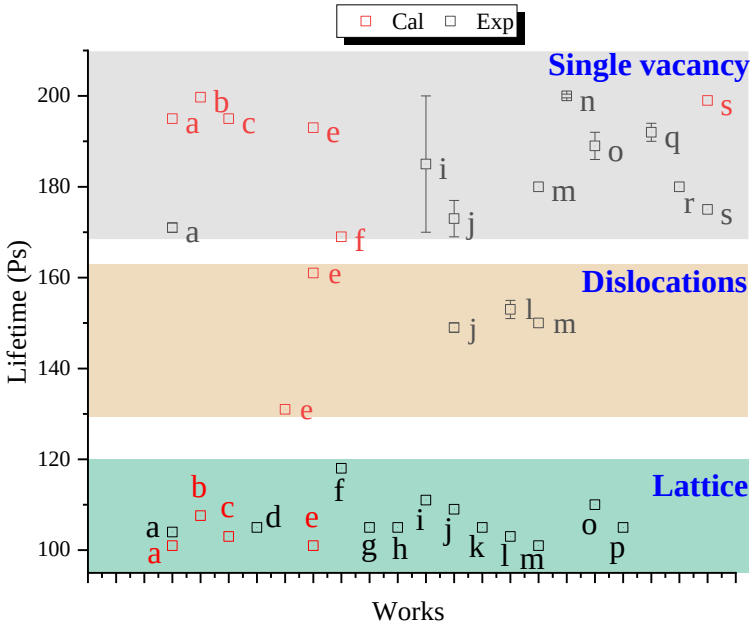

Figure 29: Experimental and theoretical works on the positron annihilation lifetime of the single vacancy (V_1), dislocation and the Lattice of the tungsten, determined by experiments (□) or theoretical (□) calculations

The mean value of the positron lifetime in the perfect lattice of tungsten is comparable for both theoretical and experimental works, about 105 ± 5 ps, and the theoretical work predicted a lifetime of about 195 ps for V_1 in tungsten. However, the lifetime of the single vacancy (V_1) is more controversial in the experimental works.

	τ_L (ps)		τ_{disl} (ps)		τ_{V1} (ps)		Ref
	EXP	THE	EXP	THE	EXP	THE	
a	104	101			171 ± 1	195	[124]
b		107.6				199.7	[133]
c		103				195	[134]
d	105						[135]
e		101		131, 161		193	[136]
f	118				169		[137]
g	105						[138]
h	105						[139,140]
i	111 ± 1				185 ± 15		[93]
j	109 ± 1		149 ± 1		173 ± 4		[141]
k	105				170 ± 10		[142]
l	103 ± 2		153 ± 1				[143]
m	~105		150		180		[144]
n					200.0 ± 0.4		[74]
o	115 ± 5				189 ± 3		[75]
p	105 ± 1						[145]
q			163 ± 7		192 ± 2		[146]
r			<180		180		[147]
s					175	199	[148]

Table 5: Positron annihilation lifetime in the Lattice τ_L, dislocation τ_{disl}, and single vacancy τ_{V1} of the tungsten determined by experiments (EXP) or theoretical (THE) calculations

Some experimental works have also found values equivalent to those of the simulation, such as 200 ps in [74], 192 ps in [146], and 189 ps in [75], whereas a short lifetime of about 180 ps was found in [127, 128]. In the recent experiments carried out by Yabuuchi et *al.* [124], a reduced positron lifetime was detected from 171 to 195 ps for single vacancy like defects. In their simulation they found the single vacancy decorated by hydrogen atoms has a shorter lifetime of about 184 ps, 169 ps, and 164 ps for the complex V_1-H_1, V_1-H_2, and V_1-H_3, respectively. Same reduction of the positron lifetime is also calculated for V_1-O (168 ps) and for V_1-C (171 ps). Thereby, it is reasonable to consider the shorter lifetime of the V_1 is in fact related to the LEs-decoration of vacancies. Nonetheless, as that lifetime of

the dislocations in tungsten was found around 150 ps, it might be difficult even impossible to distinguish these defects in experiment by measuring positron lifetime, when they coexist.

Vacancy cluster Vn n = 2, …	Positrons lifetime (ps)	
	Exp	Cal
V_2		226 [136]
V_{3-4}	319 [135] 270-280 [75]	247 ± 10 [133]
V_{6-9}	300-312 [137]	
V_{8-9}	380 [135]	355 ± 10 [133]
V_{10}	410 [149]	
Cavity	400-450[140]	<437 [133]

Table 6 : Positron annihilation lifetime in the vacancy cluster Vn, where n = 1, 2 …. of the tungsten determined by experiments (EXP) or theoretical (THE) calculations

Furthermore, the positron lifetime at various size of vacancy clusters was also determined in tungsten. Table 6 summarizes the value obtained by the experiments and simulations. It should be noted that the size of the cluster determined by experimental works is estimated by using the lifetime values predicted in the work of Troev et *al.* [133]. The positron lifetime increases with the size of vacancy cluster or with the number of vacancies in the cluster up to saturation. The positron lifetime saturates at nearly 450 ps [133] when the cluster is large enough, which is also observed in experiment. When the cluster is large enough (~V_{27}), its size is roughly estimated to be about 1 nm in diameter. At such size, positron annihilates essentially at the periphery of the cluster. The curvature of the vacancy cluster is so low compared to the size of the positron that the periphery is equivalent to the tungsten atoms' surface. So the annihilation characteristics do not evolve any more if the vacancy cluster is large enough.

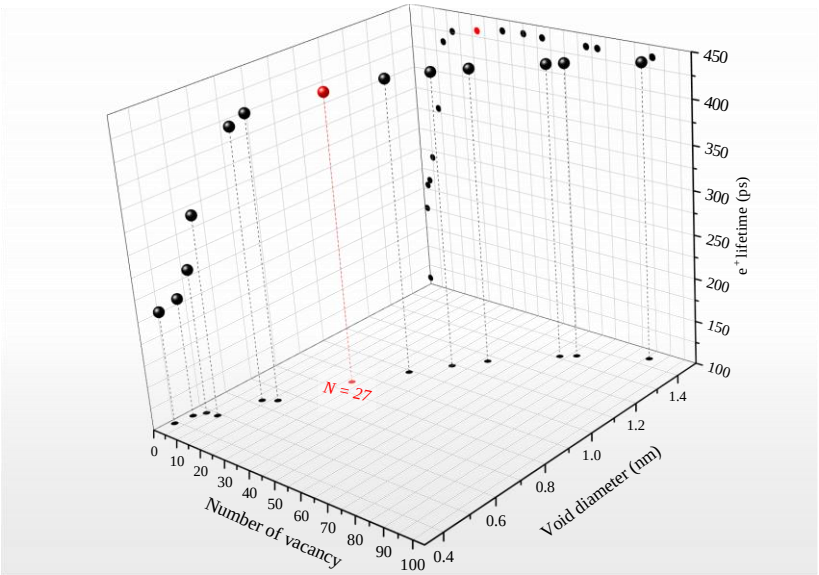

Figure 30: Simulating prediction of the positron annihilation lifetime in tungsten with increasing size of the vacancy cluster.

Bedside, the measurements of the Doppler broadening of the 511 keV gamma emitted from annihilation of positron and electron can be also used to determine the nature of vacancy defects. Most of the time the ***S*** and ***W*** annihilation fractions namely low (and high respectively) momentum annihilation fractions of the electron positron pairs are measured (see Chap II.3.1.3 for details on how these parameters are measured and determined). Some values of annihilation characteristics ***S*** and ***W*** have been already identified in tungsten: for *the defect free* **Lattice**, *the single vacancy, and the largest vacancy cluster ever detected*. Their values as measured with the DB-Spectrometer of CEMHTI in previous works [36,126] in polycrystalline tungsten are given in Table 9. As the lifetime, ***S*** increases when positron is trapped in a vacancy and with the size of the vacancy cluster. In contrast ***W*** decreases and it is also important to notice that it is sensitive to the chemical environment of the positron when it annihilates, as it has been shown in several studies on semiconductors [150].

Summary

Controlled fusion is considered as one of the solutions to nowadays energy and environmental issues. With this in mind, the ITER project, a new generation of tokamak, was launched to demonstrate the energy production capability of these fusion reactors. Not only numerous technological obstacles remain to be overcome, but materials research is also one of the key issues in achieving the production of the energy with fusion. Tungsten, the most promising PFM, has been selected to cover the divertor, a very critical component, in ITER and is being considered for the inner wall of the future TOKAMAK where it will have to withstand the high heat flux and the bombardment of energetic particles. Tungsten has several suitable properties of major importance to withstand these extreme operating conditions, namely efficient thermal conductivity, low sputtering rate and a very high melting temperature. However, the degradation of some properties has been found when exposed to conditions close to those expected in TOKAMAK. This degradation was proved to be related to the microstructural evolution of the material induced by exposure to energetic products of the fusion reactions and to the plasma. These exposures induce defects in the material and their accumulation and transformation lead to this microstructure evolution. The investigation of the behaviour of radiation-induced defects is therefore essential to better recognize the origin of the various degradations and to be able to predict the evolution of the material during its operation and lifetime.

The study of defects in tungsten has been the subject of research for several years in various laboratories. At CEMHTI, we specifically used PAS to investigate vacancy defects. The fundamental properties of single vacancy and vacancy clustering in tungsten have been revealed experimentally. Defects induced by various ions (^{1}H, ^{3}He, Fe, W...) under different conditions were studied. The use of isochronous annealing after the irradiations allowed to highlight the behavior of single vacancy and vacancy clusters and the interaction between vacancy defects and He atoms was observed. Preliminary

results also showed that the evolution of vacancy clusters varies for samples from two batches of different purity.

In this chapter, the different consequences of irradiation of tungsten by energetic particles have been explained. The types of induced defects have been distinguished and their fundamental properties have been defined. Their evolution was described in different steps related to these fundamental properties. It was also pointed out that many theoretical studies predict that light elements (LEs: hydrogen, nitrogen, carbon and oxygen) interact strongly with defects, especially vacancies, but that little experimental work has been done. Positron annihilation spectroscopy has been demonstrated to be a very useful technique to characterize irradiation-induced vacancy defects in materials and their decoration with impurities.

The objective of this thesis is therefore to carry out several experimental studies to better understand these potential interactions and their consequences on the microstructure of irradiated tungsten. Tungsten samples of different purities (99.95 to 99.9999 wt. %) were irradiated under different conditions: **i/** electron irradiations to introduce countable point defects, **ii/** self-irradiations to create neutron-like defects. The nature and distribution of the radiation-induced defects (RIDs) were characterized by PAS and TEM. In addition, quantitative chemical analysis techniques (SIMS, NRA) were used to access the distributions of LE atoms (C and O), and correlate them with the defect results obtained by PAS and TEM.

We believe that the state-of-the-art experimental data acquired in the present work could help to verify the theoretical simulations and be useful to predict further microstructural evolutions in tungsten, which could lead to the degradation of tungsten properties under extreme conditions in the fusion reactor in the future.

Chapter II : Methodology

In this chapter, the material preparation and experimental techniques have been explained.

The first section presents the chemical composition of as-received polycrystalline tungsten samples of two purities from different suppliers (Neyco, Goodfellow, and FZJ), as well as the preparation procedures: pre-polishing, polishing, and annealing…

In the second section, the conditions of various irradiations and implantations (e^-, C, O, and W) performed in tungsten are reported. The damage and implantation profiles calculated using SRIM are shown.

The third part, is dedicated to the description of the characterization techniques used in this work. Positron annihilation spectroscopy (PAS) is used to detect the vacancy-type defects, in particular to probe the defects with low concentration and/or small size. PAS allows to detect the defects within a range from single vacancy to vacancy clusters in metals (W [73], Fe [150]). Secondary Ion Mass Spectrometry (SIMS) is a sensitive technique for depth profiling of chemical composition and Nuclear Reaction Analysis (NRA) is an ion beam analysis technique especially adapted to probe the light-elements close to the surface. In this thesis, SIMS and NRA are used to quantify the light-elements impurities (LEs) such as C, O in the tungsten. Meanwhile, Transmission Electron Microscopy (TEM) provides a direct observation of the large vacancy defects. In the present work, it is combined with PAS for the characterization of the radiation-induced vacancy defects in tungsten, ranging from single vacancy to large vacancy cluster.

II.1 Preparation of the samples

In this work, various types of polycrystalline tungsten samples of two purities were provided by different suppliers. The extra-high purity (XHP, 99.9999 wt.%) samples with a thickness of about 500 µm were provided by Forschungszentrum Jülich (FZJ) from Plansee in two batches, namely FZJ1 and FZJ2. The two batches were cut from the same rod by electrical discharge machining (EDM). the potential contamination of copper should be removed by the staining after cutting. Figure 31.a shows the chemical composition of the XHP samples determined by Laser Ablation Inductively Coupled Plasma Mass Spectrometry (LA-ICP-MS) and provided by the supplier. Besides, the rolled and sintered high purity (HP, 99.95 wt.%) samples with a thickness of around 150 µm and 300 µm were purchased from Goodfellow (GP) and Neyco (N) company, respectively. The samples of two purities were purchased in two shapes, squares (7 × 7 mm^2) and discs (Ø 3 mm), in order to be adapted to the characterization techniques (PAS and TEM respectively). The concentration of impurities as given by the providers are reported in Figure 31.b. It has to be noticed that the concentration of most of the elements are maximum values reflecting the detection limits of the techniques used for determination.

The concentration of light elements such as carbon (C), oxygen (O) and nitrogen (N) is either not provided or is a maximum value and not a precise value.

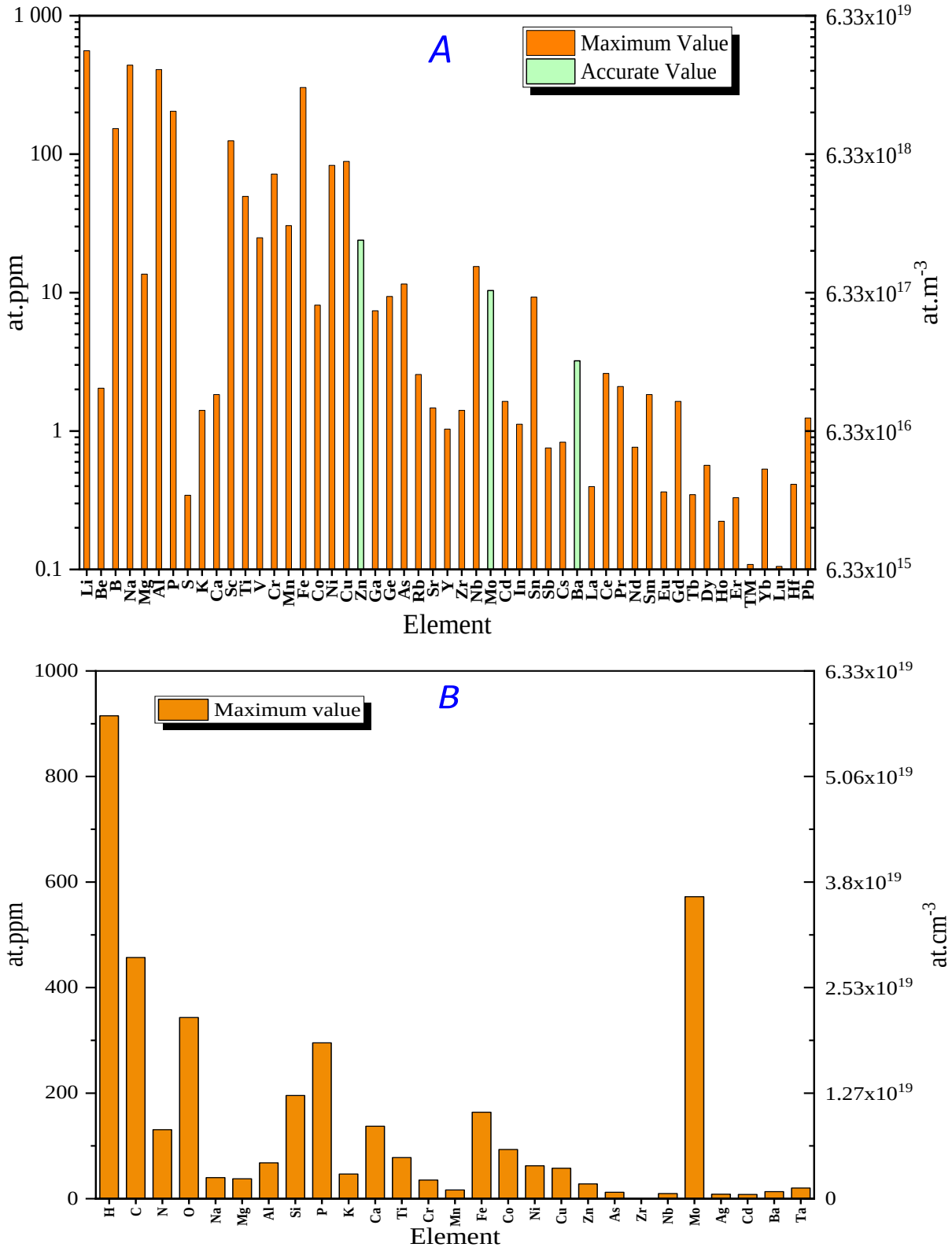

Figure 31: Concentration of the impurity elements A: in XHP (99.9999 wt.%) tungsten sample provided by FZJ and B: in HP (99.95 wt.%) purchased from Goodfellow

Before the irradiations, the as-received samples were prepared following the same procedures. Firstly, to remove the surface-layer which probably contains induced defects and impurities introduced during the manufacture, the samples were mechanically pre-polished using abrasive silicon carbide (SiC) papers with different grains size, within a range from P320 to P2500 purchased from the ESCIL company. The choice of the grain size depends on the aspect and thickness of the sample, for eliminating as much as possible the scratches left by the earlier paper with the larger grains. Thus, the abrasive papers were used with decreasing grains size in succession. Next, the surface of the sample was improved by flocked felt ranging from FD 3 µm to 1 µm, with applying the corresponding diamond paste to obtain a mirror-like aspect. Then, the as-polished samples were cleaned up in the ultrasonic bath with acetone and ethanol in sequence for 20 min. Lastly, the as-polished samples were annealed to eliminate the defects induced during the polishing procedures.

II.1.1 Electron bombardment furnace

As mentioned in P.E Lhuillier's thesis [36], the samples annealed in a high vacuum give out the annihilation characteristics close to perfect tungsten ***Lattice*** in contrast to those annealed in argon-hydrogen (Ar-H_2) chamber. Therefore, all as-polished samples in this work were annealed under a high vacuum (<10^{-6} mbar) level at 1700 °C for at least one hour. The annealing was carried out in a furnace in which the heating is generated through electron bombardment. The sample holder in tungsten is situated above a tungsten filament in which an electronic current flows, and a high voltage of 1400 V is applied between the sample holder and the filament. A series of pumping systems keep the vacuum in the furnace chamber at the level between 10^{-9} and 10^{-7} mbar for a temperature ranging from room temperature (RT) to 2000 °C. The vacuum chamber is cooled during annealing thanks to the circulation of cooled water in a pipe welded to the exterior walls of the chamber to avoid potential contamination. The annealing temperature is controlled with a pyrometer aimed at a molybdenum (Mo) sample through a quartz viewport. This pyrometer works in a range of wavelength λ between 0.85 to 1.1 µm, the transmittance (without viewport) is fixed at about 0.9 for each annealing. The emissivity of Mo rises from 0.06 to 0.27 with increasing temperature from 100 to 2400 °C, and the relative error is significantly greater with increasing of the temperature [151]. At the same time, the emissivity depends also on the wavelength as well. Therefore, according to the mean value of various experimental and theoretical results [152], at around 1700 °C, the emissivity of 0.25 is used for each annealing of the preparation. The pyrometer had been checked recently by aiming on a black body with certainly an emissivity of about 1, this experiment guarantees the temperature measurements, ranging from 300 to 2000 °C, and the error of the lecture was estimated far less than 1 °C with or without the viewport in the temperature range from 600 to 2000 °C.

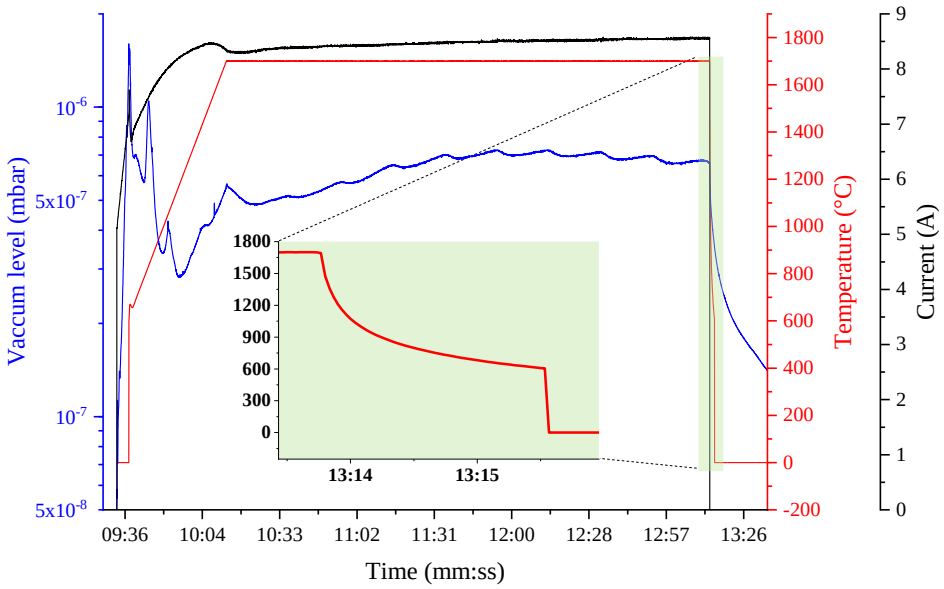

Figure 32: An instance of the annealing temperature, vacuum level, and applied current versus time and insert plot show the natural cooling of the end of the annealing.

During the annealing, the temperature, the vacuum level, and the applied current were monitored and recorded. Figure 32 illustrates an example of the curves of the annealing temperature, vacuum level, and applied current versus annealing time, and the inserted plot shows the natural cooling at the end of the annealing. To reach a high temperature of 1700 °C, a current of around 8.5 A was applied with additional polarization of the emitted electrons at 1.4 kV, which is triggered when the temperature is superior to 1000 °C. The temperature is controlled with a continuous slope of 30 K/min to guarantee the longevity of the furnace.

As shown in the blue curve of Figure 32, not surprisingly, the vacuum level increases with increasing temperature. At the beginning of the annealing, the pressure increases with fluctuation in a short time before stabilizing at a relatively high vacuum level (~6 × 10^{-7} mbar). This increase step is probably due to the desorption of residual impurity atoms on the sample or heated component of the system. Moreover, the natural cooling is extremely fast at the beginning, the temperature decreases from 1700 to 600 °C in around two seconds. Because of the out-of-range of the pyrometer, the monitor of the natural cooling ends at 600 °C. Taking the long natural cooling into count, the as-annealed samples were generally taken off in two hours after each annealing, when the difference of the in-out temperature of the furnace is minimal.

Figure 33 shows the microstructure of the as-annealed polycrystalline tungsten samples from different suppliers (a: Neyco (N), b: Goodfellow (GP), and c: FZJ). The mean grains sizes of each sample were roughly estimated using an optical microscope, at about a few tens micron for Neyco, and a few hundred microns for Goodfellow, and FZJ, respectively. This difference might be first related to the fabrication procedures, because the samples purchased from Neyco were produced by sintering, differing to those of GP (rolled) and FZJ samples. In addition, the N-samples were annealed at lower

temperature with a shorter time (1600°C, 1h) in contrast to 1700 during 3h for GP and FZJ samples, so that the recrystallization is less complete in the case of the N-sample.

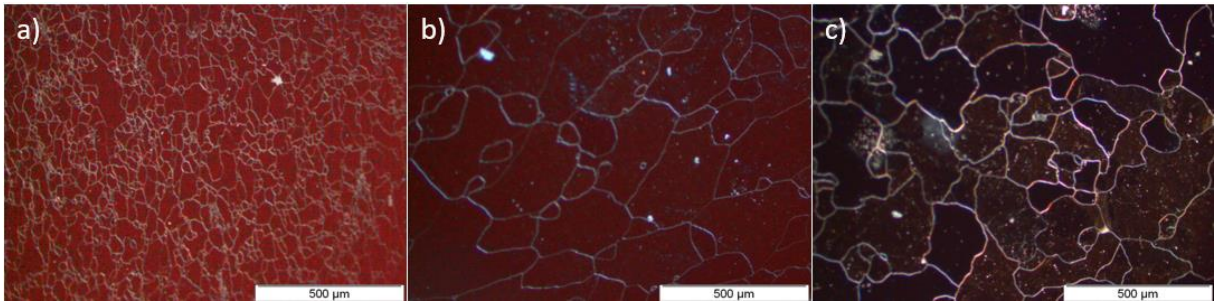

Figure 33: Optical Images of as-annealed polycrystalline tungsten samples a) Neyco, b) Goodfellow and c) FZJ obtained by optical microscope

The as-annealed discs (Ø 3 mm) prepared for TEM observations were further electropolished into thin foils (electron transparent areas of ~60 nm thickness) using Tenupol-5 with a double jet of prepared NaOH solution (0.05 mol. L^{-1}, 15 °C, and 15 V) for ~10 minutes. Lastly, the thick square samples (thickness > 100 µm) were checked before irradiation by using PAS for further comparison, and the thin foil samples were qualified by TEM. The qualified thin foil samples have homogenous large grains with the lowest possible dislocation density and other microstructural defects (see Figure 34).

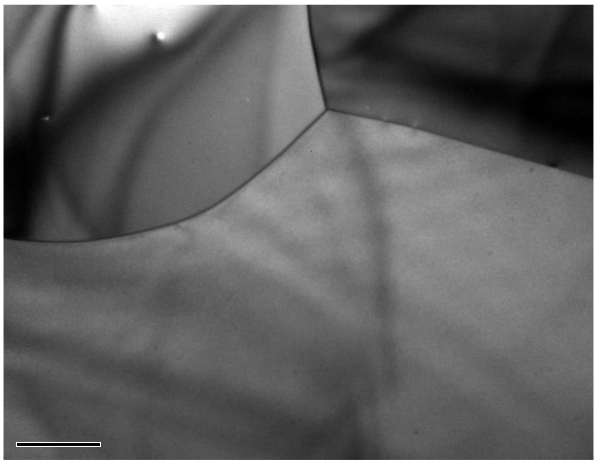

Figure 34 : TEM image acquired just before irradiation of an irradiation zone with an interaction of three grains boundaries

II.2 Creation of defects and introduction of impurities

Tungsten has been selected to cover the divertor of the ITER TOKAMAK and the first interior wall of the DEMO, and these two parts suffer the high-energy neutron irradiation generated from the D-T fusion reaction. Moreover, the light-element impurity (C and O) in the plasmas and in the reactors should not be ignored [24,153,154]. Therefore, it is crucial to understand the radiation-induced damage in various conditions. In this work, because of the generation of similar defects (vacancy, dislocation, dislocation loop, void…), the self-ions irradiation was used as the proxy of the neutron irradiation with different conditions. To investigate the effect of the impurities, the ion-implantation of carbon and oxygen was carried out, the irradiated samples were utilized for the quantification of carbon and oxygen concentration in the samples. In addition, the electron irradiation at room temperature was performed, expecting to induce the simplest detectable defects, i.e. single vacancy.

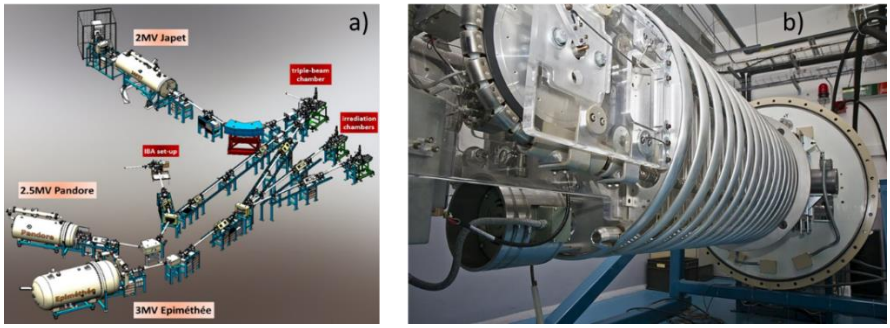

Figure 35: Ooverview of the electrostatic accelerator Épiméthée (Saclay) and b) SIRIUS (LSI)

Accordingly, several ions (C, O, and W) irradiations were carried out on the 3 MV electrostatic accelerator (Épiméthée) at CEA Saclay, JANNuS (Joint Accelerators for Nano-science and Nuclear Simulation) platform. The experimental fluences were designed utilizing the SRIM (Stopping and Range of Ions in Matter) program with Kinchin-Pease (K-P) formalism [155]. The used displacement threshold energy E_{disp} is fixed at 55.3 eV which averages the values of the different crystalline directions [63]. On the other hand, the electron irradiations at RT were accomplished on the accelerator SIRIUS installed at Laboratoire des Solides Irradiés (LSI). The fluences were selected by operating the POLY et SMOTT program [156–158], expecting to introduce detectable single vacancies.

II.2.1 Electron irradiations

The 2.5 MeV electron irradiations were performed on HP (99.95 wt.%) samples (slabs: Neyco, disc: Goodfellow) with the same flux (5.5×10^{13} $cm^{-2}. s^{-1}$) for two fluences, namely low fluence (LF: 1×10^{19} cm^{-2}) and high fluence (HF: 2×10^{19} cm^{-2}), respectively. The irradiation temperature was kept at around 50 °C. An image of the experimental sample holder is shown in Figure 36.a, which contains three slabs, five discs, and one thin foil sample. The calculated damage profile of 2.5 MeV electron in tungsten for the experimental fluences (LF, HF) is plotted in Figure 36.b. The damage dose of both fluences decreases with increasing depth, and becomes negligible at about 220 µm, the damage evolves linearly until 150 µm. Besides, as shown in Figure 36.c, the damage dose is approximately a plateau in the first 1 µm, corresponding to a mean damage value of about 8.33×10^{-4} dpa for HF, and 4.16×10^{-4} dpa for LF with the same standard deviation around 1×10^{-6} dpa.

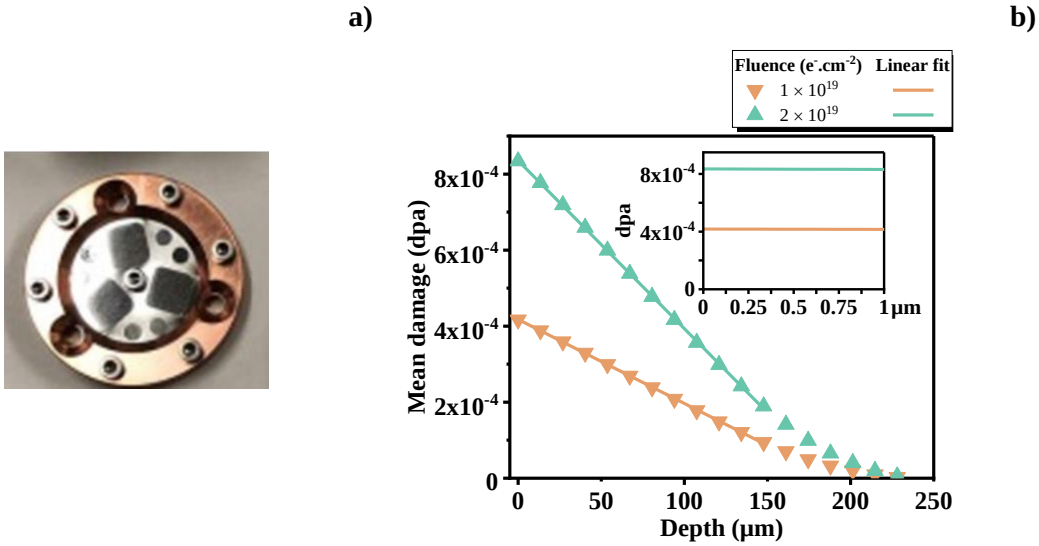

Figure 36: a) experimental sample holder used for electron irradiation. b) Calculated damage profile of 2.5 MeV electrons in tungsten by POLY ET SMOTT program for two fluences LF: 1×10^{19} cm^{-2} and HF: 2×10^{19} cm^{-2}, c) the zoom of the damage profile in the first 1 µm

II.2.2 Self-ion irradiations

In order to be adapted to the PAS characterization with slow positrons, the 20 MeV self-ion irradiations were ex situ accomplished on the two purities (HP: 99.95 wt. %, XHP: 99.9999 wt. %) thick square and disc samples with various fluences rising from 4.14×10^{12} to 1.1×10^{14} cm^{-2} at several temperatures (from RT to 700 °C). According to simulating results (SRIM-2008), the corresponding damage doses range from 0.01 to 0.32 dpa in the probed region of the slow positrons (~700 nm, see in Chap II.3.1.1). For high temperature (HT) irradiations, the temperature is controlled by a thermocouple (TC1) inserted in the heating plate which is in contact with the sample holder. In addition, a thermal camera cross-checks the temperature by measuring the surface temperature at different positions on the samples.

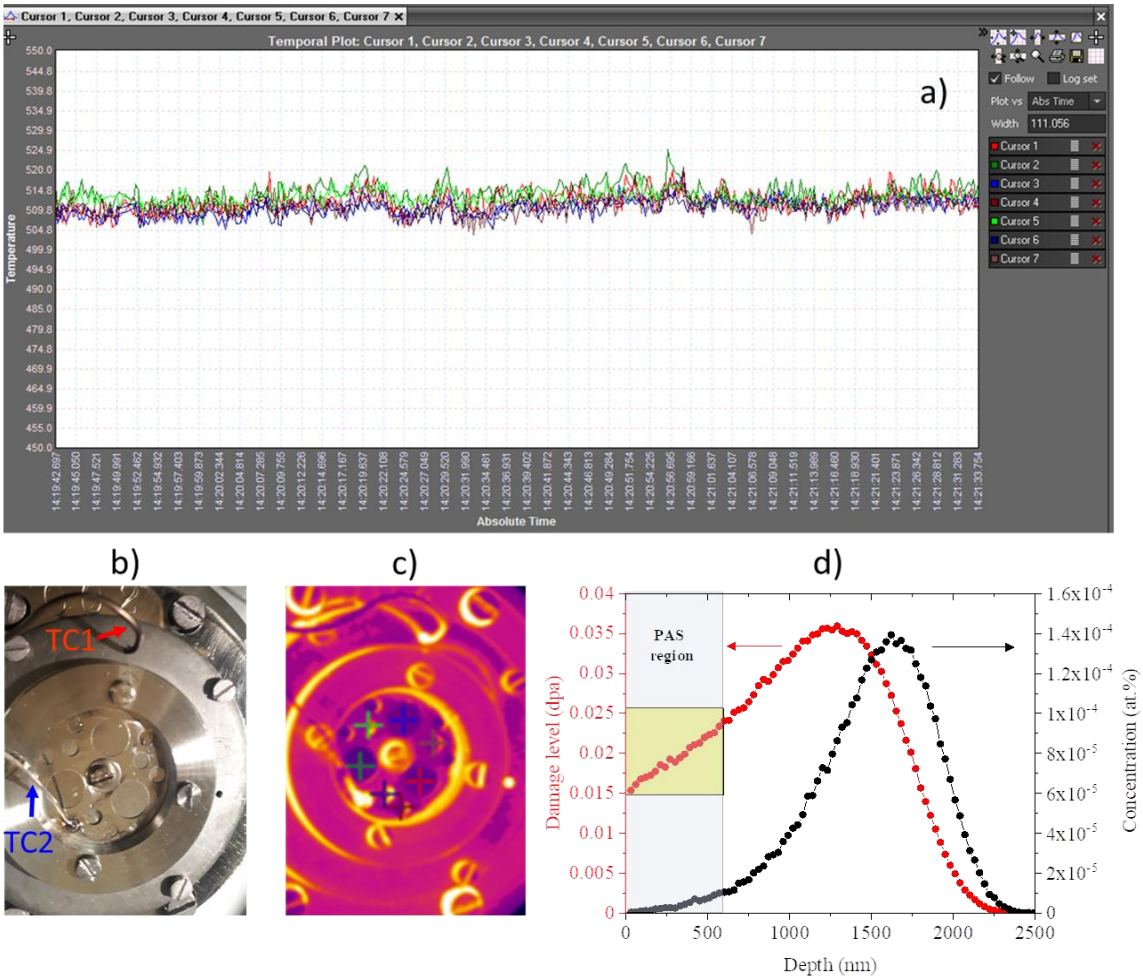

Figure 37: Self-ion irradiation at high temperature (500 °C) to a mean damage dose of about 0.02 dpa in the PAS probed region and 0° for the experimental ion-incident angle, ***a)*** *temperature evolution during the irradiation at several places on the sample holder monitored by a thermal camera* ***b)*** *the sample holder contains three squares, eight discs tungsten samples, and one iron sample on which a thermocouple is welded* ***c)*** *the image recorded by a thermal camera and* ***d)*** *the corresponding implantation ans damage profiles were estimated by using SRIM-2008 in Kinchin-Pease formalism [155] with a fluence of 7.48 × 1012 cm-2 and the displacement threshold energy fixed at 55.3 eV [63]*

Figure 37.a shows the camera-recorded temperature corresponding to the selected positions (Figure 66.c) during an irradiation at 0.02 dpa and 500 °C. To verify the temperature measurement, as shown in Figure 37.b, another thermocouple (TC2) was welded on an iron disc sample. Thus, a difference of less than 25 °C between the real and expected irradiation temperature was observed. Figure 37.d illustrates the damage and implantation profiles of 20 MeV self-ion irradiation of tungsten calculated by SRIM-2008 (K-P mode, E_{disp} = 55.3 eV) with an ion fluence of 7.48 × 10^{12} cm^{-2} and normal incident angle (the irradiations at RT performed with an incident angle of 15°), corresponding to a damage level of about 0.02 dpa in the first 700 nm of the sample, i.e. the region probed by PAS.

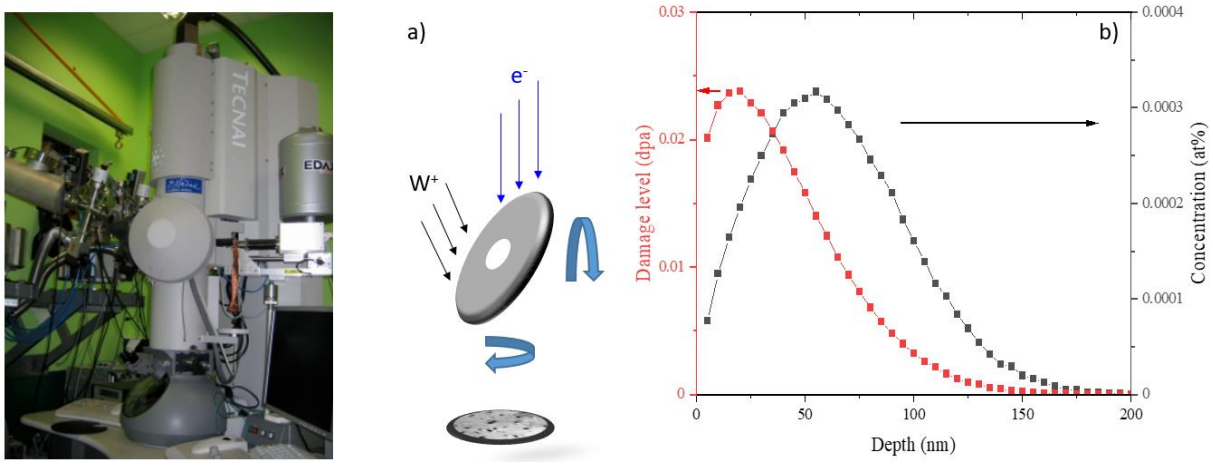

Figure 38: a) overview of the in situ TEM equipment with a sketch of in situ 1.2 MeV self-irradiation of tungsten, b) the calculated damage and implantation profiles by SRIM-2008, K-P formalism with a displacement threshold energy of 55.3 eV for an ion fluence of 1.8 × 10¹² cm⁻² and the ion incident angle of 45°

To monitor the evolution of the defects during the irradiation, the self-ion irradiations at 1.2 MeV were realized in the in situ TEM facility at JANNuS platform in the Laboratoire de Physique des 2 infinis Irène Joliot-Curie (IJCLab). The qualified tungsten thin foil was in situ irradiated in 200 kV FEI Tecnai G2 TEM with two fluences (1.8×10^{12} cm^{-2} and 3.6×10^{12} cm^{-2}) at various temperatures (RT, 500, 700 and 800 °C). Figure 38 illustrates the outline of the in situ irradiation and TEM observation, the incident angle of the tungsten ions is of about 45° to the sample for whole irradiations. During the irradiation, the ion bombardment and the heating might tilt the thin foil, if that is the case, a little adjustment with the double-tilt sample holder is needed as sketched in Figure 38.a.

Figure 38.b shows the damage profile of the 1.2 MeV self-ion irradiation of the tungsten as predicted using SRIM-2008 (K-P mode, E_{disp} = 55.3 eV) for a fluence of 1.8×10^{12} cm^{-2} with an incident angle of 45°. As the thin foil has a thickness of about 50 nm, the mean damage level is about 0.021 dpa, similar to that of the 20 MeV ex situ self-ion irradiation with the fluence of 7.48×10^{12} cm^{-2}. Moreover, the experimental fluxes for ex situ and in situ irradiations were fixed at values as close as possible ~2.8×10^{10} cm^{-2}. s^{-1} and ~3.0×10^{9} cm^{-2}. s^{-1}, respectively, to obtain a comparable mean damage rate of about 5×10^{-5} dpa. s^{-1}.

Apart from the 1.2 MeV and 20 MeV, a series of 2 MeV self-ion damaged tungsten samples (99.95 wt.%, Plansee) provided by Culham Centre for Fusion Energy (CCFE) were also studied in this work. The samples were irradiated at RT with several fluences, ranging from 1×10^{12} to 2×10^{14} cm^{-2}. Figure 39 shows the calculated damage profile with SRIM of 2MeV self-ion irradiation of tungsten (K-P mode, E_{disp} = 55.3 eV), for a fluence of 1×10^{12} cm^{-2}, the related damage dose at the peak of the damage profile i.e. of about 70 nm around 0.0085 dpa.

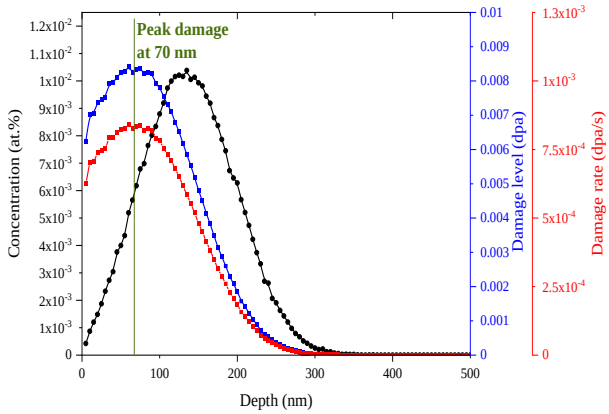

Figure 39: Damage profile of the 2 MeV self-ion irradiation of tungsten calculated by SRIM-2008 (K-P mode, E_{disp} = 55.3 eV) for a fluence of 1 × 10^{12} cm^{-2}, the related peak damage level at 70 nm is around 0.0085 dpa.

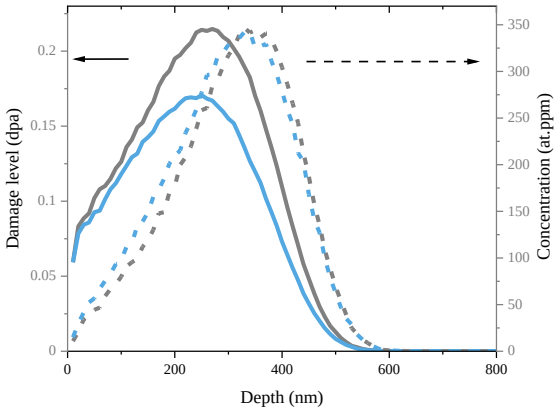

Figure 40: Damage (solid lines) and implantation (dashed lines) profile of 450 keV carbon (grey), and 510 keV oxygen (blue) in tungsten calculated by SRIM-2008 (K-P mode, Edisp = 55.3 eV, 15°) for a fluence of 8.29 × 10^{14} cm^{-2}, 6.29 × 10^{14} cm^{-2}, and 6.59 × 10^{14} cm^{-2}, repectively. The concentration of implanted ions is about 340 at.ppm at 330 nm for each implantation

II.2.3 Ion implantations

Furthermore, for quantifying the concentration of the principal light-element impurities (C, O) in the samples and at the same time to study the ion effects on the generation of the defects, several ions (C, and O) implantations were realized in tungsten with three fluences at RT. By operating the SRIM-2008 (K-P mode, E_{disp} = 55.3 eV, 15°) program, the three fluences of each type of implantation were selected, i.e. low fluence (LF), middle fluence (MF), and high fluence (HF) with a factor of about fourteen and two between MF and LF, HF and MF, respectively. Figure 40 shows the damage (solid lines) and implantation (dashed lines) profile for 450 keV carbon (grey), and 510 keV oxygen (blue) ions in tungsten for the MF 6.29 × 10^{14} cm^{-2} for carbon, and 6.59 × 10^{14} cm^{-2} for oxygen, respectively. The quantity of implanted ions is about 340 at. ppm and 680 at. ppm at RP (330 nm) for MF and HF, respectively of each type implantations. Because the quantity of the carbon, oxygen in the HP samples is predicted to be superior to 200 at. ppm (according to the providers), the implantations were carried out only in the XHP samples, in which the quantity of both LEs is below the detection limit of the LA-ICP-MS technique.

Table 7 summerizes the whole irradiation conditions used in this thesis. It should be noticed that the samples were put in the chamber at least a half-day before the irradiation, so that all the experiments were realized under a high vacuum level around 10^{-5} Pa.

Sample	***Ion / energy***	***Temp (K)***	***Flux ($cm^{-2}.s^{-1}$)***	***Fluence (cm^{-2})***	***Damage dose at the peak of the damage profile (~ 70 nm)***
10 × 10 × 0.5 mm^3 slab HP	2 MeV-W	RT	1.89×10^{10}	1×10^{12}	0.0085
			2.10×10^{10}	1×10^{13}	0.085
			2.18×10^{10}	5×10^{13}	0.425
			2.26×10^{10}	1×10^{14}	0.85
			2.38×10^{10}	2×10^{14}	1.7
Sample	**Energy / Ion**	**Temp (K)**	**Flux ($cm^{-2}.s^{-1}$)**	**Fluence (cm^{-2})**	**Mean Damage dose in the first 700 nm**
7 × 7 × 0.15 mm^3 slab Ø 3 mm disc HP, XHP	2.5 MeV-e-	323	3.86×10^{13}	1.00×10^{19}	8.34×10^{-4}
				2.00×10^{19}	4.17×10^{-4}
	450 keV - C	RT	5.26×10^{11}	4.64×10^{13}	0.016
			5.95×10^{11}	6.29×10^{14}	0.215
			5.32×10^{11}	1.26×10^{15}	0.430
	510 keV - O		4.96×10^{11}	4.64×10^{13}	0.012
			4.96×10^{11}	6.59×10^{14}	0.106
			5.34×10^{11}	5.88×10^{13}	0.342
	20 MeV - W	RT	2.50×10^{10}	4.10×10^{12}	0.012
			2.80×10^{10}	1.10×10^{14}	0.318
		773	3.54×10^{10}	7.48×10^{12}	0.021
			2.22×10^{10}	1.49×10^{13}	0.042
		993	2.23×10^{10}	7.43×10^{12}	0.021
Ø 3 mm thin foil HP, XHP	1.2 MeV - W	RT	3.00×10^{9}	1.80×10^{12}	0.021
				3.60×10^{12}	0.042
		773		1.80×10^{12}	0.021
				3.60×10^{12}	0.042
		993		1.80×10^{12}	0.021
				3.60×10^{12}	0.042
		1093 (Only 3N-HP)		1.80×10^{12}	0.021

Table 7 : Irradiation conditions used in this work.

II.3 Characterization techniques

In this section the characterization techniques used in this work are described. Positron annihilation spectroscopy (PAS) is used to detect the vacancy-type defects, in particular to probe the defects with low concentration and/or small size. Secondary Ion Mass Spectrometry (SIMS) and Nuclear Reaction Analysis (NRA) are used to measure the concentration depth profiles of the light-element such as C, O in the tungsten. Meanwhile, Transmission Electron Microscopy (TEM) provides a direct observation of the large vacancy defects. In the present work, it is combined with PAS for the characterization of the radiation-induced vacancy defects in tungsten, ranging from single vacancy to large vacancy clusters.

II.3.1 Positron annihilation spectroscopy (PAS)

In the past few decades, positron annihilation spectroscopy has been wildly used for characterizing solid materials (semi-conductors [159,160], metal [161], and ceramics [162]), because of its high sensitivity for vacancy-type defects and because it is non-destructive for the matter. In metals, this technique can probe from the smallest vacancy-type defect (single vacancy) to vacancy-cluster by measuring the gamma rays from the annihilation of positron-electron pairs (e^+-e^-), which depends on the local electron density where the annihilation occurs.

II.3.1.1 Physical properties of positrons in matter

A. Positron source and emission

Contrary to electron, positron does not exist in nature, one of the ways to obtain positron is through the beta 'plus' decay (eq. 6), This corresponds to the transformation of a proton into a neutron within the radionuclide, resulting in the release of a positron and a neutrino. In general, most of the radioactive sources allow to generate positron by (p-n) or (n-ɣ) nuclear reactions, some examples are shown in [163].

$$ {}^{A}_{Z}X_n = {}_{Z-1}{}^{A}X_{n+1} + \beta^+ + \nu_e \qquad \textit{eq. 6} $$

With X: a radionuclide

A: atomic mass of X

Z: number of proton

n: number of neutron of element X

β^+ or e^+: positron

ν_e: neutrino

Because of its suitable half-time of decay ($T_{1/2}$ = 2.6 years), the source ^{22}Na is frequently used in the laboratory to produce positron. It is made by depositing (drop by drop) aqueous NaCl solution enriched in ^{22}Na on a thin metal sheet (e.g. Al or Ni). The ^{22}Na disintegration scheme is illustrated in Figure 41, collected from [164]. Positron (β^+) emission occurs with a fraction of 90.06 % (90 % for 540

keV, 0.06 % for 1.82 MeV) by nuclear decay of ^{22}Na to metastable nucleus ^{22}Ne*. It is accompanied with electronic capture[3] (9.94 %). The transition from metastable to stable ^{22}Ne state releases a 1.275 MeV gamma-ray, 3.7 picoseconds (ps) after positron emission. We consider that the emission of positron coincides with the 1.275 MeV gamma-ray. This feature gives the second advantage of the source ^{22}Na. In Positron Annihilation Lifetime Spectroscopy (PALS), the detection of the 1.275 MeV gamma-ray is designated as 'start' and allows to know the birth of positron, and that of 511 keV is referred as 'stop' and indicates the annihilation of positron-electron (e^+-e^-) pairs. The time interval between these two signals characterizes the positron lifetime in the sample which depends on the states (lattice, defects...) where the annihilation occurs.

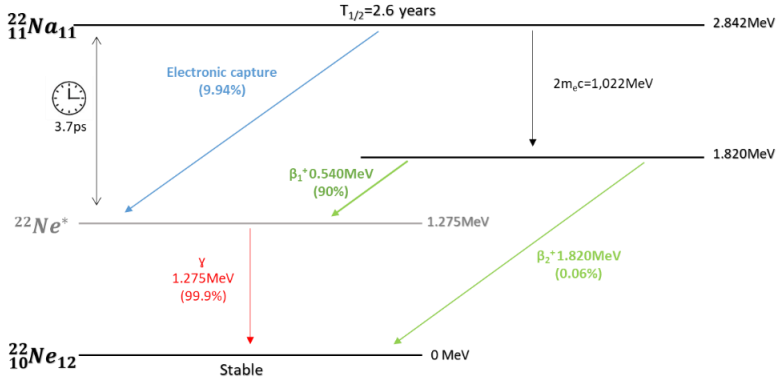

Figure 41: Scheme of ^{22}Na decay. The minimum energy to trigger decay is 1.022 MeV, equivalent to two-electron masses (i.e. $2m_0c$). Positron emission occurs in 99.06% of disintegration (9.94 % for Electronic capture) before reaching metastable state ^{22}Ne, finally, attain a stable state ^{22}Ne by emitting 1.275 MeV ɣ ray*

B. Positron penetration profile

In general, we distinguish two types of positrons in experiment. The first are the *fast positrons*, naturally emitted from a ^{22}Na source, and their energy reaches 540 keV at maximum. Due to the energy distribution of fast positrons, their penetration can be described by a decreasing exponential given by equation (eq. 7) : the penetration depth depends on the density ρ and the atomic number Z of the studied material. In tungsten, the majority of the fast positrons (> 99.99 %) are stopped before 50 µm below the incident surface. The penetration profile of fast positrons in tungsten is plotted in Figure 42 using the modeling parameters from [165].

[3]Electronic capture: an electron captured by a proton near to nucleus, and transforms a proton to neutron emitting a neutrino $P + e^- \rightarrow n + \nu_e$

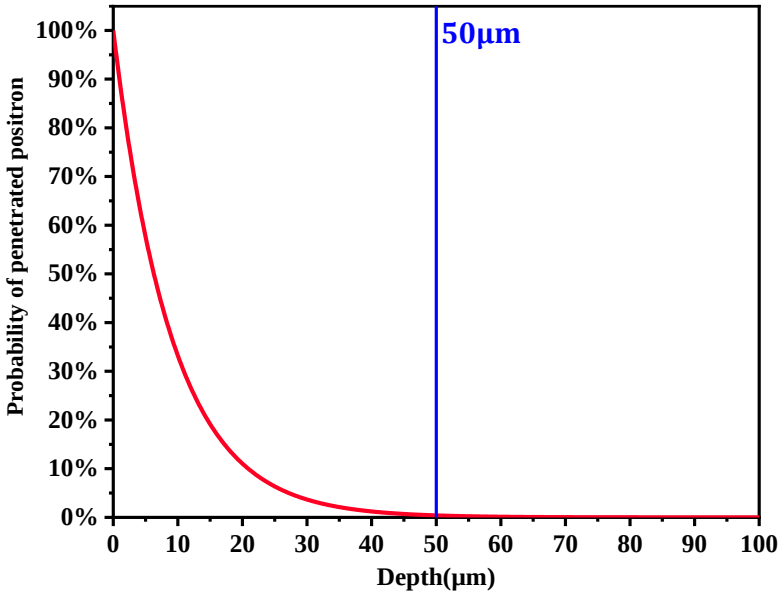

Figure 42: Fast positron penetration profile in tungsten

$$P(d) = e^{-\alpha \cdot d} \qquad \textit{eq. 7}$$

With d: depth,

$$\alpha = \frac{12.6\rho Z^{0.17}}{(E_{\max})^{1.28}}$$

for tungsten with ^{22}Na source,

ρ: density =19.32 g.cm^{-2},

Z: atomic number Z = 74,

$E_{max} =$ *0.541 keV*

The second type of positrons is the moderated *fast positron* i.e. the *slow positrons* produced in a mono-kinetic beam thanks to an accelerator (Figure 47). Among several calculations [165,166], the Makhovian model (eq. 8) represents conveniently the slow positron penetration profile in the material. Figure 43 presents the slow positron penetration profile in tungsten. The penetration profile depends on the density of material ρ (19.32 g/cm^2 for tungsten), the positron incident energy and material less-dependent parameters ($A_{1/2}$, m, and n). The value of m and n vary slightly, however, the parameter $A_{1/2}$, depends not only on the incident energy of positron, but also on the atomic number of the material [167]. Various values of $A_{1/2}$, ranging from 3- 4 [166,168,169] have been reported in semiconductors, and the most recommended value for $A_{1/2}$ is 4.0 (3) µg.cm^{-3}. keV$^{-1.7}$[170]. Nevertheless, the value of $A_{1/2}$ = 2.95 µg.cm^{-3}. keV$^{-1.7}$) was used in previous works of tungsten and iron at CEMHTI [36,126,171,172] and was compared to the simulation work. We checked that the depth profile calculated in copper (Cu) using the parameters $A_{1/2}$ = 2.95 µg.cm^{-2}. keV$^{-1.7}$, m = 2 and n = 1.7 gives the same results as the simulating work [165,173]. With these parameters, the slow positron beam of CEMHTI probes the near-surface defects as deep as 700 nm in tungsten.

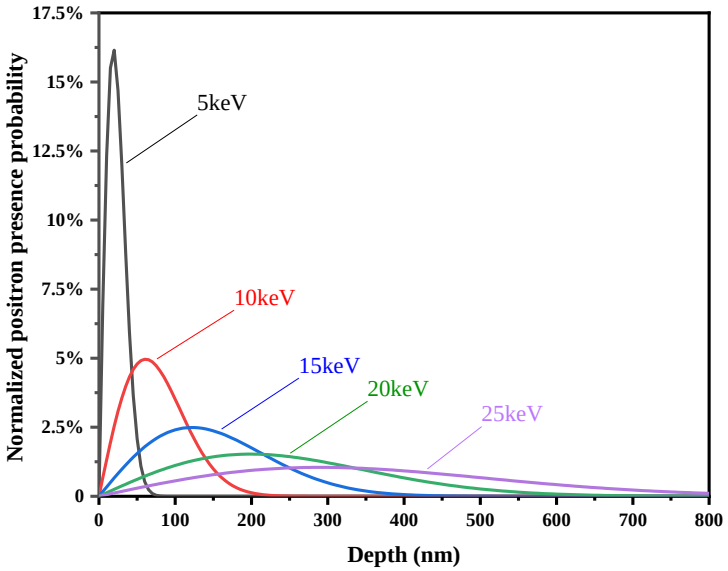

Figure 43: Slow positron penetration profile with various energy in tungsten

$$P(z) = -\frac{d}{dz}\left(e^{-(\frac{z}{z_0})^m}\right) \rightarrow P(z) = \frac{mz^{m-1}}{z_0^m}(e^{-(\frac{z}{z_0})^m}) \qquad \textit{eq. 8}$$

With $z_0 = \frac{z_{1/2}}{(\ln 2)^{\frac{1}{m}}}$ and $z_{1/2} = \frac{A_{1/2}}{\rho} E^n$

$z_{1/2}$ Median implantation depth of positron (cm)

ρ: Density of material (µg.cm^{-3})

$A_{1/2}$ = 2.95 µg.cm^{-2}. keV$^{-1.7}$, m = 2 and n = 1.7

E: Incident energy of positrons (keV)

C. Thermalization, Diffusion, and Trapping

When a positron penetrates in the matter, because of its positive charge, it suffers repulsion: Coulomb force from the nucleus and the free electron screening gas, which makes the positron slow down until thermal energy[4] during 1 - 10 ps [167,174] in metal. In general, the annihilation of the particle with its antiparticle, emits in most cases two gamma rays. Concerning interaction of the positron and matter, the most of the positrons lose almost their kinetic energy before the annihilation with an electron. Therefore, the total energy of the electron-positron pairs is close to twice of the electron[5] ($2m_ec^2$) and depends essentially on the kinetic energy of electrons. It follows that the emitting-gamma rays provide information of the momentum distribution of electron with which positron annihilated. Once the positron is thermalized, it starts to diffuse (migrates freely in all space) in the matter, the diffusion coefficient can be expressed by Nernst-Einstein equation (eq. 9):

$$D_+ = \frac{\mu_+}{e} k_B T = \frac{k_B T}{m_+} \tau_{relaxation} \qquad \textit{eq. 9}$$

[4] The energy at room temperature E = k_BT, where k_B = 1.38 × 10^{-23} J.K^{-1}, at T = 20 °C, E ≈ 0.025 eV.
[5] Electron mass: m_e = 9.109 × 10^{-31} kg, the speed of light in vacuum: c = 2.9979 × 10^8 m.s^{-1}

With μ_+: Mobility of positon

k_B: Boltzmann constant 1.38×10^{-23} J.K^{-1}

T: Temperature K

e: Elementary charge 1.6×10^{-19} C

m_+: Effective mass of positron

$\tau_{relaxation}$: Positron relaxation time for diffusion.

In the bulk of material where the defect concentration is very low, and the material can be considered as a perfect ***Lattice***, the positron thermalization and trapping time is neglected compared to the diffusion time, so that the total positron diffusing time is considered to be the positron lifetime τ_L, which is the reciprocal of the positron annihilation rate of the positron in the ***Lattice*** λ_L. The intrinsic diffusion length in the ***Lattice*** of material, can be written by equation (eq. 10):

$$L^+ = \sqrt{\frac{D_+}{\lambda_L}} = \sqrt{D_+ \tau_L} \qquad \textit{eq. 10}$$

With λ_L: annihilation rate in the lattice

τ_L: diffusion time in the lattice or lifetime of the positron in the lattice

D_+: intrinsic diffusion coefficient of positron ($D^+ = 1.26 \times 10^{-4}$ m^2.s^{-1} for tungsten [174])

It is important to note that the diffusion length of positron can be affected by the concentration of defects (vacancy-type defects, dislocation...) along its path. Indeed, the positrons can be trapped by these defects before annihilation in an interval spanning from 100 to 500 ps in metals [159], thus shortening its path. One defines the effective diffusion length (L^+_{eff}) of positron which depends on the positron trapping rate besides their diffusion. The effective diffusion length ($\boldsymbol{L^+_{eff}}$), can be written as in the equation (eq. 11):

$$L^+_{eff} = \sqrt{\frac{D_+}{\lambda_L + K_d}} \qquad \textit{eq. 11}$$

With K_d: Trapping rate at the defect d

L^+_{eff}: Effective diffusion length of positron

D^+: *intrinsic d*iffusion coefficient of positron

The trapping rate K_d at the defect d is the product of its concentration C_d and the specific trapping coefficient μ_d,

$$K_d = C_d \cdot \mu_d \qquad \textit{eq. 12}$$

With C_d: Defect concentration

μ_d: Specific trapping coefficient

In the literature, one can find values of atomic specific trapping coefficient μ_d^{at}, which can be defined as:

$$\mu_d = \frac{\mu_d^{at}}{N^{at}} \qquad \textit{eq. 13}$$

Where N^{at} is the atomic density of the material, about 6.316×10^{22} at.cm^{-3} for tungsten.

In metals, the atomic specific trapping coefficient μ_d^{at} varies between 10^{14} and 10^{15} s^{-1} [175]. For the single vacancy of pure tungsten, the most similar and available value is that of the positron trapping at single vacancy i.e. μ_{V1} in Tantalum (Z = 73, versus Z = 74 for W), with a value of $(6 \pm 3) \times 10^{15}$ m^{-3}.s^{-1}[159].

D. Annihilation of positron-electron pairs

The annihilation of positron-electron pairs (e^+-e^-) depends strongly on the spin of positron-electron pairs. The two following annihilation modes can be distinguished. When an e^+-e^- pair annihilates at a singlet spin state *S = 0* (para), the number of emitting photon gamma (γ) is an even number; meanwhile, when annihilation occurs at a triplet spin state *S = 1* (ortho), the number of the emitting-photons γ is an odd number. Concerning the positron-electron pairs, there are two configurations. The first one is ***quasi-free pair***, meaning the positrons interact with surrounding electrons but without correlation with anyone of them. For this configuration, the annihilation emitting triple - photons γ (occurs at state *S = 1*) is negligible compared to that which generates double - photons γ (at *S = 0* state) [176]. In the second configuration, the ***linked pair*** stands for positron correlated with a surrounding electron, such a pair is also denoted positronium (Ps). This configuration is generally formed at the surface of the material or in the large open volumes. In this case, due to the *'pick-off'* phenomena, i.e. the positron annihilates with another electron in the medium instead of the correlated one giving rise to the annihilation of two photons γ. As a consequence, the mainly counted annihilation event is two photons γ of the free e^+-e^- pairs in dense materials. Furthermore, it should be noted that the annihilation of e^+-e^- pairs gives at least two photons γ [177], but under some specific conditions, the generation of a single-gamma becomes possible [178,179], however, it is not the case in our experimental conditions.

- Delocalized state

Concerning the free- e^+-e^- pairs, the annihilation occurs either at delocalized states in the crystal as referred as ***Lattice*** state or in localized traps in the matrix, in particular, the vacancy-type defects. When positron penetrates in a solid crystal, after thermalization, it is subjected to the periodic potential of the crystal lattice. Therefore, its wave function approximates to a Bloch function in the term of:

$$\psi(r) = e^{ikr} \cdot U_k(r) \qquad \textit{eq. 14}$$

Where $U_k(r)$ is a function with the identical periodicity of the crystal lattice, as shown in Figure 44. The repulsive force from the nuclei of the crystal atoms leads as much as possible the positrons to be present in the interstitial region in the crystal lattice. The annihilation rate in the lattice is as mentioned early, λ_L (in s^{-1}), which is the reciprocal of the positron annihilation lifetime τ_L (in s). These annihilation characteristics in the delocalized state symbolize the perfect ***Lattice*** of the crystal, in which the trapping of the positrons does not take place.

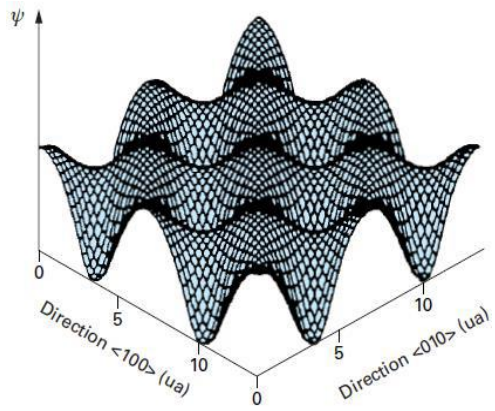

Figure 44: Wave function of the delocalized state in Nickel Crystal: localized state [176,180]

- Localized state

As a result of the lack of nucleus or the presence of vacancy-type defects in the crystal lattice, the open volume is larger than in a close-packed lattice. In addition, the repulsion of positive nuclei is smaller. For these reasons, the open volume defects (vacancy, vacancy clusters, and dislocation…) are all potential traps (Figure 45) at which the positron would tend to be localized or trapped.

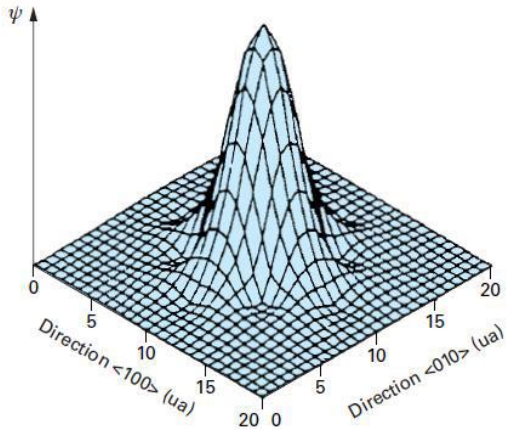

Figure 45: Wave function of the localized state in Nickel Crystal: localized state [176,180]

Two techniques, Doppler Broadening Positron Annihilation Spectroscopy (DB-PAS) and Positron Annihilation Lifetime Spectroscopy (PALS) are currently used to investigate the microstructural defects in the solid crystals. They consist in the measurement of the momentum distribution of the emitting

photons from annihilation and the distribution of the positron annihilation lifetime, respectively. These characterizations provide information on vacancy-type defects present in the crystals.

II.3.1.2 Positron annihilation lifetime spectroscopy (PALS)

Positron Annihilation Lifetime Spectroscopy (PALS) allows to measure the positron lifetime in matter which can be related to the nature and concentration of the defects.

A. Principle

The principle of positron annihilation lifetime spectroscopy consists in the measurement of the time between the entrance of the positron in the sample and its annihilation. When *fast positrons* emitted from 22Na radioisotopes are used, the 1.28 MeV photon gamma quasi-simultaneously emitted with the positron indicating its birth, is collected as 'start' signal, and the 511 keV photon gamma issuing from the annihilation of the e^+-e^- pairs, as the 'stop' signal. The time interval between the 'start' and 'stop' signals is considered as the positron lifetime.

Figure 46 illustrates the conventional experimental setup of the PALS in CEMHTI. A metal -Al-^{22}Na (~60 µCi) source is sandwiched by two identical samples. The sandwich is placed between the two detectors of the lifetime spectrometer which is a fast-fast coincidence spectrometer. This spectrometer is made of two separate detection channels allowing to detect the time of positron birth (channel 'start' for the detection of 1.28 MeV γ ray) and the time of its annihilation (channel 'stop' for the detection of 511 keV γ ray). Each channel is composed of one fast detector (made of plastic scintillator coupled to a photomultiplier) supplied with high voltage and connected to an electronic module (constant fraction discriminator) that dates the detection of gamma photons. The signals generated in each channel are fed into a time-amplitude converter. When detecting the 'start' and 'stop' signals this module generates a signal whose amplitude is proportional to the time between their detections. In general, the quality of a lifetime spectrometer is determined by its time resolution which has a full width at half maximum (FWHM) which allows the decomposition of the short exponential components of the lifetime spectrum. The FWHM of two spectrometers (TV1 ≈ 215 ps and TV2 ≈ 230 ps) at CEMHTI is short enough to extract exponential components in the order of 50- 100 ps with an upper limit of about 500 ps. In addition, to obtain a reliable result in terms of statistic, each spectrum contains more than 2×10^6 counts, which ensures a correct decomposition of the spectra.

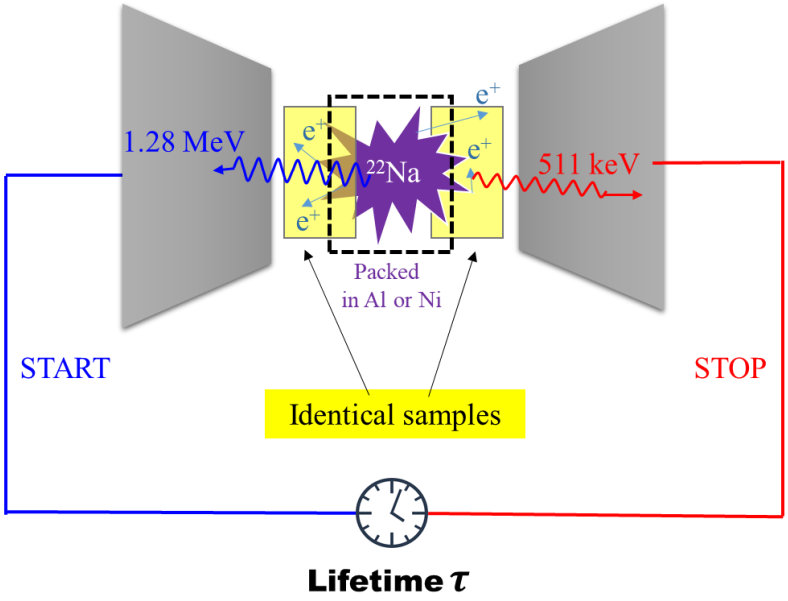

Figure 46: Schematic diagram of the experimental setup of PALS in CEMHTI

B. Decomposition of the PALS spectrum

The positron lifetime spectrum represents the probability $P(t)$ of a positron emitted at instant t_0 to be annihilated after a time t. It can be expressed as the differential equation (eq. 15), in which $N_i(t)$ is the total number of positrons which are still alive after a time t after their birth at t_0.

$$P(t) = -\frac{dN_i(t)}{dt} \qquad \textit{eq. 15}$$

with $dN_i(t) = -\lambda_i N_i(t) dt$

The total number of alive positrons after time t could be expressed by an exponential decay function (eq. 16)

$$N_i = N_0 e^{-\lambda_i t} \qquad \textit{eq. 16}$$

where the λ_i (s^{-1}) is the annihilation rate at state i and N_0 the initial number of the positron at instant t = 0.

Hence, if several annihilation states exist in the material, the total number $n(t)$ of the annihilated positrons at each state at the instant, t can be expressed as a sum of the exponential decay function which has different lifetime components $\tau_i = 1/\lambda_i$ with an intensity I_i ($\sum_1^n I_i = 1$) (eq. 17).

$$n(t) = \sum_{i=1}^{n} I_i e^{-\frac{t}{\tau_i}} \qquad \textit{eq. 17}$$

In the experiment, a raw lifetime spectrum $S(t)$ is the sum of background noise (BG) and the convolution of the probability of positron annihilation at instant t, $L(t)$ with a function $R(t)$ of the spectrometer resolution (eq. 18).

$$S(t) = BG + L(t) \otimes R(t) \qquad \textit{eq. 18}$$

The resolution function $R(t)$ is most of the time a Gaussian function. In practice a part of annihilations occurs in the source so that the probability of annihilation at instant t, $L(t)$ can be expressed as (eq. 19):

$$L(t) = L_{sample}(t) + L_{source}(t) \qquad \textit{eq. 19}$$

The contribution of the source annihilations $L_{source}(t)$ (eq. 20) has to be removed to get the lifetime components from the sample exclusively, which is also the absolute value of the time-derivative of the positron decay function n(t).

$$L_{sample}(t) = \sum_{j=1}^{n} \frac{I_j}{\tau_j} e^{-\frac{t}{\tau_j}} \qquad \textit{eq. 20}$$

Therefore, the decomposition of the experimental lifetime spectrum can be obtained by fitting the experimental spectrum using the ANAPC programme which is the improved version of the program POSIFIT [181]. This programme allows to calculate the theoretical spectrum from eq. 20, taking into account some parameters as guessed first values and makes evolving their values to get the best agreement between the experimental and theoretical spectra.

Thus the exponential components τ_j and I_j related to annihilation in the sample can be extracted. The average lifetime τ_{av} is defined by the sum of each lifetime component τ_j extracted from the spectrum weighting by the corresponding intensity I_j [175].

$$\tau_{av} = \sum_{i=1}^{n} I_j \, \tau_j \qquad \textit{eq. 21}$$

C. Source Corrections

Some positrons can annihilate in the source (NaCl salts, coated materials, air...). Generally, three principal contributions affect the experimental lifetime spectrum. The first contribution (C_1) was identified coming from the source wrapping foil. At CEMTHI, the source of fast positrons for the PALS is wrapped in an Al foil with a thickness of about 6 µm. The second one (C_2) is the sodium chloride salt itself and or the surface of the wrapping foil. The third one (C_3) is generally weak, and is due to the annihilations of the Positronium probably formed at the surface of the samples or in the air between them [182,183]. The corresponding time components τ_{c1}, $\tau_{c2,}$ and τ_{c3} are fixed at 230 ps, 450 ps, and 1500 ps, respectively. In the experiments, the intensities of these three contributions C_1, C_2, and C_3 were determined by decomposing the PALS spectrum of a well-qualified sample with the Z number the closest as possible to the sample material, due to its impact on the back diffusion of the positrons toward the source. In this work two well annealed tungsten samples from the batch FZJ1, have been used to determine the source corrections for this material. Table 8 summarizes the source corrections in the case of the tungsten, which are taken into account in the decomposition of the spectrum obtained with the program ANAPC. It should be noticed that only the intensity of the C_1 contribution is a fixed value, calculated through the formula determined by Bertolaccini et al.[184]. The C_2 and C_3 can vary with the ageing of the source, so that the source corrections have to be checked approximately every three months.

τ (ps)	***Source ^{22}Na correction in the case of tungsten***
230	23.59 %
450	1 - 2.5 %
1500	0.18 - 0.37 %

Table 8: Experimental source corrections in the case of tungsten

D. Defect identification via interpretation of lifetime components

The lifetime components τ_j can be compared to the specific lifetimes of various annihilation states in order to identify the nature of the defects that are detected. Nevertheless, in the case where the annihilation lifetime at several states (≥ 2) is very close, the resolution of the spectrometer is insufficient to distinguish them. Consequently, the extracted lifetime components can also be a mixture of more than one annihilation state. In this case, it is impossible to identify the nature of the defects with such components, despite the value might be occasionally equivalent to the characteristic value of a defect found in the literature.

The positron lifetimes are specific to the state in which the positron annihilates: the one of the ***Lattice*** corresponds to annihilation of positron at a delocalized state in the interstice of the perfect lattice. The lifetime for vacancy defects is longer than the lattice one because the electron density around the positron when it annihilates decreases in the single vacancy compared to the interstice of the perfect lattice. According to eq. 22 [176], the positron lifetime is inversely proportional to the surrounding electron density. It should be noticed that the formula is related to quasi-free e^+-e^-pairs emitting two gamma-rays, the constant for one of three gammas-rays is more complicating (details see [176]), but it is still inversely proportional to surrounding electron density. For this purpose, the lifetime increases with the increasing size of the vacancy-type defects, however, when the defect is large enough, the lifetime will saturate at a threshold size (see Chap I.3.7).

$$\tau_{2\gamma} = \frac{1}{\pi r^2 c} {n_e}^{-1} \qquad \textit{eq. 22}$$

With r: Electron radius 2.82×10^{-15} m

c: Light speed 3×10^8 m.s^{-1}

n_e: Annihilation state surrounded electron density

II.3.1.3 Doppler broadening Positron annihilation spectroscopy (DB-PAS)

A. Principle

At CEMHTI laboratory, a Doppler Broadening Spectrometer is coupled with a slow positron accelerator (SPB-DB). This device generates a mono-energetic positron beam and allows to probe the vacancy-type defects in thin films close to the surface. As we already showed (Figure 43), the penetration depth decreases with increasing density of the material. Figure 47 shows the principal components of the slow positron beam installed at CEMHTI.

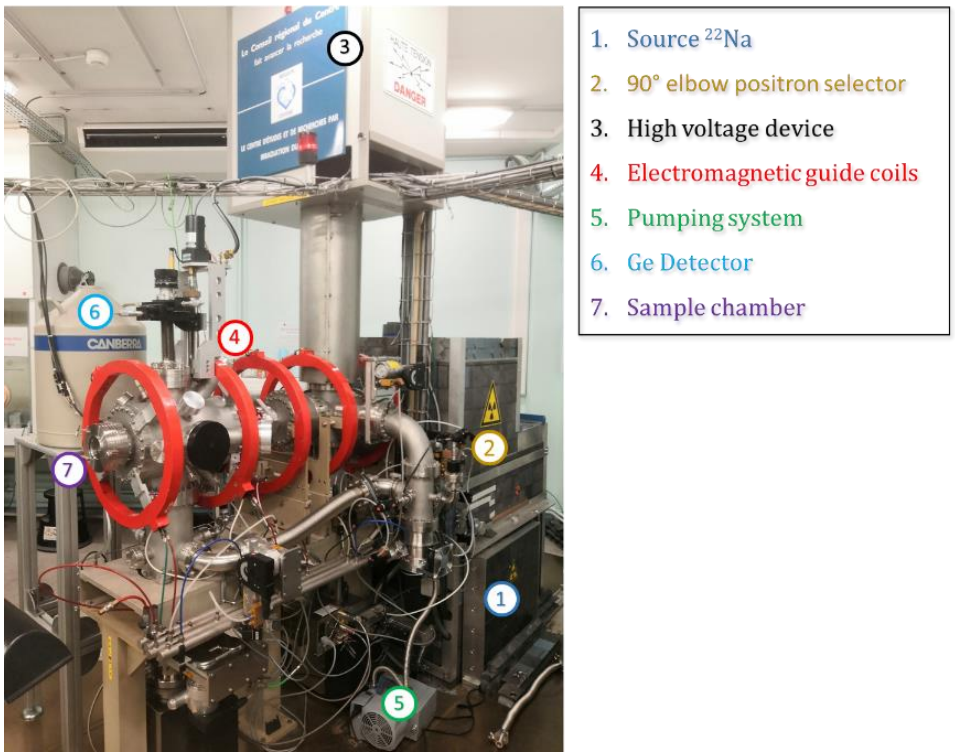

Figure 47: Principal components of slow positron accelerator in CEMHTI

A radioactive source ^{22}Na (~50 mCi[6] in July 2018), with a size of half of inch, generates naturally positrons through β^+ decay (see Chap II.3.1.1). A part of the generated positrons is moderated by a tungsten thin foil (~3µm), until an energy of around 3 eV. The moderated positrons are next selected in terms of energy by using a 90° elbow on top of which a magnetic field is applied. The 'slow' positrons are accelerated by a high voltage that can reach 30 kV at the maximum and a series of magnetic coils guide the positrons toward the sample holder. A permanent magnet is installed behind the sample holder to focus the positron beam on the sample (Figure 48). As the positron in vacuum is quite stable, its lifetime reaches about 10^{22} years [174], a series of pumping systems were used to maintain a high vacuum environment ($< 5 \times 10^{-7}$ mbar) for starting the experiment. The energy of the monoenergetic e^+

[6] 1 curie (Ci) = 3.7×10^{10} Becquerel (Bq), 1 Bq = 1 decay per second

beam can be fixed at energies in the range from 0.5 and 25 keV with a flux in the order of 10^5 $e^+.cm^{-2}.s^{-1}$. The beam diameter on the sample is roughly estimated to about 2-3 mm.

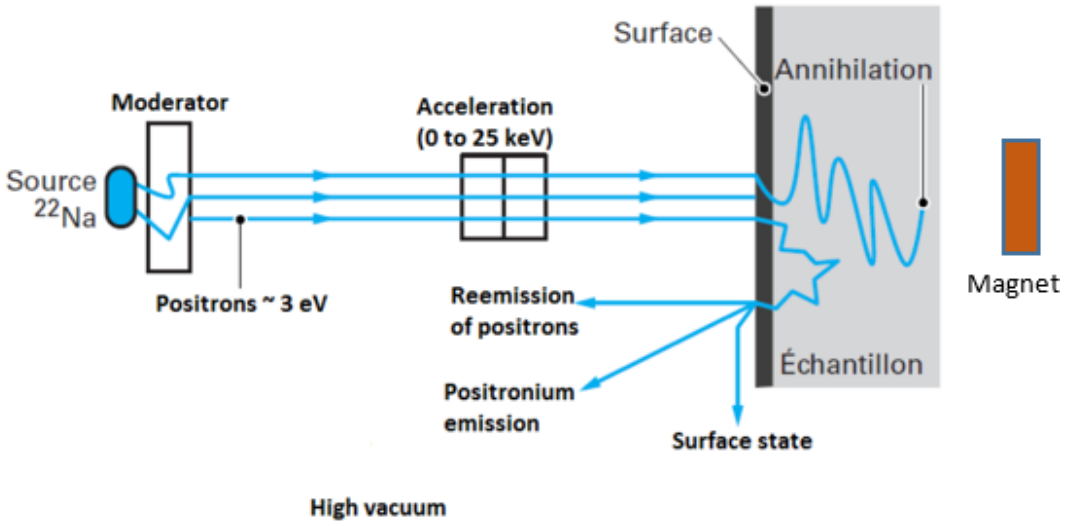

Figure 48: Diagram of functioning of the slow positron beam in CEMHTI [176]

During the SPB-DB experiment, the positron penetrates in the crystals, it loses almost its whole kinetic energy during the thermalization before forming a free pair with an electron. Accordingly, the kinetic energy of free e^+-e^-pairs is approximately equal to that of the electron. According to the equivalence of mass and energy (eq. 23), the total kinetic energy of the pairs is around 1022 keV.

$$E = m_0 c^2 \qquad \textit{eq. 23}$$

With: the electron or positron mass: $m_0 = 9.109 \times 10^{-31}$ kg

the speed of light in vacuum: $c = 2.9979 \times 10^8$ m.s^{-1}

As a result of the law of energy conservation before and after the annihilation, and considering that electron and positron have the same mass, the free pairs with a kinetic momentum P generate two-photons gamma with an energy of about 511 keV ± ΔE_γ emitted in the quasi-opposite direction (emission angle 180° ± θ). The deviation of energy ΔE_γ and angle θ are expressed as follows:

$$\Delta E = \frac{c \cdot P_L}{2} \quad \text{and} \quad \theta = \frac{P_T}{m_0 \cdot c} \qquad \textit{eq. 24}$$

Where the P_T and P_L are the transverse and longitudinal projection of the kinetic momentum projections of the pairs, respectively. The dispersion in energy ΔE_γ and angular deviation θ originate from the Doppler effect on the emission of gamma rays due to the kinetic energy or momentum of the electrons. The SPB-DB experiment records the broadening of the emitted gamma spectrum centered at the 511 keV, caused by the Doppler effect. This measurement determines the projection of the momentum distribution of the e^+-e^- pairs in the direction towards the detector (Figure 49).

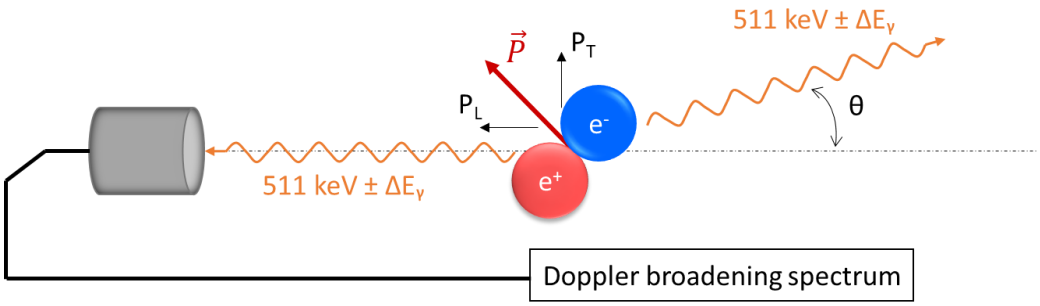

Figure 49: Diagram of the measurement of Doppler Broadening of the kinetic momentum spectrum of e^+-e^- pairs

It is worth remarking that the experimental Doppler broadening spectra represent the number of annihilation events as the function of either the kinetic energy (usually in keV) or the longitudinal kinetic momentum (unusually in $10^{-3}\ m_0c^2$) of the pairs. The conversion of the two quantities can be done via equation (eq. 25):

$$P_L(10^{-3} \times m_0c^2) = \frac{2\Delta E(keV)}{511} \times 1000 \qquad \textit{eq. 25}$$

DB-PAS involves the detection of photons emitted during the annihilation of e^+-e^- pairs, more precisely the broadening of the annihilation line centered at 511 keV (or $0 \times 10^{-3}\ m_0c^2$ on the momentum distribution). The slow positron accelerator is coupled to a gamma spectrometer, which collects a DB spectrum for each incident positron energy set between 0.5 and 25 keV.

B. Processing of data

The data acquisition system includes a high purity germanium (Ge) detector used to collect emitting photons gamma, with a resolution of about < 1.3 keV at 511 keV and an efficiency around > 25 % at 1.33 MeV, and its dead time is around 10 %. The Ge detector is cooled permanently by liquid nitrogen (LN_2) and polarized at a high voltage of about +3500 V to favor its performance. The collected signals undergo a series of electronic devices (amplification, anti-stack system…), before being converted into numeric data through an Analog-to-digital converter. Generally, one Doppler Broadening spectrum has at least 2×10^6 total counts containing 4×10^5 counts under the peak of the Doppler region (Figure 50).

As shown in Figure 50.a, the raw DB spectra have a non-negligible fraction of background noise (BG). Due to the Compton scattering in the detector during the collection of the gamma-rays, the background noise at the left side is more pronounced. Therefore, to remove as much as possible the background noise of both sides of the raw spectrum, the BG is expressed by an energy-depending equation (eq. 26):

$$BG(E_\gamma) = A + (B - A)\frac{F(E_\gamma)}{F_{total}} \qquad \textit{eq. 26}$$

Where $BG(E_\gamma)$ is the background noise at gamma energy E_γ, the parameters A and B are the mean values of plateau at low energy ($E_\gamma < E_l = 504$ keV) and high energy ($E_\gamma > E_r = 523$ keV), at left and

right side of the peak, respectively. The $F(E_\gamma)$ is the event count in the integral area between a given energy E_γ and the E_r (fixed at 523 keV). F_{total} is the total number of events counted in the integral area between the energies El and Er. After subtracting the BG, a DB spectrum measured at a given positron energy E is approximately symmetrical and centered at 511 keV (or $0 \times 10^{-3}\ m_0c^2$). The annihilation characteristics, two line-shape parameters can be extracted and determined from the center part and two wings of the spectrum, the ***S*** (Shape) and ***W*** (Wing).

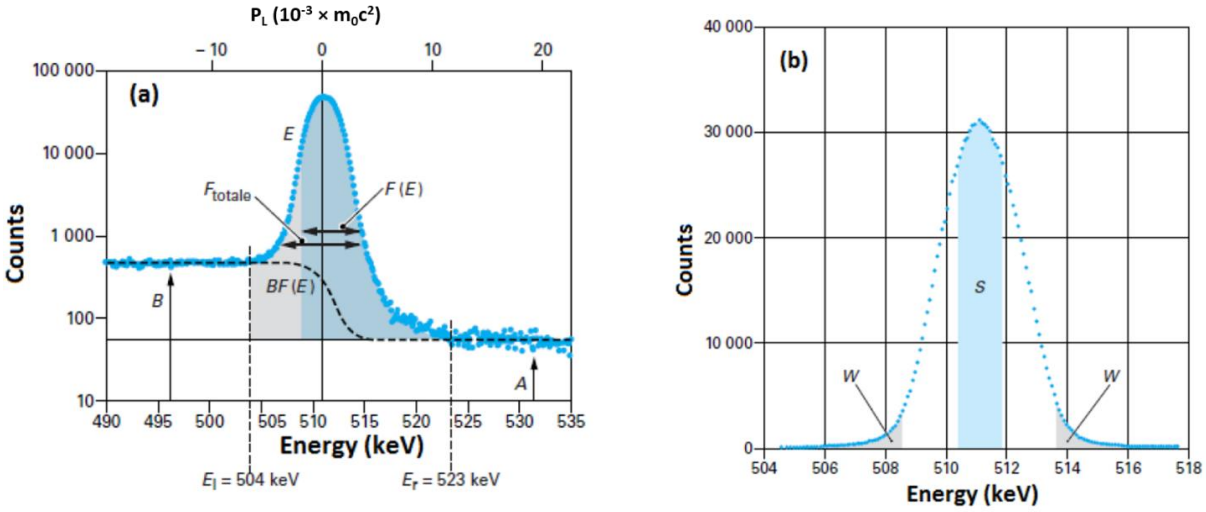

Figure 50: Doppler broadening spectrum a) before subtracting background noise b) after subtracting background noise

Physically, the parameter ***S*** (resp. ***W***) represents the fraction of annihilation with mostly valence (resp. core) electrons which are far (resp. close) from the surrounding nuclei, that is the reason why energy deviation is weaker (resp. stronger) for ***S*** (resp. ***W***) taking reference to central line 511 keV. And hence, the ***S***, ***W*** designate the low and high momentum parameters, respectively. The value of parameter ***S*** (resp. ***W***) is the ratio of the annihilation photon counts **N** in the selected center (resp. wings) region over the total photon counts $\mathbf{N}_{total}$ of the DB spectrum (eq. 27).

$$S = \frac{N[-E_S:E_S]}{N_{total}}, \qquad W = W_L + W_R = \frac{N[-E_{W_1}:-E_{W_2}]+N[E_{W_2}:E_{W_1}]}{N_{total}} \qquad \textit{eq. 27}$$

Figure 51 shows the selected regions used for the determination of the two line-shape parameters ***S*** and ***W*** on the experimental spectrum collected with a slow positron beam at 25 keV for a pristine and irradiated tungsten sample. The region of ***S*** is selected within momentum range between -2.643 and + $2.643 \times 10^{-3}\ m_0c^2$], centered at $0 \times 10^{-3}\ m_0c^2$, corresponding to 511 eV, and that of ***W*** is chosen from two lateral areas with a width of 49 channels, from -24.88 to $-9.796 \times 10^{-3}\ m_0c^2$ for left wing and 9.796 to $24.88 \times 10^{-3}\ m_0c^2$ for right one. The relation between the channel and energy is expressed by equation (eq. 28):

$$Energy_{(keV)} = 0.07946 \times Channel + 17.8 \qquad \textit{eq. 28}$$

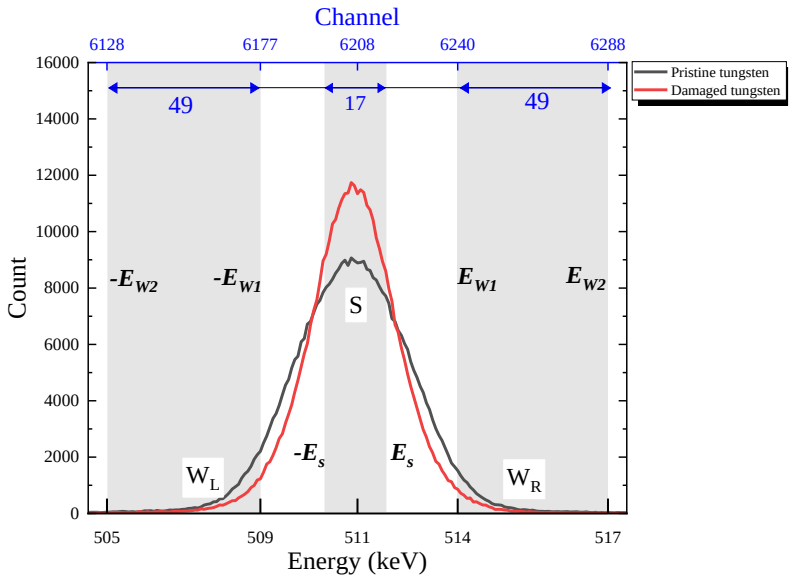

Figure 51: DB spectra of extra high purity (XHP, 99.9999 wt.%) pristine and damaged (20 MeV-W, 0.02 dpa, 500 °C) tungsten sample for positron energy of ~25 keV with the selected region for calculating the Parameter S and W of DB spectrometer of CEMHTI

It has to be noticed that the inevitable perturbations (vibration, signal conversion…) that occur during the experiments, impact the accuracy of the measurements and lead to the dispersion of the measurement. Therefore, the relative error was estimated from the measurement of the reference sample, i.e. one dioxide Uranium (UO_2) disk is used as a reference sample which must be measured at the beginning of each measurement series, consisting of up to eight samples. It has been proved that ***S(E)*** and ***W(E)*** curves do not change with time in this sample, and shows a plateau value from 5 to 25 KeV. The measurement of such reference allows to check the correct operation of the DB-PAS system. Thus, the measured and corrected value of ***S*** and ***W*** are normalized by making a ratio of the referential[7] and verification measurement of the UO_2 sample made at the first of each DB experiments, i.e. $A_{norm} = A_{mes}^{Cor} \cdot \frac{A_{UO_2}}{A_{ref}}$, where A is line-shape parameters (***S*** or ***W***).

C. Defect identification via interpretation of line-shape parameters

The interpretation of the Doppler broadening spectrum is essential to identify the defects. The two line-shape parameters ***S*** and ***W*** depend on the local electron density and to their momentum distribution. Hence, if the positron annihilates as localized at a vacancy-type defects, the local high momentum electron density is lower than that of annihilation in the delocalized ***Lattice***[8] state of the crystals. As shown in Figure 51, for the damaged tungsten sample (self-irradiated to 0.02 dpa at 500 °C), which contains a considerable fraction of the vacancy-type defects, the positrons are trapped in these defects and annihilate with surrounding electrons, mainly with the valence electrons. Compared to the DB

[7] The DB measurement of UO_2 (Ga16) in 2010, S_{ref} = 0.37126, W_{ref} = 0.07912
[8]The concentration of the smallest defects (single vacancies) is below the detection limit of the DB spectrometer at CEMHTI (< 10^{24} m^{-3}) estimated using one-trap model

spectrum of the pristine sample, the annihilation in irradiation-induced vacancy defects leads to an increase of the ***S*** and a decrease of the ***W***. Thus, the DB spectrum of the damaged sample is narrower (black line curve in Figure 51) than the one measured in perfect crystal. Therefore, the increase of ***S*** is accompanied by a decrease of ***W*** indicating the detection of the vacancy-type defects.

Each annihilation state has a specific value for ***S*** and ***W***, such as that of the ***Lattice*** of each material, denoted: (S_L, W_L). Hakala et *al.*[185] demonstrated in Silicon, the two shape parameters ***S*** and ***W*** depend on the type of defects: the larger the defect volume, the higher (resp. lower) the value of ***S*** (reps. ***W***). In polycrystalline tungsten, the annihilation characteristics (***S, W***) of the ***Lattice***, single vacancy, and that of the largest vacancy cluster were determined with the DB-Spectrometer of CEMHTI in previous works [36,126]. The values are listed in Table 9.

	S	d*S*	*W*	d*W*
Lattice	0.367	0.001	0.084	0.001
Monovacancy	0.417	0.003	0.057	0.002
The largest vacancy cluster	0.503	0.003	0.036	0.002

Table 9: The experimental annihilation characteristics (S, W) in polycrystalline tungsten obtained from DB spectrometer at CEMHTI

Contrary to the lifetime spectroscopy where the decomposition of the spectrum allows in most of the cases to distinguish different annihilation states, the ***S*** and ***W*** characteristics measured in the sample cannot be deconvoluted and correspond to the average of annihilations at several states. *S* and *W* can be expressed as:

$$\begin{cases} S = \sum_{i=1}^{n} f_i \cdot S_i \\ W = \sum_{i=1}^{n} f_i \cdot W_i \end{cases} \quad \text{eq. 29}$$

with $\sum_{i=1}^{n} f_i = 1$, the f_i is the fraction of positron annihilated at state i with the S_i and W_i specific annihilation characteristics. When annihilation occurs only at merely one state, the low momentum parameter ***S*** and high momentum parameter ***W*** represent the characteristics of the annihilating state. To check if the ***S*** and ***W*** parameters could correspond to a specific annihilation state, ***S*** is plotted as a function of ***W*** (or vice-versa). In the case where the annihilation takes place at two states, one of them is the ***Lattice***, another is a defect, no matter the positron energy, equation (eq. 29) becomes:

$$\begin{cases} S(E) = f_L S_L + f_d S_d \\ W(E) = f_L W_L + f_d W_d \end{cases} \quad \text{eq. 30}$$

The sum of the fraction of annihilation in the ***Lattice*** f_L and that of the defect f_d is equal to 1, and the low momentum parameter $S_d > S_L$ and the high momentum parameter $W_d < W_L$. As shown in the

illustration (Figure 52), the absolute value of the slope R of the trend line linking the ***Lattice*** characteristics (S_L, W_L) and those ones of the defects V_n (n = 1,2,3,4 or 5) increases with the defect size. This feature enables to identify the type of defects, and the R can be expressed by the following equation (eq. 31).

$$R = \left|\frac{S_n - S_L}{W_n - W_L}\right| \qquad \textit{eq. 31}$$

Where ***(S_L, W_L)*** are the line shape parameters of the ***Lattice*** and (S_n, W_n) of the defect respectively.

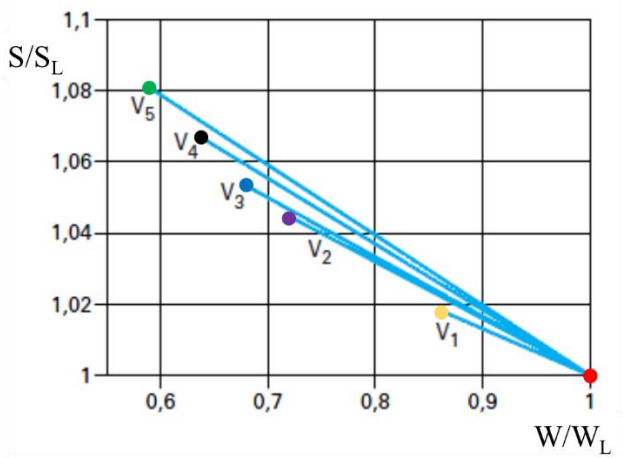

Figure 52: S-W diagram of calculated annihilation characteristics of single vacancy, di-vacancy, tri-vacancy, 4 vacancies, 5 vacancies in Si, and that of the Lattice [185]

Moreover, the annihilation characteristics ***S***, ***W*** is also sensitive to the chemical environment where the positron annihilates. In particular, positron can be trapped at decorated vacancy-type defects, i.e. the positron can annihilate with electrons of the foreign elements trapped in the surrounding of the vacancy. P. Asoka-Kumar et *al.*[186] employed DB-PAS with two detectors in coincidence (CDB), exhibited that the high momentum parameter allows the identification of different elements. In the same period, Szpala et.*al* [187] operated also the CDB technique, they demonstrated the formation of the antimony (Sb)-vacancy complexes in Sb-doped silicon samples. Recently, Rementeria et *al.*[188] found that the DB spectrum line shape parameters' change was more pronounced in the region of the high momentum parameter ***W*** (> 10×10^{-3} m_0c) for the bainite phase iron: the changes were considered as the consequence of the formation of carbon-vacancy complex. On the other hand, precipitates can only be probed by positrons when the positron affinity to the precipitate is higher than that of the matrix.

Furthermore, it should be noted that, not only the volume of defects modifying the annihilation characteristics ***(S, W)***, but also their concentration. A higher (resp. lower) concentration of a defect 'd' makes raise (resp. reduce) the annihilation fraction at the defect f_d, and decrease (resp. increase) that one of the annihilation in the ***Lattice*** f_L. As a consequence the increase of defect concentration on the

S-W diagram, is manifested by the measured annihilation characteristics (*S, W)* shifting closer (resp. further) to that of the defect (S_d, W_d), and further (resp. closer) to that of the ***Lattice*** (S_L, W_L).

D. Distribution of defects by using multi-layer model VEPFIT

The characterization of the defects distribution as a function of depth benefits the advantage of the variable monoenergetic beam of slow positrons. The line shape parameters ***S, W*** as a function of the positron energy gives out the information on the depth-distribution of the defects. In a special case where the diffusion of the positrons is negligible i.e. when the concentration of defects is so high that all positron impinging the sample are trapped after losing their kinetic energy, the energy can be roughly converted into positron penetration depth.

In the more general cases, the variation of the ***S(E)*** and ***W(E)*** could be fitted by using the VEPFIT program which takes into account the positron energy losses and its diffusion. One option of the VEPFIT program decomposes the sample into one or several homogeneous layers (Figure 53), for which the annihilation characteristics, the line shape parameters S_i, W_i and the effective diffusion length L_i^+, with the thickness e_i (i = 1, 2, …n) can be fitted.

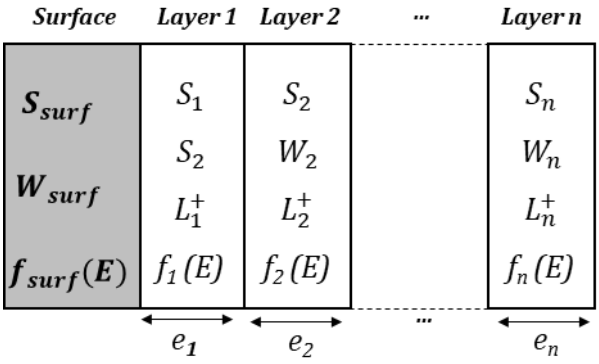

Figure 53: Schematic structure of the homogeneous layers modeled by VEPFIT

The theoretical calculation of the ***S(E)*** and ***W(E)***, expressed as:

$$\begin{cases} S(E) = f_{surf}(E)S_{surf} + \sum_i f_i(E)S_i \\ W(E) = f_{surf}(E)W_{surf} + \sum_i f_i(E)W_i \end{cases} \quad \text{eq. 32}$$

where f_{surf}(E) and $f_i(E)$ are the fraction of the positron which annihilates at the surface and in the layer i with a thickness e_i, at energy E. These fractions depend on the penetration profile of the positron with a giving incident energy E, and the effective diffusion length L_i^+. Moreover the effective diffusion length L_i^+varies with the trapping rate K_i in the different layers i. Consequently, the fitted effective diffusion length can be used to calculate the trapping rate K_d of the defects present in the corresponding layers by using eq. 11 furthermore, to estimate the concentration of the defects if the trapping coefficient μ_d is available (eq. 13).

II.3.1.4 Quantification of defects and trapping models

In addition, the experimental value of annihilation characteristics (S, W) can be used to evaluate the defects concentration through the positron trapping models [160]. The simplest model is a one-trap model, and is described in details in the following as an example. In this model, vacancy defects (vacancy or vacancy clusters) are considered as localized deep traps in contrast to dislocation loops[9]. Figure 54 illustrates the single deep trap model. One fraction of the positron annihilates in the delocalized state, the ***Lattice***; Another one annihilates in the localized state, i.e. a vacancy defect. It should be noticed that the detrapping of the positron from the localized state is assumed to be non-existent, in other words, the trapped positron annihilates at the localized state. It is true for deep traps at room temperature. In this case the thermal energy is not enough to make the positron escape from the trap before its annihilation.

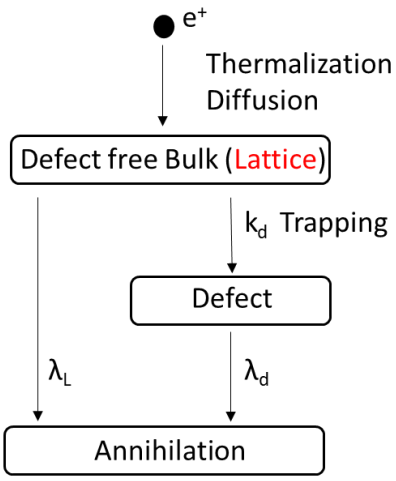

Figure 54: Schematic of one-trap model

The probability to find the positron in delocalized state (***Lattice***) is $n_L(0)$ and as trapped at localized state (vacancy defect) is $n_d(0)$, which are presented as a temporal function including the annihilation rate in the ***Lattice*** λ_L, in defect λ_d and the trapping rate in the defect k_d :

$$\begin{cases} \frac{dn_L(t)}{dt} = -(\lambda_L + k_d)n_L(t) \\ \frac{dn_d(t)}{dt} = -\lambda_d n_d(t) + k_d n_L(t) \end{cases} \quad \text{eq. 33}$$

To solve these differential equations (eq. 33), the initial probability of trapped positron in the delocalized state $n_L(0)$ is assumed to be 1 and the one in localized state $n_d(0)$ is 0. The probability of the positron being trapped at localized states and delocalized in the ***Lattice*** states are expressed:

[9] The vacancy dislocation loop is a shallow trap for positron

$$\xrightarrow{n_L(0)=1 \text{ and } n_d(0)=0} \begin{cases} n_L(t) = n_L(0)e^{-\frac{t}{\tau_1}} \\ n_d(t) = I_2(e^{-\frac{t}{\tau_1}} + e^{-\frac{t}{\tau_2}}) \end{cases} \quad \text{eq. 34}$$

Where the effective lifetime in the delocalized ***Lattice*** before trapping is $\tau_1 = \frac{1}{\lambda_L + k_d}$, with an intensity I_1=$1 - I_2$, and the positron annihilation lifetime in the defect $\tau_2 = \frac{1}{\lambda_d}$ with an intensity $I_2 = \frac{k_d}{\lambda_L - \lambda_d + k_d}$. It is essential to note that when delocalized (***Lattice***) and localized state (defects) co-exist in the material, the positron annihilates in both states. The effective lifetime of positron in the delocalized state i.e. the time that positrons spend in the delocalized state, will be shorter than that of the specific perfect ***Lattice***, ($\tau_1 = \frac{1}{\lambda_L + k_d} < \tau_L = \frac{1}{\lambda_L}$) because they are trapped before to annihilate. Furthermore, if the annihilation events occur totally in both two states, the sum of the ratio of the intensity over lifetime component of each annihilation states denoted $\frac{1}{\tau_{mod}}$ should be equal to reciprocal of the lifetime of the ***Lattice*** $\frac{1}{\tau_L}$ (see demonstration in Appendix. B).

$$\frac{1}{\tau_{mod}} = \sum_0^n \frac{I_i}{\tau_i} \quad \text{eq. 35}$$

This relationship is very useful to check if the annihilation occurs only into two states, one of them being ***Lattice*** and another a vacancy defect.

In addition, the fraction of annihilation events in the defect is expressed by the product of the annihilation rate λ_d in the defect and the probability at the time t, $n_d(t)$ determined from eq. 34

$$f_2 = \int_0^t \lambda_d n_d(t) dt \quad \text{eq. 36}$$

After integrating, the fraction of the annihilation in the localized state is a relation between the annihilation rate in the ***Lattice*** (or annihilation lifetime) and the trapping rate in the defect (eq. 37)

$$f_2 = \frac{k_d}{\lambda_L + k_d} = \frac{\tau_L k_d}{1 + \tau_L k_d} \text{ and } f_1 = 1 - f_2 \quad \text{eq. 37}$$

Hence, the low momentum parameter S, high momentum parameter W and the average lifetime can be expressed as:

$$\begin{cases} \tau_{av} = \frac{\lambda_L}{\lambda_L + k_d}\tau_L + \frac{k_d}{\lambda_L + k_d}\tau_d \\ S = \frac{\lambda_L}{\lambda_L + k_d}S_L + \frac{k_d}{\lambda_L + k_d}S_d \\ W = \frac{\lambda_L}{\lambda_L + k_d}W_L + \frac{k_d}{\lambda_L + k_d}W_d \end{cases} \quad \text{eq. 38}$$

where annihilation characteristics are distinguished by footnote L: lattice, and d: defect.

From the eq. 38, the defect trapping rate k_d and their concentration C_d can be also evaluated from the experimental values of the ***S***, ***W*** and τ_{av} provided that the defect trapping coefficient μ_d is known.

$$k_d = \frac{\lambda_L(X_L - X)}{X - X_d} \text{ and } C_d = \frac{k_d}{\mu_d} \quad \text{eq. 39}$$

With X: τ_{av}, S ou W.

The annihilation rate λ_L in tungsten ***lattice*** is determined by using the average value of the reported lifetime, which is around 105 ps [134,139,189], so λ_L is about 9.52 × 10^9 s^{-1} ($\lambda_L = 1/\tau_L$). The positron trapping coefficient μ_v at single vacancy in the tungsten matrix is approximated to that of tantalum (6 ± 3) × 10^{15} $m.s^{-1}$ [159], due to their similar Z number. With these parameters, Figure 55 illustrates the variation of the normalized line-shape parameters as a function of the single vacancy concentration. The lifetime of V_1 was fixed to about 200 ps [74].

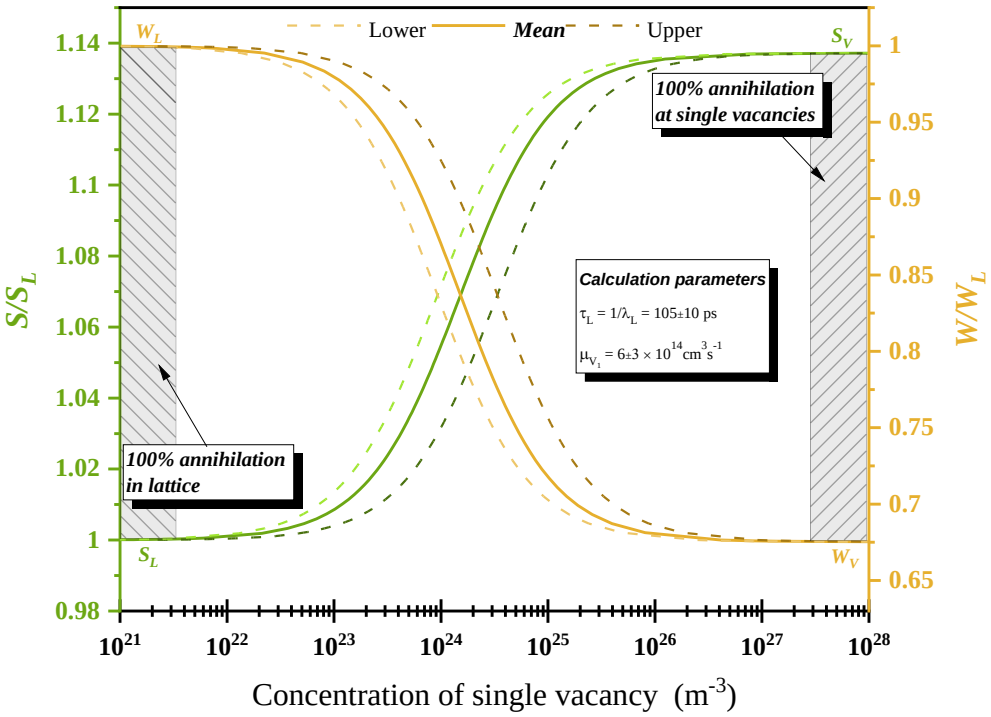

Figure 55: Normalized characteristic annihilation parameters S, and W as a function of the concentration of the single vacancy in tungsten by using minimum, mean and maximum value of specific trapping coefficient μ_v

The concentration sensitivity depends on the positron technique. The Doppler Broadening spectroscopy can quantify single vacancy with a concentration in the range between the 10^{23} m^{-3} to 10^{26} m^{-3} in the tungsten. The maximum concentration that can be determined is around 3 × 10^{26} m^{-3}, which corresponds to five isolated single vacancies in a tungsten matrix with ten thousand atoms. Indeed, this estimation depends on the single vacancy trapping coefficient μ_v. In metals, the trapping coefficient of the vacancy cluster μ_{vn} is proportional to the number n of the single vacancies making up the cluster. However, it should be noted that this relation is validated for small vacancy cluster Vn containing less than ten single vacancies (n<10) [159], and this term is independent of temperature.

$$\mu_{vn} = n\mu_v \quad \text{eq. 40}$$

II.3.2 Secondary Ions Mass Spectrometry (SIMS)

In the early 1900s, numerous works [190,191] were carried out on the interaction of the primary ions with the matter and the emission or sputtering of the secondary ions from the solid surface bombarded by primary ions was observed. The first device of Secondary Ions Mass Spectrometry (SIMS) was commercialized by the company CAMECA in the early 1960s. Figure 56 illustrates the principle of the SIMS, which is based on the collection of secondary ions being sputtered from the localized area of primary ions. Because of its considerable resolution on the in-depth quantification, SIMS is one of the most popular quantitative analyses of solid surfaces. In the present work, SIMS was employed to quantify the LEs (H, C, O…) in the tungsten samples, giving out the concentration of the impurities as a function of depth.

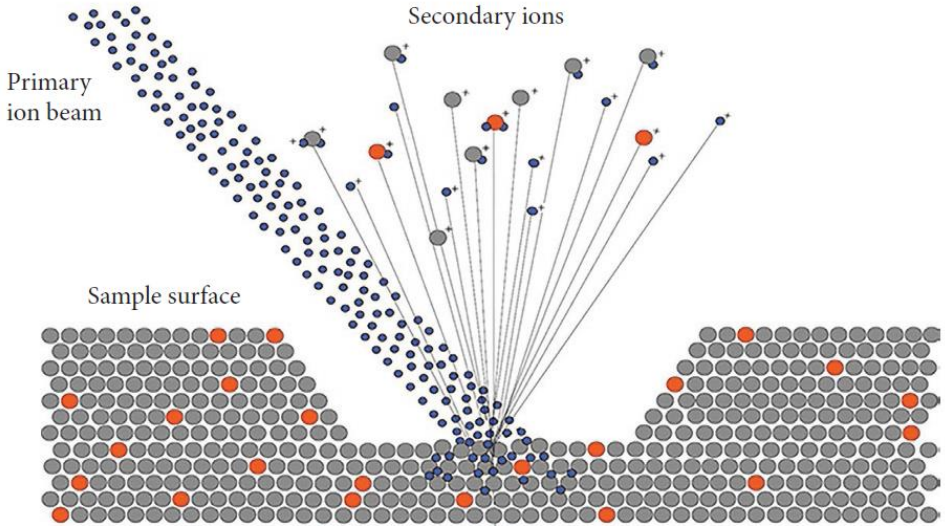

Figure 56: Schematic illustration of the sputtering and ionization process of the SIMS [192]

II.3.2.1 Description of the secondary ion mass spectrometer

The SIMS analysis was carried out in GEMAC laboratory which is equipped with a well-developed spectrometer, IMS-7f CAMECA. Figure 57 shows the principal components of the spectrometer. Since our experiment is focused on the concentration of the LEs in the bulk of the sample, the dynamic SIMS (D-SIMS) was employed. In contrast to static SIMS, the D-SIMS utilizes a high-dose bombardment of the reactive primary ions with an energy of a few tens of kilovolt (kV), to acquire the information in a depth from one to a few microns. In the following paragraph, the principal components of the set-up are described:

A. Ultra-high vacuum system

It has to be noticed that the vacuum level affects the quality of the SIMS analysis, especially for the detection of the LEs (H, C, O…) in the metallic matrix. An ultra-high vacuum is not only compulsory

to prevent sample contamination, but also to minimize the secondary ions interacting with intrusive gases. Therefore, a range of pumps is set up (turbomolecular pumps, ionic pumps ...) to keep the vacuum level in the analyzing chamber at least around 10^{-9} mbar.

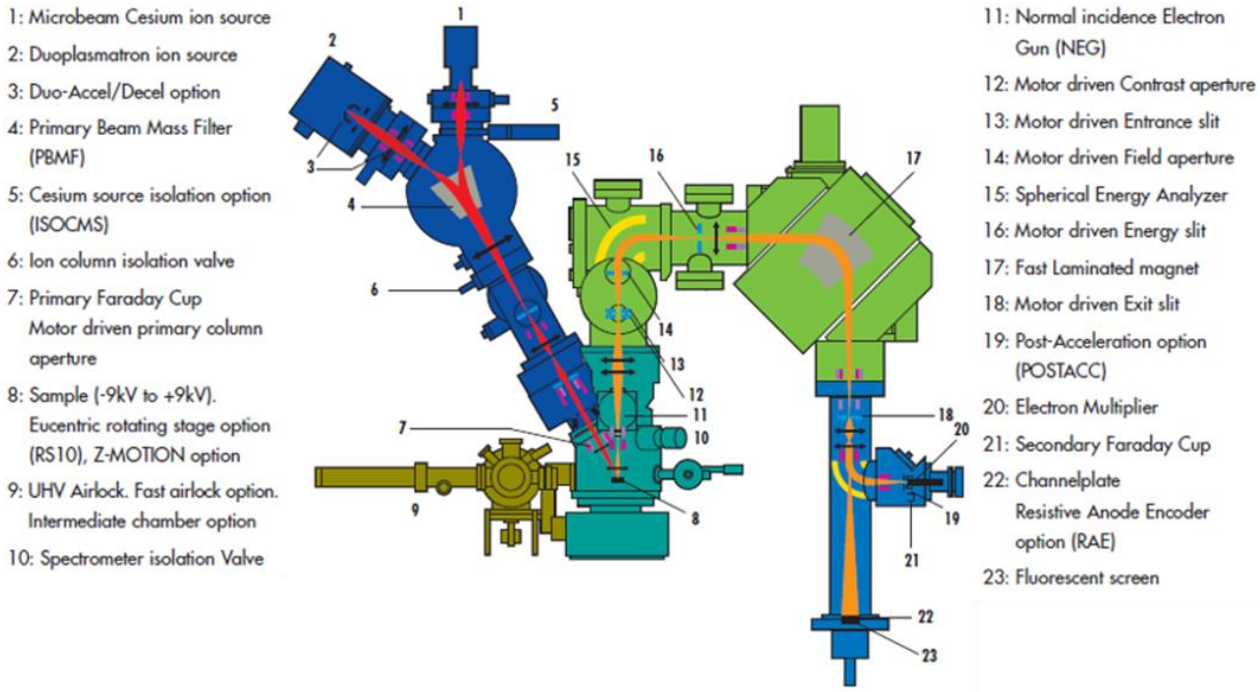

Figure 57: Principal components of the spectrometer IMS-7 CAMECA [193]

B. Primary ion source

In the dynamic SIMS, the primary ions are commonly Cs^+ and O_2^+, which favor the ionization of the electronegative and positive charged secondary ions, respectively. The source Cs^+ is produced by heating a solid cesium compound (Cesium carbonate (Cs_2CO_3) or Cesium chromate (Cs_2CrO_4)) to 400 °C. which leads to the release of Cs vapor. This vapor is drifted to strike a tungsten plate heated to around 1000 °C. The emitted electrons from thermal agitation bombard the Cs vapor, ionize a fraction of them and Cs^+ ions are produced (Figure 58).

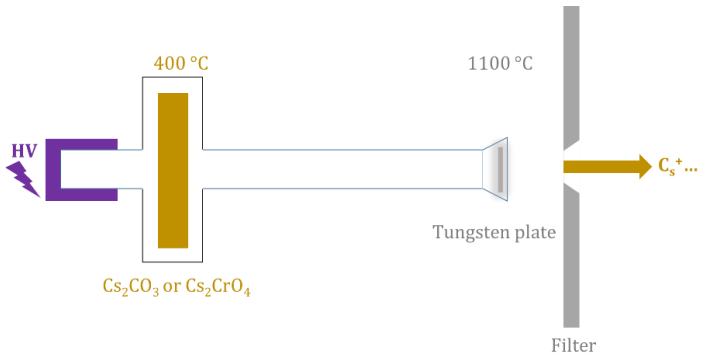

Figure 58: Components of the microbeam Cesium source of the spectrometer GAMECA IMS-7f

The source O_2^+ was yielded by utilizing a duoplasmatron (Figure 59). The oxygen gas is supplied into the cathode with low pressure. The high voltage between the cathode and the anode generates a current arc that ionizes the oxygen gas and create a plasma containing O^-, O_2^-, and O_2^+ ions. According to experimental purpose, the operator can modify the ion type by selecting the negative or positive polarity to promote the yield of the anions (O^- is dominant) or cation O_2^+, respectively. In dynamic SIMS, the cation O_2^+ is usually utilized. The Duo accel-decal option improves the beam density for O_2^+ primary beam with very low energy to limit the ballistic effect in the sample giving result in a degradation of the in-depth resolution.

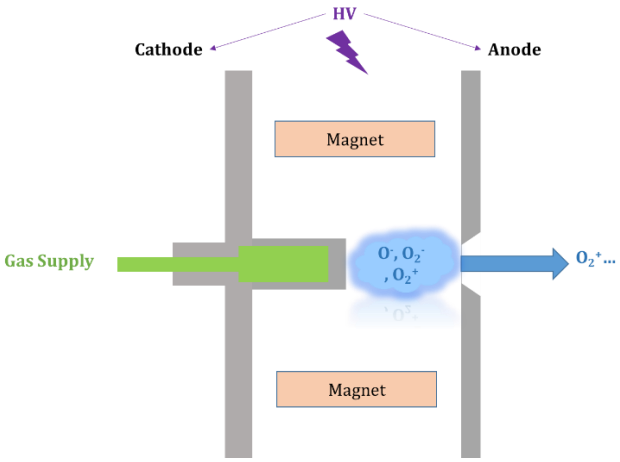

Figure 59: Schematic diagram of the duoplasmatron source installed in the GAMECA IMS-7f spectrometer.

C. Sample holder, analyzers (energy, mass)

The primary beam mass filter (PBMF) source eradicates the impurities in the experimental environment or generated in the ion sources. Without the mass filter, if the impurities interfere with interested ions in mass, these impurities impact the analysis, increasing the detection limit. The PBMF is thereby utilized to purify the primary ions. Before arriving in the analyzing chamber, the beam intensity and size can be adjusted by electrostatic lenses and apertures. The secondary ions are sputtered from the samples by the bombardment of the incident ions. As the sample holder is polarized to a high voltage (± 5000 V), the type of the sputtered secondary ions (anion or cation) to be detected can be adjusted by modifying the polarity of the sample, independently on the polarity of the primary ions. The sputtering secondary ions with wide-range energy are introduced to the ion energy analyzer through the immersion lens and transfer lens. Then only fraction of sputtered ions having the medium energy can enter the magnetic mass analyzer. In the mass analyzer, a magnetic field deflects the ions of interest, i.e. the ones with the mass-charge ratio $\frac{m}{q}$, towards the detectors. The magnetic field has to be adjusted for the detection of the ions with the mass-charge ratio $\frac{m}{q}$ following eq. 41.

$$\frac{m}{q} = \frac{B^2}{2V} r^2 \qquad \textit{eq. 41}$$

with B: the magnitude of the magnetic field (T)

V: ions accelerating voltage (V)

r: the radius of the magnetic analyzer (m)

The combination of the energy and mass analyzer enables the high mass resolution of the spectrometer (M/ΔM=10000),

D. Detection system

In the CAMECA IMS 7f spectrometer, there are four independent detectors i.e.: an electron multiplier, a faraday cup, a resistive anode encoder, and a fluorescent screen. Among them, the electron multiplier provides a count rate beyond 5×10^6 count/s and the faraday cup allows a lower count rate. The operator chooses the pertinent detector for the experiment, as only one can be used.

II.3.2.2 Detection of light-element impurities (C and O) in polycrystalline tungsten

In this section, the quantification of the light-elements impurities (C and O) is elucidated utilizing the dynamic SIMS analysis, the experimental conditions are also detailed.

A. Experimental conditions

The dynamic SIMS was employed to detect the light-element impurities (C and O) which could potentially decorate the vacancy-type defects, forming vacancy complexes. For the detection of these elements the Cs primary ion source is chosen. The energy of the ion source Cs^+ is 15 keV with an incident angle of 23° and a primary current of 40 nA, allowing the collection of the negatively charged secondary particles. In the case of O_2^+ions, the collection of positive charged secondary particles is favored, the incident O_2^+ions energy is fixed at 5 keV with an incident angle of about 45° and a primary current of 100 nA. The beam sputters the sample on a square area of about 150×150 µm^2. It is important to note that the size of the sputtered area can be reduced (ex: 100×100 µm^2 in our experiments) to check if the detected amount of element of interest is above the detection limit or not (see below). In both cases, the analyzing area remains on a circle with a diameter of around 33 µm. Following the reduction of the sputtering area, the sputtering rate increases leading to an increase of the intensity of the signal of the matrix element, in our case, tungsten. If the signal of the interested element decreases with the same tendency, it probably means that the detection limit of the element of interest is reached with current experimental conditions. Otherwise, the signal illustrates the distribution with true concentration of the element of interest in the sample.

B. Calibration and quantification

The raw spectrum from the SIMS analysis is the intensity (I, in counts. s^{-1}) as a function of the sputtering time (t, in s), which can be converted to the concentration as a function of the depth, so that illustrates the concentration depth distribution of the analyzing element in the sample. The sputtering time-depth conversion can be done by directly measuring the crater depth formed under the condition for which the sputtering rate is assumed to be homogenous for each analysis. A contact profilometer DEKTAK is available at the GEMAC laboratory with a vertical resolution of around 0.1 nm enabling the depth measurement of the carter. Concerning the intensity-concentration conversion, the typical method consists in determining the relative sensitivity factors (RSF), considering that the concentration of the matrix element is constant. The relation of the concentration of the analyzed element and RSF is expressed as:

$$C_E = RSF\frac{I_E}{I_M} \qquad \textit{eq. 42}$$

with C_E: the concentration of the analyzed element

I_E: the SIMS intensity of the analyzed element

I_E: the SIMS intensity of the matrix element

The RSF factor can be expressed as follows

$$RSF = \frac{\phi \cdot I_{Matrix}}{\int_0^t I(t)dt \cdot V} \qquad \textit{eq. 43}$$

with: ϕ: implantation fluence (at. cm^{-2})

I_{Matrix}: Intensity of signal of the 184W isotope (count. s^{-1})

$\int_0^t I_x(t)dt$: integral surface SIMS profile of element x (count. s^{-2})

V: sputtering rate ($cm.s^{-1}$)

To obtain the RSF for the quantification of the carbon and oxygen, tungsten ultra-pure samples were implanted with each ion at the JANNuS platform using 3 fluences, the high fluence (HF) and the medium one (MF), having a factor of two. As the lowest one introduced a quantity of the atom below the detection limit of the SIMS, the implantation with the lowest fluence can solely be used to study damage effect. However, the implantation profile of the MF and HF were correctly obtained by SIMS. In the following, the SRIM calculated depth profile is considered as the implanted real one. It has to be noticed that the SIMS profile can be superimposed to the real implanted one with potential superficial pollution (C and O) and a background due to the detection limit (DL) of the technique, as illustrated in Figure 60. The largest difference between the SIMS measured profile and the real implanted one comes from the detection limit, causing a non-detectable fraction A3; Meanwhile, the overestimate fraction A4 should be compensated by underestimated fraction A1. So the main issue of the determination of the

RSF is to estimate the offset fraction A3. To estimate the fraction A3, the SRIM profile was considered as the real implantation profile, as sketched in Figure 60 (green line). The ratio B, i.e.: the non-detected fraction over the total integrated area under the SRIM profile (Figure 61.A and C) was added in the SIMS profile, by multiplying by a factor of (1+B), to compensate the non-detected fraction (below the DL) thus the SIMS profile is roughly corrected to approximate the real implantation profile. The corrected SIMS profiles are more close the simulated ones (Figure 61.B and D).

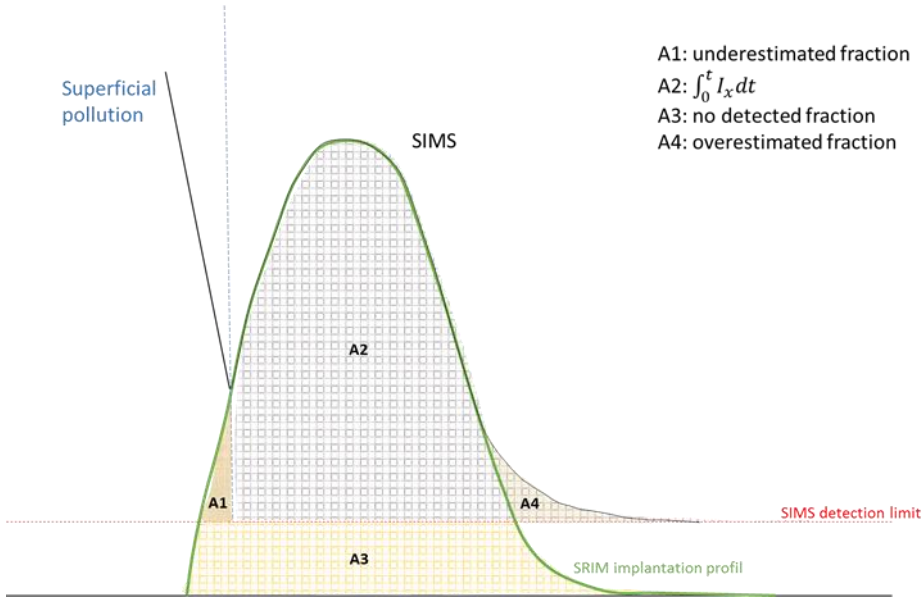

Figure 60: Comparison of the sketched real implantation profile and that determined from SIMS analysis

For instance, Figure 61 shows the SIMS profile of the extra-high pure tungsten samples implanted with 510 keV-^{16}O and 450 keV-^{12}C at the high fluence (HF = ~1.3 × 10^{15} at.cm^{-2}). For both fluences, the profile obtained with corrected RSF is closer to the 'real' one, and the SIMS profiles are not exactly reproducible, probably due to the polycrystalline nature of the samples are. Table 10 summarizes the SIMS results for the four implanted samples. The RSF determined for high and medium fluences are comparable for the implantation of C and O. Consequently, the average values of RSF determined for carbon and oxygen implantations, will be used to convert SIMS signal in concentration.

	Sample	Fluence (×10^{15} at. cm^{-2})	RSF_{cor} (×10^{20} at. cm^{-3})	Mean RSF_{cor} (×10^{20} at. cm^{-3})
C	ZH-W-P-UHP-FZJ2-C11	0.66	3.05	3.17
	ZH-W-P-UHP-FZJ2-C13	1.32	3.27	
O	ZH-W-P-UHP-FZJ1-C13	0.63	2.85	0.31
	ZH-W-P-UHP-FZJ2-C18	1.26	3.51	

Table 10: Corrected RSF value obtained from the C and O ion- implantation

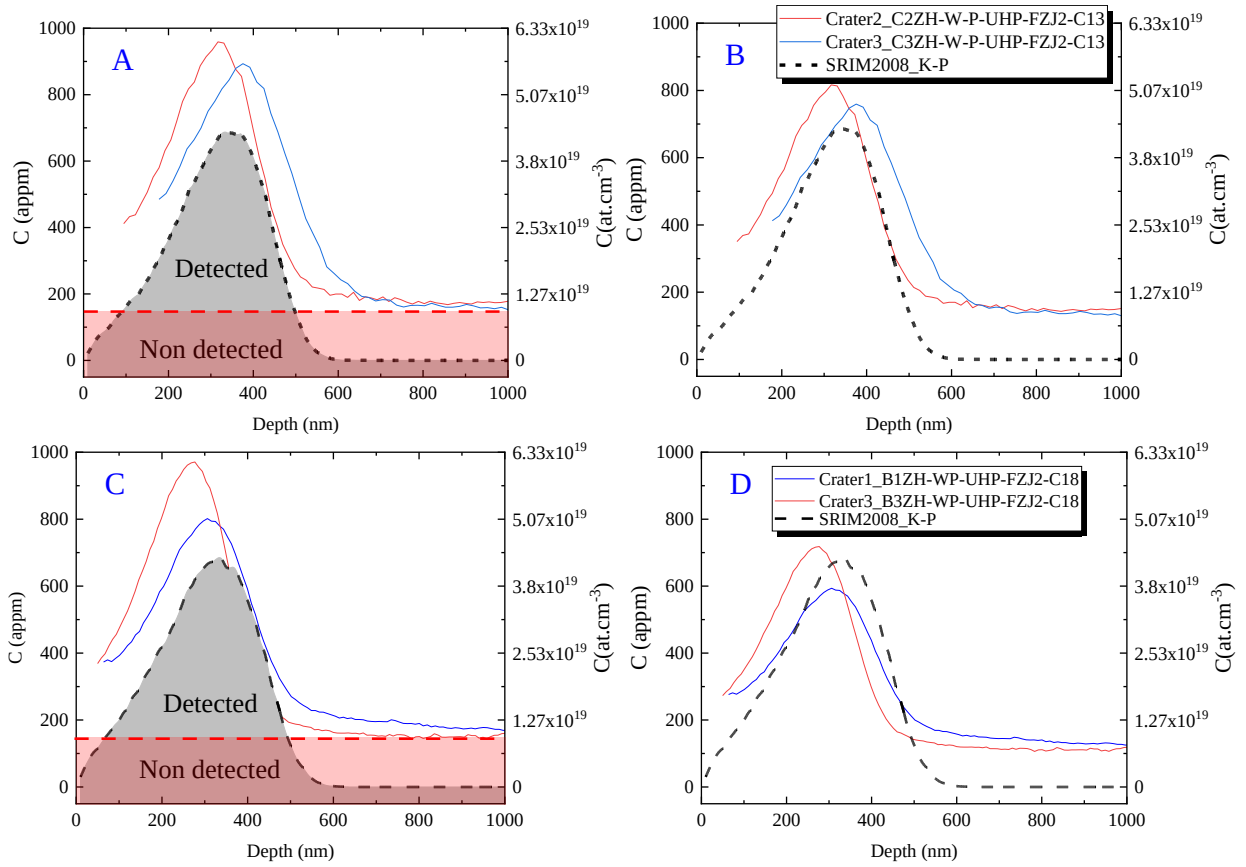

Figure 61: Depth profiles measured using SIMS at random position in XHP (99.9999 wt.%) tungsten samples implanted with 510 keV ^{16}O (ZH-W-P-UHP-FZJ2-C18, A and B) and 450 keV ^{12}C (ZH-W-P-UHP-FZJ2-C13; C and D) at the high fluence (1.32×10^{15} and 1.26×10^{15} at.cm^{-2}) compared to the SRIM calculated C and O profiles(dotted lines) . ***A, C****: calculation without correction of RSF* ***B, D****: calculation with corrected RSF using the methodology detailed in the text.*

To summarize, SIMS analysis allows to measure concentration depth profiles of various elements. It is based on the quantitative measurement of secondary ions sputtered from the surface sample using a primary ion beam. In this work we specially focused on the analysis of carbon and oxygen in tungsten. The experimental conditions were indicated, the calibration procedure was explained and the RSF values used to quantify the carbon and oxygen depth profiles in tungsten are given.

II.3.3 Nuclear reaction analysis (NRA)

II.3.3.1 Principle of the technique

The NRA technique is based on the production of nuclear reactions between the incident particles (or ions) and the nuclei of the target. The nuclear reaction is usually expressed as B (A, C) D where A is the incident particle, B is the nuclei of the target, and C, D are the products of the nuclear reaction. In general, with incident energy of the order of mega electron volt (MeV), the nuclear reaction occurs only with light nuclei in the target. Because of the strong electrostatic repulsion, heavy ions prevent the incident ions approach to the nuclei. The NRA is a technique quite sensitive for probing the Low-Z atoms (<15), in particular, enabling the in-depth detection of the concentration of the elements (^{2}H, ^{3}He, ^{12}C ^{14}N…).

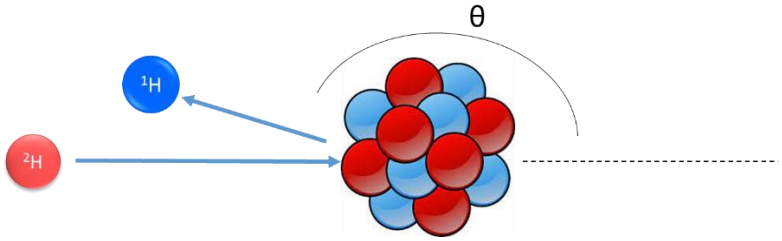

Figure 62: Schematic diagram of the NRA technique.

In this work, the NRA was carried out on the 3MV-PELLETRON at laboratory CEMHTI [194], which is used to quantify the oxygen and carbon impurity present in the tungsten sample through the nuclear reaction ^{16}O (^{2}H,^{4}He)^{14}N, and ^{12}C (^{2}H, ^{1}H)^{13}C [195], respectively. The measurement consists of impinging the sample with a 950 keV deuteron beam and collecting the alpha particles or protons produced by the nuclear reaction with a backscattering angle θ, of about 178° as a function of their energy, as sketched in Figure 62. It has to be noticed that the beam diameter is about 2 mm, allowing to quantify impurities at a scale larger than with SIMS and comparable with PAS measurements.

Figure 63.A exhibits the NRA spectrum of the matrix element (tungsten) obtained by collecting the back-diffused ^{2}H atoms as a function of channel and Figure 63.B shows the peak of the carbon atoms constructed by counting the yielded ^{1}H atoms. It is important to note that the height of the plateau value of the matrix element (Figure 63.A, for tungsten) is related to their concentration. The area below the peak of the detected carbon atoms (Figure 63.B), and its width is related to the analyzed thickness. The fitting of the experimental spectrum allows extracting distribution of the impurity elements as a function of the depth. In this work, the program SIMNRA 7.03 is used to fit the experimental spectra. The following expression is used to convert channel in energy and represent the spectra as a function of the energy of the reaction products(eq. 44):

$$Energy_{keV} = 21 + 2.347 \times channel \qquad \textit{eq. 44}$$

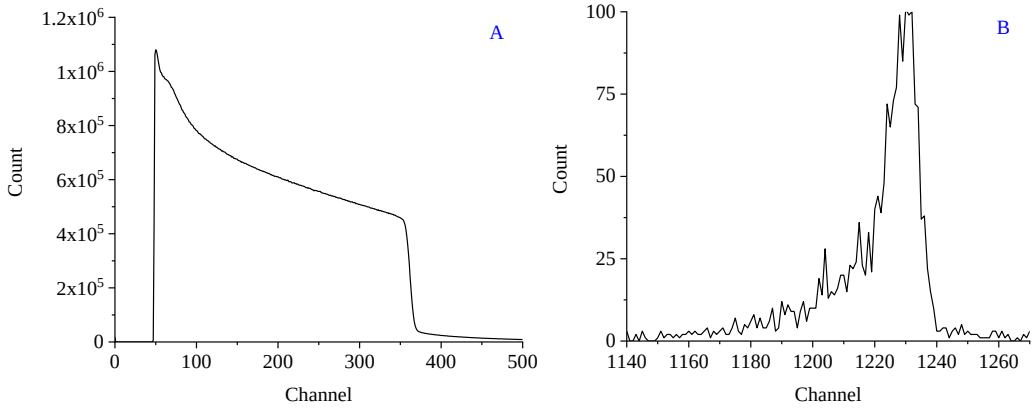

Figure 63: Raw NRA spectrum A: the $^{2}H^{+}$ backscattering spectrum of the tungsten and B: the ^{1}H NRA spectrum of the carbon atom

II.3.3.2 Data processing

Figure 64. *a* shows an experimental spectrum (red dot and line) corresponding to a carbon-enriched layer in tungsten with the fitting curve (blue line). The depth resolution was determined by using the RESNRA program [196] and is of about 480 × 10^{15} at.cm^{-2}. Thus the sample was modeled as a multi-layer with a thickness of the multiple of 480 × 10^{15} at.cm^{-2}, in which the concentration of C was adjusted to obtain the best possible fit matching to the experimental spectrum. The SIMNRA gives out the distribution of the major impurity elements in each layer, which is obtained by converting the thickness of each layer into depth by dividing by the density of the material (6.33 × 10^{22} at.cm^{-3} for tungsten).

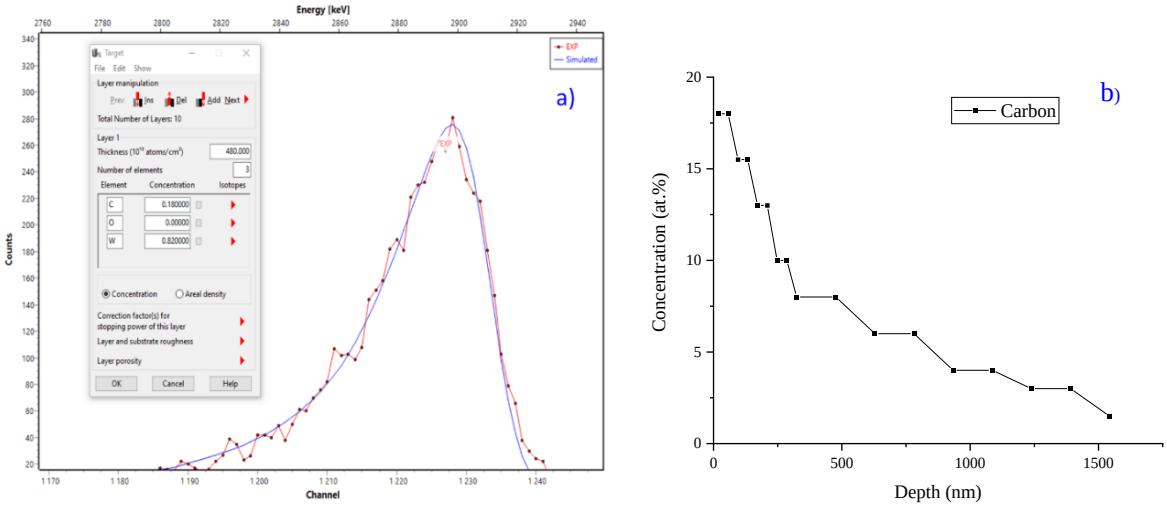

*Figure 64: **a)** NRA experimental spectrum of carbon-enriched surface of the polycrystalline tungsten **b)** the carbon distribution vs depth obtained by the SIMNRA program*

For instance, Figure 64. *b* exhibits the carbon concentration as a function of the depth at the surface of the polycrystalline tungsten, as a result of the fitting of the C-NRA spectrum plotted on the left. It should be noted that the roughness of the surface of the sample is not taken into count in the simulation, which might cause incertitude on the depth depending on the real surface aspect. It is noteworthy that the error on the concentration of the impurity atom is estimated by making a ratio between the counts in each layers of the fitting over the total count in the whole investigated region and combing a 2 % error on the count, given that tungsten is a compact material which should recoil larger number of incident particles. It has to be noticed that the detection limit is about 1 at. ppm for carbon and oxygen in tungsten. Even though, this technique is less sensitive than SIMS, but it provides larger analyzed area.

In summary, NRA is based on the production of nuclear reaction and measurement of its products to detect and profile elements in matrix. It is specially adapted to quantify light-elements impurities at the surface of solids. Even though the detection limit is higher than SIMS and the analyzed sample is activated by nuclear reaction, whereas this technique provides a comparatively larger probing area.

II.3.4 Transmission Electron Microscopy (TEM)

TEM is one of the most important and indispensable techniques for material science. It enables the characterization of both interstitial or vacancy-type extended defects (dislocation, dislocation loops, voids or cavities, etc.). The principle of this method is to use different contributions of transmitted electrons (Figure 65) to constitute micro-nano scale images and diffraction patterns, which provide abundant helpful information of material with direct observation, Yi et *al.*[127] observed dislocation loops in self-ion irradiated tungsten. Hasegawa et *al.*[197] discovered voids, dislocation loops, and precipitates after neutron-irradiated tungsten. In the present work, TEM is used as a complementary technique to PAS for characterizing the vacancy-type defects in tungsten. The following paragraphs describe the methods for characterizing irradiation-induced vacancy-type defects, in particular the vacancy clusters or voids.

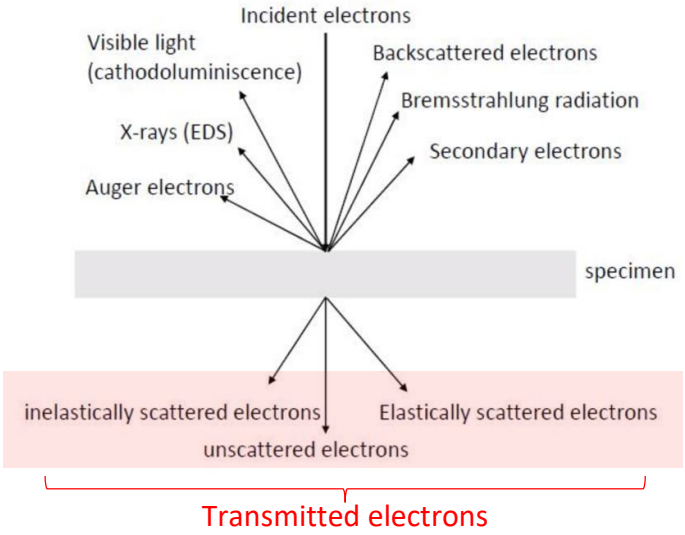

Figure 65: Different contributions of the electron yield from the interactions with matter.

II.3.4.1 Principle of the technique

Figure 66.a illustrates a schematic diagram of a conventional transmission electron microscope (CTEM) forming an image on a viewing screen. An intermediate lens is focused on an objective lens image plane. In this case, the path of the electrons should be aligned on the whole column of the TEM. Theoretically, all the transmitted electrons (scattered and non-scattered, so-called two-beams) are used to form a 2-D image. The observation can also switch to the diffraction pattern (DP) mode by putting an aperture of the intermediate lens (Figure 66. b), and the electron beam is more diffracted by objective lens, in order to obtain a DP at selected area (Selected Area Diffraction). The DP mode is usually used to identify a zone axis and the diffraction vector $\vec{g}$ in the case of characterization of the dislocation lines or loops. Coming back to image mode, there are two types of imaging mode, namely bright field (BF) and dark field (DF) mode. The BF (resp. DF) mode forms an image with the non-scattered (resp.

scattered) electrons. Therefore, the change of the contribution of the scattered and non-scattered electron for the formation of an image enables the alternation of these two modes. Since the DF mode has a strong diffraction contrast, it is in particular used to characterize small dislocation loops. In contrast, due to the higher visibility, the BF mode is commonly used to identify vacancy clusters or voids, which are observed as a light dot on the dark background. As a consequence, the best condition to observe the large voids in metals (> 5 nm) is 'in-focus' BF mode. Nonetheless, to confirm the presence of the small vacancy clusters (< 5 nm), the out-of-focus imaging increases the Fresnel contrast and a small void appears either as a black dot surrounded by a white halo in over-focused observation (OF) or as a white dot surrounded by a black halo in under-focused (UF) observation [198]. Since this work is focused on the characterization of the vacancy and small vacancy clusters in tungsten, the BF mode with out-of-focus observation is the most adequate.

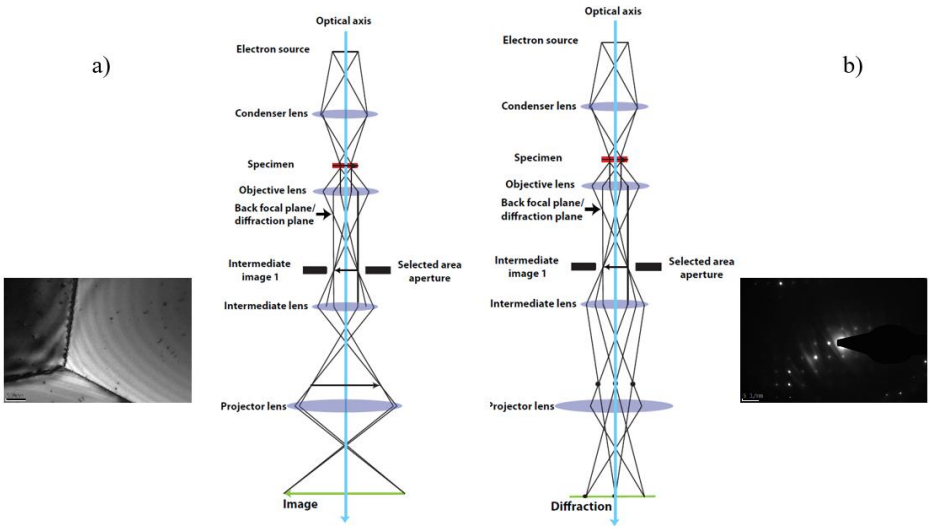

*Figure 66: Self-irradiated polycrystalline tungsten observed on **a)** image mode, a tri-junction of grain boundaries and a few defects are visible and **b)** DP mode of the CTEM*

II.3.4.2 Characterization of voids

Figure 67 shows a defocused imaging couple (± 300 nm) of a self-ion irradiated tungsten foil at 500 °C. Series of out-of-focus imaging, ranging from -400 nm to +400 nm, was recorded using a microscope Philips CM20 with 200 kV electrons. The irradiation-induced small voids were identified by the Fresnel contrast method with a limitation of about 0.5 nm. The presence of a void is confirmed by localizing at the same position of a pair-image of an object (dot with halo) that changes of color (black to white) when the out-of-focus level reverses. Once a void is confirmed, its size can be measured directly using the program Digital Micrograph.

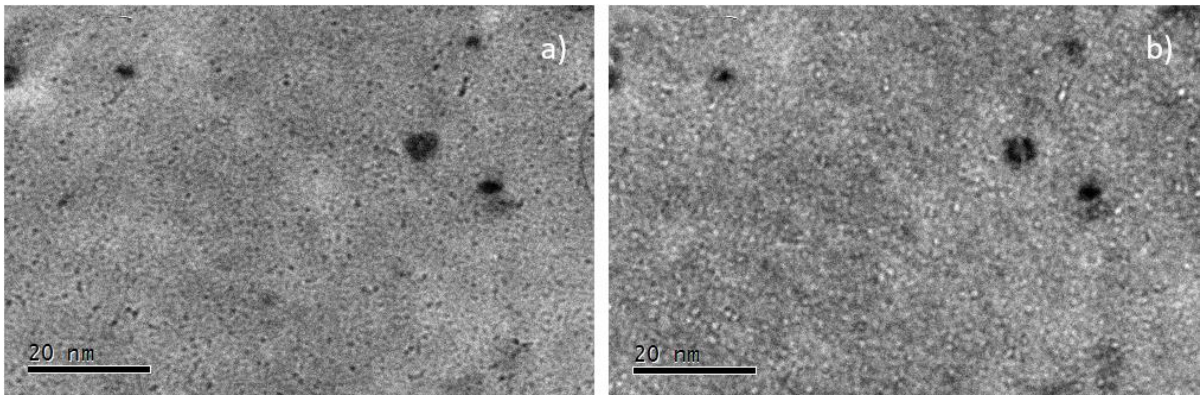

*Figure 67: A couple of the out-of-focus images of a self-ion irradiated tungsten foil at 500 °C with a fluence of about 1.8 × 10^{12} cm^{-2}, recorded with a microscope Philips CM20 with 200 kV electrons **a)** OF +300nm and **b)** UF -300nm observation*

Since both the imaging and technique conditions impact the apparent size of the voids [199], the whole TEM observations were carried out under comparable conditions, i.e. acceleration voltage, magnification, and out-of-focus level. It should be noted that the focus changes during the acquisition, thus, occasionally, the most comparable pair-image with UF and OF observation could not be at the same out-of-focus level, however, the difference was not too large, of about 50 nm. Besides, the distortion of the image could make the identification of the small voids more difficult on the pair-image. In such a case, it is important to choose several referential objects in the image. These impacts are important to take into consideration for the characterization of voids. As a result, to minimize the uncertainty on the size determination of the small voids, the sizing was performed at the best conditions, taking the compromise between the clarity of the image and the low-difference of pair image, so that the sizing of the voids was realized on the over-focused image with the close out-of-focus level (± 250 nm and/or ± 300 nm). Figure 68 shows a measurement of a small vacancy cluster induced by self-ion irradiation in tungsten foil at 500 °C with a fluence of about 1.8 × 10^{12} cm^{-2} through the Digital Micrograph program. To detrmine the concentration of the small voids, the thickness of the thin region where the voids were characterized was measured using Energy Filtered Transmission Electron Microscopy (EFTEM) and Electron energy-loss spectroscopy (EELS).

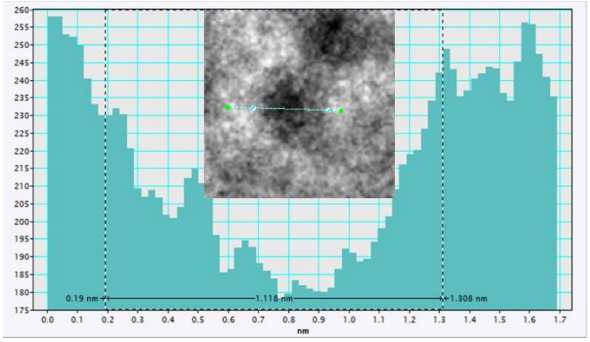

Figure 68: A measurement of the diameter of a void induced by self-ion irradiation in tungsten at 500 °C with a fluence of about 1.8 × 10^{12} cm^{-2} through Digital Micrograph

The uncertainty on the diameter d and the density D of cavities can be estimated by the following equations [200]:

$$\Delta d = d \times \left(\frac{\Delta N}{N} + \frac{\Delta d_{av}}{d_{av}}\right) \quad \textit{eq. 45}$$

where Δd is the total uncertainty of the diameter d, $\frac{\Delta N}{N}$ the error on the number N of cavities which equals to $\frac{1}{\sqrt{N}}$, and $\frac{\Delta d_{av}}{d_{av}}$ is the error on the diameter measurement which was experimentally estimated at 15 %. To determine the latter term, we chose 10 cavities of different sizes to estimate the minimum and maximum size for each cavity and finally, we found the average size and the standard deviation (for each cavity). $\frac{\Delta d_{av}}{d_{av}}$ was taken as the average ratio of the standard deviation over the average size:

$$\Delta D = D \times \left(\frac{\Delta N}{N} + \frac{\Delta t}{t}\right) \quad \textit{eq. 46}$$

where ΔD is the total uncertainty of the density D and $\frac{\Delta t}{t}$ is the error on the thickness t measurement equal to the ratio of uncertainty over measured thickness.

To sum up, TEM allows to characterize extended defects in materials. In this work it is used to characterize large vacancy clusters in irradiated tungsten as the complementary technique of the PAS.

Summary

This chapter presents the description of the material and its preparation on the one hand and the experimental techniques used for their characterization on the other hand. The polycrystalline tungsten samples of two purities were mechanically polished and annealed under a high vacuum level (< 10^{-6} mbar) at 1700 °C for 3 hours. The as-annealed samples contain grains of a few tens microns to a hundred microns.

Various irradiation/implantation conditions were used to create defects or to introduce extrinsic elements. The damage and implantation profiles were calculated using the SRIM-2008 (K-P mode, E_{disp} = 55.3 eV) for self-ion irradiation (at 1.2 MeV, 2 MeV, and 20 MeV) of tungsten and ions-implantations (450 keV-C and 510 keV-O). The experimental fluence, and flux for self-irradiation (1.2 MeV and 20 MeV) were selected to obtain an equivalent damage dose of about 0.02 dpa in both the thin layer irradiated with 1.2 MeV ions and in the depth probed by DB-PAS (~700 nm) for the bulk sample irradiated with 20 MeV ions, with a comparable damage rate around 5×10^{-5} dpa. s^{-1}. The energy and fluence of the C and O implantations were chosen to implant the same amount of ions (MF: 340 at. ppm, and HF: 680 at. ppm) at the Rp of about 330 nm. For 2.5 MeV electron irradiations with two fluences (LF: 1×10^{19} cm^{-2}, and HF: 2×10^{19} cm^{-2}), the POLY ET SMOTT program predicts a linear decrease of the damage dose as a function of the depth until 150 µm. The damage dose in the first micron is

considered as homogenous at a value of 3.74×10^{-4} and 7.47×10^{-4} dpa for respectively LF and HF fluences.

Positron Annihilation Spectroscopy (PAS) and Transmission Electron Microscopy (TEM) were used to characterize vacancy-type defects, taking the advantage of their complementary detection limits.

PAS is a powerful technique for characterizing vacancy defects in metals. It is based on the properties of the positron in solids: **(1)** as the antiparticle of the electron it annihilates with it; **(2)** because of its positive charge it can be trapped in vacancy defects. By measuring the positron lifetime and the energy of the gamma emitted when electron positron pairs annihilate, it is possible to obtain information on the electron density and momentum distribution of the annihilated electron-positron pairs. It allows to detect different types of vacancy defects from single vacancies to vacancy clusters in the bulk or in thin films by using fast or slow positrons respectively. The SPB-DB measures the gamma-ray emitted from positron annihilated with electron at different annihilation states. It provides the momentum distribution of the annihilating e^+-e^- pairs, which allows to distinguish between the different vacancy-type defects in the materials. The annihilation characteristics are represented by the line shape parameters ***S, W*** of the momentum distribution. When annihilation occurs at vacancy-type defects or open volumes rather than in the lattice of the sample, ***S*** increases and ***W*** decreases with increasing defect size and/or concentration. The line shape parameter as a function of positron energy ***S***(E), ***W***(E) reveals the depth distribution of the defects, and the ***S***(***W***) curve indicates the size of the defects or the special chemical environments of the positron. Defect concentration can be determined using trapping models. With the one-trap trapping model, the SPB-DB device can detect the concentration of the single vacancy between 10^{23} m^{-3} and 10^{26} m^{-3}.

Compared to PAS, TEM is a more conventional characterization method for metals. It allows direct observation of the microstructure of the material. It is based on collecting the various types of transmitted electrons to form a 2D projection image, from which significant information about the defect can be acquired. However, the size of the observed defect is limited to about 0.5 nm in tungsten. In this study, TEM is used to observe the large vacancy clusters induced by self-ion irradiation with 1.2 MeV-W, the characterization is determined by using the Fresnel contrast method.

In addition, Secondary Ion Mass Spectroscopy (SIMS) is used to measure the depth concentration profile of various elements in a matrix. This analysis was performed at GEMAC laboratory. The calibration of the SIMS data requires the determination of the RSF factors. The values for carbon and oxygen was determined by analyzing the implanted samples with known quantities of these two ions. These values allow the quantification of the carbon and oxygen in the tungsten.

Finally, Nuclear Reaction Analysis offers a larger detected area in contrast to SIMS for low mass elements. The quantification of the low mass element is done by collecting the stable particles produced by nuclear reaction between incident particles and the element of interest. This technique is available in

CEMHTI Laboratory, and is used in the present work to quantify carbon and oxygen, where their concentration is high (> 17 at. %) and their global distribution in the tungsten is required.

Chapter III: Qualification of the as-annealed pristine samples

The microstructural evolution of the tungsten under irradiation is one of the major issues that can affect the normal operation of the future fusion reactor. In the present work, the vacancy-type defects induced by irradiation in various conditions were investigated. The samples were carefully prepared using several preparation stages in order to get a minimum defect concentration.

In this chapter, the quality of the as-annealed pristine samples is checked by using SPB-DB and PALS measurement. Furthermore, the optical microscope observation, and chemical analysis (NRA, and SIMS) are also carried out to understand the abnormal annihilation characteristics in some as-annealed pristine samples obtained by SPB-DB measurement.

III.1 The checkup of as-annealed pristine samples

III.1.1 SPB-DB characterization

PAS is one of the most sensitive techniques for accessing the scale below the detection limit of the TEM (< 1.5 nm [198]), in particular, for probing the vacancy-type defects. Thereby, the SPB-DB and the PALS measurement were employed to check the quality of samples, especially the quantity of the defects. Before the irradiations (e^- and self-ion), the various types (Goodfellow, Neyco, FZJ) of the as-annealed polycrystalline tungsten were characterized by SPB-DB measurement Figure 69.a-b exhibits ***S(E), W(E)*** curves i.e. the low momentum parameter ***S*** and high momentum parameter ***W*** as a function of positron energy ***E***, respectively.

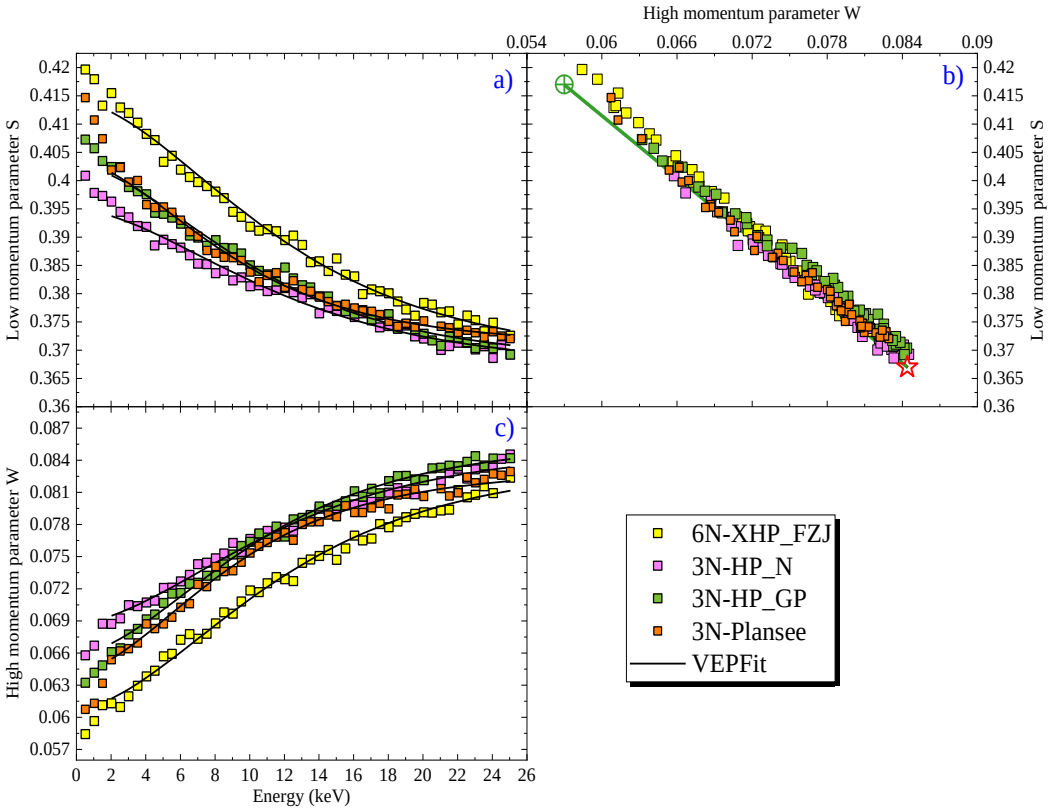

*Figure 69: **a)** Low momentum parameter S and **b)** the high momentum parameter W as a function of positron energy and **c)** the S versus W for the as-annealed polycrystalline tungsten sample of three manufactories Neyco (Magenta), Goodfellow (green) and PLANSEE (6N-yellow, 3N-orange) with the fit using a the one-layer model. The annihilation characteristics in the Lattice (☆) and at single vacancy (⊕) are also plotted.*

Within the energy range of 0.5 to 25 keV, the parameter ***S*** decreases and ***W*** increases progressively with increasing positron energy ***E***, until the highest energy (25 keV), for which ***S*** and ***W*** tend toward the annihilation state of the ***Lattice***. Moreover the ***S-W*** points corresponding to the values of ***S*** and ***W*** for the same energy follow a straight line indicating that the same annihilation states are detected whatever the energy (see Figure 69.c). One of the annihilation state is characteristic of the surface and the other of the bulk. The fraction of the positrons which annihilates at the surface of the tungsten

decreases with increasing the positron energy. This feature suggests a large fraction of positrons, which depends on the incident energy, can diffuse back toward the surface to be annihilated. In addition, the ***S(W)*** line goes to the direction of SW annihilation characteristics of the perfect ***Lattice*** (named as the ***Lattice*** point in the following) for each sample. Consequently, the positrons annihilate mainly at two annihilation states, either at the surface or in the ***Lattice*** of the tungsten in the as-annealed slabs. To validate the hypothesis of the two annihilation states, the VEPFIT program is operated to fit experimental data. A single-layer model matches quite well the data of each type of the as-annealed samples. Table 11 summarizes the fitted annihilation characteristics in the homogenous layer fitted by the VEPFIT program. For the three types of annealed samples, the VEPFIT program proposed a long effective diffusion lengths L_{eff}^{+} , which are 100 ± 3 nm, 124 ± 4 nm, and 121 ± 4 nm for 6N-XHP_FZJ, 3N-HP_GP, and 3N-HP_Neyco, respectively. These values are within the range of reported ones of well-prepared polycrystalline tungsten sample, between 80 to 140 nm [36,201]. In addition, Vehanen et *al.* [202] reported a comparable intrinsic diffusion length of 135 nm for a polycrystalline tungsten 3N-HP samples (99.95 wt.%) annealed at 2200 °C, in 6.6 × 10^{-8} mbar vacuum. Moreover, the ***S, W*** values of the homogeneous layer (corresponding to the bulk of the sample) as extracted from fitting are quasi identical to those of the tungsten ***Lattice*** (S_L = 0.367 (2), W_L = 0.084 (1)), as determined in the previous works [36]. However, the annihilation characteristics of the surface (S_{surf} and W_{surf}) of the three samples are different and vary in the range from 0.395 to 0.414 for S_{surf} and and from 0.061 to 0.069 for W_{surf}, respectively. The 3N-HP_Neyco sample shows the lowest S_{surf}, and the highest W_{surf}, and then $S_{surface}$ increases (and $W_{surface}$ decreases respectively) for 3N-HP_GP and becomes much higher (and lower resp.) for 6N-XHP_FZJ. In addition, the diffusion feature is less evident for this last sample, i.e. the ***S(E)*** (resp. ***W(E)***) decreases (resp. increases) rapidly at low energy and slow down at the high energy (~20 keV). Such difference is probably due to the long-term storage (~ a few years) leading to a surface change such as the surface oxidation which is a common issue for metals and has been observed in tungsten at RT [203]. This oxidation layer should present different annihilation characteristics compared to the proper metallic one. The results of the fitting shows that this layer is very thin and does not affect the diffusion of the positron. The effective diffusion length unveils that the samples have a low concentration of positron traps. It is possible to estimate the concentration of them considering that only one type of defects (the single vacancy) could be at the origin of trapping and using single-trap trapping model as shown in the Chap II.3.1.4. The estimated concentration of traps are reported in the last column of the Table 11. Their values are in the range from 3.25 to 13.06 × 10^{23} m^{-3} by taking an intrinsic positron diffusion length in the tungsten of 135 nm [202] and mean lifetime of Lattice obtained in present work of about 105 ps. As a consequence, the SPB-DB measurement confirms the good quality of the as-annealed pristine samples in the probed region that means in the 700 first nm under the surface.

Apart from the samples prepared at CEMHTI, an as-annealed 3N-HP sample from Plansee was provided by Culham Centre for Fusion Energy (CCFE). They used similar procedures to prepare their

samples: mechanical polishing, cleaning in ultrasonic bath with isopropanol and acetone, before annealing at 1500 °C for 20 hours in vacuum (6×10^{-6} mbar). The ***S(E)*** and ***W(E)*** curves of the pristine sample are plotted in Figure 69 (orange square). Although the ***S(E)*** and ***W(E)*** curves seem to be close to those of the other as-annealed ones plotted in Figure 69, the fitted line shape parameters $S = 0.370$ (1) and $W = 0.083$ (1) by VEPFIT are respectively somewhat higher and lower than the defined value of the tungsten ***Lattice***. That indicates the presence of a few residual vacancy-type defects (mainly V_1) after preparation where the positrons were trapped and annihilated. However, the concentration of the residual defects should not be too high, given the long effective diffusion length of about 80 ± 1 nm corresponding to a relatively higher concentration of the defect of about 2.93×10^{24} m^{-3}.

	S_{surf}	W_{surf}	S	W	L_{eff}^{+} *(nm)*	*Concentration* *(10^{23} m^{-3})*
6N-XHP_FZJ	0.413 (3)	0.0608 (3)	0.367 (3)	0.0842 (3)	123 (3)	3.248
3N-HP_GP	0.403 (4)	0.0659 (4)	0.367 (3)	0.0861 (3)	100 (3)	13.06
3N-HP_Neyco	0.395 (3)	0.0688 (3)	0.366 (3)	0.0855 (3)	121 (4)	3.886
3N-HP_Plansee		0.0641 (3)	0.370 (3)	0.0833 (3)	80 (2)	29.33

Table 11: Annihilation characteristics S,W of the bulk as extracted using VEPFIT for different as-annealed samples and the estimated concentration of the residual vacancy-type defects.

III.1.2 PALS characterization

After the quality of near-surface (~700 nm) part was qualified by SPB-DB measurement, the in-depth part (~50 µm) was checked by fast positrons using the PALS measurement. Figure 70.a shows the experimental PALS spectrum of three pairs of samples with different purities. By operating the fitting program ANAPC, the deconvolution with one lifetime component is quite adequate to fit the experimental data. Table 12 summarizes the lifetime components obtained from the deconvolution of the experimental spectra of the different as-annealed samples. The spectrum of the 6N-XHP_FZJ pairs was deconvolved by a fit with the shortest lifetime, i.e. 103 ps, and 106.8 ps in contrast to the higher value (110 ps) obtained for the 3N-HP_GP pairs, meaning a slightly lower quantity of the defects in the 6N-XHP_FZJ. As solely one sample of the 3N-Neyco left, so that, it was coupled with one 6N-XHP_FZJ which gave out the shortest lifetime. The deconvolved lifetime τ is 105 ps indicated that the lifetime in the 3N-HP_Neyco is slightly higher and lower than the one measured in 6N-XHP_FZJ and in 3N-HP_GP respectively. These values are comparable to those reported for pristine tungsten in experimental studies or calculated for ***Lattice*** as shown in Figure 70.b. For instance, Sato et al. [141] reported a lifetime of 109 ps for the as-annealed samples with similar conditions (1500 °C for 1h in 10^{-6} mbar), as a contrary a longer lifetime of 118 ps [137] was found in the samples annealed merely at 900 °C for 1 hour in vacuum.

It has to be noticed that the highest lifetime found in GP material is in agreement with the lowest effective diffusion length (100 nm, see Table 11) indicating the highest concentration of defects among the samples prepared at CEMTHI. It is arduous to identify the nature of the defects even in PALS, because it is impossible to extract a second lifetime component probably because its intensity is too low.

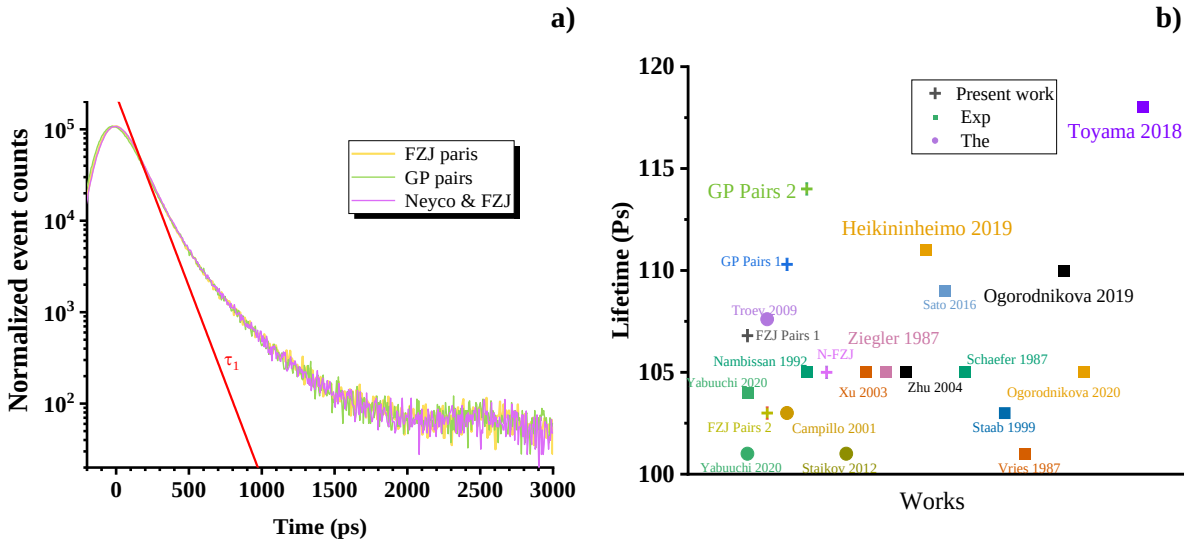

*Figure 70 : **a)** experimental PA Lifetime spectrum of different as- annealed samples and **b)** the comparison of the reported lifetime of tungsten Lattice determined by PALS in experiment or calculation*

Purity		τ_1 *(ps)*	error *(ps)*
6N-XHP_FZJ	pair 1 (J107-J108)	106.8	0.3
	pair 2 (J28-J29)	103.0	
3N-HP_GP	G13-G14	110.3	
3N-HP_Neyco & 6N-XHP_FZJ	PS6-J29	105.0	

Table 12: Measured lifetime for the as-annealed samples

Conclusion

Finally, the quality of the annealed pristine samples was verified by PAS. Both SPB-DB and PALS measurements indicate that from the near surface (~700 nm) and down to the in-depth bulk (~50 µm) of the samples, the annihilation characteristics are those of the tungsten ***Lattice***. The positron effective diffusion length extracted from SPB-DB measurements give a value longer than 100 nm. Moreover, only one lifetime component was extracted from lifetime spectra with a value in the range between 103 and 110 ps. Both results indicate a low concentration of defects (< ~10^{24} m^{-3}) in these different types of as-annealed pristine samples.

III.2 Unexpected carbon-enriched layer

It has to be noticed that, a fraction of the samples of 6N-FZJ samples exhibited abnormal annihilation characteristics, as-shown in Figure 71, a comparison of two as-prepared samples, namely ***J15*** and ***J31***. As mentioned in the Chap III.1.1, the annihilation characteristics of the ***J15*** are similar to those of the perfect ***Lattice*** of the tungsten with comparable fitted value of ***S*** and ***W*** and an effective diffusion length of about 123 nm (Table 11). Nonetheless, the ***J31*** shows different annihilation characteristics. The curves ***S(E)*** and ***W(E)*** were plotted in Figure 71. a and c. With increasing positron energy, the ***S*** (resp. ***W***) decreases (resp. increases) to a first short plateau between around 14 to 16 keV, before coinciding with the end of the diffusional trend of the ***J15***. It seems that the diffusion of positron toward to the surface was interfered. After checking their surface aspect by means of the optical microscope (see Figure 72), the J15 has large grains of about few hundred microns with the visible grain boundaries (GBs). On the contrary, no visible GBs was observed in the sample ***J31***. Instead, countless dark dots ("sesame seeds") are observed, which probably indicates a different chemical composition at the surface of the ***J15*** and ***J31***. And this might be the reason for which the annihilation characteristics of the positrons differ from one to another in the low energy range (< 16 keV).

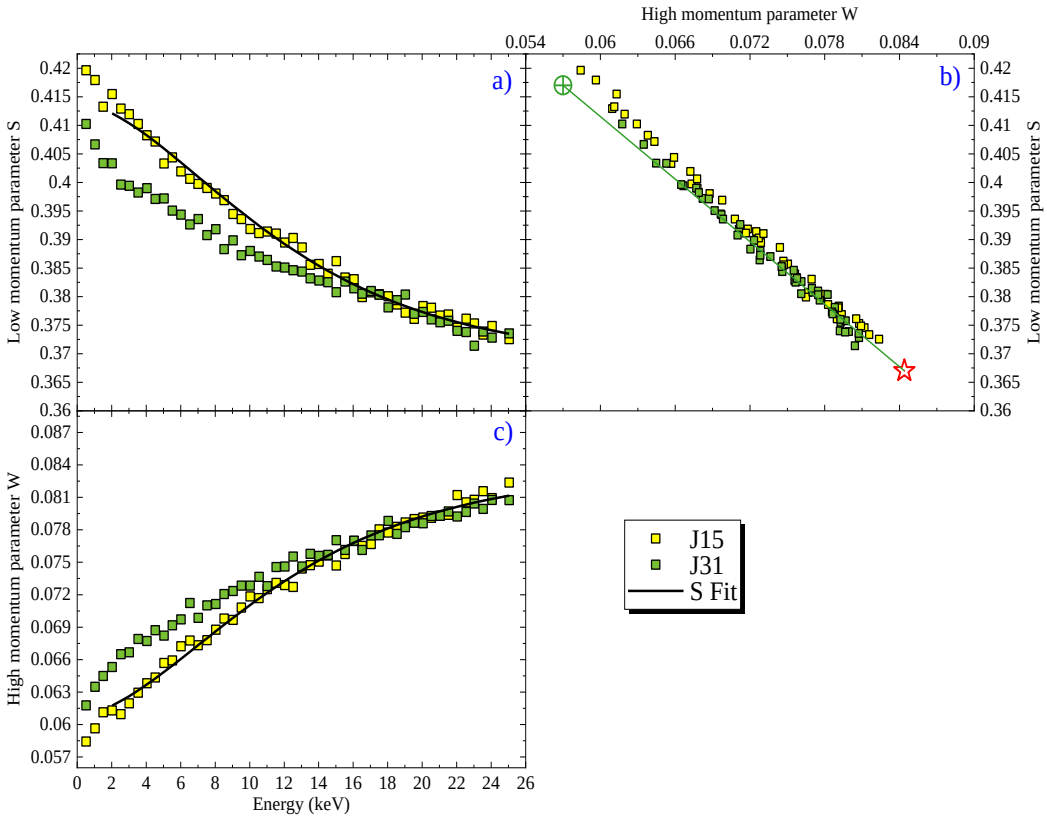

Figure 71: Comparison of the a) the low momentum parameter S and b) the high momentum parameter W as a function of positron energy and c) the S versus W for the as-annealed polycrystalline tungsten samples of FZJ (yellow) with the fit of the one-layer model and the annihilation characteristics in the Lattice (☆) and at single vacancy (⊕) are also plotted

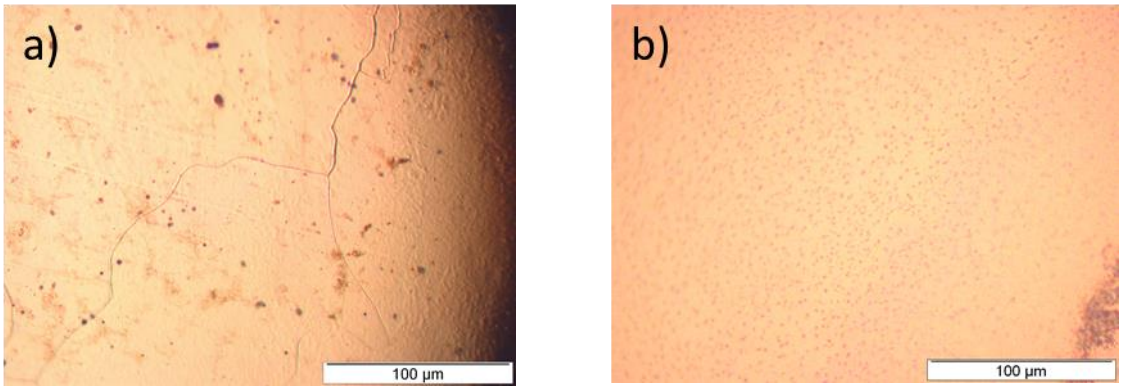

Figure 72: Surface aspect of the a) J15 and b) J31 obtained by optical microscope

To check the chemical composition of the surface of the sample ***J31***, SIMS analysis were carried out on two random positions of the sample surface (as shown in). Figure 73 shows the SIMS profiles of both ^{12}C, ^{16}O light elements concentration and the matrix major isotope ^{184}W raw signal for both craters (1 and 2). It should be noted that the ***J15*** was neither checked by SIMS nor NRA, but the entirely different microscopic morphology was already confirmed.

On the one hand the ^{16}O profiles are almost the reverse to those of the ones of ^{184}W. After some times of measurement, the sputtering area is reduced, it leads to an increase of the signal of the matrix element (see the step in the ^{184}W signal Figure 73.a) At the same time the concentration of the ^{16}O decreased, which probably means the ^{16}O detection reached the limit of the operated area (sputtering area: 150 × 150 µm^2, analyzed area: Ø 33 µm) under the vacuum level in the analysis chamber (~2 × 10^{-9} mbar). The mean concentration of Oxygen is around 200 to 300 at. ppm.

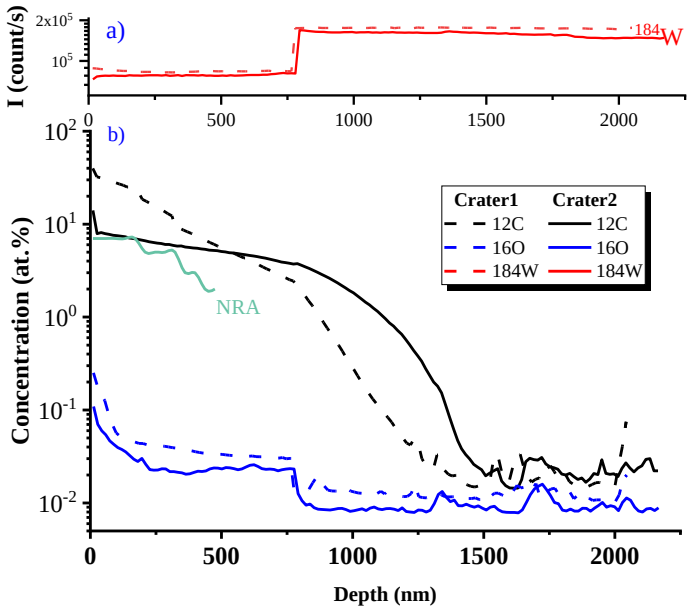

Figure 73: SIMS profile of the ^{12}C , ^{16}O and, Matrix element ^{184}W of two random positions of the J31 in comparison of the NRA profile of ^{12}C

On the other hand, it is surprising that the quantity of the ^{12}C is quite high. More than one atomic percent of carbon (1 at. %) was detected in both craters up to ~1µm depth. At the surface region, between

200 to 400 nm, in which the vacancy-type defects should be efficiently probed by slow positron. Moreover, dissimilar profiles were obtained in the two craters (Crater 1 and Crater 2) of the J31 sample. More carbon was detected in Crater 1 and the depth distribution is different, indicating that the carbon enriched layer is not homogeneous. Meanwhile, NRA analysis was performed to verify the unexpected concentration of carbon obtained by the SIMS. It has to be noticed that the analyzed area of NRA (2 × 2 mm^2) is much larger than SIMS one and more compatible with the PAS one. However, the detection limit is higher (of about 1000 at. ppm) and the probed depth is lower (1-2 µm) compared to those of the SIMS. As shown in Figure 73.b, about 7 at.% carbon was detected at the surface by NRA, and the NRA ^{12}C profile is similar to the one of the sputtered Crater 2 for depth below ~400 nm. Despite a discrepancy of the profiles between the Crater 1 and Crater2 of SIMS, which might be caused by the localized analyzed area, a high concentration of carbon, more than 5 at. % was confirmed at the surface of the ***J31***. As a result, this C-enriched layer probably impacts on the annihilation of the positrons.

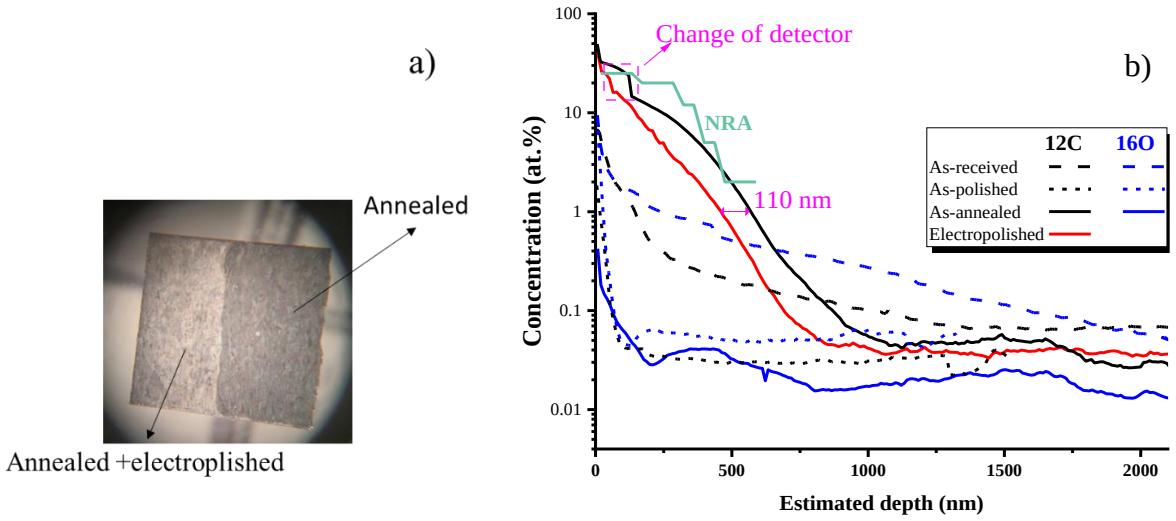

*Figure 74: **a)** Surface aspect of the samples **J12** has been half-electropolished **b)** SIMS profile of the ^{12}C ,and ^{16}O of two random positions of the **J12** before / after annealing and further electropolished after annealing in comparison of the NRA profile of ^{12}C. It is noteworthy that the steep drop of the concentration of the ^{12}C (marked by the magenta square) did not concern the decrease of the carbon concentration in the sample but the switch of the detectors, from faraday cup to electron multiplier*

To access the origin of the carbon, the SIMS analysis were carried out on a 6N-XHP sample **J12** at each step during the preparation (as- received, polishing, annealing…). As shown in Figure 74.b, the as-received sample contains 0.1 to 1 at.% ^{12}C and ^{16}O in the first 2 µm. After polishing (close to 80 µm of matter was removed), the ^{12}C and ^{16}O concentration are between 0.03 and 0.06 at. %, respectively, if the first 100 nm are considered as the environmental pollution on the sample surface. After annealing, the ^{16}O concentration was still comparable to that of the as-polished one, but the ^{12}C concentration became much greater and the enriched carbon layer remains up to approximately 1 µm. NRA measurements confirmed this high value of carbon concentration. It seems that the C-enriched layer is created during the annealing. Then the sample was electropolished on roughly half part of its surface (Figure 74.a) with two electrodes (Graphite and sample) immersed in NaOH solution (0.05 mol. L^{-1}, 20 °C) during two

minutes, in order to remove the C-enriched layer. The carbon layer is found approximately 110 nm thinner on the ^{12}C concentration profile, suggesting about 110 nm of the C-enriched layer was removed away. These preliminary results show that the C-layer could be removed but a higher concentration of the NaOH solution and/or extension of the electropolishing time have to be used.

Since the C-enriched layer was probably formed during the annealing, following this assumption, two hypotheses were thought about. On the one hand, the intrinsic carbon in the bulk of the sample-self could diffuse back to the surface during the annealing because of the carbon high mobility at 1700°C (diffusion length > 10 µm) (see Figure 27 in ***Chapter I: Bibliography*** for details); on the other hand, the external source of carbon could be deposited on the samples during the annealing. To verify these two hypotheses, two clean samples (J33, J34) checked by SIMS analysis (the profiles are in Appendix. C) were annealed twice (1h/1700 °C + 3h/1700 °C) by half-covering the surface with a third clean sample (***J13***) (Figure 75.a), to obtain 4 hours of annealing in total but several exposure times in the vacuum during the annealing, from 0 to 4 hours.

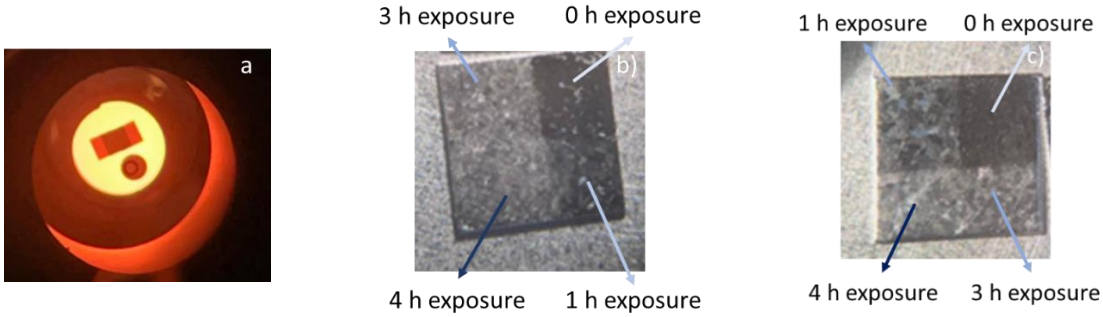

*Figure 75: **a)** Configuration used during annealing with a temperature at about 1700 °C in vacuum, and **b-c)** the surface aspect of the samples J33 and J34*

Figure 75.b-c shows the surface aspect of the samples. It is evident that the longer the exposure time, the more modified surface aspect is. Different parts can be distinguished: one is dark for no exposure to the vacuum, two others are more or less white (with a 'cotton-like' surface) depending on the exposition time to the vacuum 4 hours, 3 hours and 1 hour respectively. By observing with optical microscope (Figure 76.a-i), it is not spuriously that the 'sesames seeds-like' surface was revealed once more, the density of the black dots ('sesame seeds') increased with increasing exposure time. As the concentration of the carbon we already measured in the enriched layer is above 10 at. % at the surface of the sample ***J12***, we decided to use NRA analysis which presents interesting advantages (it is faster, allows to characterize larger area and is available in our laboratory) to check the concentration of carbon at the surface of ***J33*** and ***J34***. The ^{12}C concentration profiles were obtained by operating the SIMNRA fitting on the NRA spectra, and plotted below the corresponding micrographs. The quantity of carbon increased with increasing exposure time during the annealing, the concentration varies from below ~0.01 to above ~20 at. % and the thickness of the C-enriched layer increases for exposure of 0 and 4 hours, respectively. This result confirmed the second hypothesis of the origin of carbon. It comes from outside of the samples, and the 'sesame-like' micrograph and 'cotton-like' surface could be used as a proof of

the C-enriched layer presence, which impacts on the annihilation of the positron and should be aware after the preparation. Moreover, electropolishing and recovering annealing are potential two methods to remove or avoid the contamination before identifying the source of carbon.

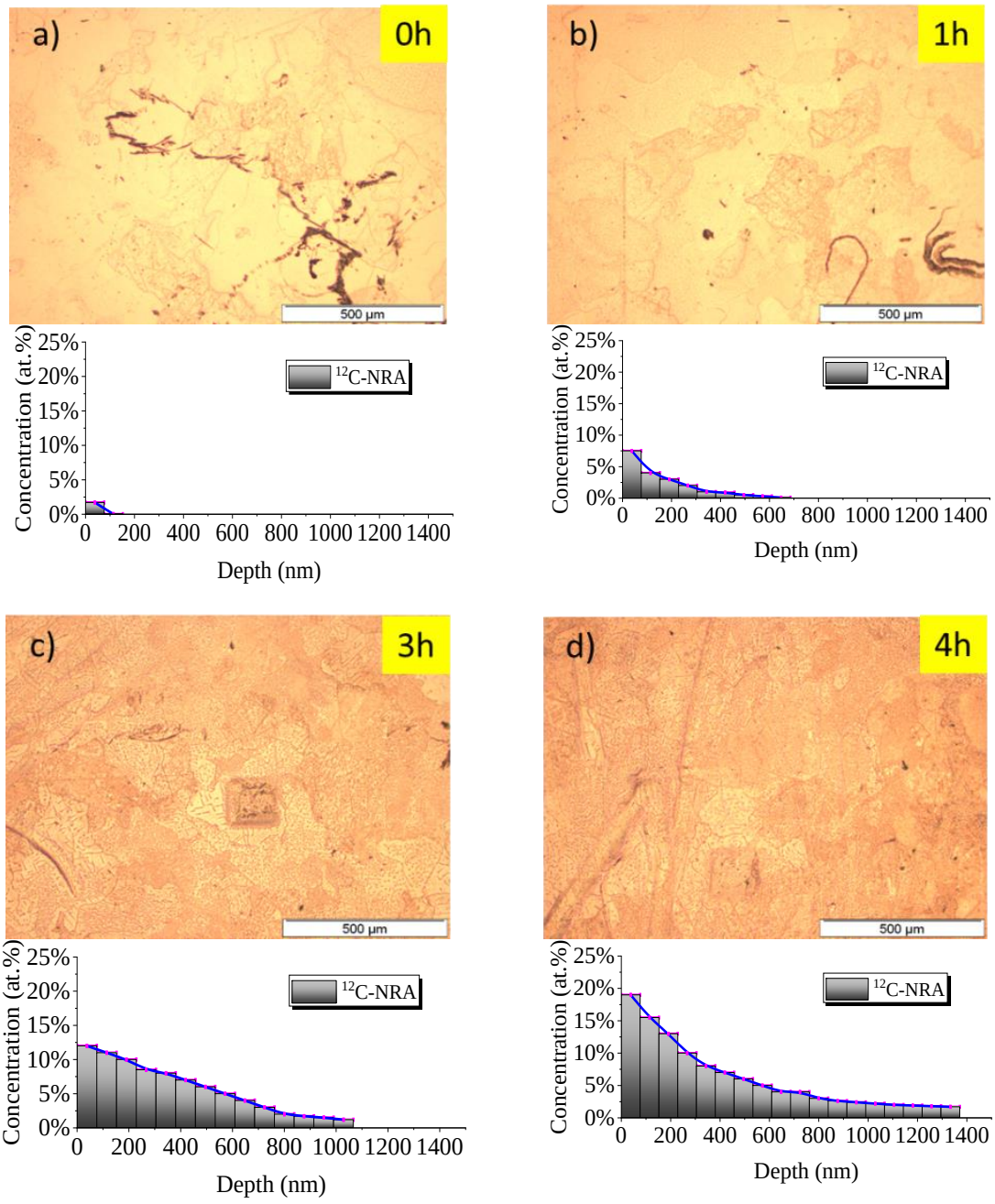

New experiments have been performed to identify the C-source in the furnace. First, it has been supposed that Carbon could be evaporated from the parts of the furnace, which are heated at high temperature from the 'hottest parts'. The components of the furnace were dismounted in September 2020, and cleaned with ethanol. The new NRA measurements showed still the formation of the C-enriched layer as it was observed before the cleaning of the 'hottest parts'. Then, the sample holder (in tungsten) on which the samples are placed during the annealing was replaced for a purer one. The novel

tungsten samples were annealed in the same configuration as shown in Figure 75.a. did not show any 'cotton-like' surface. These last results have to be confirmed.

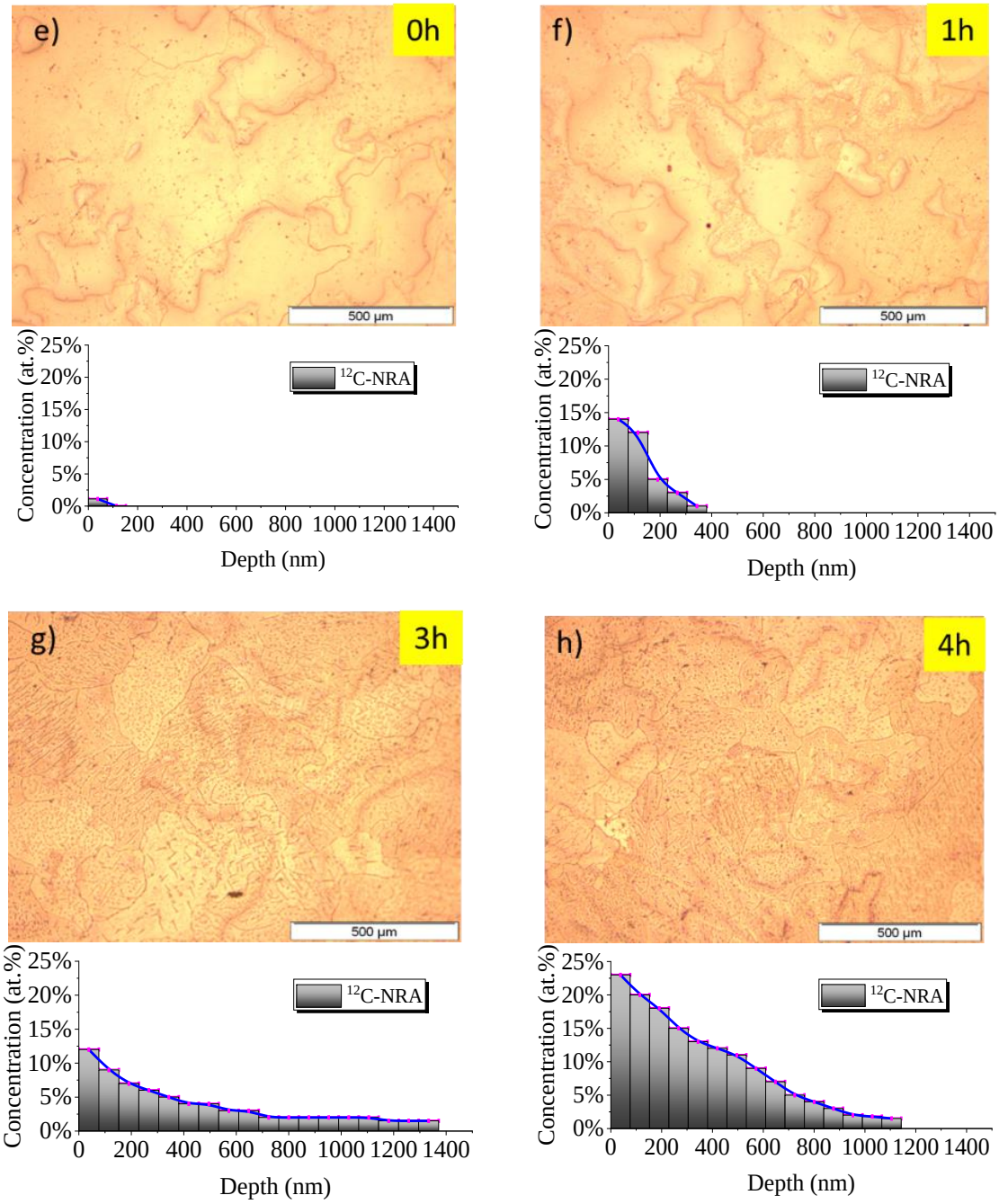

*Figure 76 : Surface aspect acquired by optical microscope of the sample J33 (**a-d**) and J34 (**e-h**) with different exposition time during the two annealing (1h/1700 °C and 3h/1700 °C) from 1 to 4 hours)*

Summary

In this chapter, the quality of the as-annealed pristine samples of several types (FZJ1, FZJ2, GP, Plansee...) was checked by different techniques. The SPB-DB measurements showed the annihilation characteristics in the as-annealed samples are comparable to those of the perfect lattice. A long effective positron diffusion length, ranging from 80- 123 nm, is found which suggests a low concentration of the vacancy-type defects after annealing in the near-surface region of the samples (~700 nm in tungsten). This concentration is close to the lowest detection limit of the SPB-DB measurement (~10^{24} m^{-3} in tungsten). In addition, only one lifetime component was obtained from the deconvolution of the lifetime spectra acquired by PALS. This lifetime value ranges from 103 to 110 ps. These values are within the range of values reported for tungsten perfect Lattice, confirming the quality of the as-annealed pristine samples in the bulk up to a maximum depth of approximately 50 µm.

Moreover, abnormal ***S(E)*** and ***W(E)*** curves were measured in one sample (***J31***), compared to the qualified pristine sample ***J15.*** Optical microscopy observations showed a different surface aspect for both samples. Then, SIMS and NRA analysis indicated the presence of a carbon enriched layer containing a concentration of about 7 at. % in the first 500 nm under the surface of the ***J31*** which was considered as the reason for the abnormal positron annihilation characteristics.

The chemical analysis (SIMS, and NRA) indicated that a part of several prepared samples contains a carbon-enriched layer of about up to ~2 µm with a maximum concentration of about ~20 at. %. This C-enriched can be identified by the special morphology (‘cotton-like’) of the surface, which contains innumerable small dark dots (‘sesame like’) when observed using an optical microscope.

Systematic SIMS and NRA analysis were performed in samples annealed at high temperature (1700°C) with varying times. Contamination is proven to come from an external source to the samples. New annealing performed after replacing the sample holder (a tungsten plate) with a purer material and cleaning of the furnace components, the cotton-like surface disappeared, indicating that contamination has been reduced. Moreover, it seems that the C-enriched layer has an effect on the annihilation characteristics.

Chapter IV: Radiation-induced vacancy-type defects in tungsten: effect of irradiation conditions and sample purity.

The microstructural evolution of the tungsten under irradiation is one of the major issues that could affect the normal operation of the future fusion reactor. As mentioned in ***Chapter I: Bibliography***, the self-ion irradiation generates the same types of defects as in neutron-damaged tungsten [44], such as dislocations, dislocation loops, and vacancy-type defects (from single vacancies to cavities). To avoid activation and the production of transmuted elements, self-ion irradiation is used as an alternative method to simulate neutron irradiation. In addition, electron irradiation creates the simplest quantifiable defects, i.e. Frenkel pairs (FPs), which allows characterization of the early-stage evolution of the Radiation-induced defects (RIDs).

This chapter will be divided into two parts.

In the first part, couples of samples irradiated with 2.5 MeV electrons at two fluences (1×10^{19} and 2×10^{19} cm^{-2}) and at around 50 °C were studied using PALS and SPB-DB. To complement the PAS results, TEM observations were used to obtain more information about the eventual extended defects, and SIMS analysis were performed to quantify the concentration of the Light-element (LE) impurities, such as carbon (C) and oxygen(O), which could interact with induced defects.

In the last part, tungsten slabs self-ion irradiated at RT and at high temperature (500 and 700°C) with various ion energies (1.2, 2 and 20 MeV) and damage doses between 0.0085 and 1.7 dpa were investigated. The self-ion damaged thick slabs and thin foils were characterized using the SPB-DB and TEM, respectively. In addition, SIMS was also carried out to better understand the evolution of the RIDs.

IV.1 Identification of defects induced by 2.5 MeV electron irradiation

In this part, the defects induced in tungsten Neyco samples by irradiation with 2.5 MeV electrons at two fluences (1×10^{19} and 2×10^{19} cm^{-2}) with a flux of 5.5×10^{13} $e^{-}.cm^{-2}.\ s^{-1}$ and at around 50 °C were investigated using PALS and SPB-DB measurements. To complement the PAS results, TEM observations were carried out to get more information about the defects, and SIMS analysis were performed to quantify the concentration of the Light-element (LE) impurities, such as carbon (C) and oxygen (O), which could interact with induced defects.

IV.1.1 SIMS measurements

So far, an unexpected C-enriched layer was discovered in some samples, and it seems that the presence of the C-enriched layer at surface of the sample has an impact on the SPB-DB result, in particular on the aspect of the ***S(E)*** and ***W(E)*** curves. In addition, since the chemical composition is unknown for the batch of the samples purchased from Neyco (N-batch), therefore, a pristine (Ps6) and an electron-irradiated (e^{-}-irr.) sample with high fluence (HF) (Ps3) were analyzed by SIMS, respectively.

Figure 77.a-*b* show the profiles of the carbon and oxygen collected by SIMS at three random positions with a source of Cs^{+} as the primary ions bombarding on the surface of the pristine and damaged sample. The details of the craters are presented in Appendix. A. The sputtering area is still a square of about 150×150 μm^2 including a circular analyzed zone with a diameter of around 33 µm. First and foremost, the profiles of carbon and oxygen are both comparable for the pristine and damaged sample, suggesting a homogeneous distribution of both light elements in this batch of sample. The carbon profiles decrease hastily from an elevated value of about ten thousand at. ppm at the surface of the samples to a much lower value reached at around 100 nm. Then, it remains constant at a plateau value below ~150 at. ppm, 50 at. ppm for a sputtering area of 150×150 μm^2 and 100×100 μm^2, respectively. To check if this value corresponds or not to the detection limit, the sputtering zone is reduced on purpose to increase the sputtering rate, without changing any of the other parameters. After reduction of the analyzed zone, the concentration of the carbon decreased in contrast to the matrix element, i.e. tungsten (^{184}W), which signifies detection limit[10] of the carbon is reached and attained at about 60 at. ppm in the both pristine and damaged samples with used experimental conditions. Meanwhile, the concentration of oxygen is higher than the carbon one with a factor of ten at the surface, and it decreases slowly until 200 nm. Then, the profiles fluctuate showing peaks more or less close to each other and the O concentration changes in a range which depends on the crater position up to 1.5 µm depth. For Crater 1 and 3 of the pristine sample and Crater 3 for the damaged one, the oxygen concentration varies from 60 to 100 at. ppm before reducing the sputtered area, a value which is very close to the detection limit. For the other

[10] Detection limit: this value depends experimental conditions (ex: the vacuum level, crater size…)

craters, the oxygen concentration fluctuates from 100 to 400 at. ppm. Indeed, the fluctuation of the oxygen concentration might be related to its heterogeneous distribution probably due to the presence of a few oxide nanoparticles.

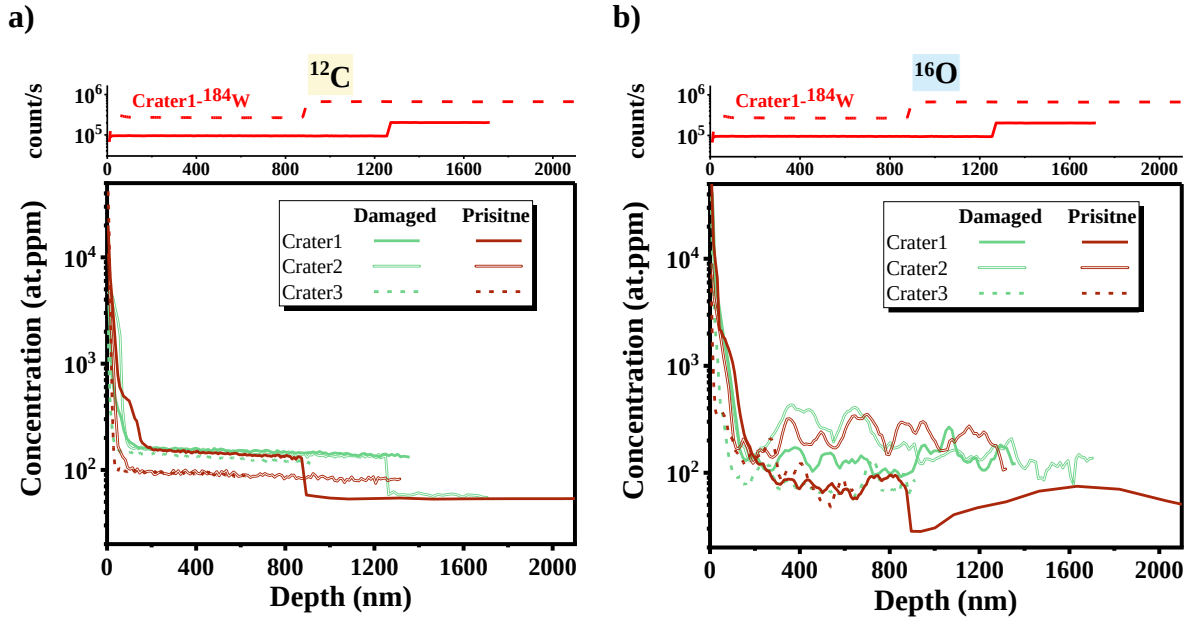

*Figure 77: **a)** Carbon and **b)** oxygen profiles of pristine (**Ps6, bleu**) and electron-damaged (**Ps3, black**) sample obtained using SIMS for three random positions (crater 1 to 3) distinguished by different types of the line.*

Furthermore, SIMS was also employed to collect the ions sputtered from the sample within a mass range from 0 to 250 a.m.u with Cs^+ and O_2^+ primary ions. Figure 78.a-b show detected negative and positive charged ions, respectively.

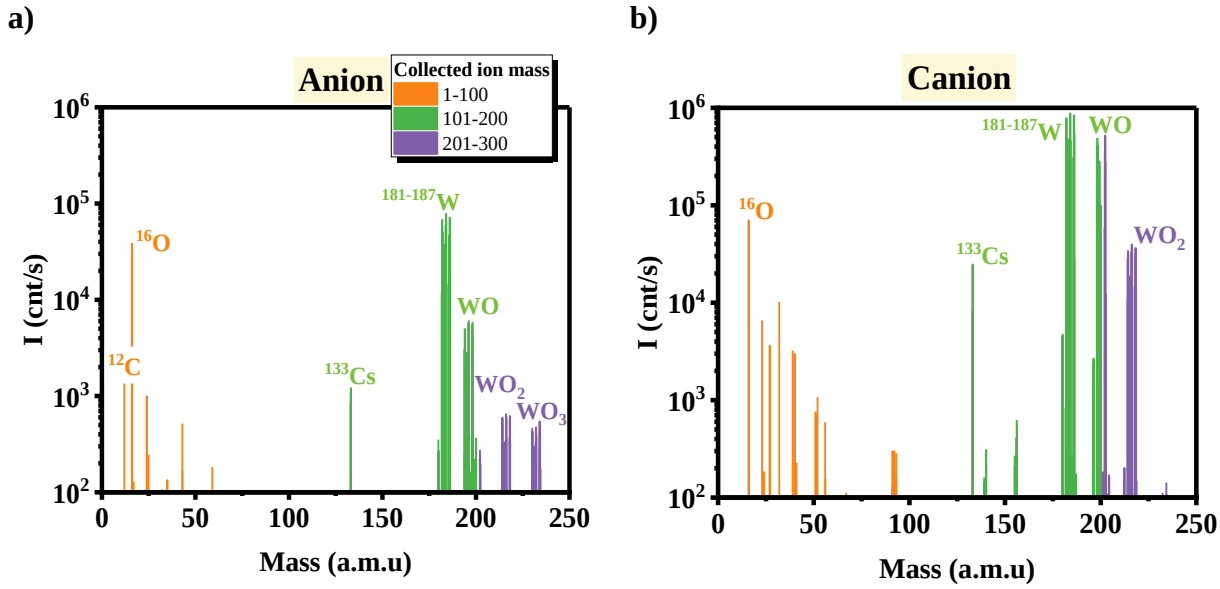

*Figure 78: SIMS analysis of the secondary particles sputtered from the sample Ps3 (2×10^{19} cm^{-2}) collected in the mass range from 0 to 250 a.m.u., **a)** collected anions with Cs^+ primary ions and **b)** collected cations using O_2^+ primary ions.*

It is not surprising that the isotope of tungsten appears with the highest intensity with a major impurity, the oxygen. In addition, as the intensity of the ^{16}O and the isotopes of tungsten, the other

masses cannot be ignored at around 200, 216, and 232 a.m.u., respectively, which corresponds probably to the oxidized isotopes of tungsten (WO_x). Besides, a fraction of the primary ion Cs^+ is discovered and a few carbon impurities only obtained in the case of collection of anions. It is noteworthy that the cations collected with primary O_2^+ ions cannot be used as the argument of the presence of the oxygen in the samples themselves, on the contrary of spectrum of anions collected by Cs^+.

To summarize, the C and O concentrations for both pristine and irradiated samples are similar indicating that irradiations did not introduce any pollution. No C-enriched layer was found in the N-batch samples. The carbon concentration is low equal or below the detection limit of 50 at. ppm. The O concentration is heterogeneously distributed and fluctuates from 60 to 400 at. ppm probably due to the presence of oxide nanoparticles. Besides, it is noteworthy that SIMS is a powerful technique to detect the contamination due to the ion-implantations [204], no evident increase on the concentration of the carbon and oxygen was revealed after irradiation, meaning the unavoidable surface contamination [205] (H, C, and O) during the irradiation is negligible comparing to the concentration of the internal impurities.

IV.1.2 SPB-DB measurements

After analyzing the chemical composition of the samples, the SPB-DB measurement was carried out to characterize the RIDs. Figure 79.a-b show the ***S*** and ***W*** parameters as a function of the positron energy ***E***, respectively. After electron-irradiation at about 50 °C, the vacancy-type defects were revealed through the simultaneous increase of the curve ***S(E)*** and decrease of the curve ***W(E)***. The ***S, W*** versus positron energy for low fluence (LF, 1×10^{19} cm^{-2}) and high fluence (HF, 2×10^{19} cm^{-2}) of electrons were plotted with down and upward triangle, respectively. The samples irradiated at the same fluence exhibit an equivalent evolution of the ***S*** and ***W*** versus positron energy ***E***. In addition, a slightly greater value of the ***S*** and lower ***W*** was found for the entire energy range above 2 keV in the HF-irradiated pair, suggesting first a homogeneous distribution of the defects in the slow positron probed region (the first 700 nm under the surface). Starting from 2 keV, as positrons penetrate relatively deep and probably annihilated at defects in the sample, so that the fraction of the annihilation characteristics at the surface decreases, the gap on the ***S(E)*** and ***W(E)*** between pristine and damaged samples is more and more evident when positron energy increased. Besides, in contrast to the measurement of the pristine sample, the irradiated ones have an important fluctuation of the ***S*** and ***W***, signifying the heterogeneous distribution of the RID or the environmental variations during the experiments. As a consequence, the fit with homogenous multi-layers model is no longer valid. An allometric function[11] was firstly utilized to try to describe the tendency of the experimental data with more smooth curves. Furthermore, the ***S-W*** curves of both fluences were plotted in Figure 79.c, all the points (***S, W***) are located at the trendline

[11] $S = \boldsymbol{a}.E^{\boldsymbol{b}}$ where ***a*** and ***b*** are two parameters of the allometric fit

L_2 linking the annihilation characteristics of the ***Lattice*** and ***Single vacancy*** (V_1), indicating that the electron induced mainly single vacancies in the samples. Moreover, the ***S, W*** points are closer to the annihilation characteristics of V_1, when the fluence increases indicating that the vacancy concentration increases with increasing fluence. The ***S-W*** points remain below the V_1 point suggesting that the trapping at this defect is not saturated.

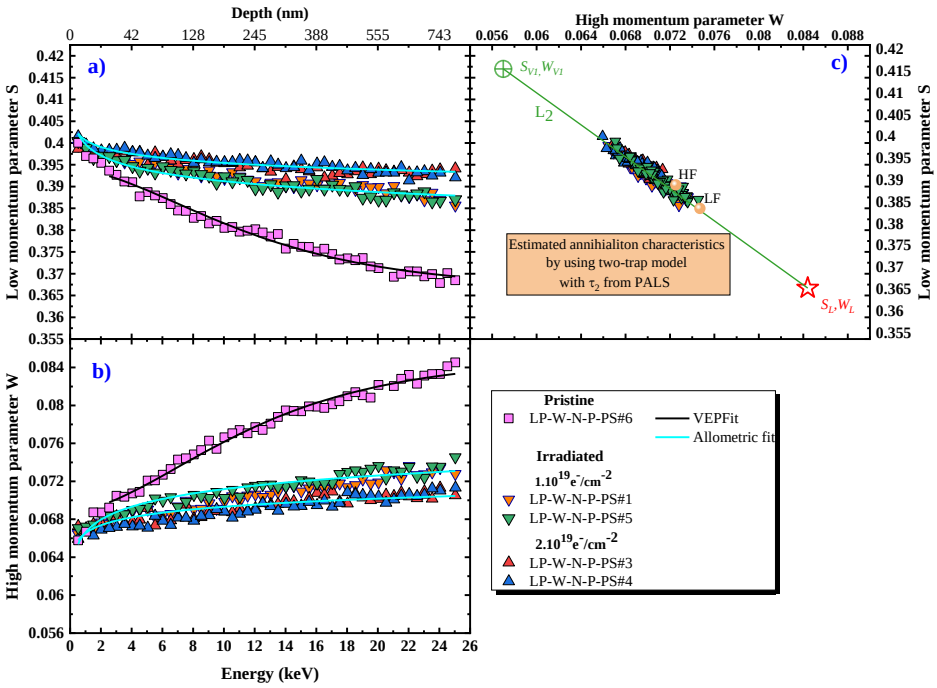

Figure 79: Annihilation characteristics of pristine sample (Neyco, ●) in comparison to 2.5 MeV electron irradiated ones with two fluences, LF 1 × 10^{19} (▼) and HF 2 × 10^{19} cm^{-2} (▲) at RT, a) low momentum parameter S b) high momentum parameter W as a function of the positron energy E and estimated maximum positron penetrated depth, and c) the S versus W. The cyan lines are drawn to guide the eyes

IV.1.3 PALS measurements

According to the simulated damage profile of the POLY et SMOTT program, the 2.5 MeV electrons induced the damage until 220 µm in the tungsten. SPB-DB measurement gave out the information of the vacancy-type defects in the surface-region (~700 nm), so PALS measurement was also employed to access the information on the defects in the in-depth bulk. The PALS measurement was carried out with conventional configuration, the fast positrons emitted from a ^{22}Na source penetrated around 50 µm in tungsten (see Figure 42). Figure 80.a shows the raw experimental spectrum of a pair of pristine samples (N&FZJ1), and in comparison of those of 2.5 MeV electron-damaged ones at RT with both fluences.

Compared to the raw spectrum of the pristine pair, those of the damaged ones exhibited more than one component with a longer average lifetime for both fluences, (the right-side of the spectrum is more wide). Hence, the spectrum was firstly decomposed into ***two exponential components***. The experimental spectra with > 5M counts were deconvoluted by using the ANAPECR1 program, and a fixed Full Width

at Half Maximum (FWHM) or time resolution of 212 ps corresponding to the resolution of the spectrometer. The obtained variance was close to 1. Table 13 summarizes the fitted lifetime components and their intensity. A long lifetime of 187 ± 2 and 197 ± 4 ps with near half of the intensity was found in LF and HF irradiated pairs, respectively. These values are close to the one of the single vacancy of tungsten, i.e. 193-199 ps for the theoretical work (193 ps [136], 195 ps [124] and, 199 ps [148]), and 180-200 ps obtained by experiments (180 ps [147], 195 ps [124], and 200 ps [74]), indicating the generation of the single vacancies as it is expected in electron irradiated sample.

2.5 MeV electron RT											
			Component 1				Component 2				
PALS TEM P (K)	*Fluence* (× 10^{19} cm^{-2})	τ_{av} (ps)	τ_1 (ps)		I_1 (%)		τ_2 (ps)		I_2 (%)		τ_{mod} (ps)
~300	0	105	105	± 0.3	100		-		-		
	1	147	102	± 2	47	± 2	187	±2	53	± 2	135
	2	155	127	± 2.4	60	± 4	197	±4	40	± 4	148

Table 13: Comparison of the exponential components deconvoluted from experimental spectra by using the ANAPC program for pristine and 2.5 MeV electron-irradiated pairs of the sample (Neyco)

However, it is surprising that a shorter lifetime with a value (102 ps and 127 ps) close to the one of the ***Lattice*** of tungsten was also found for both fluences. As explained in ***Chapter II : Methodology*** (eq. 34), when the positron and electron annihilate at more than one state, for instance, at a deep defect (no detrapping) and in the lattice (delocalized state), the lifetime of positron in the ***Lattice*** will decrease because a lot of positrons are trapped before to be annihilated in the delocalized state. Moreover the τ_{mod} estimated with eq. 35, is greater than the ***Lattice*** one.

Therefore, it means firstly that at least a second trap differing to single vacancy also exists. The questions are now (1) on the nature of this trap (only one defect or several?) (2) what is the corresponding annihilation lifetime? (3**)** Are the lifetime components simply related to one specific trap or represent mixtures of traps with close lifetimes?

Following these questions, a decomposition of the spectra measured in the damaged samples with ***three components*** was attempted. The long lifetime (197 ps for HF and 187 ps for LF) extracted in the free decomposition was slightly shorter than 200 ps, the lifetime expected for single vacancy in tungsten which was already found in other irradiation conditions (^{3}He-800 keV)[74,75] . It has to be noticed that in these analysis the vacancy clusters with a size larger than the single vacancy were not been taken into account, because they are not expected to be formed in electron irradiation at RT: (1) due to the low energy of the PKA, the local density of displacements is low and no cascades are expected; And (2) single vacancies are not mobile at RT, their migration energy is high E_m(V)=1.66 [81]. So that, to simplify and make possible the fitting with three-components, a lifetime component τ_3 was fixed to 200 ps.

2.5 MeV electron RT									
			Component 1		Component 2		Component 3		
PALS TEMP (K)	*Fluence (× 10^{19} cm^{-2})*	τ_{av} (ps)	τ_1 (ps)	I_1 (%)	τ_2 (ps)	I_2 (%)	τ_3 (ps)	I_3 (%)	τ_{mod} (ps)
~300	0	105	105 ± 0.3	100	-	-	-	-	-
	1	135	11 ± 0.1	11 ± 3	122 ± 2	56 ± 2	200	33 ± 1	62
	2	147	12 ± 0.2	7 ± 2	135 ± 2	63 ± 1	200	30 ± 1	84

Table 14: Lifetime components deconvoluted from experimental spectra using the ANAPC program for pristine and 2.5 MeV electron-irradiated pairs of samples taking into account 3 components with the third one fixed at 200 ps.

Table 14 includes the result of the fit. An intensity of 30 % for the component of the 200 ps was found in both fluences, suggesting that a part of positrons annihilated at single vacancies (V_1). Meanwhile, an extreme short lifetime τ_1 of about 10 ps with a relatively low intensity of about 10%, is extracted indicating a minor fraction of the annihilation occurred in the ***Lattice***. Besides, an intermediate lifetime τ_2 of about 122 and 135 ps was extracted in both irradiated pairs. Its intensity is of about 56 % for the lowest fluence and increases to 63 % for the highest one, leading to an increase of the average lifetime of 135 and 147 ps (Figure 80.b) for LF and HF, respectively. So far, more than half of the annihilation events occurred at an unexpected state, suggesting that apart from the ***Lattice*** and V_1, a new trap (namely defect ***X*** for the following discussion) with regard to positron was created in electron-irradiation at room temperature (RT).

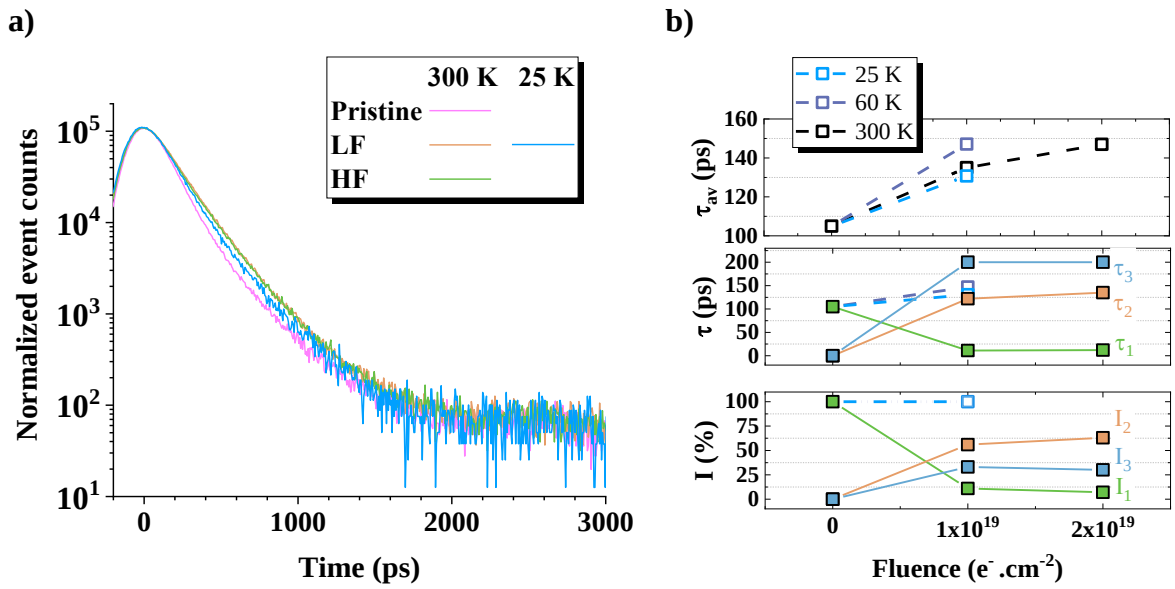

*Figure 80 : **a)** Raw experimental lifetime spectrum for pristine and 2.5 MeV electron irradiated pairs, and **b)** the average lifetime and each component with corresponding intensity from the lifetime spectra versus irradiation fluence, using the ANAPECER1 program*

Since at least two types of defects were determined from the lifetime spectra, a trapping model of two-trap was utilized to describe the RID after electron-irradiation. As shown in eq. 33, the probability to find the positron annihilation at delocalized state (***Lattice***) is $n_L(0)$ and at two localized states (vacancy defects) is $n_{d1}(0)$ and $n_{d2}(0)$, which are presented as a temporal function including the

annihilation rate in the ***Lattice*** λ_L, at the defect 1 $\lambda_{d1}$and the defect 2 λ_{d2} with corresponding trapping rates k_{d1} and k_{d2} :

$$\begin{cases} \frac{dn_L(t)}{dt} = -(\lambda_L + k_{d1} + k_{d2})n_L(t) \\ \frac{dn_{d1}(t)}{dt} = -\lambda_{d1}n_{d1}(t) + k_{d1}n_L(t) \\ \frac{dn_{d2}(t)}{dt} = -\lambda_{d2}n_{d2}(t) + k_{d2}n_L(t) \end{cases} \quad \textit{eq. 47}$$

To solve these differential equations, the initial probability of trapped positron in the delocalized state $n_L(0)$ is assumed to be one and that one in localized states $n_{d1}(0)$ and $n_{d2}(0)$ is zero. The probability of the positrons that annihilate at localized and delocalized states are expressed:

$$\xrightarrow{n_L(0)=1 \text{ and } n_d(0)=0} \quad \begin{cases} n_L(t) = I_1 e^{-\frac{t}{\tau_1}} \\ n_{d1}(t) = I_2(e^{-\frac{t}{\tau_1}} + e^{-\frac{t}{\tau_2}}) \\ n_{d2}(t) = I_3(e^{-\frac{t}{\tau_1}} + e^{-\frac{t}{\tau_3}}) \end{cases} \quad \textit{eq. 48}$$

After resolving the equation system, the lifetime of each component and their intensity are expressed in eq. 49. The lifetime τ_1, τ_2, and τ_3 characterize the annihilation in the ***lattice***, defect 1 and defect 2, with corresponding intensity I_1, I_2 and I_3.

$$\begin{cases} \tau_1 = \frac{1}{\lambda_L + k_{d1} + k_{d2}} \\ \tau_2 = \frac{1}{\lambda_{d1}} \\ \tau_3 = \frac{1}{\lambda_{d2}} \end{cases} \text{ with } \begin{cases} I_1 = 1 - I_2 - I_3 \\ I_2 = \frac{k_{d1}}{\lambda_L + k_{d1} + k_{d2} - \lambda_{d1}} \\ I_3 = \frac{k_{d2}}{\lambda_L + k_{d1} + k_{d2} - \lambda_{d2}} \end{cases} \quad \textit{eq. 49}$$

By matching eq. 49 with the result of the three-component fit, the lifetime τ_2, and τ_3 could be attributed to the defect ***X*** and single vacancies (V_1) with their intensity I_2 and I_3, respectively, and the trapping rates k_{d1} and k_{d2} could correspond to the one for defect X and V_1, respectively. As the annihilation rate λ is reciprocal of the lifetime ($\tau_L = 105\ ps, \tau_3 = 200\ ps$, and $\tau_2 = 122\ or\ 135\ ps$ for LF or HF), the concentration of V_1 can be roughly calculated by taking the trapping coefficient μ_V of a positron trapped at a single vacancy in tantalum (Ta, Z = 73), which equals to $(6 \pm 3) \times 10^{-15}$ $m^3.s^{-1}$ [159]. Table 15 summarizes the estimated concentration of the single vacancies C_V in both FF and HF fluences. The C_V values are 37 and 21 at. ppm for HF and LF, respectively. A factor of two was ideally found between both fluences. The mean dpa value calculated using the POLY et SMOTT program in the probed depth of the fast positrons (~50 µm) for both fluences, is 7.47×10^{-4} and 3.74×10^{-4} dpa for HF and LF respectively. By assuming there is no recombination of the Frenkel pairs (FPs) the V_1 concentration should correspond to 747 at. ppm (or 4.7×10^{25} m^{-3}) and 374 at. ppm (or 2.4×10^{25} m^{-3}), for HF and LF, respectively. These values are 20 times higher than the ones extracted using the two-trap trapping model.

	λ_L (s^{-1})	λ_{d2} (s^{-1})	λ_{d1} (s^{-1})	K_{d1} (s^{-1})	K_{d2} (s^{-1})	C_{V1} (cm^{-3})	C_{V1} (at. ppm)	Mean damage 0-50 µm (*dpa*)
HF	9.52×10^{9}	5.00×10^{9}	7.43×10^{9}	2.77×10^{10}	1.42×10^{10}	2.36×10^{18}	37	7.47×10^{-4}
LF			8.23×10^{9}	1.20×10^{10}	8.06×10^{9}	1.34×10^{18}	21	3.74×10^{-4}

Table 15 : Estimated trapping rate at defect X and V_1, and concentration of V_1 (C_{V1}) utilizing the two-trap trapping model

As a consequence, the identified concentration of V_1 represents solely about 5-6 % of the values simulated using POLY SMOTT codes.

Furthermore, the fraction of annihilation events in three states i.e. f_L, f_{d1} and f_{d2} can also be determined as shown in eq. 50.

$$\begin{cases} f_L = 1 - f_{d1} - f_{d2} \\ f_{d1} = \int_0^{\infty} \lambda_{d1} n_{d1}(t) dt = \frac{k_{d1}}{\lambda_L + k_{d1} + k_{d2}} \\ f_{d2} = \int_0^{\infty} \lambda_{d2} n_{d2}(t) dt = \frac{k_{d2}}{\lambda_L + k_{d1} + k_{d2}} \end{cases} \quad \text{eq. 50}$$

with λ_L,the annihilation rate in the Lattice and k_{d1} and k_{d2} the trapping rates in the defect X and V1 respectively.

In addition, the annihilation characteristics (S, W, and τ_{av}) should be equal to the sum of the ones of each states weighting by the corresponding annihilation fraction, as expressed in eq. 51.

$$\begin{cases} \tau_{av} = f_L \tau_L + f_{d1} \tau_{d1} + f_{d2} \tau_{d2} \\ S = f_L S_L + f_{d1} S_{d1} + f_{d2} S_{d2} \\ W = f_L W_L + f_{d1} W_{d1} + f_{d2} W_{d2} \end{cases} \quad \text{eq. 51}$$

Table 16 summarized the calculated annihilation fractions by using the trapping ra.te at defect X, K_{d1} and V_1, K_{d2}. From these values it is possible to determine the annihilation characteristics S_X and W_X of the defect X by using the eq. 51 if we consider that at least 80 % of fast positrons stop in the first 15 µm under the surface in which the damage level of the RIDs is almost invariable according to the simulated damage profile (Figure 36.b). The line shape parameters of the single vacancy and the ***Lattice*** of the tungsten were determined from a previous work [36] as well as the annihilation lifetime for the single vacancy V_1 [74] in tungsten, and the positron annihilation lifetime of the pristine sample was measured to be of about 105 ps. It should be noted that the used ***S*** and ***W*** values considered as representative of both fluences are those at 25 keV on the fitted curves (cyan lines in Figure 79.a-b). Thus, the annihilation characteristics of the defect X, S_X, W_X were determined, and reported in Table 16. *It is interesting to notice that the S_X, W_X values are not the same for both fluences, which are plotted on the Figure 79.c (orange spherules). They are located almost at the half-lower part of the line L_2, close to the **Lattice** point (red star in Figure 79.c), and the distance between the **Lattice** and the (S_X, W_X) point moves away from the Lattice point.*

Damage	f_{d1}	f_{d2}	f_L	Sx	Wx	τ_{av} (ps)
HF	0.54	0.28	0.19	0.3904	0.0725	130
LF	0.41	0.27	0.32	0.3850	0.0747	107

Table 16 : Annihilation fractions calculated through trapping rate at defect X and V1 and the estimated annihilation characteristics of the defect X

The average annihilation lifetime calculated with annihilation fractions extracted from the two traps model (given in Table 16) for both fluences are shorter than the measured ones i.e. 130 against 147 ps for HF, and 107 versus 135 ps for LF, respectively. This result suggests that defect ***X*** is not a single type of defects, but a mix of several defects. Additionally, the value of the reference lifetime τ_{mod} is shorter than that of the ***Lattice*** (HF: 76 ps, LF: 61 ps in Table 14), which is in consistence with the hypothesis of a mix of several defects.

Furthermore, this result is consistent with some PALS measurements on the proton-irradiated tungsten (99.95 wt.%, Goodfellow). For instance, Lhuillier et ***al.*** [36] employed PALS to characterize 12 MeV-^{1}H damaged tungsten with two fluences 1×10^{16} and 4×10^{16} cm^{-2} at RT, corresponding to the average damage levels in the depth probed by fast positrons (~50 µm) of about 1.1×10^{-4} and 4.4×10^{-4} dpa as determined by using SRIM-2008 (K-P, E_{disp}= 55.3 eV). The PALS spectrum of proton-irradiated tungsten could be also deconvoluted with three components, containing one short lifetime of 20 ps (10, 17 %) and longer one above 200 ps (217, 248 ps) with an intensity around one quarter, and also an unidentified lifetime between the one of the ***Lattice*** and that of the single vacancy, increasing from 113 ps to 143 ps, when the irradiation fluence rise from 1×10^{16} cm^{-2} to 4×10^{16} cm^{-2}. The deconvolution of the spectra measured in electron irradiated samples was also limited to three components, seeing an extreme short lifetime (11 ps for both LF and HF).

Therefore, to obtain more information about defect X, the PALS measurement were carried out at cryogenic temperatures 25 and 60 K on the LF-irradiated pairs. The spectra of PALS measurement performed at cryogenic temperatures (25 K and 60 K) differ from those acquired at RT (~300 K), in particular, those obtained at 25 K which is between the spectrum of the pristine and irradiated samples measured at about 300 K. Figure 80.a shows the raw spectrum measured at 25 K, it is different than the one obtained at 300 K. The raw spectrum measured at 60 K, is not shown because it is superposed with those measured at 300 K. Thereby, a decomposition of the spectrum acquired at 25 K and 60 K was realized. The spectra can be merely decomposed in only one component with a lifetime increasing from 130.7 (4) to 147.1 (3) ps when the temperature of the sample raised from 25 to 60 K. The annihilation at ***Lattice*** or V_1 were no longer revealed at low temperature of 25 K. The trapping of positrons at a defect with a short lifetime of about 120 ps is promoted at 25 K. This lifetime is the same as the second component extracted from lifetime spectrum (122 ± 2 ps see measured at 300 K in the same sample and

which is relative to one or more defects X. Considering that the concentration of the different types of defects cannot change when the sample temperature decreases, it indicates that the defects X are shallow traps in regard to positron. It means that the trapping energy at these defects is low enough to allow the positron to escape from them at RT. When the temperature decreases, the detrapping rate becomes lower and lower. It follows that the effective trapping rate at such shallow traps increases so much when temperature decreases that positrons can only be annihilated in this state.

As mentioned in [159] the dislocation loop is one of the common shallow traps in both metals and semiconductors. Likewise, the trapping rate of decorated vacancy-complexes are also shown depending on the temperature, so that, these two types defects are potentially the shallow traps in our irradiated samples, this will be discussed in the following paragraphs.

It can be concluded that for LF-irradiated samples, the trapping rate at an or several unknown shallow traps increases with decrease of the temperature during the PALS measurement. At less than or equal to 60 K, only one lifetime component was extracted from the spectrum, whereas at least three components were extracted from the spectrum measured at RT for both LF and HF-irradiated samples, and the intermediated lifetime τ_2 was dominant (122 ps for LF, and 135 ps for HF) with over half of intensity (LF: 56 %, and HF: 63 %). The longer lifetime τ_2 for HF-irradiated samples suggests the formation of shallow traps with larger size in HF-irradiated samples compared to LF-ones. The calculated τ_{mod} value (see Table 14) is different to the one of the tungsten ***Lattice***. As well, the average lifetime τ_{av} (Table 16) calculated using two-trap trapping model is shorter than the experimental one, which probably suggests other components exist, which implies that several types of defect X with quite close lifetime could exist and that it is impossible to deconvolve them from the experimental spectra.

IV.1.4 TEM Observations

In our experiment, one tungsten thin foil (Goodfellow, 99.95 wt.%) was irradiated with 2.5 MeV electrons at the highest fluence of 2×10^{19} cm^{-2} (2×10^{23} m^{-2}, HF) with a flux of 5.5×10^{13} $e^-. cm^{-2}. s^{-1}$ (or 5.5×10^{17} $e^-. m^{-2}. s^{-1}$) at same time with thick samples at around 50 °C. The thin foil was observed using a JEOL-ARM200F field emission gun microscope operating at 200 kV available at platform MACLE in CNRS Orléans campus. The observations were carried out in the zone axis [001] at various magnifications from 50 kx up to 600 kx, in various zones of the thin part of the samples and with various g (200), (020) and (110), in order to detect both types of dislocation loops expected in tungsten, the ones with ½a<111> and <100> Burgers vectors [206]. No dislocation loops nor black dots were observed with at least a size larger or equal to 1.5 nm which is the minimum one for which the diffuse contrast can be distinguished in TEM [207]. The thickness of the observed region was measured using EFTEM it is of about 30 nm on average.

Arakawa et *al.*[208] and Tamino et *al.*[209] have observed the formation of dislocation loops (or SIAs clusters) using TEM in electron-irradiated tungsten. We compared our experimental conditions with the ones found in the literature. In references [208,209], authors performed 2 MeV electron irradiation in high pure polycrystalline tungsten (99.9999 wt.%, JX Nippon Mining & Metals Co) at low temperatures (≤ 290 K), in a high voltage electron microscope. The beam fluxes were fixed at 1×10^{24} [208] and 3.0×10^{22} $m^{-2}.s^{-1}$ [209] respectively. The fluence was approximately the same of 4×10^{25} m^{-2} for both works [208] and [209]. The average density of the SIA clusters formed under the above conditions were found at 105 K to be approximately 4×10^{22} m^{-3} for both [208] and [209]. The average size of the dislocation loops is mentioned to be approximately 3–4 nm in [208]. In these experiments the fluence is higher than the one used in our study by a factor of 200 and what is even more remarkable is the difference of the electron fluxes. Indeed, these authors performed their irradiations in a high voltage microscope in which the electron flux is very high (due to the focused beam size), 3 to 6 orders of magnitude higher than the one we used. In such high flux irradiation, the local instantaneous density of SIA should be much higher than the one used in our experiment: the damage rate is 1.3×10^{-4} dpa. s^{-1} for the flux 3.0×10^{22} $m^{-2}.s^{-1}$ [208,209] and five orders of magnitude lower (2.3×10^{-9} dpa.s^{-1}) in present study. It makes the interaction of SIA much less probable to form clusters in our irradiations.

As a result, no dislocation loops were observed in the tungsten lamella irradiated with the 2.5 MeV electrons at around 50 °C and the highest fluence, i.e. 2×10^{19} cm^{-2}, HF. It suggests that no loops should exist in the thick samples irradiated in the same conditions and measured using PAS.

IV.1.5 Discussion

Generally, electron irradiations with a low energy (< 3.5 MeV) generates mainly Frenkel pairs. We estimated the damage dose at 833 and 417 dpa for both fluences HF and LF respectively in the 0-700 nm region under the surface. It should correspond to a high single vacancy concentration of about 5.27×10^{25} m^{-3} and 2.63×10^{25} m^{-3}, respectively. The SPB-DB experiments show the formation of the single vacancy V_1 after electron irradiation with both low LF and high HF fluences at surface of the sample (in the ~700 nm below the surface), and the concentration of the electron-induced V_1 increases with increasing fluence. It is interesting to note that the ***S*** and ***W*** values measured at the highest fluence HF are far from the ones expected for trapping saturation at the single vacancy V_1, where the annihilation characteristics are ($\boldsymbol{S_{V1}}$, $\boldsymbol{W_{V1}}$) as it could be expected from the high estimated value of single vacancy concentration.

In the following we assume that only pure single vacancies are created by irradiation, but a fraction is lost during irradiation due to recombination with interstitials. The V_1 concentration can be estimated considering different FPs recombination rates, R_C, ranging from 0 to 80 %, and assuming that the damage

doses (POLY et SMOTT program) for both fluences are in mean value in the slow positron probed region (0-700 nm).

$$C_{V1} = R_C \times dpa^{0-700\ nm}_{POLY\ ET\ SMOTT} \qquad eq.\ 52$$

where R_C is the FPs recombination rate: R_C = 0 - 80 %

Once, V_1 remaining concentrations for each R_C value are estimated, corresponding ***S*** and ***W*** values can be calculated using one-trap trapping model (see Chap II.3.1.4).

$$X = \frac{C_{V1}\mu_{V1}X_{V1} - \lambda_L X_L}{C_{V1}\mu_{V1} - \lambda_L} \qquad eq.\ 53$$

where ***X*** is given for ***S*** *or* ***W***

C_{V1} is the estimated concentration of single vacancies

μ_{V1} is the specific trapping coefficient at single vacancies, μ_{V1} =(6 ± 3) × 10^{15} $m^{-3}.s^{-1}$ [159]

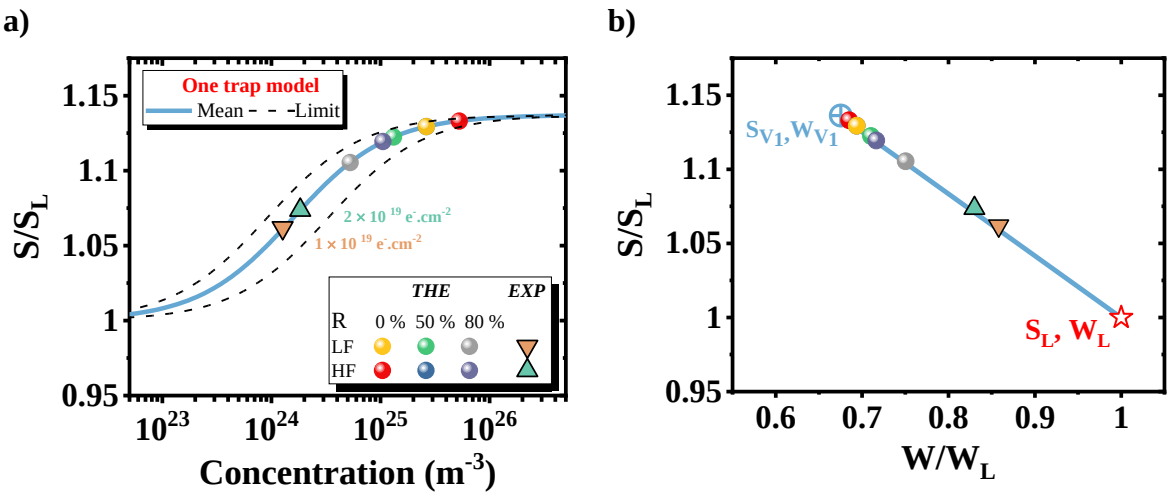

*Figure 81: **a)** estimated **S/S$_L$** value as a function of single vacancies concentration using the mean, maximum and minimum values of the specific trapping coefficient **b)** estimated **S/S$_L$** versus **W/W$_L$** (with the mean value of the specific trapping coefficient) using one-trap trapping model for different V-I recombination rates, from 0 to 80 %. Experimental S-W points are averaged value between 13-16 keV (HF:▲ and LF:▼)*

The variation of ***S*** as a function of single vacancies concentration are presented in Figure 81.a for mean, maximum and minimum values of the specific trapping coefficient (blue curve in Figure 81.a). The ***S*** values obtained for both fluences and various specific R_C values 0, 50 and 80% are also plotted (colored spherules in Figure 81.a). Theoretically, if FPs recombination rate is less than 50 % during the irradiations, induced single vacancies concentration should be close to the saturation (> ~10^{26} m^{-3}) i.e. the ***SW*** point should be close to the annihilation characteristics of V_1 in ***S-W*** curve (green cross-circle in Figure 81.b). However, measured ***S*** values for both fluences (LF: 1 × 10^{19}, and HF: 2 × 10^{19} cm^{-2}) are much lower than the remaining estimated ones, even though 80 % of FPs recombined during the irradiation. The experimental ***S-W*** values for both fluences would correspond to a recombination rate from 88 % to 98 %, taking into account the error bar on the specific trapping coefficient (Figure 55.a)

for both fluences. It is not clear yet which is recombination rate R_C in tungsten for the irradiation conditions we chose in our study. From Was et al the displacement efficiency under electron irradiations in Ni should be close to 100 % or in other words the recombination factor R should be close to 0 [210] The FP recombination rate R_C depends on the FP density (damage dose), the SIA and V properties (migration energy), the irradiation temperature and damage rate and the concentration of sinks (solutes, grain boundaries, defects themselves ...) that could trap vacancies or interstitials. Ortiz et *al.* [211] calculated the total number of defects created for electron irradiations in Fe at a damage dose of 10^{-6} dpa. Up to 90% of defects have been annihilated at 400 K. In tungsten the SIA has very low migration energy migration energy (< 0.2 eV [104,212,213]), whereas vacancy is immobile at room temperature. As SIA is known to migrate in 1D pattern, that should lead to a relative lower recombination probability. De Backer et *al.* [214] showed that the R increases from 80 to 95 % for ^{3}He 800 keV irradiated tungsten at RT with various fluences, ranging from 10^{17} to 5×10^{20} cm^{-2}, i.e. a range of damage dose from 0.019 to 95 dpa (as calculated using SRIM with E_{disp} = 55.3 eV, K-P model). However, these conditions are unmatched with our experiments. Besides, Neely et *al.* [215] found approximately 30 % of resistivity recovery in 99.99 % pure W irradiated with 2.1 MeV electrons at 70 K and a fluence of 5×10^{17} e$^-$.cm^{-2} and the authors claimed that the recovery rate can be impacted by a non-negligible concentration of impurities. For summarizing the above, the evaluation of the recombination rate is still an open question in irradiated materials. As a consequence, we wonder if the lower ***S*** and higher ***W*** values measured in SPB-DB measurement are only due to recombination of FPs.

To test this hypothesis, theoretical positron lifetime spectra were calculated assuming only single vacancies are detected by positrons, and their concentration at the end of the irradiations is the product of that expected from the damage dose and the recombination rate R_C estimated just above from SPB-DB experiments. In the following, we compare calculated spectra to experimental ones measured at 300 K (see Figure 82). For both damage doses, LF and HF, it can be noticed that the theoretical spectra are different from the respective experimental ones. It can be clearly observed that the number of counts in the region included between 360 and 1400 ps is higher in the theoretical spectra than in the experimental ones. This confirms that a lifetime component with a value shorter than the lifetime of V_1 and larger than the lifetime of the ***Lattice***, included in the experimental spectra as they were extracted from the deconvolution fit. This comparison confirms that a new trap different from the pure single vacancy was detected by positrons. These traps have annihilation characteristics ***S*** and ***W*** which should tend to ***Lattice*** annihilation characteristics ($\boldsymbol{S_L}$, $\boldsymbol{W_L}$).

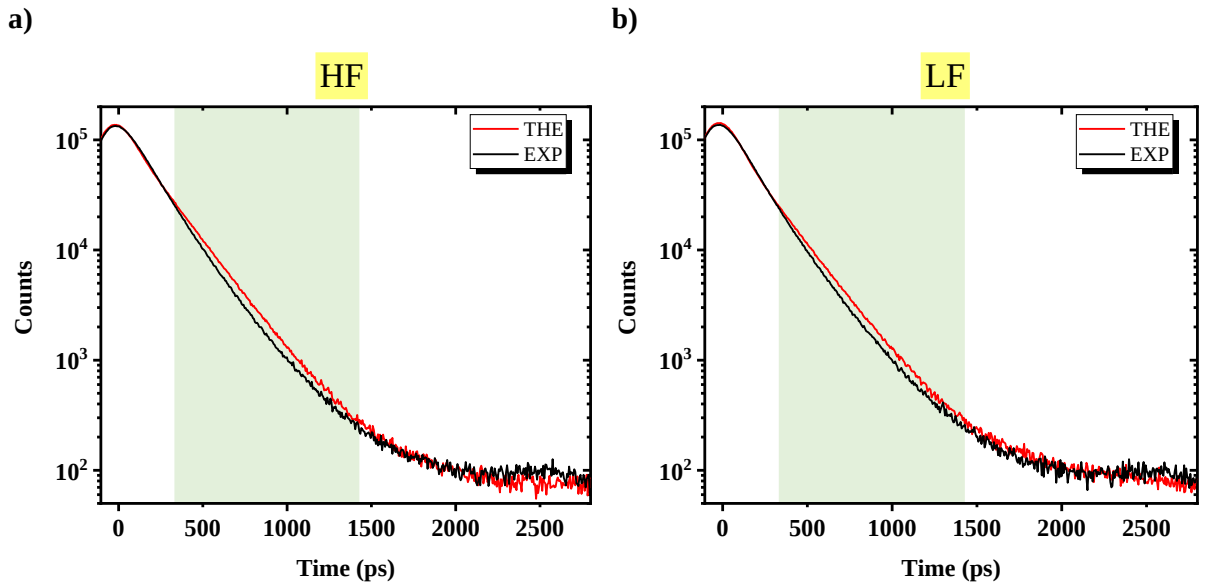

Figure 82 : Comparison of theoretical and experimental lifetime spectra for W irradiated with 2.5 MeV electrons at 323K. The theoretical spectra were calculated assuming only single vacancies are detected by positrons and that their concentration at the end of irradiation is the product of that expected from the damage dose by the recombination rate R_C estimated just above from SPB-DB experiment.

To sum up, the PALS measurements showed that at least three components can be extracted from experimental spectra of LF and HF damaged samples in the first 50 µm depth. The PALS measurement identified the single vacancies, which appeared in the spectra with a long lifetime component of about 200 ps. this component is expected in our irradiation conditions, as they were performed at around 323 K, at which the generated single vacancies are thermally immobile (< migration temperature of 523 K [131]). Unlike ion-irradiations, displacement cascades cannot be created because the maximum transferred energy to W atoms by 2.5 MeV electrons is about 100 eV less a factor of two than the displacement threshold energy of 55.3 eV [216]. Moreover, for a similar work on electron-damaged tungsten with comparable conditions (1.8 MeV, 8.2×10^{18} cm^{-2}, RT), Igata et Sato [217] observed solely single vacancies by using FIM. As a consequence, the vacancy defect induced by electrons should be mainly isolated single vacancies. In contrast solely 30 % annihilation events occurred at V_1, in our electron irradiated W samples. Moreover, beside this longest lifetime component another one with a value of about 122 and 135 ps for LF and HF, respectively can be also deconvolved from the experimental spectra with an intensity of more than 50%. It suggests that positrons annihilated at one or more states, namely defects X, which are different of the lattice and the pure single vacancy. PALS measurements at low temperature showed that these intermediate lifetimes could be related to shallow traps. We discuss in the following what could be the nature of these shallow traps considering i/ the lifetimes results and ii/ the Doppler broadening ones found in the literature.

i/ First the values of the intermediate lifetime component are close to the calculated lifetimes for screw dislocation i.e. 130 ps [136] in tungsten, moreover a median lifetime of 150 ps was attributed to

vacancy-edge dislocation complex in BCC iron [218]. The experimental lifetime values within a range from 149 to 163 ps [141,143,144,146] were measured in the insufficiently annealed tungsten samples ($T_{annealing}$ < 1000 °C), and these lifetimes were attributed to the annihilation of positrons at dislocations. It has to be noticed that the samples used for present work have been well-annealed, and the PALS measurement detected only one lifetime component in the pristine samples, around 105 ps being attributed to the tungsten ***Lattice***. So no or a very few dislocations or other defects are present in the samples before irradiations.

ii/ Moreover, Asplet et al. [172] employed the SPB-DB measurement to investigate the evolution of microstructure of laminated BCC iron samples as a function of a series of isochronal annealing of 1 hour in high vacuum (10^{-7} mbar) from 100 to 500 °C with a step of 50 °C. An obvious shift was revealed on the ***S*** versus ***W*** curve after annealing at 573 K, suggesting a change in the detected annihilation states attributed to dislocation loops or vacancy-associated dislocation loops. PALS measurements and the use of a trapping model of two traps, allowed to determine the annihilation characteristics of these defects. The ***SW*** point corresponding to these traps, is located below the line corresponding to the annihilation of positrons as trapped at the single vacancy in iron in the ***S-W*** plot. The slope of the line corresponding to annihilation in such dislocations i.e. the R ratio is much lower ($R_{dis.}$ = 1.19) than the one for single vacancy (R_{V1} = 1.85). The slope of the L_1 line corresponding to the annihilation of positrons as trapped in pure single vacancy in tungsten is also R_{V1} = 1.85(3). Because of the microstructural similarity of the BCC iron and tungsten, similar trends should be expected in the annihilation characteristics of the dislocation or vacancy-associated dislocation. That means we should expect that the detection of such defects should shift ***SW*** points below the L_1 line i.e. characteristic of positron annihilation in V_1. However, in our work we can see that the ***SW*** points obtained for the electron irradiated samples are located on the V_1 characteristic line, it suggests that such dislocation type defects are not detected by positrons.

Moreover, in TEM observations no irradiation induced defects were observed even at the maximum magnification (very close to the atomic resolution) in different area of the thin parts of the electron irradiated sample (~ 30 nm thick). It means that if such defects would exist their density should be very low. This such low concentration is not in agreement with the annihilation fraction of positron at the X defects.

Numerous works indicated that dislocation loops can be created by electron-irradiation even at RT. Amino et al.[209] operated TEM and identified the interstitial loops in e^--irradiated tungsten thin foils at RT. The flux was very high of 3×10^{22} $e^-.cm^{-2}.$ s^{-1} and the fluence as well ($> 1 \times 10^{21}$ $e^-.cm^{-2}$). The formation of SIAs loops was considered as a consequence of the high mobility of the SIAs even at RT, due to a commonly recognized low migration energy (< 0.2 eV), which had been determined in theoretical [104,212,213] and experimental [76,78,90] works. It follows that SIAs can meet each other

to agglomerate and form loops if their density is large enough. The expected density in our condition is about 5×10^{25} m^{-3} at the maximum -if no recombination is taken into account- it is considerably lower than the one expected when irradiation is performed at very high flux as it is the case for Amino et *al.* [209] experiments for which the flux is nine orders of magnitude higher (3×10^{22} $e^{-}.cm^{-2}.\ s^{-1}$) and the fluence about 100 times greater ($> 1 \times 10^{21}$ $e^{-}.cm^{-2}$) compared to our irradiation conditions. In a similar e^{-}-irradiation experiment (1-3 MeV, 4×10^{21} cm^{-2}) with TEM, Arakawa et al. [208] observed in tungsten the shrinkage of SIA clusters (dislocation loops), because a part of SIAs annihilates with radiation-mobilized vacancies. However, regarding the vacancy-type dislocations, only Yi et *al.* [127] observed such defects in self-ion irradiated tungsten and Wan et *al.* [219] identified them in hydrogen-implanted BCC iron after post-irradiation annealing at 770 K. Therefore, the formation of the predominant dislocation loops under our experimental conditions is not favored and it is why no visible loops in our experiment.

Therefore, we propose that the intermediate lifetime component found in our electron irradiated samples should be related to new vacancy defects generated during the irradiations which exhibit a low open volume to be in agreement with the short lifetime and the character of shallow trap with respect to the positron (see Figure 79.c).

As shown in Figure 77.b, the SIMS analysis revealed that the samples contain high concentration of oxygen atoms fluctuating between 100 to 400 at. ppm, and with a heterogeneous distribution and the C concentration is low, equal or below the detection limit of 50 at. ppm. Meanwhile, the mean damage dose estimated by POLY et SMOTT program in the probed depth with fast positrons (~ 50 µm) is 3.74×10^{-4} and 7.48×10^{-4} dpa for LF and HF, respectively. By assuming that the displacement efficiency of tungsten atoms is $\varepsilon = 100$ %, these damage doses correspond to 374 and 748 at. ppm for maximum concentration of single vacancies created by LF and HF. These values are of the same order of magnitude as the oxygen concentration in the samples and much higher than that of Carbon. Furthermore, according to the diffusion equation (see Figure 27), the single vacancies created have a diffusion length of 6.3×10^{-9} nm, while that of an oxygen atom is about 1.3 µm in a second at 50 °C, so that the V_1 is considered as immobile, but the oxygen atoms are quite mobile. And O atoms can travel several mm in the sample during the long irradiations. In some simulating works [110,111,125], the single vacancy can trap up to six oxygen atoms with binding energy of 3.04 eV to 11.21 eV [110] depending on the number of trapped oxygen atoms. Thus, it is reasonable to imagine that the oxygen atoms could be trapped at single vacancies forming stable impurity-vacancy complexes. In contrast to pure V_1, the positron annihilation lifetime at the oxygen decorated V_1 is expected to be reduced, as it has been predicted that the oxygen atom should be located in the first nearby octahedral position of pure V_1 [110] In the V_1-O_1 complex, the lifetime was calculated at 168 ps using DFT [124].

Overall, it seems to be difficult to unambiguously identify the nature of the defect *X* created after electron-irradiation. If 100 % of positron annihilated at identified states, the parameter τ_{mod} should be equal to the lifetime of the ***Lattice***, i.e. $\tau_{lattice}$, the demonstration is shown in Appendix. B. However, for both fluences, LF and HF, the calculated τ_{mod} equals ~50 ps and does not reach the tungsten ***Lattice*** lifetime (~105 ps). In addition, the annihilation fraction was calculated by eq. 50 at each states i.e. ***Lattice***, defects *X*, and single vacancies (V_1), and these fractions were used to calculate the average lifetimes of both measured pairs. The calculated value is shorter than that of the one obtained from the spectra deconvolution. These arguments suggest that the positrons did not annihilate at three states, in which the ***Lattice*** and V_1 were confirmed states. In other word, the intermediate lifetime should correspond to a mix of several defects. Nonetheless, the limit of the deconvolution of the experimental spectrum was attained. It is impossible to extract another lifetime component that should be close to the intermediate one. Thus, the fit cannot distinguish two lifetimes with a difference shorter than 50 ps [220], which is probably the case for various decorated single vacancies. For instance, as reported in [124], the calculated lifetime of one single vacancy associated to one C, N, and O atom are 171, 170, and 168 ps. We have seen that the concentration of C in the electron irradiated samples is low (≤ 50 at. ppm) compared to the O one. Moreover, theoretical study on the vacancy-complexes, predict the formation of vacancy-type complexes made of several oxygen atoms and one single vacancy (O_n-V_1). It should reduce the lifetime to a value between the one of the ***Lattice*** and single vacancies. So far, impurity-vacancy complexes are the most possible nature for the defect X.

Therefore, to verify the hypothesis, a simulating work was carried on by collaborators from KTH Royal Institute of Technology. By using an improved two-component density functional theory (DFT) they calculated the annihilation characteristics of various vacancy defects in tungsten[12] including the oxygen complexes. The simulation work in the localized density approximation (LDA) indicated that one single vacancy can be decorated with at most six oxygen atoms, in agreement with other simulation works [110,111]. They calculated lifetime and ***S*** and ***W*** annihilation fractions for various decorated oxygen-vacancy complexes. Figure 83 shows, in the $\boldsymbol{S/S_L}$ *versus* $\boldsymbol{W/W_L}$ map, (a) the theoretical ***SW*** points, of V_1 decorated with n (n = 1 to 6) atoms of oxygen and (b) the experimental data obtained in electron irradiated samples. The ***SW*** points for ***Lattice*** and V_1, are also plotted together with the L_1 line which is characteristic of annihilation in single vacancy. According to the simulation, the annihilation characteristics of the V_1-O_1 and V_1-O_2 complexes are close to the L_1 line.

In addition, as-shown in Table 17 the lifetimes of the oxygen-vacancy complexes lie between that of the ***Lattice*** and that of V_1. A relatively high binding energy was found when the oxygen atom is located at first (1NN) and second (2NN) near neighbor of the vacancy, suggesting a stable configuration of the complexes. Taking the high mobility of the oxygen atoms in tungsten even at RT it suggests that

[12] A co-authored paper submitted to Journal of Nuclear Materials

the defects X are mix of several oxygen atoms decorated vacancy-complexes. Moreover, these type of defects were identified as shallow traps for positrons in silicon [160]. This could explain the PALS spectrum measured at cryogenic temperatures (25 and 60 K) showing positron trapping in shallow traps with lifetimes of about 130 and 147 ps for LF and HF, respectively. Both lifetimes are included in the range of the calculated lifetimes for V_1-O_n complexes between the one of the ***Lattice*** (105 (5) ps) and that of the single vacancy (195 (5) ps), spanning from 124 to 170 ps. (Table 17).

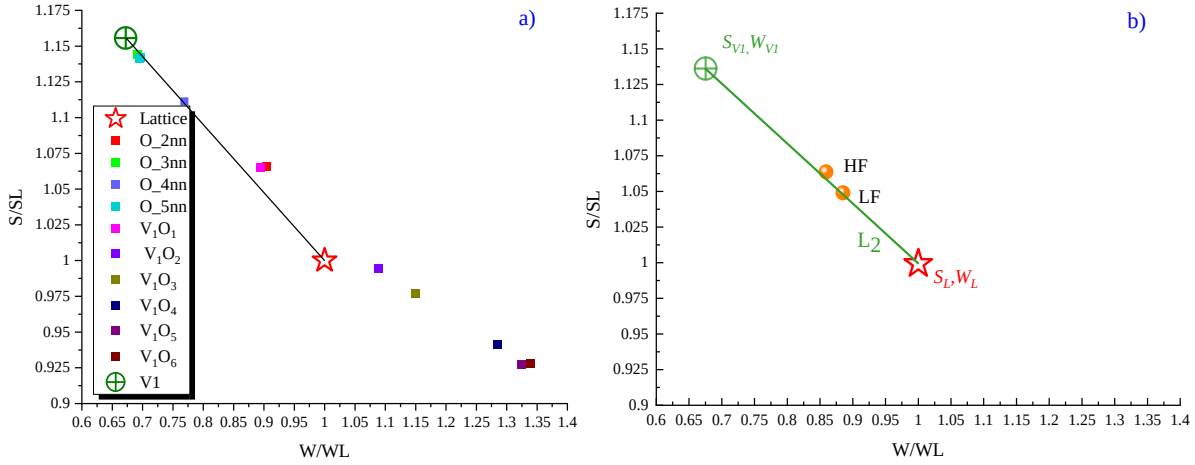

Figure 83 : **a)** *LDA theoretical S-W curve of several oxygen correlated vacancy defects in tungsten in comparison with* **b)** *estimated S_x,W_x using two-trap model*

V_1-O_n	E_b (eV)	Lifetime (ps)	V_1-O_1	E_b (eV)	Lifetime (ps)
O1	3	170	1 NN	3	170
O2	5.9	142	2 NN	1.98	175
O3	6.9	143	3 NN	-0.12	197
O4	8.6	130	4 NN	0.88	175
O5	10.1	124	5 NN-2	0.08	193
O6	11.9	132	5 NN-2	-0.35	195

Table 17: Lifetime of the V_1-O_N complexes obtained from LDA simulation

These comparisons suggest that the complexes V_1-O_X (x = 1, 2, or 3) are most favorable defects, in view of the heterogeneous of oxygen distribution detected by SIMS analysis. It has to be noticed that vacancy decoration with other undetected impurity atoms could be also detected with positrons. Yabuuchi et *al.* [124] reported a reduced positron lifetime from 168 to 200 ps for single vacancy associated with one LEs atom (H, C, N, O, P…).

Summary

The electron-irradiated tungsten samples with two fluences (LF: 1×10^{19} $e^{-}.cm^{-2}$, and HF: 2×10^{19} $e^{-}.cm^{-2}$) at RT were characterized by SPB-DB, PALS, TEM and SIMS.

Firstly, SIMS analysis detected a heterogeneous distribution of oxygen in contrast to carbon up to 2 µm below the surface of the irradiated and pristine samples. For irradiated (PS#3) and pristine (PS#6) samples, the carbon concentration reaches the lowest detection limit of about 50 at. ppm with applying experimental conditions, while oxygen concentration fluctuated between 100 and 400 at. ppm in most cases. Furthermore, the collection of positively or negatively charged secondary particles with a mass from 0 to 250 a.m.u. confirmed that the oxygen is the main impurity in the 3N-Neyco samples. Moreover, it is interesting to note that the mass (200, 216, and 232 a.m.u.) which has the most intense signal coincides with the mass overlap of matrix element (W) and that of the main impurity (O) (WO, WO_2, and WO_3), so that the presence of oxides nanoparticles was speculated.

Secondly, the SPB-DB measurements indicated that the detected defects are mainly single vacancies, and that their concentration increases with fluence. In parallel, the PALS measurements confirmed the positron annihilation at the single vacancies for both fluences, with a concentration of about 21 and 37 at. ppm estimated by using a two-trap model for LF and HF, respectively. This factor of two is consistent with the fluence ratio. Nevertheless, a lifetime component corresponding to an unidentified X defect with intensity greater than half was extracted from the PALS spectrum for both fluences. Furthermore, the X-defect trapping rate appears to be temperature dependent, as only one lifetime component was extracted from the spectrum acquired at 25 K and 60 K, indicating the X-defects could be a shallow trap for positron. Furthermore, the reference lifetime τ_{mod} calculated with a two-trap model for the RT measurements indicates that the experimental spectra should have more than three components. Among the possible shallow traps that could correspond the X defects, dislocations could be excluded because there are no visible defects in the TEM images as expected due to the irradiation conditions which should not favor their formation. The comparison of the experimental data with DFT simulations and SIMS analysis, suggests that the most probable nature of X-defect is the mixture of several types of vacancy-oxygen complex.

IV.2 The characterization of vacancy-type defects induced by self-ion irradiations

For Self-ion irradiation is used as an alternative method to simulate neutron irradiation. In this section, the effect of (1) irradiation conditions (temperature, fluence - or damage dose -, incident ion energy) and (2) sample purity on the defects distribution are studied. Different tungsten slabs were irradiated with W (self-ion) ions at different energies (1.2, 2, 20 MeV), temperatures (RT, 500 °C and 700 °C) and fluences or damage doses in the range 0.0085 to 1.7 dpa. Thick damaged slabs and thin sheets are characterized using SPB-DB and TEM respectively. In addition, SIMS is also performed to better understand the evolution of RIDs.

PART I: Identification of defects induced by 2 MeV self-ion irradiation and effect of fluence for irradiation at room temperature

It has to be noticed that this part of the manuscript is based on the paper that has been published [221] in Journal of Nuclear Materials 558, 153373 (2022) (https://doi.org/10.1016/j.jnucmat.2021.153373).

IV.2.1 2 MeV self-irradiations

A series of 2 MeV self-ion irradiated 3N-HP (99.95 wt. %, Plansee) samples were provided by the Culham Centre for Fusion Energy (CCFE) to characterize vacancy-type defects induced by 2 MeV self-ions. The pristine stample was characterized by SPB-DB measurement (see detail in Table 11). The irradiations were carried out at the University of Helsinki with a series of fluences ranging from 1×10^{12} to 2×10^{14} cm^{-2} at RT. According to the SRIM-2008 simulation performed in the K-P mode (E_{disp} = 55.3 eV), these fluences correspond to maximum damage levels at the peak of the damage profiles (~75 nm) ranging from 0.0085 to 1.7 dpa. The self-ion irradiated samples were characterized by employing the SPB-DB measurement.

Sample Shape	***Energy / Ion***	***Temp (K)***	***Flux ($\times 10^{10}$ $cm^{-2}.s^{-1}$)***	***Fluence (cm^{-2})***	***Damage dose at the peak = 70 nm***
10 × 10 × 0.5 mm^3 slab 3N-HP (Plansee)	2 MeV-W	RT	1.89	1×10^{12}	0.0085
			2.10	1×10^{13}	0.085
			2.18	5×10^{13}	0.425
			2.26	1×10^{14}	0.85
			2.38	2×10^{14}	1.7

Table 18 : Irradiation conditions of 2 MeV self-ion damaged samples, the value of the damage is at the peak (~70 nm) of the damage profile calculated by SRIM-2008 (K-P mode, E_{disp} = 55.3 eV).

IV.2.1.1. SPB-DB results in RT, 2 MeV self-irradiated samples

The calculated damage profile is plotted in Figure 39 : the 2MeV-W ions generate defects until 300 nm under the surface of the samples, which is included in the depth probed by slow positrons in tungsten (~700 nm). Figure 84 shows the comparison of the annihilation characteristics measured in the pristine sample with those of self-ion irradiated ones.

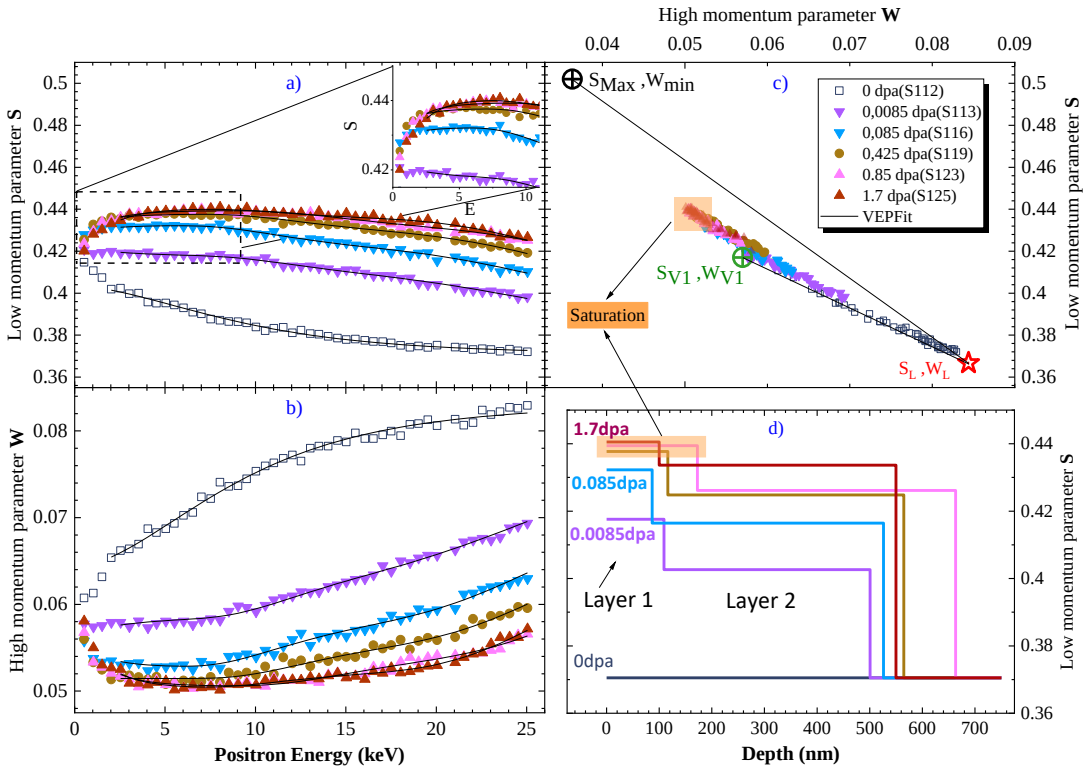

Figure 84: Evolution of the positron annihilation characteristics in a pristine sample and the damaged samples after irradiation with 2 MeV W ions at the fluences ranging from 1 × 10^{12} to 2 × 10^{14} cm^{-2} and at RT ***a)*** *Low momentum fraction S, and* ***b)*** *high momentum fraction W as a function of the positron energy.* ***(c)*** *S versus W. The S, W values for the annihilation are in the* ***Lattice*** *(S_L, W_L),* ***single vacancy*** *(S_{V1}, W_{V1}),* ***largest vacancy cluster*** *(S_{Max}, W_{min}) are also plotted. The experimental data are plotted in solid symbols and the fitted curves using VEPFIT are given in continuous lines.* ***(d)*** *the S(z) and W(z) depth profiles were extracted from S(E) and W(E) using VEPFIT.*

For the irradiated samples, the line shape parameter ***S*** increases and ***W*** decreases with increasing fluence of the self-ions, which means that positrons detect the vacancy-type defects created during the irradiations. For the sample irradiated at the lowest damage dose of 0.0085 dpa, no evident variation of the ***S*** (resp. ***W***) is observed in the energy range between 0.5 and 8 keV before a monotonous decrease (resp. increase) up to the maximum energy of 25 keV. This damage profile showing a high damaged layer close to the surface and lower damage deeper is consistent with SRIM calculations. Furthermore, the VEPFIT program is used to better know the depth distribution of damage. To correctly fit these curves, a model with at least three homogeneous layers is required. In these fits the annihilation characteristics of the last layer, which is considered to be undamaged, have been fixed in agreement

with fitted values of the pristine sample values $S_{Lay}(3)$ = 0.370, $W_{Lay}(3)$ = 0.083, and the effective diffusion length $L_{Lay}(3)$ was fixed to be 80 nm. Table 19 summarizes extracted characteristics for the first and second layers, including thickness, annihilation characteristics, S_{Lay}, W_{Lay}, and L_{Lay}, effective diffusion length and the annihilation characteristics S_{Surf} and W_{Surf} at the surface of the samples for the various damage doses. In this table, the ratio R= $\left|(S_{Lay} - S_L)/(W_{Lay} - W_L)\right|$ is also reported for the first layer. The thickness of the first layer is about 100 nm when the fluence remains lower than 5×10^{13} cm^{-2} (~0.425 dpa at the peak of the damage profile). For the greater fluences, 1×10^{14} cm^{-2} (~0.85 dpa) and 2×10^{14} cm^{-2} (~1.7 dpa), the thickness of the first layer extends to about 170 nm. The fitted $S_{Lay}(1)$, $W_{Lay}(1)$ values of the first layer corresponds to the maximum damage induced for each damage dose.

For the lowest damage level (~0.0085 dpa), the fitted annihilation characteristics of the most damaged layer $S_{lay}(1)$ and $W_{lay}(1)$ are quite close to those of the single vacancies (S_{V1} = 0.417(1), W_{V1}=0.057(1) [74]), suggesting that the majority of the positrons annihilated at single vacancies.

Damage dose (dpa)		0.0085	0.085	0.425	0.85	1.7
Surface	$\boldsymbol{S_{surf}}$	0.419 (1)	0.430 (1)	0.432 (1)	0.431 (1)	0.431 (1)
	$\boldsymbol{W_{surf}}$	0.057 (1)	0.054 (1)	0.053 (1)	0.054 (1)	0.054 (1)
Layer 1	$\boldsymbol{S_{Lay}}$	0.418 (1)	0.432 (1)	0.438 (1)	0.440 (1)	0.440 (1)
	$\boldsymbol{W_{Lay}}$	0.058 (1)	0.053 (1)	0.051 (1)	0.050 (1)	0.050 (1)
	$\boldsymbol{R}$	1.96 (4)	2.10 (4)	2.15 (4)	2.15 (4)	2.15 (4)
	$L^{+}_{Lay\ (nm)}$	14 (4)	5 (1)	5 (1)	6 (1)	6 (1)
	Thickness (nm)	100 (10)	93 (6)	105 (10)	135(35)	135 (35)
Layer 2	$\boldsymbol{S_{Lay}}$	0.402 (2)	0.417 (2)	0.425 (3)	0.428 (5)	0.428 (7)
	$\boldsymbol{W_{Lay}}$	0.067 (2)	0.059 (2)	0.057 (1)	0.054 (2)	0.054 (4)
	L^{+}_{Lay} *(nm) fixed*	60	50	45	30	30
	Thickness (nm)	510 (10)	510 (20)	570 (10)	610 (65)	610 (65)

Table 19: Annihilation characteristics S_{Surf} and S_{Surf} for surface, $S_{Lay(i)}$, $W_{Lay(i)}$, and $L_{Lay(i)}$ for layers i = 1,2, extracted from the fitting of the S(E) and W(E) curves with the VEPFIT program using a three layers model for irradiated samples at different damage doses between 0.0085 and 1.7 dpa.

As shown in Figure 52, the R slope value of the trend line extending from the ***Lattice*** point to another point relative to different type of defects in the ***S-W*** map (Figure 84.c) reveals the size of the defects. The R value for the single vacancy is R_{V1}=1.85(3). Therefore, the fitted ***S, W*** values of the layer 1 for each fluence was used to calculate R. Whatever the fluence or damage dose, R remains higher than R_{V1} indicating that vacancy clusters have been generated during the irradiations, these clusters are most probably formed in collision cascades since the irradiation was carried out at RT, at which temperature single vacancies are immobile, so that no clustering of V_1. Following the increase of the fluence, from

1×10^{12} cm^{-2} (~0.0085 dpa) to 5×10^{13} cm^{-2} (~0.425 dpa), the fitted annihilation characteristics in the first layer, an obvious increase (resp. decrease) of $S_{Lay}(1)$ (resp. $W_{Lay}(1)$) was revealed. When the fluence rises to 1×10^{14} cm^{-2} (~0.85 dpa), no longer noticeable change of the $S_{Lay}(1)$ and $W_{Lay}(1)$ was observed. Then, they remain constant when the fluence increases again by a factor of two. The $S_{Lay}(1)$ and $W_{Lay}(1)$ saturated at around 0.440(1) and 0.050(1), respectively.

Figure 85 illustrates the ratio of the low momentum parameter ***S*** extracted for the highest damaged region using VEPFIT to that of the ***Lattice*** , $\boldsymbol{S_{Lay}(1)/S_L}$ for the 2 MeV tungsten irradiations at RT with various fluences as a function of the damage dose. This curve shows that the ratio of $\boldsymbol{S/S_L}$ steeply raises at low damage levels and stabilized at around 0.5 dpa. Besides, the effective diffusion length L_{Lay} *(1)*, is 14(4) nm after the irradiation at the lowest damage level (~0.0085 dpa). It is much shorter than in the pristine sample (80(1) nm) indicating a high trapping rate of positrons at induced defects. While increasing the fluence, $L_{Lay}(1)$ decreases to a quite low value of 4-6 nm, indicating the increase of the concentration of the defects. Then $L_{Lay}(1)$ remains constant when the fluence reaches 1×10^{13} cm^{-2} (~0.085 dpa) indicating the saturation of the ***S*** and ***W*** parameters. Meanwhile, the R value also increases slightly when the damage dose rises to 0.425 dpa, indicating that the proportion of the larger vacancy clusters increases with the damage dose, probably because of the overlap of collision cascades. Finally, the ratio R does not change from ~0.85 dpa as the value of $\boldsymbol{S_{Lay}(1)}$, $\boldsymbol{W_{Lay}(1)}$, and $L_{Lay}(1)$. These values are equivalent to the one determined in 20 MeV self-ion irradiated tungsten samples with a mean damage level in the region probed by slow positrons around 1 dpa (3.7×10^{14} cm^{-2}) and ~13 dpa (4.5×10^{15} cm^{-2}) at 90 K, which have been reported in the M. Sidibe's thesis [126]. A similar saturation effect was also observed using deuterium exposure and release measurements [49].

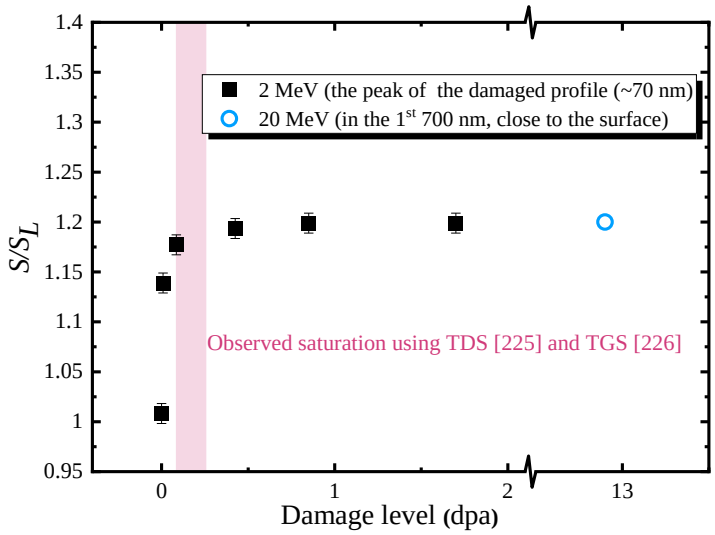

*Figure 85: Ratio of the fitted low momentum parameter **S** by VEPFIT in the most damaged layer and that of the lattice $\boldsymbol{S_L}$ for 2 MeV and 20 MeV self-irradiated tungsten at RT with various fluences*

IV.2.1.2. Discussion on the evolution of S and W value with increasing damage dose

We saw above that the ***S*** and ***W*** values obtained in the most damaged zone of self-ion irradiated tungsten samples vary with damage dose. The ***S***, ***W*** values in the sample irradiated at the lowest damage dose (0.0085 dpa) are close to the annihilation characteristics of a single vacancy suggesting that single vacancies represent the majority of the induced vacancy-type defects. The concentration of these individual vacancies C_{V1} can be estimated from the effective diffusion length using a one trap trapping model where positrons can annihilate in only one type of defect, a single vacancy (see Chap I.3.2) assuming the positrons annihilates solely in one type of defect, i.e. single vacancy. C_{V1} can be calculated by using eq. 54.

$$C_{V1} = \frac{\lambda_L}{\mu_{V1}}\left[\left(\frac{L^+}{L^+_{eff}}\right) - 1\right] \qquad \textit{eq. 54}$$

where L^+_{eff} is the effective diffusion length in the damaged layer, L^+ is the intrinsic positron diffusion length (80-135 nm), λ_L the positron annihilation rate at ***Lattice*** ($\lambda_L = 1/\tau_L$, τ_L = 105 ps), and μ_V the trapping coefficient of a positron at a single vacancy equals to $(6 \pm 3) \times 10^{-15}$ m^3.s^{-1} for tantalum (Ta, Z = 73) having close proton number to tungsten (Z = 74). For the lowest damage dose, the fitted effective diffusion length in the first layer is $L_{Lay}(1)$ = 14 (4) nm. The concentration of single vacancies is evaluated at about 9.4×10^{25} m^{-3} by averaging the shortest and the longest intrinsic diffusion length.

When the damage dose increases, the R ratio increases, and the L_{Lay} decreases, indicating that vacancy-type defects were detected which trap positrons. The one-trap trapping model is no longer suitable to fit the induced vacancy-type defects, seeing the values of ***S*** and ***W*** become the results of annihilation of positrons trapped in a variety of vacancy defects, such as single vacancies, vacancy clusters and possibly at some dislocation type defects. As the TEM results presented in [221] which showed that the dislocation loops were generated in self-ion irradiated samples as it was already observed in literature (see [127]). Their density per unit area is estimated to be $(3.94 \pm 0.1) \times 10^{13}$ loops/m² at 0.85 dpa. As it is explained in the paper [221], the fraction of positrons that could be trapped at dislocation loops is negligible and positron annihilation characteristics are only representative of vacancy defects, including single vacancies and vacancy clusters Vn.

The value of the ratio R in the damaged layer reaches 2.15 at the maximum when the damage dose becomes greater than or equal to 0.425 dpa. This value corresponds to an intermediate value between the V_N related ratio ($R_{VN} = \left|(S_{max}-S_L)/(W_{min}-W_L)\right| = 2.85$) and the one of the single vacancy ($R_{V1} = \left|(S_{V1}-S_L)/(W_{V1}-W_L)\right| = 1.85$). It suggests that vacancy clusters Vn detected in the damaged layer are small and n is probably not larger than 5–7. When the damage dose is greater than 0.0085 dpa, positrons annihilate at either single vacancy defects or vacancy clusters Vn, where n varies from 2 to 5–7. The concentration of each type of defect cannot be determined because not only the specific values S_{Vn}, W_{Vn}

of vacancy clusters Vn are unknown but also because their corresponding annihilation fractions cannot be extracted. Nevertheless, the total positron trapping rate K_{tot} can be written as the sum of the trapping rate in single vacancies and the trapping rate in each type of vacancy clusters:

$$K_{tot} = K_{V1} + \sum_{n=2}^{5-7} K_{Vn} \qquad \textit{eq. 55}$$

where K_{V1} and K_{Vn} are the positron trapping rates at the single vacancy and the vacancy clusters Vn, respectively. K_{V1} is the product of the trapping coefficient μ_{V1} by the vacancy concentration C_{V1} and $K_{Vn} = \mu_{Vn} \times C_{Vn}$ and μ_{Vn} can be considered as equal to $n \times \mu_{V1}$ when n remains smaller than 10 [159]. It follows that the total vacancy defect concentration C_V^{tot}, which is the sum of the concentration of isolated vacancies and that of vacancy clusters, could be estimated from the following equation

$$C_V^{tot} = C_{V1} + \sum_{n=2}^{5-7} nC_{Vn} = \frac{K_{tot}}{\mu_V} \qquad \textit{eq. 56}$$

It is possible to extract from the effective diffusion length L_{Lay} obtained in the damaged layer the total vacancy defects concentration. As L_{Lay} can be written as follows:

$$L_{eff}^{+} = \sqrt{\frac{D_+}{\lambda_L + K_{V1} + \sum_{n=2}^{5-7} K_{Vn}}} \qquad \textit{eq. 57}$$

Where D^+ is the intrinsic diffusion coefficient of positrons in tungsten ($D^+ = 1.26 \times 10^{-4}$ $m^2.s^{-1}$ for tungsten [174]). K_{tot} could be estimated from the value of the effective diffusion length as it has been done just above for the lowest damage dose. However, the extraction of the effective diffusion length becomes difficult for damage dose higher than 0.0085 dpa. The obtained values range between 4 and 7 nm and depend strongly on the annihilation characteristics of the second layer, in particular its thickness and the effective diffusion length. The concentration of vacancy defects cannot be determined, but it is possible to estimate a lower limit of C_v^{tot} assuming that the effective diffusion length is equal to 6 nm obtained by VEPFIT program (see Table 19). In this case, C_v^{tot} would be higher or about 5×10^{26} m^{-3} for damage dose of 0.085 dpa. From 0.425 dpa, we have seen that PAS results detect a saturation when the dpa level increases indicating that the same type of vacancy defects were detected. Such saturation can be due to either the saturation of the induced damage or to the saturation of positron trapping at the detected type of defects. Moreover, the values of $S_{Lay}(1)$ and $W_{Lay}(1)$ and L_{Lay} (1) do not change for the highest damage doses larger or equal than 0.85 dpa and the R_{Lay} (1)= $|(S_{Lay}(1)-S_L)/(W_{Lay}(1)-W_L)$ ratio remains also constant indicating that if the concentration of defects would increase with damage dose, the proportion of each ones would not evolve indicating a saturation state in the defects size distribution. In addition, it can be observed that the thickness of the highest damage region (layer 1) increases when the damage dose increases above 0.425 dpa and changes from approximately 100 nm for the lowest dpa levels to up to 170 nm for the highest ones. These results can be compared to the TDS inventory data [221], where overall deuterium content was found to be close, for the sample irradiated at 0.1 dpa (4.408

$\times 10^{19}$ D atoms.m^{-2}) and for the sample irradiated at 0.85 dpa (3.564×10^{19} D atoms.m^{-2}). It is known that hydrogen isotopes trapping (the number of atoms in each defect type) depends on the nature of the defects. From SPB-DB measurement, we know that the change on the distribution of the size of vacancy defects is inconspicuous between these two damage doses (0.085 and 0.1 dpa). The ratio R is 2.10 (4) for 0.085 dpa and reaches the saturation value of 2.15(4) for 0.85 dpa. It follows that the change in concentration of vacancy defects should be also insignificant if we consider the H-release is lower for the highest damage dose. It concludes that the concentration of vacancy defects reaches a saturation when irradiation induced damage becomes higher than 0.5 dpa.

The formation of vacancy defects detected in SPB-DB is in agreement with MD simulations at least for low damage dose. MD simulations [69] showed that in collision cascades of 150 keV-W^+ ions mainly single vacancies (approximately 70 %) are created together with some small clusters (about 28% with 2 to 5 vacancies in) and a very low fraction of large clusters which depends on the empirical potential which is used. It has been also shown that the number of defects increases with the PKA energy, E_{PKA} in metals and also in tungsten [222] and their size distribution is a power law for E_{PKA} = 50 keV [66] which depends on E_{PKA}. The fraction of larger vacancy clusters and their size increases with E_{PKA} at least up to the cascade fragmentation energy threshold as it has been shown in Fe [223] The PKA energy spectrum induced in the region probed with the slow positrons (0-150 nm) by 2 MeV-W ions in tungsten is plotted in Figure 86.

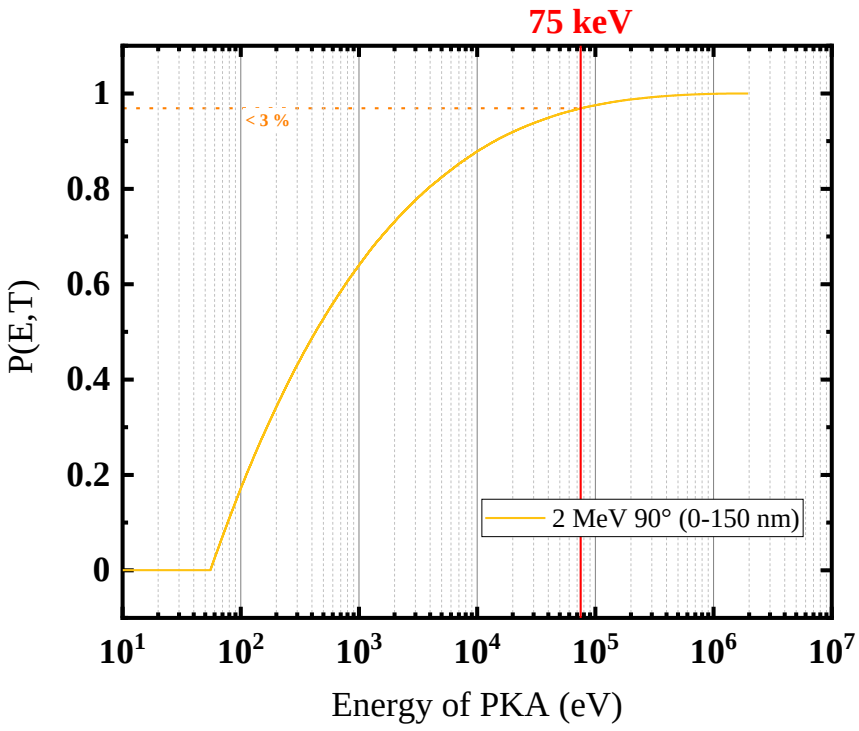

Figure 86: PKA energy distribution spectrum as calculated using full-cascade option of SRIM-2008 and E_{disp} = 55.3 eV for 2 MeV ions in the region probed by the slow positrons (0-150 nm).

In this Figure 86, the PKA energy ranges from the displacement energy threshold fixed at 55.3 eV in this calculation to about 1.9 MeV. We also marked the energy threshold (75 keV) determined for cascade fragmentation in tungsten [71]. About 3 % of PKA have energy higher than 75 keV. Above the fragmentation energy the defect size distributions should be the convolution of size defect distributions produced in individual subcascades and the subcascade size distribution [224]. It has also to be noticed that when subcascades are formed they can overlap and it can impact the size distribution. Sand et *al.* [72] showed that the size distribution deviate from the power law and a second slope appears in the scale law indicating a larger fraction of large vacancy clusters.

Concerning the effect of ion fluence (or damage dose) on the defect distribution, the effect of pre-damage was investigated in the MD calculations. It has been shown in Fe that the number of surviving defects decreases depending on the size distribution of defects present before the cascade and on E_{PKA} [223] at least for low damage dose. It is still ambiguous what could be the effect of high pre-damage on the defects distribution. It can be concluded that the general tendency we observed in our experiments are in agreement with the MD calculations. **i/** Vacancy clusters are created during collision cascades and survived **ii/** their size increases with the ion fluence (or damage dose) at low dpa. The saturation effect will be discussed more in details in the Chap IV.2.2.2 when the SPB-DB results of 20 MeV self-ion irradiated samples will be compared to the 2 MeV ones.

PART II: Identification of defects induced by 20 MeV self-ion irradiation and effect of fluence for irradiation at room temperature (RT)

IV.2.2 20 MeV self-irradiations

To further study the induced vacancy-type defects, a couple of 3N-HP (99.95 wt. %, GP) and 6N-XHP (99.9999 wt. %, Plansee (FZJ1)) tungsten samples were irradiated with 20 MeV self-ions with two fluences (4.10×10^{12} cm^{-2} and 1.10×10^{14} cm^{-2}) at RT; the irradiation conditions are included in Table 20. According to the SRIM-2008 simulations, in contrast to 2 MeV self-ion irradiation, the thickness damaged by 20 MeV self-ions extends from surface to ~2.25 µm, and the peak damage value shifts from 70 nm to 1.34 µm, so that, the probed thickness by slow positrons is fully damaged with a more homogenous damage distribution. This section is concentrated on the investigation of the evolution of the vacancy-type defects induced by 20 MeV self-ion in tungsten by using SPB-DB measurement, and compare to that obtained of 2 MeV self-ions.

Damage (dpa)	*Square Samples (7 × 7 mm^{-2}) Irradiated by 20 MeV-W*			
Mean value in the first 700 nm	**Purity**	**Flux ($\times 10^{10}$ $cm^{-2}.s^{-1}$)**	**Fluence ($.cm^{-2}$)**	**RT**
0.012 (3)	HP	2.5	4.14×10^{12}	ZH-W-GP-343/1-C04
				ZH-W-GP-343/1-C06
				ZH-W-P-UHP-FZJ1-C05
0.318 (8)	HP	2.8	1.09×10^{14}	ZH-W-GP-343/1-C08
	XHP			ZH-W-P-UP-FZJ1-C09
				ZH-W-P-UHP-FZJ1-C10

Table 20 : Irradiation conditions of 20 MeV self-ion damaged samples, the damage is mean value in the first 700 nm of the damage profile calculated by SRIM-2008 (K-P mode, E_{disp} = 55.3 eV).

IV.2.2.1. SPB-DB measurement in RT, 20 MeV self-irradiated samples

Figure 87 shows the SPB-DB results for the samples irradiated with 20 MeV self-ions at **RT** with two fluences 4.10×10^{12} cm^{-2} and 1.10×10^{14} cm^{-2}, corresponding to a mean damage level in the depth probed by slow positrons (~700 nm) of about **0.012** *(downward triangle)* and **0.318 dpa** *(upward triangle)*, respectively.

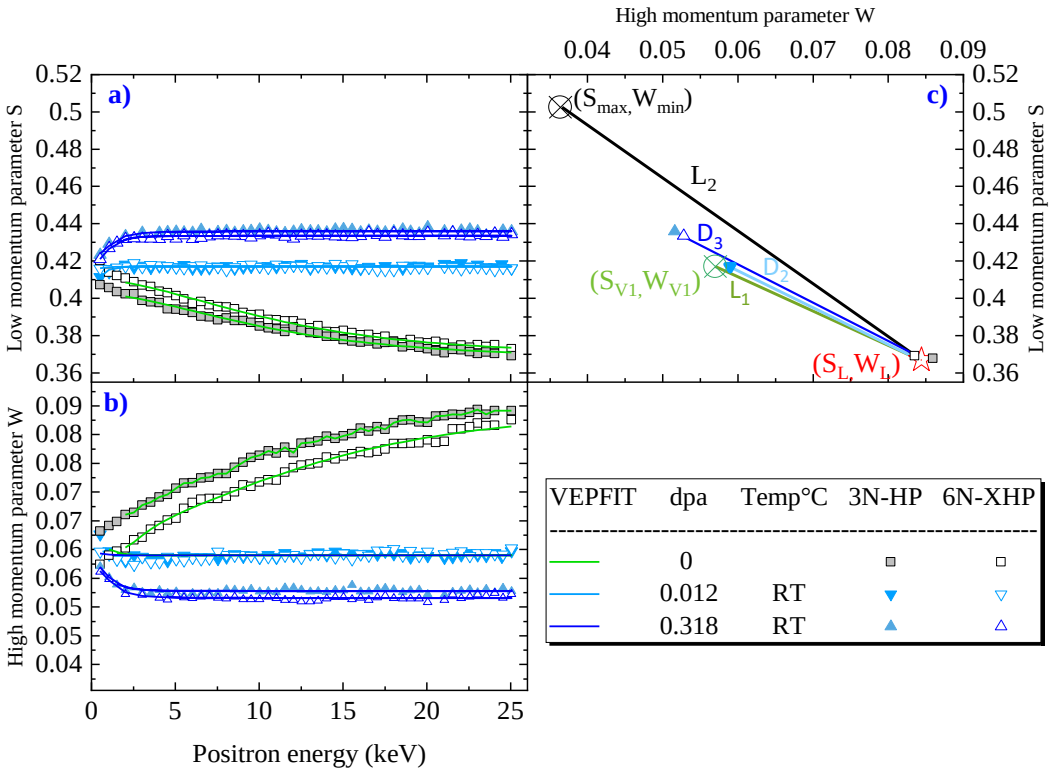

*Figure 87: **a, b)** the annihilation characteristics **S, W** as a function of the positron energy E and **c), S** versus **W** plot in 3N-HP W samples (solid symbols) and 6N-XHP samples (open symbols), before irradiation ■(3N) □(6N) after irradiation at **room temperature**, **0.012 dpa** (downward triangle ▼(3N) ▽(6N)), and **0.318 dpa** (upward triangle ▲(3N) △(6N)).*

Comparing to the pristine samples *(squares)* with two purities (6N-XHP (open) and 3N-HP (solid)), the low momentum parameter ***S*** is higher and the high momentum one ***W*** is lower on the whole energy range for self-ion damaged samples, suggesting the generation of the vacancy-type defects after irradiation. When the energy increases up to 3 or 4 keV, ***S*** (and ***W***) increases (decreases respectively) quickly first and then both ***S*** and ***W*** remain at plateau values for all the irradiation damage doses. The plateau value increases with damage dose but for one damage dose, both purities give the same or very close ***S*** and ***W*** parameters. The ***S(E)*** and ***W(E)*** curves were fitted with a homogeneous single-layer model by using VEPFIT. The fitted data are plotted as continuous lines, which superimpose with experimental data. Table 21 summarizes the annihilation characteristics in the damaged layer obtained from the fit. The values of ***S*** and ***W*** in the region probed by slow positrons (the first 700 nm under the surface) are equal to those of the plateau of ***S(E)*** and ***W(E)*** curves. They were plotted on the ***S-W*** curve (Figure 87.c).

	Purity (wt.%)	*Tempe °C*	*Damage dose (dpa)*	S_{surf}	W_{surf}	*S*	*W*	L_{eff}^{+} *(nm)*
G-13	99.95		0	0.413 (3)	0.0608 (3)	0.367 (3)	0.0842 (3)	123 (3)
J1-29	99.9999			0.403 (4)	0.0659 (4)	0.367 (3)	0.0861 (3)	100 (3)
G-04	99.95	RT	**0.012**	0.414 (10)	0.060 (5)	0.417 (1)	0.0590 (6)	0.6 (2)
J1-05	99.9999			0.414 (10)	0.060 (5)	0.417 (1)	0.0590 (9)	0.4 (2)
G-08	99.95	RT	**0.318**	0.416 (4)	0.059 (2)	0.434 (1)	0.0528 (3)	1.4 (5)
J1-10	99.9999			0.420 (11)	0.058 (1)	0.437 (2)	0.0516 (2)	2.0 (7)

*Table 21: Annihilation characteristics S,W of the fitted layer by VEPFIT for self-ion irradiated samples of two purities **6N-XHP (99.9999 wt.%)** and **3N (99.95 wt.%)** at **RT** with different damage doses (**0.012 and 0.318 dpa**) in contrast to pristine samples.*

The ***S, W*** points measured for the lowest damage dose (0.012 dpa) are very close to the single vacancy point as it is the case for 2 MeV self-irradiation at the lowest damage level of 0.0085 dpa. For the highest damage dose (0.318 dpa), ***S, W*** points are clearly above the L_1 line characteristic of annihilation of positrons as trapped in single vacancy. In Figure 87.c, the ***S, W*** points for 0.012 and 0.318 dpa are linked to the one of the tungsten ***Lattice*** (red star) by blue lines D_2 and D_3, respectively. The slope R_2 of the trend line D_2 (R_2 = 1.97) exceeds slightly that of the single vacancies one (R_{V1} = 1.85), i.e. L_1. It means that the detected defects are mostly related to small vacancy clusters Vn, in which the majority are single vacancies in the sample irradiated to a damage level of about 0.012 dpa. The D_3 line is located between the line L_1 and L_2 which is characteristic of annihilation at the largest vacancy clusters ever detected (see Figure 84). Its slope R_3 (R_3 = 2.12) is also much lower than the R_{VN} (R_{VN} = 2.8) or the slope of the L_2line, indicating that intermediate sized vacancy clusters are detected at 0.318 dpa as it is also the case for 2 MeV self-ion irradiations. The estimated effective diffusion length L_{eff}^{+} of positrons in the damaged region (see Table 21) is extremely short (< 2 nm), indicating efficient positron trapping. It has to be noticed that in 20 MeV self-ion irradiations the damage evolves slightly in the probed region (see Figure 37.d) and it leads to plateau values for ***S*** and ***W*** for both fluences. Moreover, for the damage doses investigated here the ***S*** and ***W*** plateau values are very close to the annihilation characteristics of the sample surface. It is particularly true for the lowest damage dose (0.012 dpa). It follows that it is very difficult to extract correct values of the effective diffusion length of the damaged layer. The values indicated in the Table 21 are not reliable for the lowest damage dose and very questionable for the highest one. Therefore, these values cannot be used for estimation of vacancy concentration as it has been done in the case of 2 MeV self-ion irradiated samples.

IV.2.2.2. Discussion on the saturation of damage in self-ion irradiated tungsten

In the following, the SPB-DB results obtained in both 2 and 20 MeV self-ion irradiated tungsten are compared and discussed.

First of all, the SPB-DB results of 2 and 20 MeV self-ion irradiated samples revealed the detection of vacancy clusters with a proportion which increases with damage dose when a saturation of low

momentum ***S*** and high momentum ***W*** in the damaged region when the damage dose is higher than 0.425 dpa. In Figure 88, the results obtained in the samples irradiated with 20 MeV-W ions at the damage dose 0.012 and 0.318 dpa are plotted together with the 2 MeV self-ion irradiated ones. Other data obtained in samples self-irradiated at 20 MeV and RT have been also added. The ratio of the low momentum parameter ***S*** for the damaged region to that of the ***Lattice***, S/S_L is plotted as a function of damage dose on the left (Figure 91.a) and as a function of the high momentum ratio W/W_L on the right (Figure 88.b) for the 2 MeV and 20 MeV tungsten irradiations at RT with various fluences as a function of the damage dose. These new data confirm the saturation of the ***S*** and ***W*** annihilation characteristics at a damage dose around 0.5 dpa.

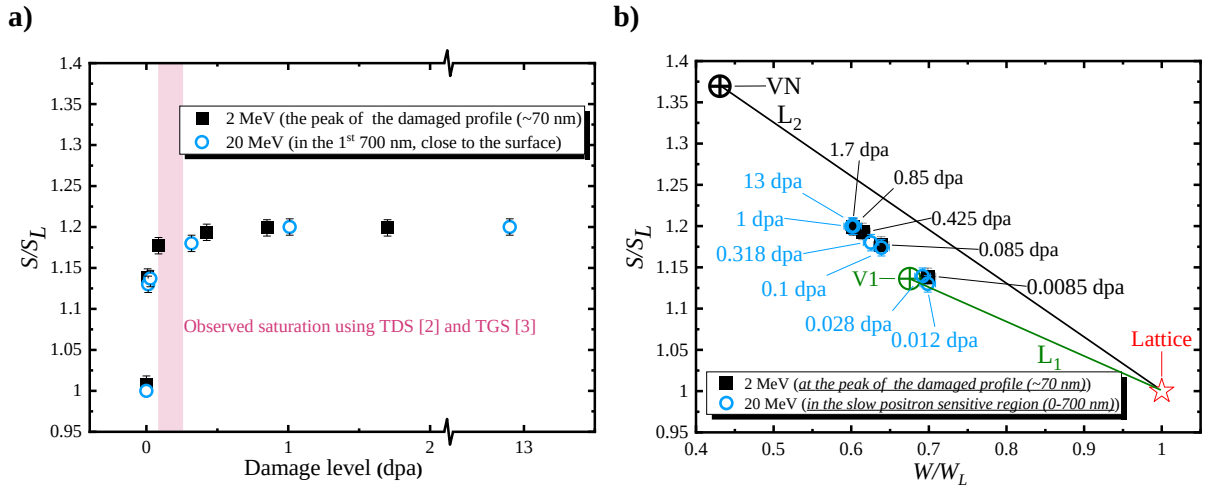

*Figure 88: **a)** the ratio of the fitted low momentum parameter **S** extracted by VEPFIT in the most damaged layer and that of the lattice S_L for **2 and 20MeV self-irradiated** tungsten at **RT** with various fluences, the pink rectangular marks the observed saturation damage level, from 0.1 to 0.28 dpa in self-irradiated tungsten with TDS and TGS technique [225–227], **b)** the S/S_L versus W/W_L. The data obtained for 20 MeV irradiations at 0.028, 0.1 dpa1 dpa et 13 dpa are extracted from previous studies [126].*

Such saturation can be a result of either the saturation of the radiation-induced defects (RID) or the saturation of the positron trapping at the distinct types of defects yielding equivalent annihilation characteristics. As discussed above (see Chap IV.2.1.2) the analysis of the 2 MeV self-ion irradiated samples suggests that the concentration of vacancy defects reaches a saturation when irradiation induced damage becomes higher than 0.5 dpa. As shown in Figure 94, (see Chap IV.2.3.1), when the irradiation was carried out at high temperatures, the SPB-PB still enables to detect larger vacancy clusters, thus, the saturation should be related to the distribution of the defects induced in the sample.

A similar saturation has been observed in numerous studies of 20 MeV self-ion irradiated tungsten. Reza et *al.* [226] employed transient grating spectroscopy (TGS), to measure the thermal diffusivity in comparable self-ion irradiated tungsten (20 MeV, RT) with damage doses ranging from 10^{-4} to 10 dpa (calculated using SRIM-2008 in the K-P mode and with E_{disp} = 68 eV, corresponding to 1.23×10^{-4} to 12.3 dpa when using the displacement threshold energy we chose in this work E_{disp} = 55.3 eV). The thermal diffusivity is found to decrease with increasing damage dose, and becomes constant above 0.1

(0.12 for TDE = 55.3 eV) dpa at a value 55 % lower than the initial one. The thermal diffusivity depends on the impurities in the samples and on the defects introduced during irradiation. They estimated that the amount of Frenkel pairs responsible of the thermal diffusivity at 0.1 dpa is 2400 at. ppm or about 1.5×10^{26} m^{-3}. It means that about 1×10^{26} m^{-3} vacancies could contribute to the thermal diffusivity decrease. This number can be compared to the total vacancy concentration C_v^{tot} roughly estimated from SPB-DB measurements in tungsten samples 2 MeV self-irradiated at a damage dose of 0.085 dpa (see Chap IV.2.1.2). In this damage dose (0.085 dpa) C_v^{tot} should be higher or about 5×10^{26} m^{-3}. This value is in the same order of magnitude as the concentration estimated from the thermal diffusivity measurement. Nevertheless, the five times higher factor found in the SPB-DB estimation could be due to the fact that in our estimation we took into account the presence of vacancy clusters whereas Reza et *al.* [226] only consider point defects (PDs) as electron scattering centers.

Ogoronikova and Gann [225] have studied the deuterium (D) concentration which is trapped in 20 MeV self-irradiated tungsten using thermal desorption spectroscopy (TDS). They observed a saturation of the D release -attributed to a saturation of the introduced amount of deuterium- at ~0.45 dpa, a damage dose calculated using SRIM-2008 in the K-P mode with E_{disp} = 90 eV. This damage dose should correspond to approximately ~0.8 dpa when using the displacement energy threshold of 55.3 eV. In contrast, in a similar TDS work realized by R. Hoen et *al.* [227], a saturation was found in 12.3 MeV-W self-ion irradiated tungsten at ~0.2 dpa (SRIM-2008, K-P, E_{disp} = 90 eV) corresponding to approximately ~0.3 dpa when using the displacement energy threshold, we chose (E_{disp} = 55.3 eV).

As a result, the saturation of the damage has been observed by different techniques in self-irradiated tungsten at RT, varying from 0.1 to 0.8 dpa after normalizing the damage dose at the displacement threshold energy we used in the present work (E_{disp} = 55.3 eV). In our study the saturation threshold is between 0.425 and 0.85 dpa. In a rough analysis of these data, we can consider that our results are in agreement with the ones found in the literature, if we take into account the inaccuracy of the fluence measurement during irradiation that can reach about 25%. The saturation is observed at higher damage dose (about 0.5 dpa) in our study compared to the one of Reza et al [226] (about 0.1 dpa). It could be due to the fact that PAS (SPB-DB) and the ***S*** and ***W*** values are not only sensitive to the concentration of defects but also to their nature and specifically to their size. As we already showed, the R ratio -which increases with the size of vacancy clusters- slightly increases when damage dose changes from 0.085 dpa (R = 0.210(4)) to 0.425 dpa (R = 0.215(4)) indicating that for damage dose in this range the size of the vacancy clusters still slightly increases.

It is also interesting to notice that the curve of the relative value of $\boldsymbol{S/S_L}$ low momentum ratio as a function of damage dose are superimposed for both energies 2 and 20 MeV (see Figure 88.a). In the same way, the $\boldsymbol{S/S_L}$, $\boldsymbol{W/W_L}$ points (see Figure 88.b) are very close for close damage doses except for the lowest one. It should be noted that the damage dose corresponds to the mean values in the positron

probed depth (~0-700 nm) for 20 MeV self-ion irradiated samples and to the maximum value at the peak (~70 nm) of the damage profile for 2 MeV ones. That means that in the case of 20 MeV irradiations, positron probe much more along the tracks of ions, whereas for the 2 MeV ions they probe the cascade region. It suggests that damage created along the tracks of ions is close to the one which is created at the end of the range of the ions. Moreover, it should be noted that this saturation does not depend on the irradiation energy. The PKA spectrum (see Figure 89) calculated using SRIM-2008, in full-cascades option using E_{disp} = 55.3 eV in positron-probed region for 20 MeV tungsten ions (0-700 nm) is compared to that of 2 MeV (0-150 nm).

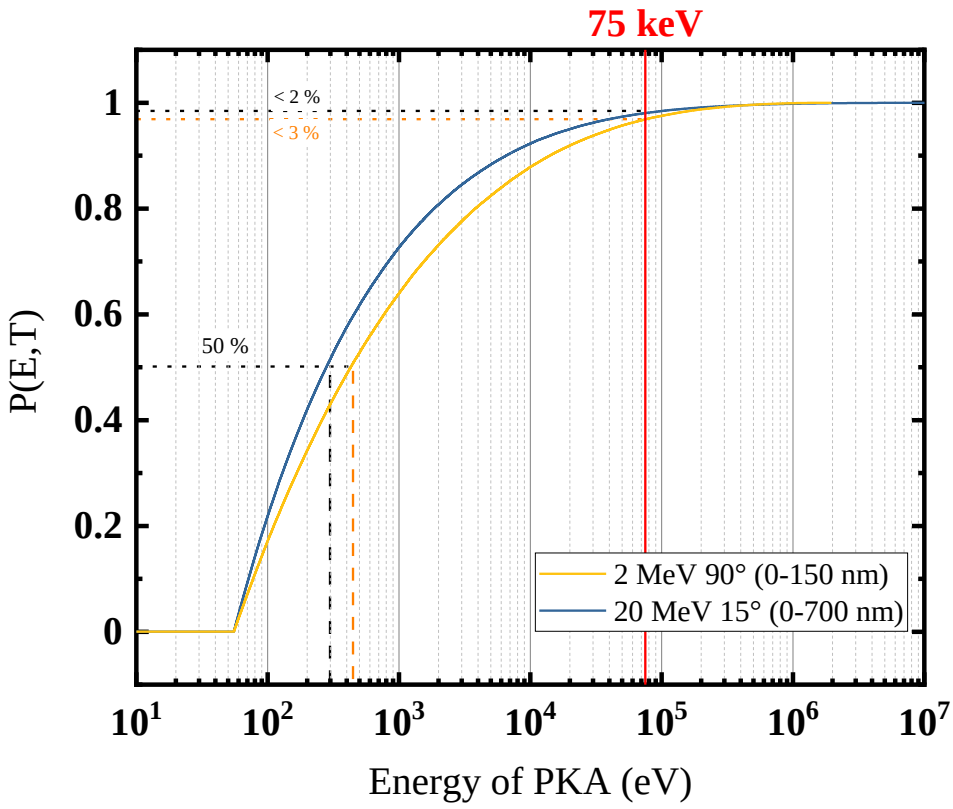

Figure 89: PKA energy distribution spectrum as calculated using full-cascade option of SRIM-2008 and E_{disp} = 55.3 eV in the 0-150 nm and 0-700 nm for 2 and 20 MeV ions, respectively.

The PKA energy is slightly lower for 20 MeV (the half of PKA have an energy → $P_{1/2}$(20 MeV) = 280 eV) than for 2 MeV ($P_{1/2}$(2 MeV) = 430 eV) ions. Nevertheless, the fraction of PKA with energy larger than the cascade fragmentation (75 keV) is very close (~2-3 %) for both energies. It follows that the size of defects clusters should be slightly lower in the track region of 20 MeV ions than in the highest damaged region of the 2 MeV self-ion irradiated samples at least for low damage dose, which could explain why the ***S*** is slightly lower and ***W*** slightly higher for 20 MeV irradiations than for 2 MeV for close irradiation damage dose remaining lower than 0.5 dpa (see Figure 90.a).

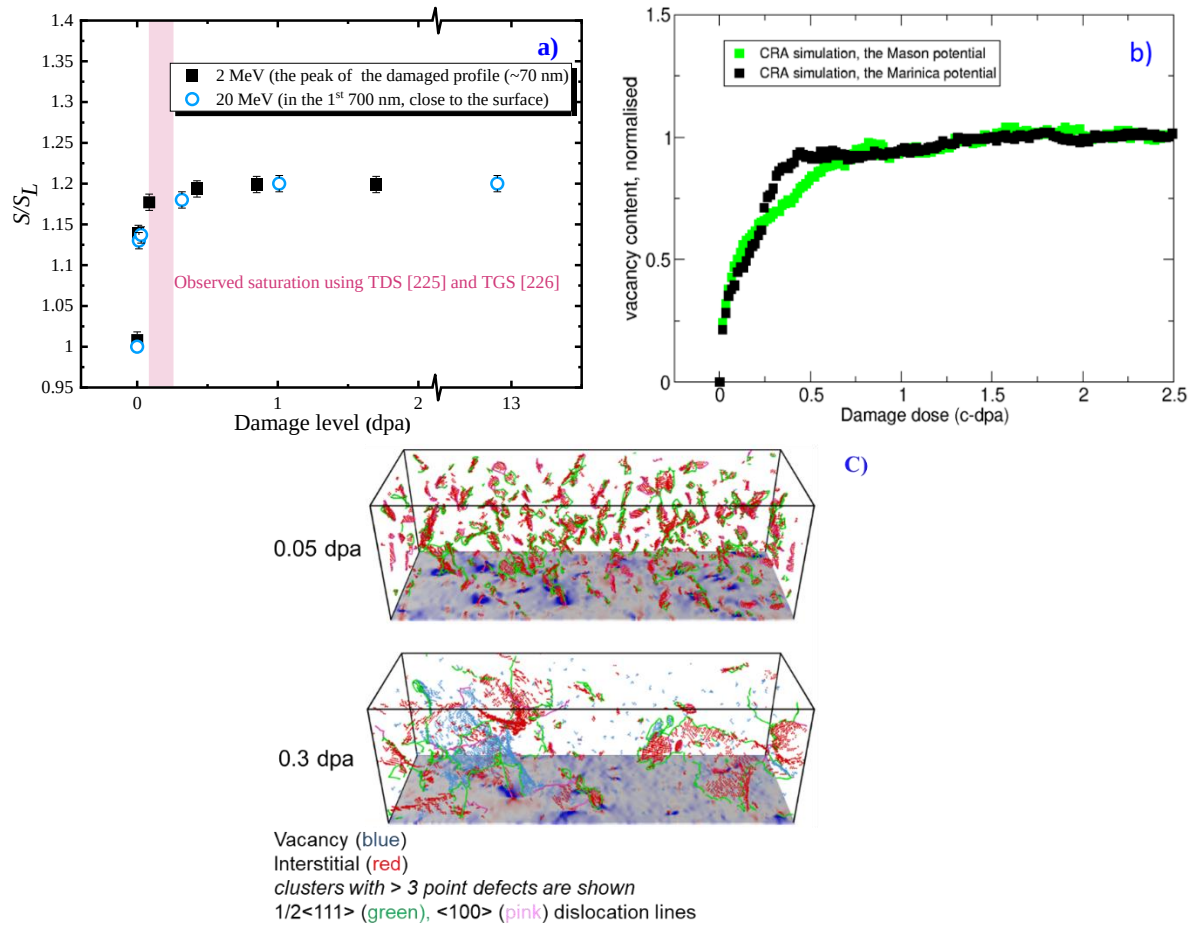

*Figure 90: **a)** Ratio of the fitted low momentum parameter **S** by VEPFIT in the most damaged layer and that of the lattice S_L for **2 and 20 MeV self-ion irradiated** tungsten at **RT** with various fluences, the pink rectangular marks the observed saturation damage level, from 0.1 to 0.28 dpa in self-irradiated tungsten with TDS and TGS technique [225–227], **b)** Variation of vacancy content in tungsten as a function of canonical dpa (c-dpa) predicted by simulations performed using the creation-relaxation algorithm (CRA) for two different interatomic potentials [228]. The values are normalized to the asymptotic high dose vacancy content, which for the Marinica potential [229] is close to 5 % and for the Mason potential [105] is close to 2 % **C)** visualization of insertion of the Frenkel pairs simulation using CRA for 0.05 dpa (top) and 0.3 dpa (bottom) [230].*

Furthermore, a similar trend, indicating that the vacancy content in the tungsten exposed to irradiation increases as a function of dose and reaches saturation at a dose above approximately 0.5 dpa, was also found in direct atomistic simulations of highly irradiated tungsten and iron performed using the creation-relaxation algorithm (CRA) [228]. This simulation approach assumes a uniform spatial probability distribution of generation of Frenkel pairs (FP), where at each step of execution of the algorithm, a randomly chosen atom is displaced to a random location within the simulation cell. Then the energy of the cell is relaxed using MD. The Figure 90.b is extracted from [221] and shows the vacancy content evolution as a function of damage dose for two different interatomic potentials (developed by Mason and Marinica). It increases quickly first and then remains constant from about 0.5 dpa. The concentration of vacancy defects at the saturation level is about 2 % and 5 % for the Marinica and Mason potentials, respectively. In PAS (SPB-DB) we estimated a vacancy concentration higher

than approximately 0.8 % for the 0.085 dpa irradiated sample that means at damage dose lower than the saturation of about 0.5 dpa. These theoretical results are in good agreement with our PAS measurements. It has to be noticed that this saturation is also found in the interstitials type defects distribution. These calculations showed that SIA loops are created and accumulated when the FP dose increases up to be transformed into dislocation lines. An equilibrium phase is reached and made of a dislocation lines network in which vacancy clusters are incorporated (see Figure 90.c).

This saturation was also found in other materials, such as in Eurofer steel at a damage level of about 0.25 dpa [231], while another study [232] found a rapid saturation (below 0.1 dpa) in Fe-Cr alloy but a decrease of deuterium concentration in Eurofer at 1 dpa compared to 0.1 dpa. Moreover, Kanzaki et *al.* [233] have observed saturation of the production of the defects in gold irradiated with 400 keV Xe ions with a fluence of about 1.5×10^{11} cm^{-2} at 300 and 473 K, by performing TEM observations. Combining to the theoretical works, the origin of the saturation was argued as a result of the competition of point defects recombination and cascades overlapping [234], giving rise to shrinkage of generated vacancy clusters, this phenomenon was found in BCC iron by Agarwal et *al.* [235]. Overall, such saturation as a function of the damage dose might be expected for all the materials.

Finally, we conclude above that the ***S*** and ***W*** parameters for irradiation at RT are very similar for both material sets 3N-HP and 6N-XHP. The concentration of C and O was measured in both types of self-ion irradiated samples (0.02, 0.04 dpa, RT). The values remain low for both elements in both materials 3N-HP and 6N-XHP. It is at the detection limit for C (about 50 at. ppm) for both materials and the O concentration is slightly higher in 3N-HP (about 100 at. ppm) than in 6N-XHP (about 70 at. ppm) (see Appendix. D). Moreover, Calder et *al.* [236] investigated the effect of the presence of C with concentration in the range from 0 to 1 at.% in the Fe MD simulation box. Neither change on the number of defects nor the cluster fraction produced in collisions cascades were discerned. Only a significant fraction of single defects is trapped in C in the cascade process. Nevertheless, this fraction remains lower that 5 % for a C concentration of 1000 at. ppm. Thereby, it suggests that even though for less pure samples the trapping of vacancy defects at impurities should play an insignificant role at RT because of the low mobility of vacancy defects (see Figure 27).

Summary

In these sections, we compared SPB-DB measurements in tungsten samples, which were self-irradiated with 2 MeV and 20 MeV ions at RT. An equivalent evolution of low momentum ***S*** and high momentum ***W*** fractions was revealed in the damaged regions. ***S*** increased and ***W*** decreased when the damage dose increases up to saturation values. This saturation is reached when damage dose is in the range from 0.425 to 0.85 dpa. Under such irradiations vacancy defects are created and their size distribution varies with the damage dose up to the saturation. At the lowest damage level (~0.0085 dpa), a few small vacancy clusters were detected by positrons in the first 100 nm under the surface, which is composed mainly of single V_1 vacancies as predicted by collision cascades MD simulations. Their concentration was estimated at about 9.4×10^{25} m^{-3}. When damage dose increases to the value of 0.085 dpa, small vacancy clusters V_n containing about 5-7 vacancies were clearly detected and the total concentration of vacancies (V_1 or in V_n clusters) should have a minimum value of 5×10^{26} m^{-3}.

In addition, these experimental results were compared to other experimental studies which confirm saturation of the defect density for damage dose between 0.1 to 0.8 dpa depending on the technique which is used for damage characterization (TGS, D exposure and TDS). Modelling (CRA) also predicted such saturation for a damage dose threshold of about 0.5 dpa. This saturation showed that an 'equilibrium' microstructure is formed when damage dose reaches this threshold value, which could be due to competition between defect recombination, cascades overlapping, and agglomeration of self-interstitials loops. This 'equilibrium' microstructure is made of vacancy defects (single (V_1) and clusters (V_n)) dispersed in interstitial-type dislocations network.

PART III: Identification of defects induced by 20 MeV Self-ion irradiation and Effect of irradiation temperature and tungsten purity on the defects distribution

In this third part, we focused on the effect of irradiation temperature and material purity on the distribution of induced defects by self-ion irradiation in tungsten. A series of irradiations were performed using 20 MeV and 1.2 MeV ions at two dpa levels 0.02 and 0.04 dpa in two sets of samples with two different purities (3N-HP and 6N-XHP) at the same time for 20 MeV beam (see Table 22). Two irradiation temperatures were chosen 500 and 700 °C because they are above the value at which migration of single vacancy is expected and just below the maximum value that could be reached in the irradiation system. The list of all the samples irradiated at high temperatures (500 and 700 °C) and at both damage doses (0.02 and 0.04 dpa) is summarized in Table 22.

It should be noticed that a part of the data and discussion is extracted from the paper [201] we published in Journal of Nuclear Materials 556, 153175. https://doi.org/10.1016/j.jnucmat.2021.153175.

Damage (dpa)	Square Samples (7 × 7 mm^{-2}) Irradiated by 20 MeV-W						
Mean	**Purity**	**Flux (× 10^{10} $cm^{-2}.s^{-1}$)**	**Fluence (cm^{-2})**	**500°C**	**Flux (× 10^{10} $cm^{-2}.s^{-1}$)**	**Fluence (cm^{-2})**	**700°C**
0.020 (5)	HP	2.77	7.48×10^{12}	ZH-W-GP-343/1-C05	2.34	7.43×10^{12}	ZH-W-GP-343/1-C02
	XHP			ZH-W-P-UHP-FZJ1-C11			ZH-W-P-UHP-FZJ1-C03
				ZH-W-P-UHP-FZJ1-C06			ZH-W-P-UHP-FZJ1-C04
0.04 (1)	HP	2.22	1.49×10^{13}	ZH-W-GP-343/1-C01			
	XHP			ZH-W-P-UHP-FZJ1-C01			
				ZH-W-P-UHP-FZJ1-C02			

Table 22 : Irradiation conditions of 20 MeV self-ion damaged samples with low damage level (0.02, and 0.04 dpa) at high temperatures (500, and 700°C), the damage is the mean value in the first 700 nm of the damage profile calculated by SRIM-2008 (K-P mode, E_{disp} = 55.3 eV).

IV.2.3.1. SPB-DB results in 500 and 700 °C 20 MeV self-irradiated samples

Firstly, the effect of the temperature on the evolution of the distribution of the induced vacancy-type defects was studied by employing SPB-DB measurement. A set of 3N-HP (99.95 wt.%, GP) and 6N-XHP (99.9999 wt.%, Plansee (FZJ1)) samples was self-ion irradiated to a low fluence (7.4×10^{12} $W^{+}. cm^{-2}$) to cumulate a damage dose of about (0.01, 0.02 and 0.04 dpa) in the slow positron sensitive region (~700 nm). The results will be presented into separate sections: firstly, we will show the effect of irradiation damage dose and temperature in 3N-HP samples, and then, the effect of the purity on the SPB-DB results.

a) Effect of irradiation and temperature fluence in the 3N-HP samples

Figure 91 exhibits the SPB-DB results for the *3N-HP samples* irradiated at 500 °C, for both damage doses 0.02 (Low Damage, LD) and 0.04 (High Damage, HD) dpa and compared to the irradiation at 0.01 dpa and RT. It is not surprising that the distribution of the induced vacancy-type defects differs for the irradiations performed at high temperatures (500 °C).

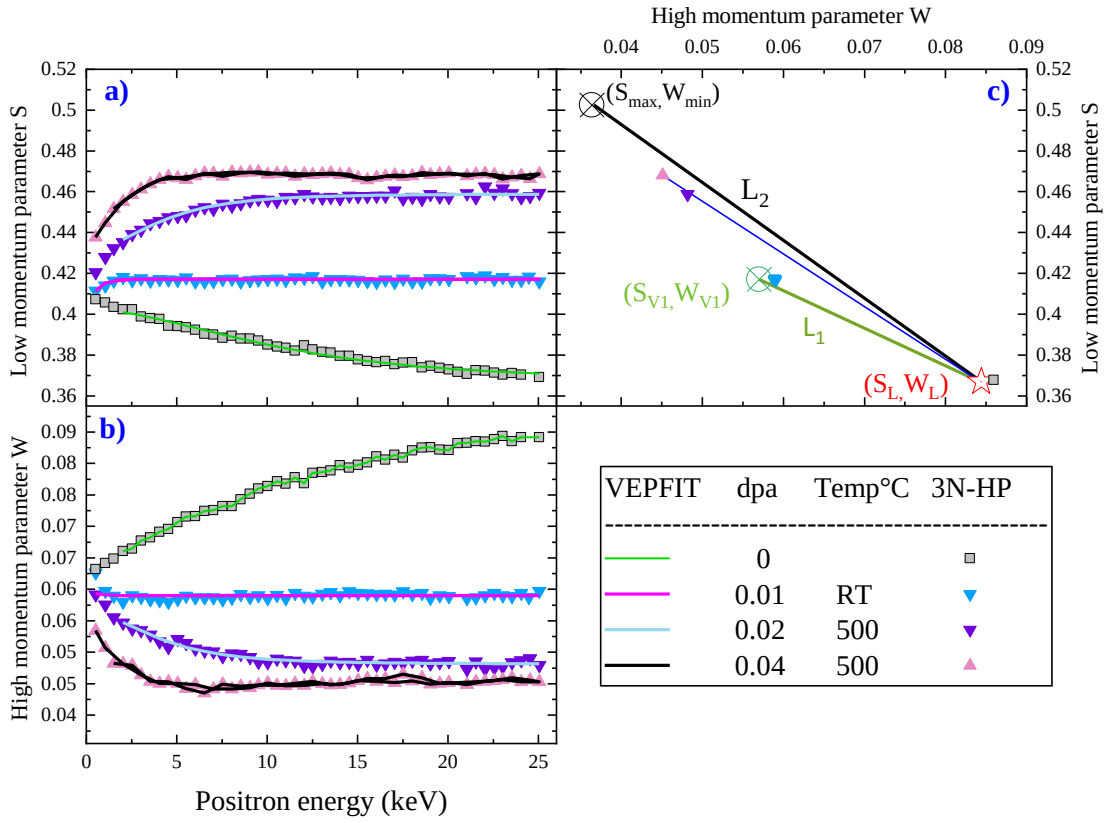

*Figure 91: **a, b)** Annihilation characteristics **S, W** as a function of the positron energy E and **c), S** versus **W** plot in 3N-HP W samples (solid symbols), before irradiations ■(3N) after irradiation at **500 °C** , **0.02 dpa** (purple downward triangle ▼(3N) and **0.04 dpa** (magenta upward triangle ▲(3N))*

For positron energies above 2 keV, the line shape parameters ***S*** (and ***W)*** are strongly higher (and lower respectively) in the samples irradiated at 500 °C for both fluences compared to the ones irradiated at RT. It suggests a drastic change in the vacancy defects distribution when the irradiations are performed

at high temperature. After fitting with a single-layer model by operating the VEPFIT program, a homogenous distribution of vacancy clusters was confirmed. The annihilation characteristics extracted in the first 700 nm under the surface are reported in the Table 23. The fitted values of the ***S*** versus ***W*** are plotted in Figure 91.c.

The ***SW*** points for both damage doses 0.02 and 0.04 dpa are located at the lower left part of the ***S*** versus ***W*** plot, close to the L_2 line characteristic of the largest vacancy clusters detectable by using the SPB-DB measurement. The ratio of R (R= $|(S-S_L)/(W-W_L)|$) is much higher for irradiation at 500 °C (R ≈ 2.6) compared to RT irradiation (R ≈ 2.0). It indicates that larger vacancy clusters are detected for irradiations at 500 °C. The effective diffusion length of positron L_{eff}^{+} was found to be about 17 nm for 500 °C, which is a short value and indicates a high trapping rate of positrons even though L_{eff}^{+}(500 °C) is longer compared to samples irradiated at RT (about less than 1 nm). It suggests that the concentration of the vacancy defects becomes lower when irradiation temperature is higher. All these observations reveal that the size of the induced clusters is close to the maximum detectable (~1 nm) with the technique for the irradiations at 500 °C compared to RT. It is noteworthy that the fitted values of the ***S*** (and ***W)*** are slightly greater (and lower respectively) in the samples irradiated at the highest damage dose 0.04 dpa. As shown on the ***S-W*** plot, in Figure 91.c, the trend line connecting the fitted characteristics from the ***Lattice*** point go through the extracted ***SW*** point for the HD dose (0.04 dpa) and the LD one (0.02 dpa), which suggests probably the defection of the same type of defects, and the concentration of detected defects is greater for 0.04 dpa. In addition, the effective diffusion length of positron L_{eff}^{+} was adjusted to about 3-5 nm for HD (0.04 dpa), compared to about 17 nm for LD (0.02 dpa), indicating higher positron trapping in HD samples and consequently a higher concentration of vacancy clusters in HD samples. Furthermore, the cluster size is evidently larger for irradiation at high temperature (500 °C) than those formed during the irradiations at RT.

Figure 92 exhibits the SPB-DB results for the *3N-HP* samples irradiated at the damage dose of 0.02 dpa, for both temperatures 500 and 700 °C compared to the irradiation at 0.01 dpa and RT. As for the fluence, the irradiation temperature impacts the damage induced in the 3N-HP samples. Even if the damage depth distribution remains homogeneous in the region probed by slow positrons the ***S*** and ***W*** plateau values change. The annihilation characteristics extracted in the first 700 nm under the surface using single-model VEPFIT fitting are reported in the Table 23. A slight shift in the ***S*** and ***W*** values is observed for irradiation at 700 °C compared to 500 °C. As for the larger damage dose, irradiation at higher temperature (700 °C) induces the formation of larger vacancy defects.

To summarize, 20 MeV self-ion irradiations 0.02 dpa in 3N-HP samples leads to the formation of vacancy clusters in the damaged region. Larger clusters are observed when the temperature increases from RT to 700°C. For HD samples (0.04 dpa) at 500 °C, the same type of defects was detected but their concentration is greater by comparing LD samples.

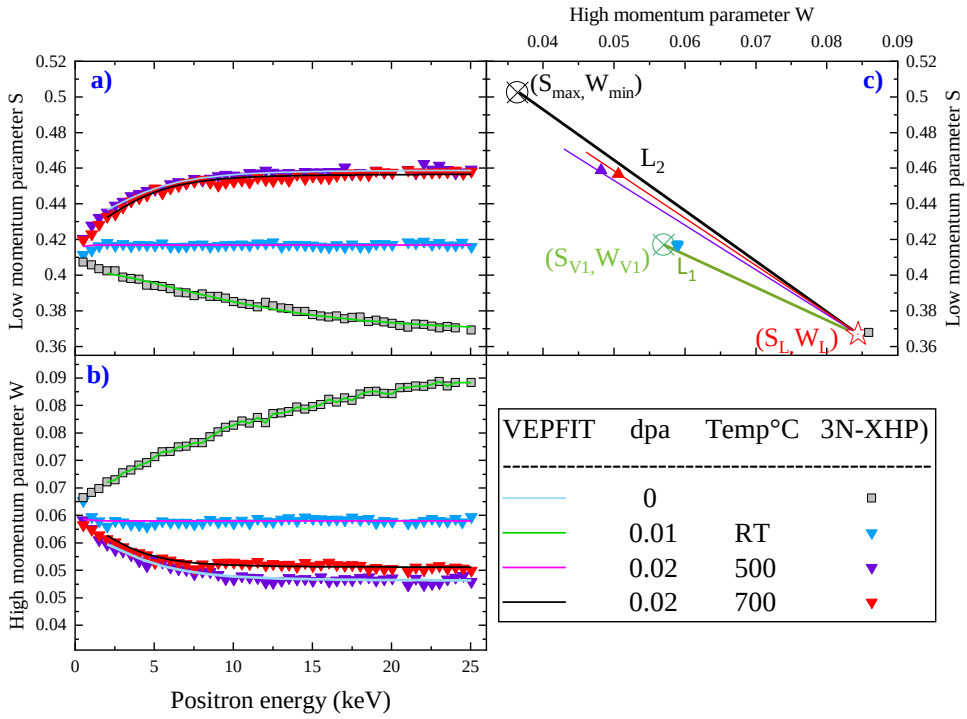

*Figure 92 : **a, b)** Annihilation characteristics **S, W** as a function of the positron energy E and **c), S** versus **W** plot in 3N-HP W samples (solid symbols), before irradiations ■ (3N), after irradiation at **RT** , **0.02 dpa** ▼(blue), **500 °C** , **0.02 dpa** ▼ (purple), and **700 °C** , **0.02 dpa** ▼ (red)*

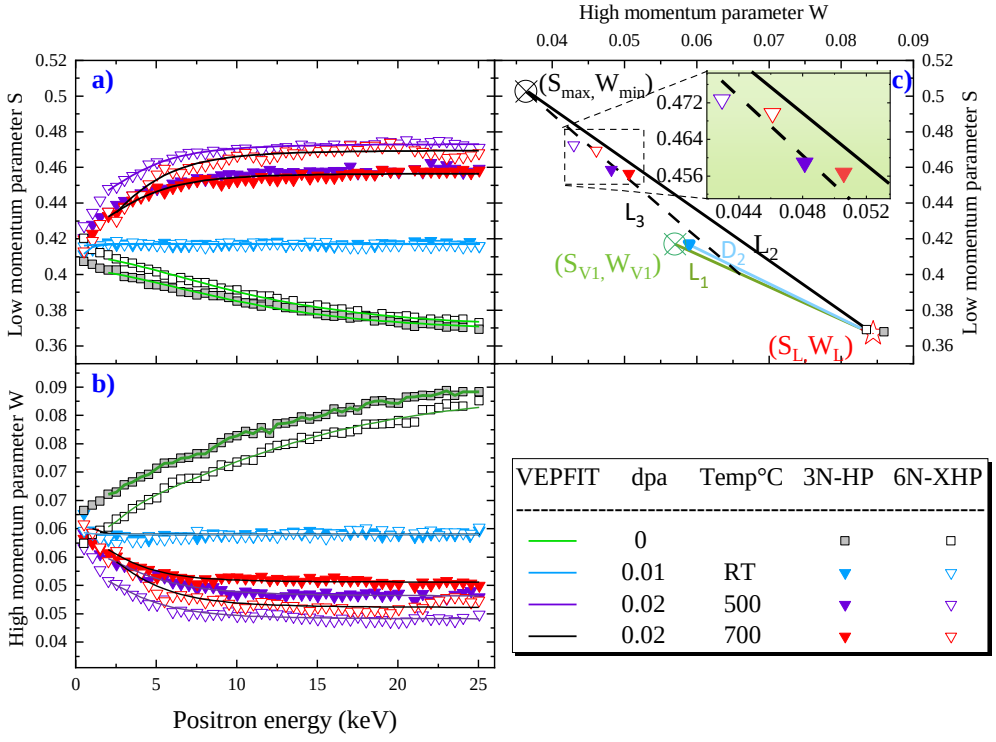

*Figure 93: **a, b)** Annihilation characteristics **S, W** as a function of the positron energy E and **c)** the fit extracted values S as a function of the high momentum annihilation fraction W ones in 3N-HP W samples (solid symbols) and 6N-XHP samples (open symbols), before irradiations ■(3N) □(6N) after irradiation at **room temperature** **0.01 dpa** (downward triangle ▼(3N) ▽(6N)), at high temperatures (upward triangle ▲(3N) △(6N), plotted in purple for irradiation performed at **0.02 dpa, 500 °C**, and in red for **0.02 dpa 700 °C**).*

b) *Effect of the sample purity*

To verify the effect of the sample purity, several 6N-XHP (99.9999 wt.%, Plansee (FZJ1)) samples were also irradiated together with the 3N-HP samples using the following conditions: at 0.02 dpa and both temperatures 500 and 700 °C, and at 0.04 and 500 °C. The SPB-DB results for 6N-XHP samples are represented in Figure 93 in comparison to the 3N-HP ones for irradiations at 0.02 dpa and both temperatures 500 and 700 °C.

As for the 3N-HP samples, the ***S(E)*** and ***W(E)*** curves form plateaus for the highest positron energy range (>12 keV) in the 6N-XHP samples. A single-layer model allows to fit the ***S(E)*** and ***W(E)*** curves by operating the VEPFIT program. The fitted value of the ***S*** versus ***W*** is plotted in Figure 93.c, and the annihilation characteristics extracted in the first 700 nm under the surface are reported in the Table 23 The damage depth distribution is homogeneous in the region probed by slow positrons. As for the 3N-HP samples these irradiation conditions induced vacancy clusters in the damaged region and irradiation at higher temperature (700 °C) leads to slightly larger vacancy defects than for 500 °C.

Sample	Purity (wt.%)	Tempe °C	Damage level (dpa)	S_{surf}	W_{surf}	S	W	R	L_{eff}^{+} (nm)
G-13	99.95		0	0.413 (3)	0.0608 (3)	0.367 (3)	0.0842 (3)		123 (3)
J1-29	99.9999			0.403 (4)	0.0659 (4)	0.367 (3)	0.0861 (3)		100 (3)
G-04	99.95	RT	0.012	0.414 (10)	0.060 (5)	0.417 (1)	0.0590 (6)	1.97 (12)	0.6 (2)
J1-05	99.9999			0.399 (10)	0.070 (5)	0.417 (1)	0.0590 (9)	1.97 (12)	0.4 (2)
G-08	99.95	RT	0.318	0.416 (4)	0.059 (2)	0.434 (1)	0.0528 (3)	2.12 (8)	1.4 (5)
J1-10	99.9999			0.420 (11)	0.058 (1)	0.437 (2)	0.0516 (2)	2.13 (9)	2.0 (7)
G-05	99.95	500 °C	0.02	0.424 (5)	0.058 (1)	0.459 (2)	0.0482 (2)	2.54 (9)	17 (1)
J1-15	99.9999			0.426 (6)	0.057 (1)	0.473 (2)	0.0430 (2)	2.56 (9)	17 (2)
G-01	99.95	500 °C	0.04	0.430 (9)	0.055 (1)	0.468 (2)	0.0451 (2)	2.57 (9)	3.1 (5)
J-01	99.9999			0.439 (7)	0.052 (1)	0.479 (2)	0.0418 (2)	2.63 (8)	4.7 (6)
G-02	99.95	700 °C	0.02	0.418 (5)	0.059 (1)	0.456 (2)	0.0506 (2)	2.63 (10)	14 (2)
J-03	99.9999			0.411 (5)	0.061 (1)	0.469 (2)	0.0463 (2)	2.68 (9)	12.8 (8)

*Table 23: Annihilation characteristics S,W of the fitted layer by VEPFIT for self-ion irradiated samples of two purities **6N-XHP (99.9999 wt.%)** and **3N-HP (99.95 wt.%)** at **RT**, **500 °C**, and **700 °C** with different damage levels (**0.012, 0.02 and 0.318 dpa**) in contrast to pristine samples.*

The most interesting result in this comparison is the obvious difference in ***S*** and ***W*** values obtained for samples of different purity. Clearly higher ***S*** values and lower ***W*** values are obtained for the 6N-XHP samples compared to the 3N-HP ones for both irradiation temperatures 500 and 700 °C. The ratio R is also slightly higher for the 6N-XHP samples compared to the 3N-HP ones, while the effective diffusion length L_{eff}^{+} remains short of about 13-17 nm for both purities. It suggests that larger vacancy clusters are detected in the purest samples (6N-XHP) than in the 3N-HP ones. It is also interesting to notice that no difference was observed when irradiations were performed at RT. The same ***S*** and ***W*** values and depth distribution were found for both purities (see Chap IV.2.2.1).This difference is also observed when irradiation is performed at 500°C for higher damage dose (0.04 dpa) as shown in Figure 94. Larger vacancy defects are detected for the purest material 6N-XHP, compared to 3N-HP.

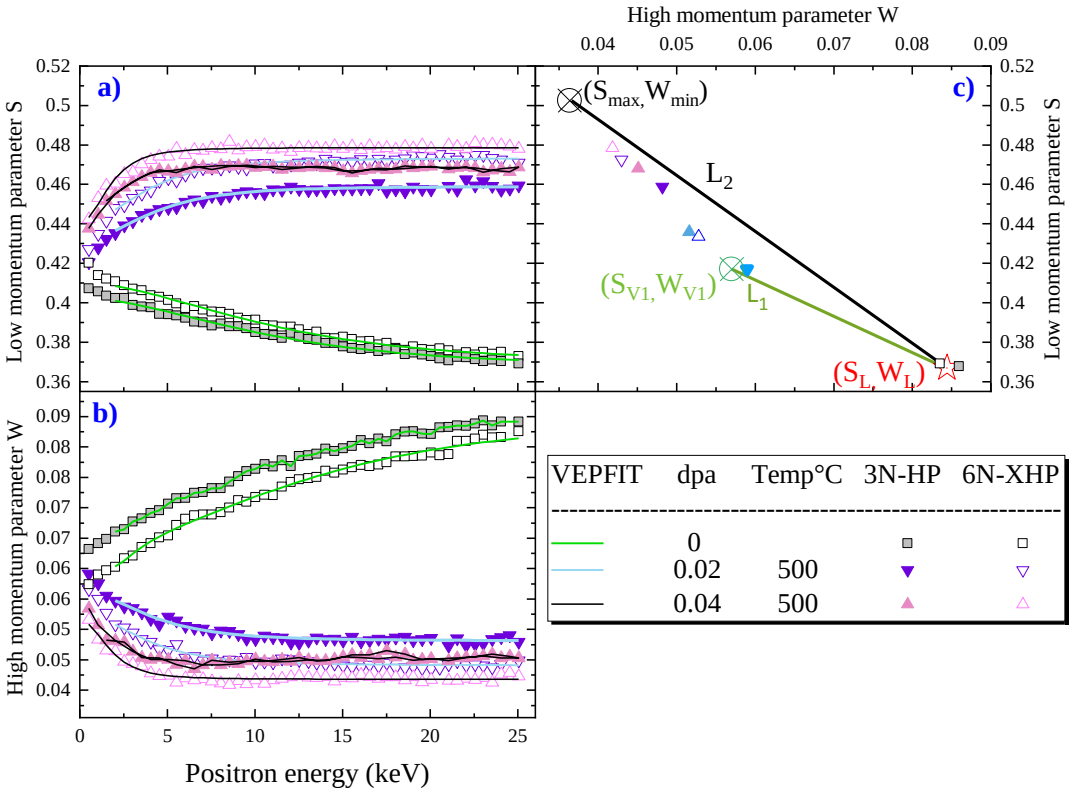

*Figure 94: **a, b)** Annihilation characteristics **S, W** as a function of the positron energy E and **c), S** versus **W** plot in 3N-HP6N-XHP W samples (solid symbols) and 6N-XHP samples (open symbols), before irradiations ■(3N) □(6N) after irradiation at **500 °C**, **0.02 dpa** (purple downward triangle ▼(3N) ▽(6N)), and **0.04 dpa** (magenta upward triangle ▲(3N) △(6N)).*

Furthermore, to verify that the annihilation characteristics differs with purity, other 6N-XHP samples (500 °C, 0.02 dpa) were irradiated in a second series. The SPB-DB result for the new irradiated samples were plotted in Figure 95. The sample ***J11*** (orange upward open triangle) exhibits the same ***S(E)*** and ***W(E)*** curves as those measured for the first 500 °C irradiation series (sample ***J15*** -purple upward open triangle in Figure 95), giving similar values of ***S***, ***W*** and L_{eff}^{+}. Nevertheless, it is interesting to notice that another 6N-XHP sample ***J16*** irradiated in the second series, shows different annihilation characteristics (-pink upward open triangle in Figure 95). First for the lowest positron energy range (<12 keV approximately), the parameter ***S*** (resp. ***W***) is quite lower (resp. greater) than the one obtained in all other samples. Then ***S*** (resp. ***W***) increases (resp. decreases) while remaining lower (resp. higher) than the values measured in the 3N-HP sample ***G05***. At positron energy of 12 keV, a second increase (decrease respectively) step is observed which goes on up to 20 keV where the ***S(E)*** and ***W(E)*** curves overlap with those of the ***G05***. Therefore, a model with two layers has to be used to fit the ***S(E)*** and ***W(E)*** curves of ***J16*** and describe the distribution of the defects in this sample.

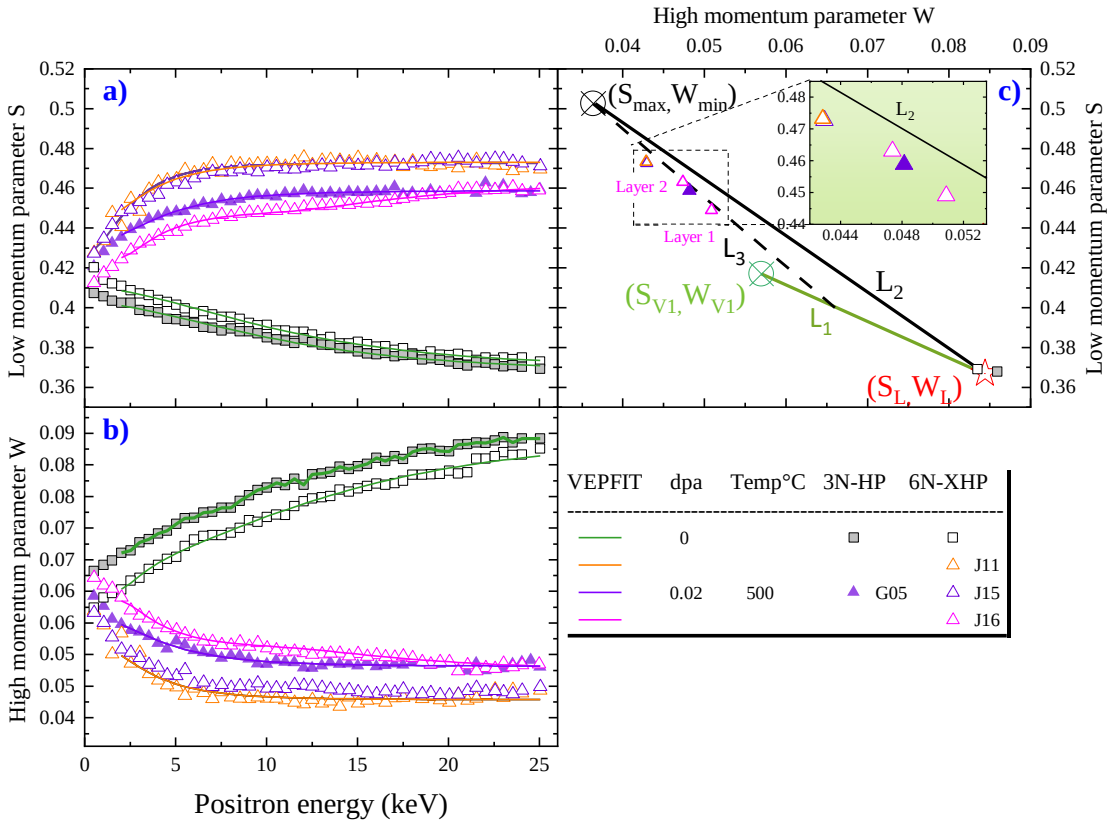

*Figure 95 : **a, b)** Annihilation characteristics **S, W** as a function of the positron energy E and **c)**: the fit extracted values S as a function of the high momentum annihilation fraction W ones in 3N-HP W samples (solid symbols) and 6N-XHP samples (open symbols), before irradiations (3N) (6N) after irradiation at high temperatures (upward triangle (3N) (6N), plotted in purple for irradiation performed at **0.02 dpa, 500 °C***

The fitted annihilation characteristics for the 6N-XHP ***J11*** and ***J15*** samples irradiated in the second series are reported in Table 24 in comparison with the results of the samples 3N-HP sample ***G05*** and 6N-XHP samples ***J15*** irradiated in the first series. Compared to fitting results of other samples, ***J16*** contains an additional first layer of about 200 nm thick with lower ***S*** and higher ***W*** than all other values obtained. The ***S*** and ***W*** values extracted in the second layer are close to the data obtained in ***G-05***. It confirms that the distribution of annihilation states is different in the 6N-XHP sample, ***J16*** than the ones obtained for the others 6N-XHP samples. Much smaller vacancy clusters are detected in this special ***J16*** sample than in the others of the same 6N-XHP batch.

	Purity (wt.%)	***Temp °C***	***Damage level (dpa)***	S_{surf}	W_{surf}	S_{lay1}	W_{lay1}	L_{eff}^{+} ***(nm)***	***Layer (nm)***	S_{lay2}	W_{lay2}	L_{eff}^{+} ***(nm)***
G-05	99.95			0.424(5)	0.058(1)	0.459(2)	0.0482(2)	17(1)				
J1-15				0.426(6)	0.057(1)	0.473(2)	0.0430(2)	17(2)				
J1-11	99.9999	500	0.02	0.437(6)	0.053(1)	0.473(1)	0.043(1)	14(2)				
J2-16				0.414(5)	0.062(1)	0.449(5)	0.051(1)	13(1)	200	0.463 (5)	0.047 (1)	13 (1)

*Table 24 : The annihilation characteristics S,W of the fitted layer by VEPFIT for self-ion irradiated samples of two purities **6N-XHP (99.9999 wt.%)** and **3N (99.95 wt.%)** at **500 °C** with a damage levels of **0.02 dpa***

In summary, for irradiations performed at low damage dose (0.02 dpa) and high temperature (500 and 700 °C), the ***SW*** points are well above the single vacancy line L_1, clearly indicating that large vacancy clusters were formed. Furthermore, it was found that the ***S,W*** points for the irradiation performed at 500 and 700 °C are very close, although, for the 700 °C irradiation, the data are closer to the L_2 line suggesting the detection of largest vacancy clusters. However, it is difficult to distinguish them from those get at 500 °C, considering the measurement discrepancy for these samples. Finally, and more remarkably, at the same irradiation temperature and damage dose, the ***S,W*** points measured for the purest sample (6N-XHP) are the furthest away from the annihilation characteristics of the single vacancy, indicating that the fraction of positrons annihilated at vacancy clusters is greater in the 6N-XHP than in the 3N-HP sample. A straight line can be plotted to go through the fitted ***S,W*** points in the samples irradiated at the same damage level (0.02 dpa) for 500 °C and 700 °C, which will be denoted L_3 (see Figure 95.c). When extending this line toward larger ***S*** and lower ***W***, it joins the S_{VN}, W_{VN} point corresponding to annihilation at the largest vacancy clusters detected in tungsten (20-30 vacancies clusters). When L_3 is extended to another extremity i.e. the lower ***S*** and larger ***W***. the line does not coincide with the ***Lattice*** point but it intersects at two-thirds of the line L_1, which links the single vacancy point with the ***Lattice*** one. As shown in Table 23, the estimated effective diffusion length L_{eff}^{+} of positrons in the damaged region is quite short (<17 nm) for all irradiation conditions and tungsten purities.

$$K_D = \lambda_L \left[\left(\frac{L^+}{L_{eff}^+} \right)^2 - 1 \right] \qquad \textit{eq. 58}$$

From *eq. 58*, we can deduce a high trapping rate K of positrons of about 1 x 10^{12} s^{-1} for the mean value of the estimated effective diffusion length L_{eff}^{+} of 13 nm. It follows that the fraction of positrons annihilated in the delocalized state, i.e. the perfect lattice, is negligible (< 1 %). Moreover, the ***SW*** points of irradiated samples are located below the annihilation characteristics of the largest vacancy clusters V_N containing 20 - 30 vacancies or with a diameter equal to or greater than 1 nm. This indicates **i/** that positrons detected either mainly vacancy clusters with a diameter smaller than that of V_N –i.e. 1 nm- or **ii/** that positrons are trapped and annihilate at different vacancy defects, i.e. the vacancy clusters V_N and defects for which the annihilation characteristics ***S-W*** are not yet known but which should be located on the L_3 line. We will denote this defect D_x in the following discussion. Consequently, in the first case, the trapping rate is equal to K_{Vn} which means the trapping rate at V_n vacancy clusters (which are smaller than V_N ones). In the second case, K is the sum of two trapping rates, $K_{VN,}$ for trapping at V_N, and K_{DX} for trapping at D_X.

It has to be noticed that for the ***J16*** sample both ***S-W*** points (for the first and second layers) are still located on the L_3 and that the one for the first layer is closer to the L_1 line. It suggests that the number

of vacancies in vacancy clusters is lower, so that more Dx could trap positrons in the ***J16*** than in the ***J11*** and ***J15*** and specially in the first layer. We will discuss about the vacancy clusters formation and the existence of D_x defect and its possible origin in the last paragraph (see the Chap IV.1.5)

IV.2.3.2. TEM observations in 1.2 MeV self-irradiated samples

To complement SPB-DB characterization on the vacancy-type defects, several 3N-HP and 6N-XHP thin foils (~60nm) were in-situ irradiated with 1.2 MeV-W ions with a comparable damage dose as the 20 MeV irradiations at 500 and 700 °C. The TEM observations of the foils were performed using two instruments. A JEOL ARM200F field emission gun microscope operating at 200 kV and equipped with double spherical aberration correctors was used for the irradiation at 500 °C. The thin lamellae irradiated at 700 °C were observed with a Philips CM20 also operating at 200 kV. It should be noted that the size of the vacancy-type defects varies with instrumental parameters, and might also differs from one device to another. Therefore, the comparison was only accomplished for the images acquired under the identical conditions (acceleration voltage, magnification…) from the same device.

The Fresnel contrast method (see Chap II.3.4.2) was used to identify the cavities. Figure 96 shows the typical over-focused images (+300 nm) of the 3N-HP and 6N-XHP tungsten lamellae damaged by 1.2 MeV self-ion to ~0.02 dpa at 500 °C. For the samples irradiated at 700 °C, the over- and under-focused images were recorded in several adjacent zones in the same grain. Figure 96.c-h exhibits the cavities which were counted in 4 TEM-shots (Figure 96. c-f) for 3N-HP and 2 TEM-shots (Figure 96.g-h) for 6N-XHP to obtain a reliable statistical analysis. For the 3N-HP lamella irradiated at 500 °C, because of a low contrast quality, an area (red mask) on the left side of image shown in Figure 96.a in which the cavities are difficult to be identified, so that, this part was removed for calculating the volumetric density. The apparent size distribution of the cavities, i.e. the number of the cavities versus the apparent diameter, was plotted and overlapped on the corresponding TEM-shot in Figure 96. For the 3N-HP lamella, irradiated at 500 °C and 700 °C, respectively, 491 and 479 cavities were identified, and 1015 (500 °C) and 346 (700 °C) cavities for the 6N-XHP one. Table 25 summarizes the average value of the apparent diameters of the identified cavities, obtained by a Gaussian fitting of the size distribution (dash line).The centroid of the Gaussian distribution was considered as the average value of the apparent diameter of the cavities. The density of the identified cavities in 3N-HP and 6N-XHP for both irradiation temperatures was also determined, for which the volume of the probed region was roughly calculated by multiplying the effective analyzed surface by the measured or estimated thickness. The corresponding errors on the diameter and density were estimated by using eq. 45 and eq. 46 in Chap II.3.4.2. For the irradiation at 500 °C, the density of the cavities was comparable for both purities of about $1.6 \pm 0.5 \times 10^{24}$ m^{-3}. The density is still close for both purities when the irradiation temperature increased to 700 °C, whereas decreased by approximately a factor of two ($0.65 \pm 0.5 \times 10^{24}$ m^{-3}) comparing to the case of 500 °C. Regarding the diameter, a mean apparent size of about 0.97 nm was determined for the 3N-HP

lamella for both irradiation temperatures, which was slightly smaller than that of the 6N-XHP one (1.13 - 1.22 nm for 500 °C and 700 °C, respectively).

Furthermore, a greater fraction of cavities with a diameter above 1 nm was identified in the 6N-XHP lamellae (82 % for 500 °C and 87 % for 700 °C), in contrast to 22 % and 36 % for the 3N-HP ones at 500 and 700 °C, respectively. Figure 97.a-b shows the distribution of the cavities i.e. the number of identified cavities versus apparent diameter of the lamella irradiated to ~0.02 dpa at 500 (Figure 97.a) and 700 °C (Figure 97.b). It is clear that for both irradiation temperatures, the cavities were identified in 6N-XHP lamellas having larger apparent size. Besides, assuming that the cavities formed a spherical shape, the local swelling due to cavities was roughly estimated by dividing the volume of the identified cavities by the total analyzed volume, which is approximately of about 0.1 % in 6N-XHP lamella irradiated at 500 °C and 0.04 % in 3N-HP one irradiated at 700 °C, with a larger local swelling in 6N-XHP lamellae for both temperatures.

Damage level (dpa)	*0.02*			
Observation conditions	JEOL ARM200, 200 kV, 500 kX,		Philips CM20, 200 kV, 500 kX	
Irradiation Temperature (°C)	500		700	
Purity	3N-HP	6N-XHP	3N-HP	6N-XHP
Thickness (nm)	55 ± 20 (EFTEM)	90 ± 30 (EFTEM)	35 ± 20 (evaluated)	60 ± 50 (evaluated)
Mean diameter(nm)	0.97 ± 0.19	1.13 ± 0.21	0.97 ± 0.25	1.22 ± 0.25
Density (10^{24} m^{-3})	1.73 ± 0.71	1.56 ± 0.52	0.70 ± 0.42	0.60 ± 0.53
Swelling %	0.09 ± 0.02	0.12 ± 0.04	0.04 ± 0.02	0.08 ± 0.05

Table 25: Mean diameters of cavities observed by TEM and their density in irradiated 3N-HP and 6N-XHP samples and the measured or evaluated thickness

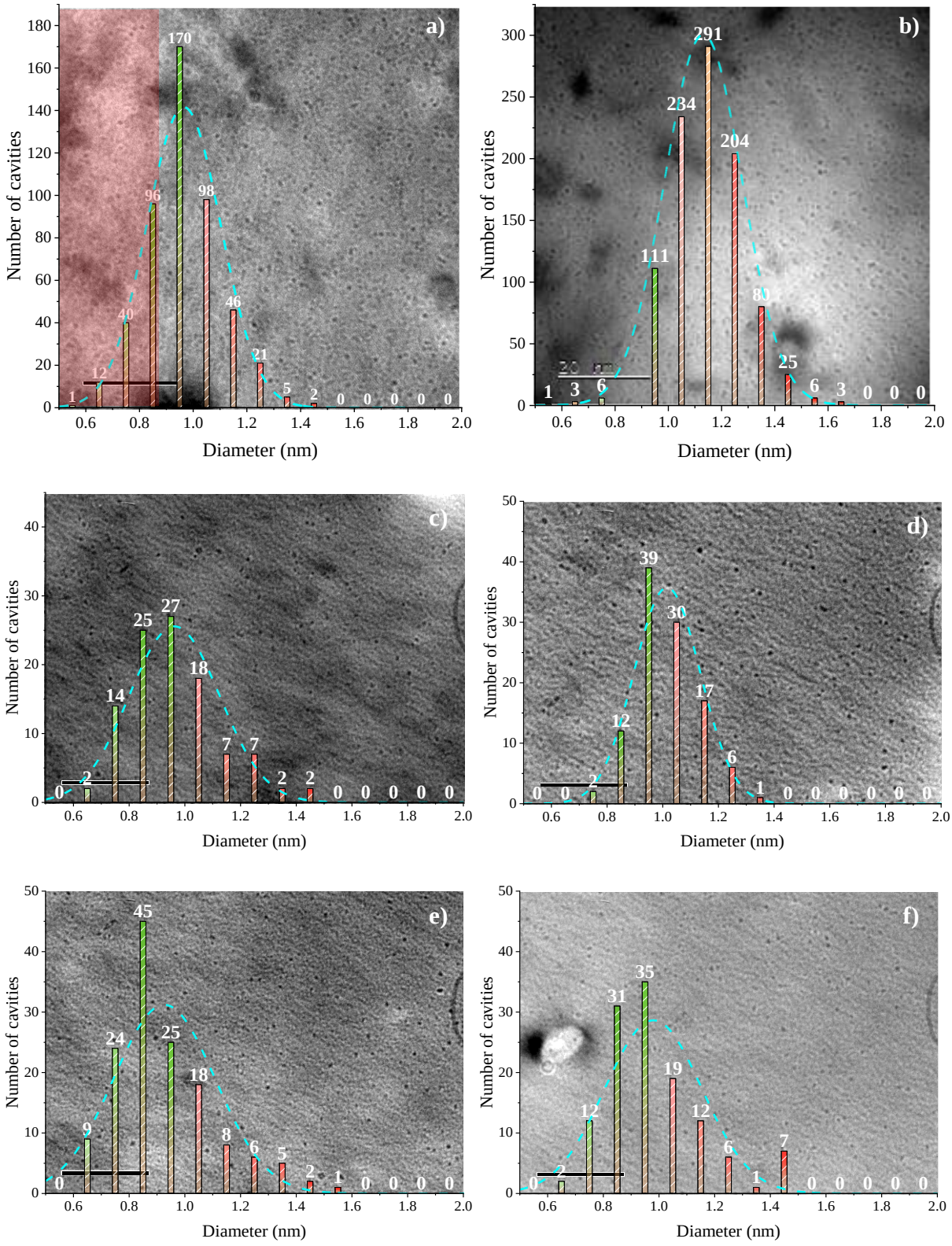
a)
Number of cavities
Diameter (nm)
1 12 40 96 170 98 46 21 5 2 0 0 0 0 0
b)
Number of cavities
Diameter (nm)
1 3 6 111 234 291 204 80 25 6 3 0 0 0
c)
Number of cavities
Diameter (nm)
0 2 14 25 27 18 7 7 2 2 0 0 0 0 0
d)
Number of cavities
Diameter (nm)
0 0 2 12 39 30 17 6 1 0 0 0 0 0 0
e)
Number of cavities
Diameter (nm)
0 9 24 45 25 18 8 6 5 2 1 0 0 0 0
f)
Number of cavities
Diameter (nm)
0 2 12 31 35 19 12 6 7 1 0 0 0 0 0

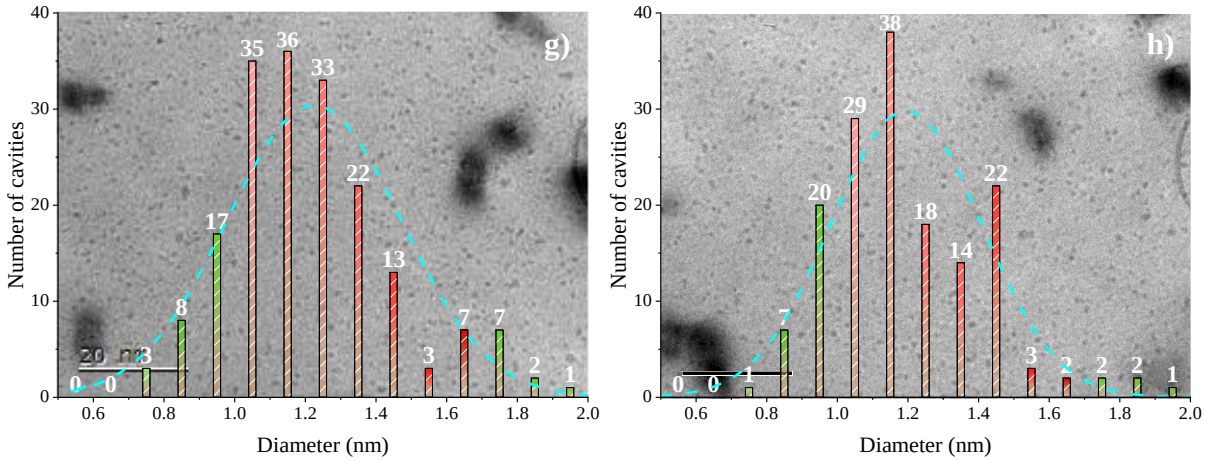

*Figure 96: Over focused (+300 nm) images **a)** 3N-HP sample and **b)** 6N-XHP sample irradiated at 500 °C (0.02 dpa) observed by a JEOL ARM200F cold field emission gun microscope and Over-focus (+300 nm) image **c-f)** 3N-HP sample and **g-h)** 6N-XHP sample irradiated at 700 °C (0.02 dpa) observed by a Philips CM20 microscope. The size distributions of cavities are superimposed on their respective images and were fitted by a Gaussian function (cyan dashed line).*

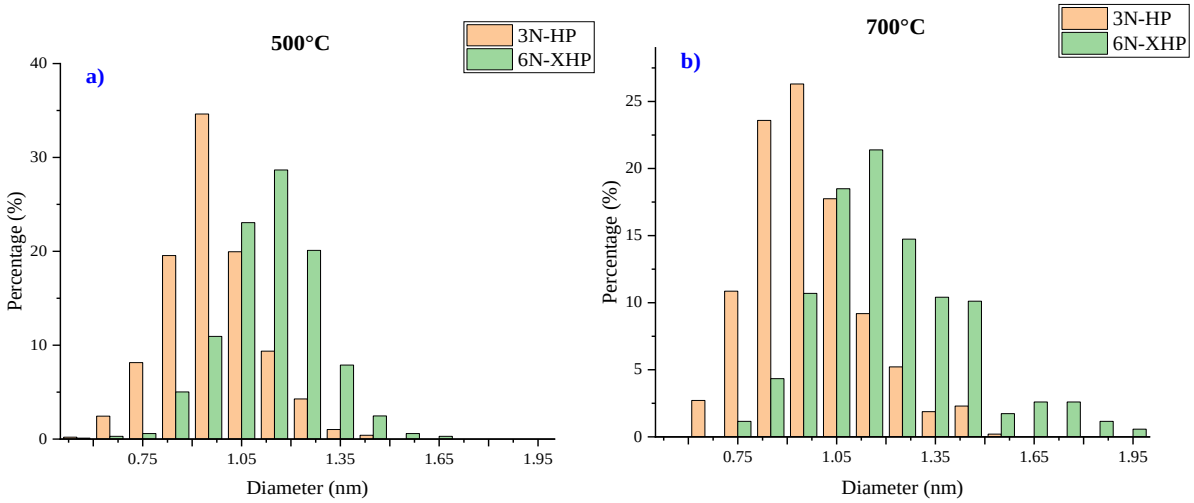

*Figure 97: Histogram of the apparent size of cavities in 3N-HP and 6N-XHP tungsten lamellas irradiated at a) **500 °C** and b) **700 °C** to **~0.02 dpa.***

IV.2.3.3. SIMS measurements

On the one hand, both SPB-DB and TEM identified larger cavities (or vacancy clusters) in 6N-XHP than in 3N-HP samples at 500 and 700 °C, for 0.02 dpa, as well for the 500 °C, 0.04 dpa only for SPB-DB. On the other hand, according to the literatures presented in Chap.I.3.4, both carbon and oxygen were identified to be able to create complexes with point defects such as vacancies. In the following, SIMS is used to measure the depth profile of these two light elements in various self-irradiated samples.

Figure 98 shows the SIMS analysis of carbon (C) and oxygen (O) in the tungsten slabs with different purities 3N-HP (orange) and 6N-XHP (green) after self-ion irradiation to 20 MeV at 500 °C with two damage doses (0.02 (a-b) and 0.04 dpa (c-d)). Each samples were analyzed in three random positions, denoted crater 1 to 3. The depth profiles corresponding to each of the craters are plotted using different types of line. The depth of each crater is measured three times by using a contact profilometer

(DEKTAK in GEMAC). The details of these measurements were summarized in Appendix A. The mean value of these depths is used to calibrate in depth the SIMS signal for each crater. Most of the craters have a mean depth of at least 2000 nm.

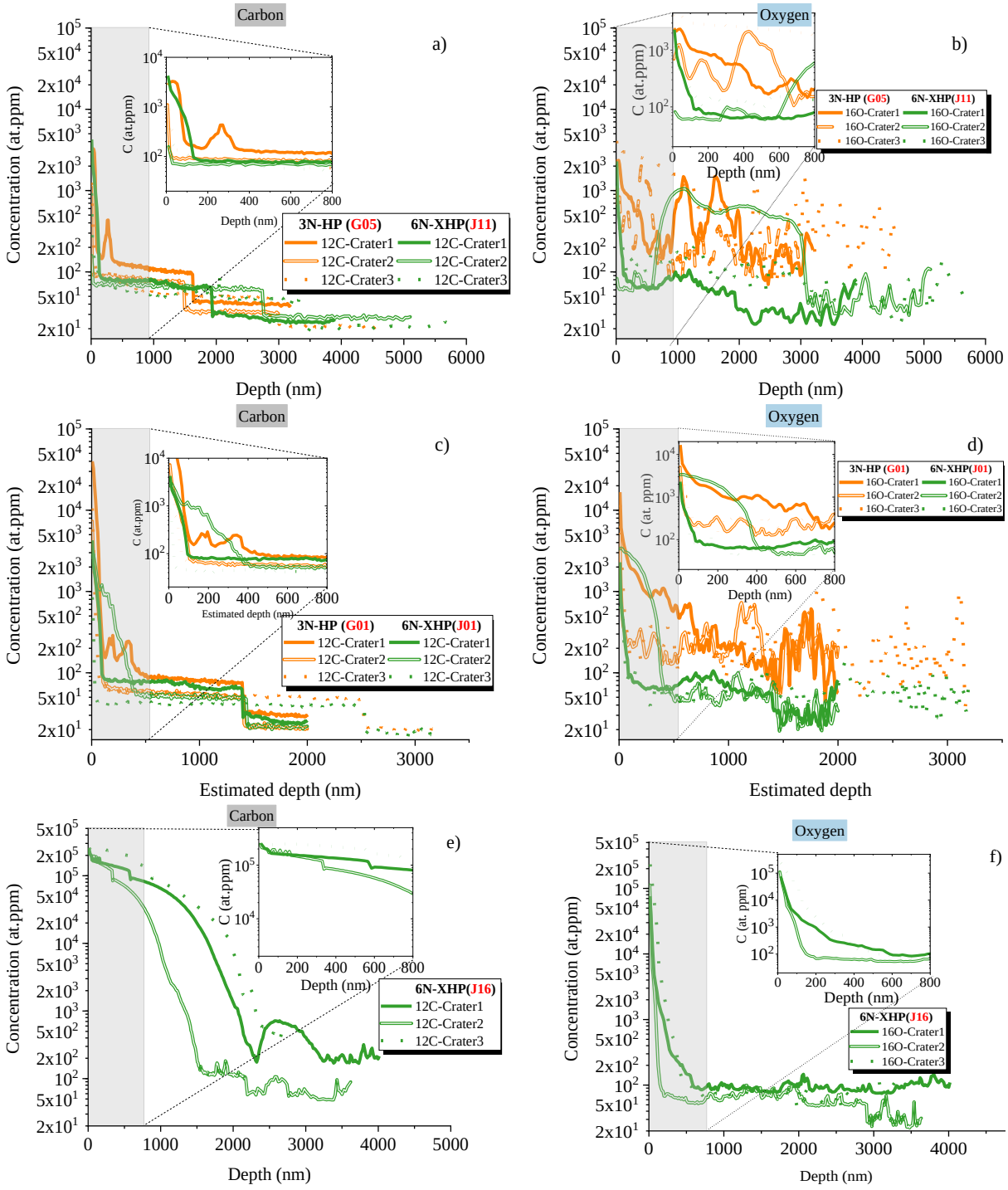

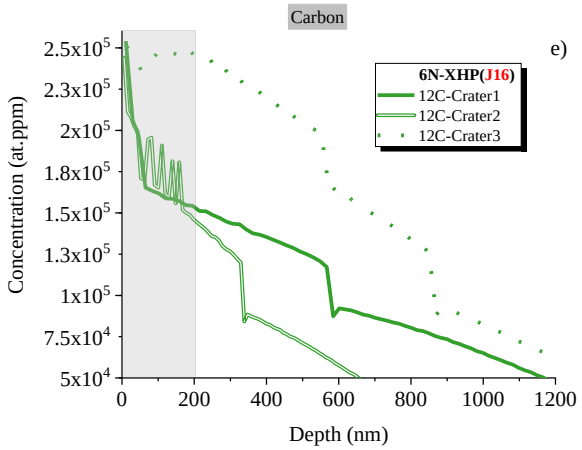

*Figure 98 : Carbon and oxygen depth profiles for two purities (6N, green and 3N, orange) self-ion irradiated samples with a damage dose of **0.02 dpa at 500°C, (a-b, e-f)**, **0.04 dpa at 500°C (c-d)** measured using SIMS at three random positions (crater 1 to 3) and plotted with different types of line. In the graph **g)** the C depth profiles measured in **J16** are plotted in linear scale and in the depth range from surface to 1200 nm.*

Overall, the carbon profiles decrease from a quite high value at the surface probably due to the presence of dust on the surface, then exhibit a smooth plateau for most case. After the reduction of the analysis area (seeing the case in Figure 77), the C concentration is reduced to a lower plateau, suggesting the analysis reached the detection limit (DL). The O profiles first decline slowly for few ones, and it is interesting to notice that instead of reaching a plateau, they fluctuate in a certain range of concentration that depend on the sample. To correlate the SIMS analysis to SPB-DB experiment, the mean value of the C and O concentration is extracted from the depth profiles in the depth range from 100 to 800 nm. These mean values and the minimum and maximum ones were reported in Table 26. The first 100 nm was discarded for avoiding the influence of the C and O dust on the sample surface.

For the samples irradiated at 0.02 dpa and 500 °C, a greater concentration of C and O was found in ***3N-HP*** sample ***G05*** than in the ***6N-XHP*** sample ***J11***. In particular, in the case of O, the concentration in the region from 100 to 800 nm of the three craters varied from a minimum value of about 105 to a maximum one of about 3000 at. ppm, leading to a mean value of 1200 at. ppm in ***G05*** against a mean concentration of 114 at. ppm, (between 58 and 576 at. ppm) in ***J11.*** The C concentration has a slightly higher mean value in ***G05*** of about 106 at. ppm (56-434 at. ppm) than in ***J11*** at around 70 at. ppm (from 52 to 85 at. ppm). In addition, an extreme high quantity of carbon was surprisingly found in ***J16***, with a mean value of about 1.3×10^5 at. ppm, which is equivalent to 13 atomic percent of carbon. If we discard the first 50 nm close to the surface, the C concentration is still enormous in the first 600 nm, then it decreases when secondary ions collected from depths of the sample, first slowly and then more quickly up to about 1000 or 2000 nm depending on the crater. Moreover, the oxygen depth profiles show also a high concentration of oxygen in the first 100 to 200 nm depending on the crater. If we discard the first 50 nm close to the surface the O concentration decreases from about 3000 or 50000 at. ppm to about 100 at. ppm plateau value reached at about 200 or 600 nm depth depending on the crater. Thus, it

suggests that the presence of the carbon and/or oxygen could be at the origin of the difference in the annihilation characteristics obtained between ***J11*** and ***J16***: that will be discussed in details later.

Sample	*Irradiation conditions*	*Depth (nm)*	*Mean concentration (min: max) (at. ppm)*	
			Carbon	**Oxygen**
G05 (HP -99.95% Goodfellow)	0.02 dpa W^+ 500 °C	100-800	106 [56 : 434]	1200 [105 : 3000]
J11 (XHP -99.9999% Plansee M192 FZJ)			70 [52 : 85]	114 [58 : 576]
J16 (XHP -99.9999% Plansee M192 FZJ)		100-350	(1.7 [0.8 : 2.5]) × 10^5	3400 [64 : 57200]
		100-800	(1.3 [0.3 : 2.5] × 10^5	546 [53 : 20400]
G01 (HP -99.95% Goodfellow)	0.04 dpa W^+ 500 °C		75 [53 : 406]	432 [114 : 1926]
J01 (XHP -99.9999% Plansee M192 FZJ)			61 [38 : 90]	67 [38 : 114]

*Table 26 : M**ean concentration** and extreme values (**[minimum : maximum]** given in this order in brackets) of carbon and oxygen in self-irradiated (0.02 and 0.04 dpa at 500°C) 3N-HP (99.95 wt.% Goodfellow) and 6N-XHP (99.9999 wt.% from Plansee M192 set material supplied by FZJ) samples.*

Concerning the samples irradiated at 0.04 dpa and 500 °C, the difference of concentration between O and C is less pronounced than in the case of the lowest damage dose (0.02 dpa). The mean value of the three craters is five times greater for oxygen than for carbon ([O] = 432 at. ppm and [C]=75 at. ppm) for the 3N-GP sample. On the one hand, as shown in Figure 98.d the O concentration in the bulk of the ***G01*** is obviously greater than in the 6N-XHP ***J01*** sample. the profiles of crater 2 of ***J01*** differ from the crater 1 and 3, after checking into details, the C and O profiles of crater 2 in ***J01*** exhibit a similar tendency, a monotonous decrease from ~3000 at. ppm at 0 nm depth until the plateau at about 400 nm (dashed line in insert graph of Figure 98.c-d). This special feature differs completely with other craters of ***J01***, it might to be that the primary ions (Cs^+) bombarded firstly on some particles of carbon-oxide dust before attaining the sample. Hence, if we reject the analysis of crater 2, a quite low value is measured for the averaged C and O concentration ([C]=61 at. ppm, [O]=67 at. ppm).

If we put aside the specific case of the sample ***J16*** which was contaminated at the surface, it is possible to extract the following major trends. It is easy to define an average value in the case of the carbon for the 6N-XHP ***J01*** and ***J11*** samples, because the depth profiles measured in the three (or two for ***J11***, see discussion abovementioned) craters of these both samples are mainly homogeneous and reproducible. It can be also noticed that the concentrations are very close in both samples. So we can conclude that the average concentration can be considered as representative of the concentration in the volume probed by slow positron (approximately 3 mm in diameter and 700 nm in depth). So, we propose that the average concentration for carbon is about 65 at. ppm (see Table 27), a value close to the detection limit of the SIMS technique for this element. However, it is more complicated for oxygen: the depth

profiles show heterogeneous distribution. The oxygen concentration remains low in general of about 100 at. ppm in 6N-XHP samples (excepted the special case of ***J16***).

X	**at. ppm**				
	3N-HP			6N-XHP	
			Average value		Average value
H	910 [a]			Ud	
C	460 [a]	106 [56 : 434] [b] ***G-05*** 75 [53 : 406] [b] ***G-01***	~ 90	70 [52 : 85] [b] ***J11*** 61 [38 : 90] [b] ***J01***	~ < 65
N	130 [a]			Ud	
O	345 [a]	1200 [105 : 3000] [b] ***G-05*** 432 [114 : 1926] [b] ***G-01***	No min 100/max 3000	114 [58 : 576] [b] ***J11*** 67 [38 : 114] [b] ***J01***	~ 100

[a] provided concentration by supplier corresponding to detection limits, [b] measured values by SIMS

*Table 27: Maximum values of H, C, N and O concentrations as given by the supplier (Goodfelow) for the 3N-HP material. No data for the 6N-XHP ((Ud: undetectable by LA-ICP-MS). The **mean concentration** and extreme values (**[minimum: maximum]** given in this order in brackets) of carbon and oxygen in self-irradiated (0.02 and 0.04 dpa at 500°C) 3N-HP (99.95 wt.% Goodfellow) and 6N-XHP (99.9999 wt.% from Plansee M192 set material supplied by FZJ) samples.*

Besides, the situation is much more complex for the 3N-HP. It is difficult to determine the concentration of carbon and oxygen in these tungsten samples due to the heterogeneous distribution revealed by SIMS measurements. It is less complicated for carbon, the main heterogeneity is observed close to the surface and could be attributed to close surface soiling. So the average concentration of carbon in the 3N-HP samples is estimated at approximately 90 at. ppm. In the case of oxygen, it is not possible to extract an average value, but if we make the integral of the different depth profiles, it is obvious that the concentration of oxygen is largely higher in 3N-HP than in 6N-XHP and relatively low concentrations were detected in 6N-XHP samples (see Table 27)

To summarize, the concentration of carbon and oxygen were measured in the 3N-HP and 6N-XHP self-irradiated tungsten samples. Even if some depth profiles differ from a crater to another and that some of them are heterogeneous, a larger concentration was found in the 3N-HP samples than in the 6N-XHP ones, especially in the case of oxygen. It is also obvious that the concentration of carbon is more heterogeneous in the 3N-HP sample. The concentrations found using SIMS in the 3N-HP samples are in agreement with the detection limit provided by the supplier (Goodfellow) for carbon (Table 27) It is not so clear for oxygen; the minimum value is lower than the detection limit but SIMS highlights also high heterogeneity with high local concentration. The amount of matter which has been analyzed is too low to be able to extrapolate the global concentration and compare it to the supplier's value. It has to be noticed that ***J16*** presents C-enriched layer (~13 at. % at the surface) with a close to constant concentration in the depth range from a few nm to about 1000-2000 nm. This layer is also rich in O and its concentration profile decreases from approximately 200 nm and then from 600 nm to reach a low value close to the detection limit. It has to be noticed that the same C-enriched layer has been observed in other samples prepared in unsatisfactory conditions due to the furnace pollution (see Chap.III.2).

IV.2.3.4. Discussion

Characterization of 20 MeV self-ion irradiated tungsten unveiled several effects on the distribution of the detected defects: the irradiation **temperature** and the **purity** of samples for high temperature irradiations (500, and 700 °C) affect the distribution. These effects are discussed in the following.

a) Irradiation temperature effect on the vacancy size distribution

The SPB-DB measurements revealed the formation of vacancy-type defects in self-ion irradiated tungsten at low damage doses (LD) of 0.01 to 0.02 dpa. Their distribution changes (migration, agglomeration…) when irradiation is performed at high temperatures (500, 700 °C). The ***S*-*W*** characteristics were quasi-identical for the samples (3N-HP and 6N-XHP) irradiated at RT (see downward blue triangles in Figure 99, situated slightly above the line L_1, near the characteristic point (S_{V1}, W_{V1}) of the single vacancy, suggesting the detected RID are mainly single vacancies. For the samples irradiated at high temperatures (500, 700 °C), the ***S*-*W*** characteristics approached the line L_2 corresponding to the annihilation of positrons in the largest clusters which have been detected in tungsten (S_{VN}, W_{VN}), containing more than 20 - 30 vacancies -or with a diameter equal to or greater than about 0.8 nm-, indicating the formation of large vacancy clusters. They have a size even superior to the ones induced by a 16 times higher damage dose at RT. Close annihilation characteristics (purple and red upward triangle in Figure 99) were found for irradiation at 500 and 700 °C showing that positrons detected vacancy clusters with close size, even if the slight difference could be due to the presence of some larger vacancy clusters for 700 °C.

Additionally, TEM observations confirmed that large clusters or cavities with a mean diameter of about 1 nm are formed at these high temperatures depending on the purity of samples. And slightly larger cavities were observed for irradiation at 700 °C. It is however interesting to note that the ***S*-*W*** characteristics measured at high temperature don't reach the (S_{VN}, W_{VN}) point characteristic of such large vacancy clusters. It suggests that positron detect smaller defects. The cavities size distribution extended from about 0.7 nm for 500 °C to 1.8 nm for 700 °C. Even if it is difficult to predict precisely the number of vacancies in a cavity of given size we could rely on the Mason et *al.* [105]: they calculated the formation energy of several configurations of vacancy clusters i.e. Vn with n ranging from 1 to 15. Most vacancy clusters with stable configurations have mainly 2D open volume. It follows that the volume of a cavity with a diameter of 0.7 nm should most probably correspond to a number of vacancies of about 12 to 15. Troev et *al.* [133] showed that the positron lifetime should not be very distinguishable for vacancy clusters of 15 to more than 30 vacancies. Some new results from Yang et al[13] that should be published soon show also that, as expected, ***S*** and ***W*** are also very close for such clusters. It follows that the contribution of the cavities which are observed using TEM to the positron ***S*** and ***W*** values should be

[13] Submitted to Journal of Nuclear Materials

mainly a fraction of the (S_{VN}, W_{VN}) characteristics. Furthermore, we also observed that the ***SW*** points in the samples irradiated at this low damage dose (0.02 dpa) for 500 °C and 700 °C follow a straight line L_3, which joins the (S_{VN}, W_{VN}) point and tends to the two-thirds of the L_1 straight line segment. This indicates that positrons are trapped and annihilate at different vacancy defects, i.e. the vacancy clusters V_N and the D_X defects for which the annihilation characteristics ***S-W*** are not yet known but which should be located on the L_3 line.

The formation of the large cavities was expected. On the one hand, MD simulations [69] showed that in collision cascades of 150 keV-W^+ ions mainly single vacancies (approximately 70 %) are created together with some small clusters (about 28 % with 2 to 5 vacancies in) and a very low fraction of large clusters which depends on the empirical potential which is used. On the other hand, Mason et al. [105] reported DFT calculations of the migration energy E_m for small vacancy clusters. E_m is 1.76 eV for the single vacancy V_1 close to the value of 1.66 eV [81]. Interestingly, it is lower for the V_3 cluster ($E_m(V_3)$ = 1.14 eV). It follows that such small vacancy defects including the single vacancy are mobile at 500 °C. As it has been already shown, the temperature of the irradiations is far above the temperature at which the migration of the single vacancies can be triggered (523 K, for 1 hour annealing duration) [131]. It means that some of the vacancies can interact and agglomerate to form larger clusters where some new vacancies can be bound to make clusters growing with ion fluence (or damage dose). It is what we observed in SPB-DB measurement: the positrons detected larger clusters when the damage dose is increased by a factor of two (at 0.04 dpa). What is not clear is if the size distribution of these defects shift to larger size or if there is a maximum size that can be reached for one temperature and only their fraction increases with the damage dose. It would be interesting to perform TEM observations in samples irradiated with increasing damage doses at the same temperature. Therefore, the migration of the small vacancy defects (V_1 and V_3) should be the most important reason for which the larger vacancy clusters were formed during the HT irradiations. As a consequence, whatever the purity of the samples, for a damage dose below or equals to 0.02 dpa, a significant agglomeration of the vacancies was revealed after irradiation at HT (500, 700 °C).

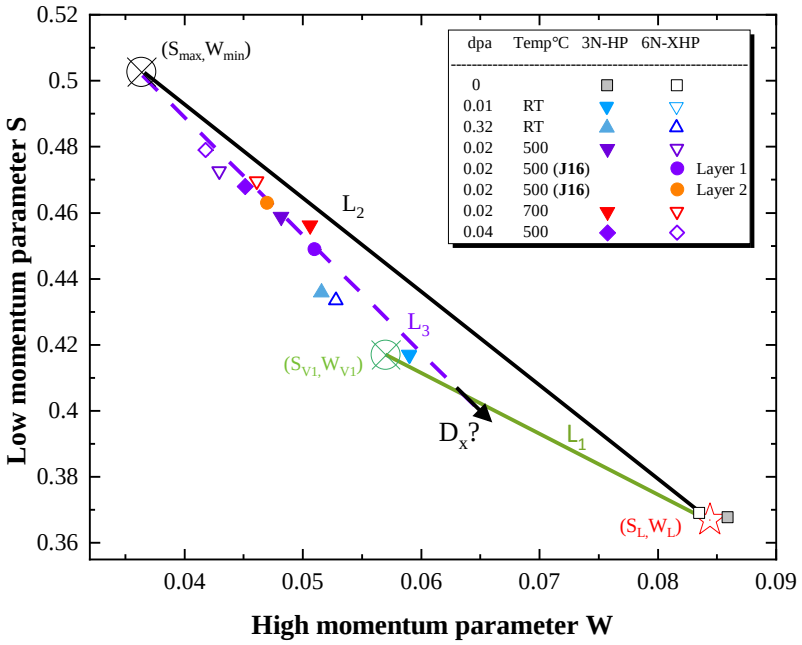

Figure 99 : Fitted annihilation characteristics S versus W for the pristine sample and damaged samples with 0.01 dpa, 0.32 dpa at RT, and 0.02 dpa at 500 and 700 °C with a single-layer model by using VEPFIT program

b) Effect of purity on the size of vacancy clusters

The SPB-DB measurement showed that a large fraction of positron annihilates as trapped at vacancy clusters when irradiation is performed at 500 (0.02 and 0.04 dpa) and 700 °C (0.02 dpa). TEM observations confirmed the presence of cavities for the irradiation at 0.02dpa and HT (500, 700 °C). As we showed above, the formation of the vacancy clusters or cavities is initiated in the collision cascades and their growth is probably a result of the migration of small vacancy clusters (V_1, V_3) and of their agglomeration which becomes favorable at the used irradiation temperatures considering the migration energy of the single vacancy (E_m^{V1} = 1.66 eV [81]). We also see above that the ***S-W*** obtained in samples irradiated at HT (500 and 700 °C) correspond most probably to annihilation of positron in different traps: the vacancy clusters V_N as observed using TEM and a defect D_x. which has annihilation characteristics somewhere along the L_3 line. It can be concluded that the positrons are sensitive to a defect D_x that could not be detected in TEM.

The differences between the SPB-DB results obtained in 3N-HP and 6N-XHP samples can be interpreted by a lower fraction of annihilation in the vacancy clusters V_N in 3N-HP than in 6N-XHP samples. In other words, a larger fraction of the annihilation in D_x was revealed in 3N-HP samples, and the nature of these defects D_x is discussed in the following.

First, since the two techniques SPB-DB and TEM show that the agglomeration of small vacancies was impeded in 3N-HP samples compared to 6N-XHP ones, it is reasonable to pay attention to the LEs (Light Elements) in the samples, such as H, C, N and O considering their properties in tungsten and their strong interactions with vacancy-type defects (see the Chap I.3.4). As shown in Table 28, since the 6N-

XHP was analyzed by LA-ICP-MS by FZJ, the quantity of the LEs could not be detected. However, the SIMS analysis indicated low concentration of C and O in the ***J11*** and ***J01***. An average concentration of about 65 at. ppm close to the detection limit for the carbon and about 100 at. ppm for oxygen was found in the depth probed by slow positrons (~700 nm).

Concerning the concentration of LEs in the 3N-HP sample, the supplier suggested a higher concentration of LEs that ranges between 130 to 910 at. ppm, within in particular 460 at. ppm of carbon and 345 at. ppm of oxygen considered as detection limit i.e. the maximum value. The SIMS concentration for C is about 100 at. ppm, in ***G-05*** and 75 at. ppm in ***G-01*** whereas that of the oxygen is much more heterogeneous and higher varying from 100 to 3000 at. ppm. It follows that the concentration of C and O is higher in the less pure (3N-HP) samples than in the purest ones (6N-XHP).

Furthermore, these LEs have quite low migration energy in tungsten, especially for O (E_m(O) = 0.17 eV [125] and E_m(C) = 1.46 eV [119]) which explains their high mobility under the irradiation conditions performed in present work (500 and 700 °C). Additionally, they can be associated firmly with single vacancies forming the V-LE complexes owing to their high binding energy. Thus, the formation of V-LE complexes could be expected in tungsten when the irradiation temperature is high enough to allow the migration of either LEs or of the single vacancies, which is the case for both from 500 °C. According to the simulation work, the most favorable occupation site for C, N, and O atoms is in the vicinity of a single vacancy, at a distance of about 1.3 Å from the center of the vacancy close to an octahedral site [111,117,121]. The dissociation energies E_{dis} of the complexes were calculated by adding the migration energy of the most mobile species with the binding energy of the complex (see E_{dis} values in Table 28). A relative high value of the dissociation energies was obtained for carbon (3.39 eV), nitrogen (3.21 eV), and oxygen (3.22 eV), in contrast to that of the hydrogen, only 1.4 eV. Consequently, for the cases of one single vacancy decorated with one atom of C, O, and N, the complexes should be stable even at high temperature (500, and 700 °C) whereas the V-H complexes should be dissociated. However, such complexes cannot be detected by TEM because of their size. Nonetheless, the positrons should be sensitive to these defects, because the LE atoms should not be trapped in the center of the vacancies and leave a few open volumes in the crystalline structure where the electron density should be lower than in the ***Lattice***.

We found in Chap IV.2.3.1, that the $\boldsymbol{S_{Dx}}$, $\boldsymbol{W_{Dx}}$ point should be located on the straight line L_3 which joins the $\boldsymbol{S_{VN}}$, $\boldsymbol{W_{VN}}$ point corresponding to annihilation at the largest vacancy clusters detected in tungsten (20-30 vacancies clusters) and which tends to two-thirds of the L_1 line segment -characteristic of annihilation in single vacancy- from the ***Lattice*** point. The annihilation characteristics $\boldsymbol{S_{Dx}}$ and $\boldsymbol{W_{Dx}}$ of these complexes should be different from those of pure single vacancies and manifested by a lower ***S*** and higher ***W*** seeing a higher electronic density as compare to an empty single vacancy. It follows that

the S_{Dx}, W_{Dx} point should be located in the lower part of the L_3 line, below the annihilation point of single vacancy.

X	Concentration (at. ppm)			E_m^X	$E_b^{V_1-X_1}$	$E_{diss}^{V_1-X_1}$
	3N-HP		6N-XHP	(eV)	(eV)	(eV)
H	910 [a]		Ud	0.21 (TIS-TIS) [118]	1.24 [237]	1.45
C	460 [a]	~ 90 [b]	~ < 65 [b]	1.46 (TIS-OIS) [82]	1.93 [82]	3.39
N	130 [a]		Ud	0.73 (TIS-OIS) [121]	2.48 [110]	3.21
O	345 [a]	1200 [105 : 3000] [b]	~ 100[b]	0.17 (TIS-TIS) [111]	3.05 [111]	3.22

[a] provided concentration by supplier corresponding to detection limits, [b] measured value by SIMS

Table 28: Minimum value of elementary composition of the 3N-HP and 6N-XHP sample (Ud: undetectable by LA-ICP-MS), and the most favorable calculated value of migration energy $E_m^{X_1}$ of element X and its binding energy $E_b^{V_1-X_1}$ with a tungsten single vacancy. The most favorable inter-site migration (TIS: tetrahedral interstitial site, OIS: octahedral interstitial site). The dissociation energy of the V_1-X_1 complex is $E_{diss}^{V_1-X_1} = E_m^{X_1} + E_b^{V_1-X_1}$ where i is the most mobile species between V and X.

Furthermore, the formation of these V-LE complexes could be more efficient in the less pure material (3N-HP) than in the purer one (6N-XHP). These complexes could impede the migration of a part of single vacancies which would have migrated and joined the vacancy clusters, contributing to their growth, in the less pure tungsten (3N-HP), as it had been shown in carbon-doped Fe for the V-C complex [122]. In addition, by employing positron measurement in Fe based alloys, in fatigued type 304 stainless steel and in bainite phase of Fe-0.66C-1.45Si-1.35Mn-1.02Cr-0.10Ni-0.24Mo alloy, respectively, Asoka-Kumar et *al.* [238] and Rementeria et *al.* [188] demonstrated the C trapping at vacancies on the electron momentum distribution. The carbon effect was more pronounced at around $10 \times 10^{-3}\ m_0c$, which is included in the ***high momentum (W) region*** of present SPB-DB measurement.

The nature of the complexes cannot be determined in the present study, and the determination of the number of LE atoms in the complexes is still challenging. In comparison with the theoretical works, they could be V-C_n, V-N_n, V-O_n, or V-C-H without excluding some more complex clusters made of more than one vacancy for which the properties are not known. Nevertheless, the number of bound LEs in the complexes should be low enough to make positron trapping at V-LE complexes still possible. If we consider the density of observed cavities in TEM of about $(1.6 \pm 0.5) \times 10^{24}\ m^{-3}$ corresponding to the largest vacancy cluster being detected by SPB-DB, i.e. V_N, the trapping coefficient of the positron at these defects is of about $1.6 \times 10^{-13}\ m^3.s^{-1}$ in 0.02 dpa irradiated samples as given in reference [159]. Then, the trapping rate K_{VN} can roughly be estimated to around $1 \times 10^{11}\ s^{-1}$. From the total trapping rate estimated from the positron effective diffusion length, the trapping rate at defects D_x is about $5 \times 10^{11}\ s^{-1}$. Considering that the trapping coefficient at defects D_x should be close to that of single vacancies ($\mu_V = 6 \pm 3 \times 10^{-15}\ m^{-3}.s^{-1}$ [159]), the concentration of D_x could be roughly estimated at about $7 \times 10^{25}\ m^{-3}$ (i.e. about 1105 at. ppm). It is interesting to notice that these roughly estimated values are of the same order of magnitude as the total concentration of C and O in the 3N-HP samples.

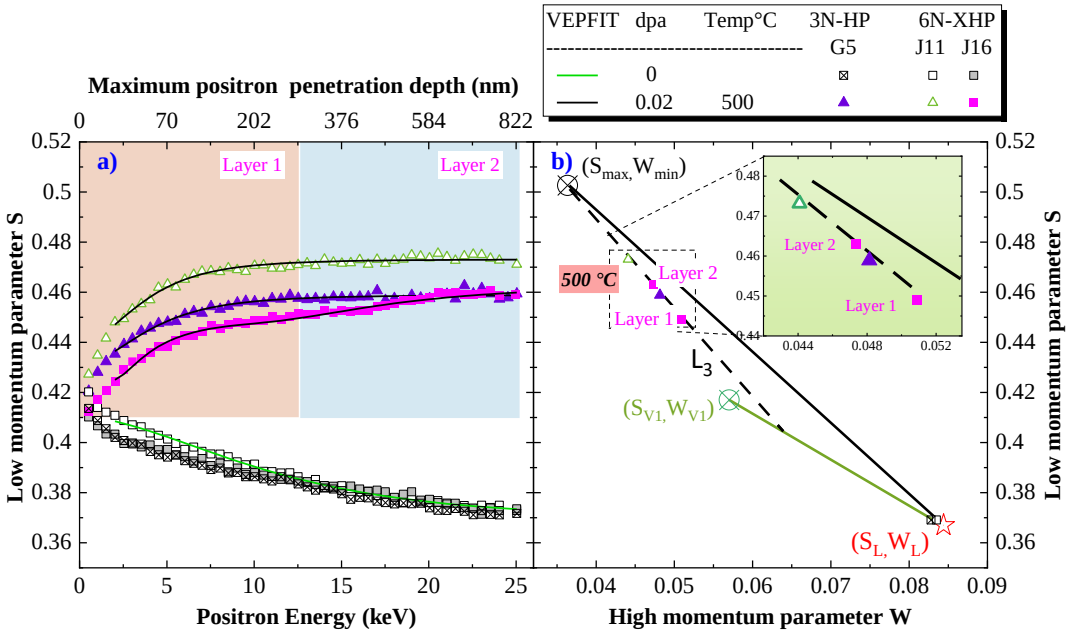

Figure 100 : SPB-DB results in self-irradiated (0.02dpa, 500°C) 3N-HP (99.95 wt.% Goodfellow) and 6N-XHP (99.9999 wt.% from Plansee M192 set material supplied by FZJ) samples.

For the special case of the 6N-XHP sample ***J16***, in which about 13 at. % C and about 1 at. % O were found by SIMS measurement of 3 random craters, the fitted SPB-DB measurement indicated that the damage depth distribution is made of at least two layers (the first one is about 200 nm thick) with different concentration and/or size of the defects. Moreover, the ***S*** (and ***W***) values in these both layers are lower (higher) than the ones obtained in the clean 6N-XHP ***J11*** sample and the corresponding ***S-W*** points belong to the line L_3. It suggests that the growth of vacancy clusters could have been also impeded in this contaminated sample as it has been observed in the 3N-HP samples. By comparing the SPB-DB results in Figure 100 with SIMS profiles shown in Figure 101, it appears that the concentration of carbon and oxygen is much higher close to the surface in ***J16*** compared to ***J11***. We can conclude that the presence of these elements have an impact on the evolution of the vacancy defects. if we look more into details and compare the ***S-W*** values obtained in the ***J16*** with the one measured in the 3N-HP ***G-05*** and the concentrations of C and O measured in the region probed by slow positrons (0-700 nm): The concentration of C is about 147700 at. ppm in ***J16*** and 100 at. ppm in ***G-05*** and that of O varies from 100 to 3000 at. ppm in ***J16*** and from 200 to 1000 at. ppm in ***G-05***. It follows that the ***S*** and ***W*** values should be more affected by the presence of C and O in the ***J16*** than in ***G-05.*** Moreover, it is noteworthy that the largest vacancy clusters proportion is the lowest in the first layer from 0 to approximately 200 nm in ***J16*** that means in the region where the oxygen concentration is the highest whereas the C concentration remains almost constant in the total thickness probed by the slow positrons (0-700nm). It suggests that oxygen could be the main origin of the limitation in the vacancy clusters growth.

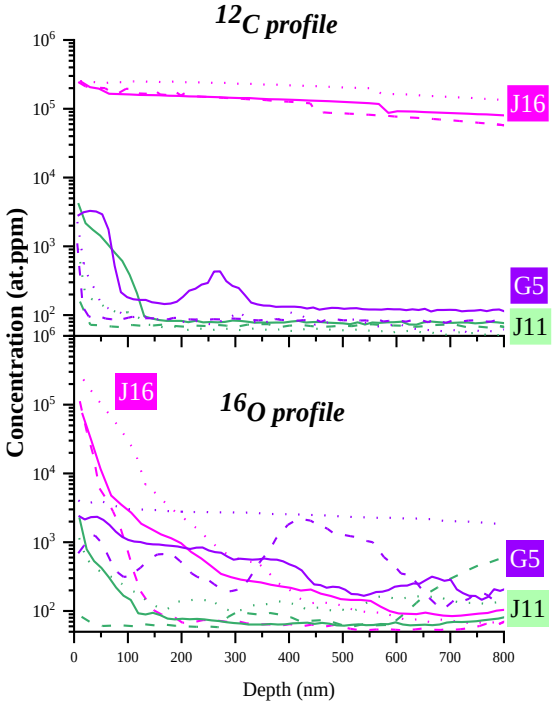

Figure 101 : SIMS results in the probed region of the slow positron in self-irradiated (0.02dpa, 500°C) 3N-HP (99.95 wt.% Goodfellow) and 6N-XHP (99.9999 wt.% from Plansee M192 set material supplied by FZJ) samples.

It is difficult to conclude on the precise origin of the vacancy cluster growth limitation observed in the less pure tungsten samples. One of the reasons is that the distribution of the C and O is not homogeneous. Moreover, the SIMS analysis remains a more localized characterization technique compared to SPB-DB. The analyzed area using SPB-DB is of about 3 mm^2, and in contrast the SIMS analyzes are localized in area of about 9×10^{-4} mm^2, i. e. 20 times smaller than the sputtering areas (blue squares in Figure 103).

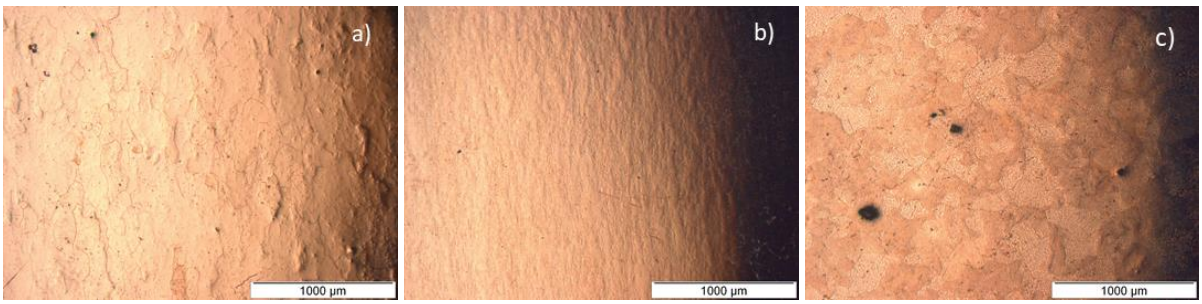

*Figure 102: **a)** Optical micrograph of the J11, **b)** G05, and **c)** J16*

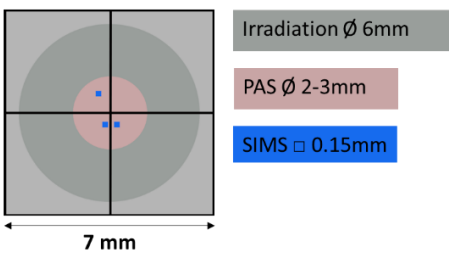

Figure 103: In-scale sketch of the irradiated area analyzed by SIMS and SPB-DB

However, from the data we have obtained on these samples the most probable origin could be the O decoration of vacancy defects. If we come back to the results obtained in the electron irradiated samples in which the type of the induced defects is more simple, we showed that O decorated vacancy defects are detected in addition with the pure single vacancies. It is more difficult to completely rule out the effect of carbon for these self-irradiations carried out at 500 °C. Compared to the electron irradiations performed at about 50 °C for which only oxygen is mobile, in the self-irradiations the temperature was much higher and allowed the migration of vacancies and C atoms. Even if the C concentration is low Vehanen et *al.* [122] showed that an effect on vacancy distribution is slightly detectable for about 70 at. ppm in Fe.

Summary

In this chapter, the irradiation of tungsten by various types of particles was investigated. In the first section, the 2.5 MeV electron-irradiated tungsten (Neyco 99.95 wt.%) with LF (1×10^{19} cm^{-2}) and HF (2×10^{19} cm^{-2}) were analyzed by PAS, SIMS and TEM. For both fluences, the SPB-DB measurements indicate the generation of the single vacancies (V_1) at the near surface region (~800 nm). However, the PALS measurement revealed a new defect X at which near 60 % of positrons annihilated, in contrast to merely ~30 % positrons annihilated at the pure V_1 corresponding to a concentration of about 1.3 and 2.4 $\times 10^{18}$ cm^{-3} by using a two-trap trapping model for LF and HF, respectively. Moreover, no defects were observed by TEM, even the dislocation loops. The SIMS analysis indicated that the concentration of the oxygen atom is at the same order of the magnitude as that of the V_1. The calculation of the two-trap model proved that defect X is probably a mix of several defects. By combining these experimental data with some DFT results, the defect X was considered as the mixture of a decorated V_1 with one or two oxygen atoms.

SPB-DB measurements in tungsten self-irradiated at RT with 2 and 20 MeV ions and different damage doses showed saturation of the defect concentration at about 0.5 dpa (SRIM-2008 K-P, E_{disp} = 55.3 eV) for both energies. The PKA spectrum is close for both energies. It means that whatever the primary or overlapped RIDs, they reached a saturation when the irradiation occurred at RT with a damage dose high enough. This saturation was considered as the consequence of the recombination of the FPs and the cascade overlapping as in the case of BCC iron. In addition, this saturation effect should be expected for all the materials according to other published works.

Meanwhile, 20 MeV self-ion irradiations were also carried out at high temperatures (500 °C, and 700 °C) in the samples with two different purities (3N-HP, 99.95 wt.%, 6N-XHP, 99.9999 wt.%). These samples were analyzed using SPB-DB. An effect of temperature and purity were clearly recorded. When irradiation is performed at high temperatures (500, and 700 °C), the vacancy clusters generated during the irradiation (~0.02 dpa) are larger than those detected for irradiation at RT probably because

migration of vacancies is possible and can allow growth of the vacancy clusters. Moreover, the formation of the largest defects was found in the purest samples (6N-XHP). The tungsten thin foils were in-situ irradiated with 1.2 MeV-W, at such flux, fluence and temperature that could allow to get same defect distribution than in 20MeV self-irradiation. The TEM observations confirmed the formation of the largest vacancy defects in the 6N-XHP samples irradiated at high temperature (500 and, 700 °C). In addition, SIMS measurements in the irradiated samples revealed heterogeneous distribution of carbon and oxygen at the near surface depth for whole analyzed samples specially for oxygen. The measured C and O concentrations are higher in less pure 3N-HP samples than in the ultrapure 6N-XHP ones in the depth region probed by positrons (0-700 nm). In addition, PAS revealed a heterogeneous distribution of the defects in carbon and oxygen contaminated ultrapure sample in contrast with non-contaminated sample of the same batch irradiated under the same conditions. A high oxygen concentration was also detected in the first 600 nm under the surface in this contaminated sample. To sum up, it seems that the presence of the LEs (C and most probably O) impeded the agglomeration of the vacancies. Based on the annihilation characteristics found in these less pure samples and on the theoretical properties of oxygen and carbon which predict strong interactions between LEs and vacancies we propose that oxygen decorated vacancy defects are at the origin of the limited vacancy agglomeration in less pure material.

General conclusion

Controlled fusion is considered as one of the solutions to nowadays energy and environmental issues. With this in mind, the ITER project, a new generation of tokamak, was launched, to demonstrate the energy production capability of these fusion reactors. Not only numerous technological obstacles remain to be overcome, but materials research is also one of the key issues in achieving the production of the energy with fusion. Tungsten, the most promising PFM, has been selected to cover the divertor, a very critical component in ITER, and is being considered for the inner wall of the future TOKAMAKs. This material will have to withstand the high heat flux and energetic particles bombardment. Tungsten has several suitable properties of major importance to withstand these extreme operating conditions, namely efficient thermal conductivity, low sputtering rate and a very high melting temperature. However, the degradation of some properties has been found when exposed to conditions close to those expected in TOKAMAK. The degradation was proved to be related to the microstructural evolution of the material induced by exposure to energetic products of the fusion reactions and to the plasma. These exposures induce defects in materials and their accumulation and transformation lead to this microstructure evolution. Hence, the investigation of the behaviors of radiation-induced defects is essential to better recognize the origin of different degradations and to be able to predict the evolution of the material during its operation and lifetime. Some fundamental properties of the single vacancy and of some vacancy clusters in tungsten were revealed experimentally and their evolution was described in different steps related to these fundamental properties. Preliminary results showed that the evolution of vacancy clusters varies for samples from two batches of different purity. It was also pointed out that many theoretical studies predict that light elements (LEs: hydrogen, helium, nitrogen, carbon and oxygen) interact strongly with defects, especially vacancies, but that little experimental work has been done.

Therefore, the aim of this thesis is to carry out several experimental studies to better understand these potential interactions and their consequences on the microstructure of irradiated tungsten. Tungsten samples of different purities (99.95 to 99.9999 wt.%) were irradiated under different conditions: **i/** electron irradiations to introduce countable point defects, **ii/** self-ion irradiations to create similar defects to those induced by neutrons. By taking into account their complementary detection limit in terms of defect size, PAS and TEM were used to characterize the vacancy-type defects for sizes ranging from single vacancies to larger clusters (~2 nm). In addition, SIMS and NRA were used to quantify the light elements (LEs). Both structural and chemical results were correlated to highlight various effects on the radiation induced defects distributions.

The quality of as-annealed pristine samples was checked by SPB-DB and PALS measurement. The majority of the samples have Lattice-like annihilation characteristics suggesting that they contain a low concentration of defects. Consequently, they are suitable for the investigation of the radiation induced defects. However, the quantitative analysis (SIMS, and NRA) indicated that a part of prepared samples

presents a carbon-enriched layer of about up to ~2 µm with a maximum concentration of about ~20 at. %. This C-enriched can be identified by the special morphology (‘cotton-like’) of the surface, which contains innumerable small dark dots (‘sesame like’) when observed using an optical microscope. Systematic SIMS and NRA analysis were performed in samples annealed at high temperature (1700 °C) with varying times. Contamination is proven to come from an external source to the samples. New annealing performed after replacing the sample holder (a tungsten plate) with a purer material and of the furnace components, the ‘cotton-like’ surface disappeared, indicating that contamination has been reduced. Moreover, it seems that the C-enriched layer has an effect on the annihilation characteristics.

On the one hand, electron irradiations were first carried out with two fluences at RT. The PALS measurements revealed that between the sample surface and a depth of about 50 µm, the concentration of single vacancies is about twice as high in the sample irradiated at high fluence (HF), compared to that detected in low fluence (LF) irradiated samples. These results are in agreement with the calculated damage profile (see Chap. II.2.1). Nevertheless, a shorter positron lifetime than that of the pure single vacancy is highlighted. This shows that positron trapping has occurred in an unknown defect X for which the annihilation is dominant unlike the other two annihilation states (***Lattice*** and pure simple vacancies). Moreover, the positron trapping rate at the X-defect appears to be favored at cryogenic temperature (25 and 60 K), at which a single lifetime component can be extracted from the lifetime spectra with a value of approximately 131 ps (25 K) and 147 ps (60 K). Direct TEM observations of the samples irradiated in the present study, showed that neither dislocation loops nor small vacancy clusters were formed in the HF-irradiated lamella. In addition, the SIMS analysis detected a non-negligible concentration and heterogeneous distribution of oxygen atoms in the samples, which is highly mobile even at RT in tungsten. Also, the estimated annihilation characteristics for the X-defect are similar to those calculated for single vacancies decorated with a different number of oxygen atoms. Finally, using the two-trap trapping model, we confirmed that the PALS spectrum contains more than three annihilation states when measured at RT. Accordingly, the most probable nature of the X-defect is the mixture of several types of oxygen vacancy complexes.

On the other hand, the evolution of the distribution of vacancy-induced defects was investigated in tungsten samples of different purities (99.95 wt.%, and 99.9999 wt.%) self-irradiated under various conditions (energy of the W ions, temperature, fluences).

Firstly, the self-irradiated samples with 2 MeV and 20 MeV ions at RT were studied using SPB-DB. The size of the induced vacancy defects grows with increasing damage dose, up to a saturation reached at about 0.5 dpa. This result is in correlation with new modelling results. It is also interesting to note that the distribution of the defects induced by 2 and 20 MeV ions at RT are equivalent probably because fragmentation of the collision cascades and the overlapping of the created subcascades drive this microstructural evolution.

Secondly, 20 MeV self-irradiations at high temperatures (HT, 500, and 700 °C) with a mean damage level of about 0.02 dpa in the region between 0 - 700 nm in the samples was compared to the ones carried out at RT (0.01 and 0.04 dpa). The SPB-DB measurements showed that compared to RT-irradiations, larger vacancy clusters were formed after self-ion irradiation at HT, and that the cluster size is close for 500 and 700 °C. It can be explained by the agglomeration of small vacancy clusters (V_1 and V_3) that becomes mobile when the temperature increases. In addition, the purity of the samples affects the vacancy-defect distribution. Smaller clusters were revealed for 3N-HP samples than those induced in the 6N-XHP samples which were both irradiated at the same time. A similar result was also obtained for samples irradiated at 500 °C with a damage dose of 0.04 dpa. Moreover, the TEM observations confirmed the PAS results: for the same irradiation conditions (a damage dose of 0.02 dpa, at HT -500, and 700 °C-), the voids with the largest mean diameter were observed in ultrapure 6N-XHP lamellas compared to the less pure 3N-HP samples. The SIMS analysis of the irradiated samples revealed heterogeneous distribution of carbon and oxygen at the near surface depth for all the analyzed samples especially for oxygen. The measured C and O concentrations are higher in less pure 3N-HP samples than in the ultrapure 6N-XHP ones in the depth region probed by positrons (0-700 nm). In addition, PAS revealed a heterogeneous distribution of the defects in carbon contaminated ultrapure sample (presenting a C-enriched layer in the first 1-2 µm depth) in contrast with non-contaminated sample of the same batch irradiated under the same conditions. A high oxygen concentration was also detected in the first 600 nm under the surface in this contaminated sample, which is unavoidable self-pollution for metals. To sum up, it seems that the presence of the LEs (C and O) impeded the agglomeration of the vacancies. Based on the annihilation characteristics found in these less pure samples and on the theoretical properties of oxygen and carbon which predict strong interactions between LEs and vacancies we propose that oxygen decorated vacancy defects seems the most likely reason for the limited vacancy agglomeration in less pure materials.

Perspectives

Different perspectives can be proposed as a result of this work both experimentally and in terms of simulation.

From an experimental point of view, the following investigations would complement the present work:

By combining the PAS and SIMS results of the electron and self-ion irradiations, it seems that oxygen atoms have a major influence on the distribution of vacancy defects, probably because oxygen decorated vacancy-complexes are formed and limit growth of vacancy clusters. To further investigate these types of defects, other characterizations with high-resolution techniques have to be planned.

- Atom Probe Tomography can provide a 3D-distribution of the O atoms, which can be used to check the O concentration dissolved in the tungsten irradiated at 500 or 700 °C, and also to access the nature of the local heterogeneities, which might be related to oxide nanoparticles in the pristine samples.
- High resolution scanning TEM might directly observed decorated cavities or small vacancy clusters.

It would be also interesting to perform some annealing studies after electron irradiations in samples containing a controlled concentration of oxygen to check the dissociation of the decorated vacancy complexes.

Because the consequences on the macroscopic properties of tungsten is the major question for TOKAMAK applications it would be also important to continue studies on the evolution of the microstructure at high damage dose. It would be of major importance to investigate how the irradiation temperature would have an effect on the damage saturation we highlighted at RT. Moreover, such microstructural studies should be combined with characterizations able to give macroscopic information such as swelling for example.

Alongside these additional experimental studies, theoretical ones should be also useful to better understand the effect of impurities and irradiation temperature on the RIDs:

- the calculation of annihilation characteristics and trapping coefficients of various V_n-LEs_m complexes could help to better identify and quantify these defects.
- The calculation of the migration properties of such complexes should allow to check if there are immobile at room temperature as the V-C is in iron.

In addition, the calculations of the ***S*** and ***W*** annihilation characteristics of various vacancy clusters in combination with the development of fitting method based on trapping model and complementary TEM observations, should be used to better quantify the different vacancy clusters, especially the smallest ones in self-irradiated samples.

Figure list

Table list

References

[1] D. Larcher, J.-M. Tarascon, Towards greener and more sustainable batteries for electrical energy storage, NATURE CHEMISTRY. 7 (2015) 11.

[2] T. Tanabe, ed., Tritium: Fuel of Fusion Reactors, Springer Japan, Tokyo, 2017. https://doi.org/10.1007/978-4-431-56460-7.

[3] J.D. Lawson, Some Criteria for a Power Producing Thermonuclear Reactor, Proc. Phys. Soc. B. 70 (1957) 6–10. https://doi.org/10.1088/0370-1301/70/1/303.

[4] It's Elemental - The Element Lithium, (n.d.). https://education.jlab.org/itselemental/iso003.html (accessed April 6, 2022).

[5] D. Perrault, Reacteurs nucleaires de fusion//considerations sur les questions de surete et de radioprotection des reacteurs de demonstration apres l'installation ITER, (n.d.) 94.

[6] Enabling Technology for Fusion: IAEA Forum Pushes Forward Advanced Mock-ups, (2019). https://www.iaea.org/newscenter/news/enabling-technology-for-fusion-iaea-forum-pushes-forward-advanced-mock-ups (accessed April 2, 2022).

[7] The beauty of the beast, ITER. (n.d.). http://www.iter.org/newsline/252/1449 (accessed April 2, 2022).

[8] R.A. Pitts, S. Bardin, B. Bazylev, M.A. van den Berg, P. Bunting, S. Carpentier-Chouchana, J.W. Coenen, Y. Corre, R. Dejarnac, F. Escourbiac, J. Gaspar, J.P. Gunn, T. Hirai, S.-H. Hong, J. Horacek, D. Iglesias, M. Komm, K. Krieger, C. Lasnier, G.F. Matthews, T.W. Morgan, S. Panayotis, S. Pestchanyi, A. Podolnik, R.E. Nygren, D.L. Rudakov, G. De Temmerman, P. Vondracek, J.G. Watkins, Physics conclusions in support of ITER W divertor monoblock shaping, Nuclear Materials and Energy. 12 (2017) 60–74. https://doi.org/10.1016/j.nme.2017.03.005.

[9] Tungsten | Plansee, (n.d.). https://www.plansee.com/en/materials/www.plansee.com/en/materials/tungsten.html (accessed April 6, 2022).

[10] S.J. Zinkle, N.M. Ghoniem, Operating temperature windows for fusion reactor structural materials, Fusion Engineering and Design. 51–52 (2000) 55–71. https://doi.org/10.1016/S0920-3796(00)00320-3.

[11] C. Chang, D. Terentyev, A. Zinovev, W.V. Renterghem, C. Yin, P. Verleysen, T. Pardoen, M. Vilémová, J. Matějíček, Irradiation-induced hardening in fusion relevant tungsten grades with different initial microstructures, Phys. Scr. 96 (2021) 124021. https://doi.org/10.1088/1402-4896/ac2181.

[12] J. Linke, J. Du, T. Loewenhoff, G. Pintsuk, B. Spilker, I. Steudel, M. Wirtz, Challenges for plasma-facing components in nuclear fusion, Matter and Radiation at Extremes. 4 (2019) 056201. https://doi.org/10.1063/1.5090100.

[13] K. Farrell, A.C. Schaffhauser, J.O. Stiegler, Recrystallization, grain growth and the ductile-brittle transition in tungsten sheet, Journal of the Less Common Metals. 13 (1967) 141–155. https://doi.org/10.1016/0022-5088(67)90177-4.

[14] R.A. Pitts, S. Carpentier, F. Escourbiac, T. Hirai, V. Komarov, S. Lisgo, A.S. Kukushkin, A. Loarte, M. Merola, A. Sashala Naik, R. Mitteau, M. Sugihara, B. Bazylev, P.C. Stangeby, A full tungsten divertor for ITER: Physics issues and design status, Journal of Nuclear Materials. 438 (2013) S48–S56. https://doi.org/10.1016/j.jnucmat.2013.01.008.

[15] T. Hirai, F. Escourbiac, V. Barabash, A. Durocher, A. Fedosov, L. Ferrand, T. Jokinen, V. Komarov, M. Merola, S. Carpentier-Chouchana, N. Arkhipov, V. Kuznetcov, A. Volodin, S. Suzuki, K. Ezato, Y. Seki, B. Riccardi, M. Bednarek, P. Gavila, Status of technology R&D for the ITER tungsten divertor monoblock, Journal of Nuclear Materials. 463 (2015) 1248–1251. https://doi.org/10.1016/j.jnucmat.2014.12.027.

[16] S. Nogami, M. Toyota, W. Guan, A. Hasegawa, Y. Ueda, Degradation of tungsten monoblock divertor under cyclic high heat flux loading, Fusion Engineering and Design. 120 (2017) 49–60. https://doi.org/10.1016/j.fusengdes.2017.04.102.

[17] W.M. Shu, G.-N. Luo, T. Yamanishi, Mechanisms of retention and blistering in near-surface region of tungsten exposed to high flux deuterium plasmas of tens of eV, Journal of Nuclear Materials. 367–370 (2007) 1463–1467. https://doi.org/10.1016/j.jnucmat.2007.04.005.

[18] M.Y. Ye, H. Kanehara, S. Fukuta, N. Ohno, S. Takamura, Blister formation on tungsten surface under low energy and high flux hydrogen plasma irradiation in NAGDIS-I, Journal of Nuclear Materials. 313–316 (2003) 72–76. https://doi.org/10.1016/S0022-3115(02)01349-1.

[19] X. Zhang, L. Qiao, H. Zhang, W. Yao, W. He, Y. Li, P. Wang, Surface modification and deuterium retention of tungsten and tungsten-rhenium alloys exposed to deuterium plasma, Nuclear Materials and Energy. 29 (2021) 101079. https://doi.org/10.1016/j.nme.2021.101079.

[20] N. Enomoto, S. Muto, T. Tanabe, J.W. Davis, A.A. Haasz, Grazing-incidence electron microscopy of surface blisters in single- and polycrystalline tungsten formed by H+, D+ and He+ irradiation, Journal of Nuclear Materials. 385 (2009) 606–614. https://doi.org/10.1016/j.jnucmat.2009.01.298.

[21] S. Nagata, B. Tsuchiya, T. Sugawara, N. Ohtsu, T. Shikama, Helium and hydrogen trapping in W and Mo single-crystals irradiated by He ions, Journal of Nuclear Materials. 307–311 (2002) 1513–1516. https://doi.org/10.1016/S0022-3115(02)01269-2.

[22] S. Nagata, B. Tsuchiya, T. Sugawara, N. Ohtsu, T. Shikama, Ion beam analysis of helium and its irradiation effect on hydrogen trapping in W single crystals, Nuclear Instruments and Methods in Physics Research Section B: Beam Interactions with Materials and Atoms. 190 (2002) 652–656. https://doi.org/10.1016/S0168-583X(01)01242-3.

[23] G.-N. Luo, W.M. Shu, M. Nishi, Incident energy dependence of blistering at tungsten irradiated by low energy high flux deuterium plasma beams, Journal of Nuclear Materials. 347 (2005) 111–117. https://doi.org/10.1016/j.jnucmat.2005.07.014.

[24] Y. Ueda, T. Shimada, M. Nishikawa, Impacts of carbon impurities in hydrogen plasmas on tungsten blistering, Nucl. Fusion. 44 (2003) 62–67. https://doi.org/10.1088/0029-5515/44/1/007.

[25] S. Kajita, N. Yoshida, N. Ohno, Tungsten fuzz: Deposition effects and influence to fusion devices, Nuclear Materials and Energy. 25 (2020) 100828. https://doi.org/10.1016/j.nme.2020.100828.

[26] L. Liu, Y. Zhang, H. Fan, D. Liu, C. Niu, L. Cheng, W. Ni, The effect of W fuzz growth on D retention in polycrystalline W, Journal of Nuclear Materials. 539 (2020) 152327. https://doi.org/10.1016/j.jnucmat.2020.152327.

[27] M.J. Baldwin, R.P. Doerner, Helium induced nanoscopic morphology on tungsten under fusion relevant plasma conditions, Nucl. Fusion. 48 (2008) 035001. https://doi.org/10.1088/0029-5515/48/3/035001.

[28] S. Takamura, Initial Stage of Fiber-Form Nanostructure Growth on Refractory Metal Surfaces with Helium Plasma Irradiation, Plasma and Fusion Research. 9 (2014) 1302007–1302007. https://doi.org/10.1585/pfr.9.1302007.

[29] K. Wang, R.P. Doerner, M.J. Baldwin, F.W. Meyer, M.E. Bannister, A. Darbal, R. Stroud, C.M. Parish, Morphologies of tungsten nanotendrils grown under helium exposure, Sci Rep. 7 (2017) 42315. https://doi.org/10.1038/srep42315.

[30] W. Ni, L. Liu, Y. Zhang, H. Fan, G. Song, D. Liu, G. Benstetter, G. Lei, Mass loss of pure W, W-Re alloys, and oxide dispersed W under ITER-relevant He ion irradiations, Journal of Nuclear Materials. (n.d.). https://doi.org/10.1016/j.jnucmat.2019.151800.

[31] D. Nishijima, M.Y. Ye, N. Ohno, S. Takamura, Formation mechanism of bubbles and holes on tungsten surface with low-energy and high-flux helium plasma irradiation in NAGDIS-II, Journal of Nuclear Materials. 329–333 (2004) 1029–1033. https://doi.org/10.1016/j.jnucmat.2004.04.129.

[32] H. Ullmaier, The influence of helium on the bulk properties of fusion reactor structural materials, Nucl. Fusion. 24 (1984) 1039–1083. https://doi.org/10.1088/0029-5515/24/8/009.

[33] L. Sun, S. Jin, X.-C. Li, Y. Zhang, G.-H. Lu, Hydrogen behaviors in molybdenum and tungsten and a generic vacancy trapping mechanism for H bubble formation, Journal of Nuclear Materials. 434 (2013) 395–401. https://doi.org/10.1016/j.jnucmat.2012.12.008.

[34] H. Iwakiri, K. Yasunaga, K. Morishita, N. Yoshida, Microstructure evolution in tungsten during low-energy helium ion irradiation, Journal of Nuclear Materials. 283–287 (2000) 1134–1138. https://doi.org/10.1016/S0022-3115(00)00289-0.

[35] W.D. Wilson, C.L. Bisson, M.I. Baskes, Self-trapping of helium in metals, Phys. Rev. B. 24 (1981) 5616–5624. https://doi.org/10.1103/PhysRevB.24.5616.

[36] P.-E. Lhuillier, Etude du comportement de l'helium et des defauts lacunaires dans le tungstene, phdthesis, Universite d'Orleans, 2010. https://tel.archives-ouvertes.fr/tel-00587482 (accessed January 7, 2021).

[37] M.I. Baskes, Recent Advances in Understanding Helium Embrittlement in Metals, MRS Bull. 11 (1986) 14–18. https://doi.org/10.1557/S0883769400069116.

[38] X. Fang, A. Kreter, M. Rasinski, C. Kirchlechner, S. Brinckmann, C. Linsmeier, G. Dehm, Hydrogen embrittlement of tungsten induced by deuterium plasma: Insights from nanoindentation tests, J. Mater. Res. 33 (2018) 3530–3536. https://doi.org/10.1557/jmr.2018.305.

[39] K. Yutani, H. Kishimoto, R. Kasada, A. Kimura, Evaluation of Helium effects on swelling behavior of oxide dispersion strengthened ferritic steels under ion irradiation, Journal of Nuclear Materials. 367–370 (2007) 423–427. https://doi.org/10.1016/j.jnucmat.2007.03.016.

[40] G.M. Bond, D.J. Mazey, M.B. Lewis, Helium-bubble formation and void swelling in nimonic PE16 alloy under dual-ion (He+, Ni+) irradiation, Nuclear Instruments and Methods in Physics Research. 209–210 (1983) 381–386. https://doi.org/10.1016/0167-5087(83)90827-X.

[41] F. Kong, M. Qu, S. Yan, A. Zhang, S. Peng, J. Xue, Y. Wang, Helium-induced hardening effect in polycrystalline tungsten, Nuclear Instruments and Methods in Physics Research Section B: Beam Interactions with Materials and Atoms. 406 (2017) 643–647. https://doi.org/10.1016/j.nimb.2017.02.029.

[42] V.K. Sikka, J. Moteff, Superlattice of voids in neutron-irradiated tungsten, Journal of Applied Physics. 43 (1972) 4942–4944. https://doi.org/10.1063/1.1661050.

[43] T. Tanno, A. Hasegawa, J.-C. He, M. Fujiwara, S. Nogami, M. Satou, T. Shishido, K. Abe, Effects of Transmutation Elements on Neutron Irradiation Hardening of Tungsten, Mater. Trans. 48 (2007) 2399–2402. https://doi.org/10.2320/matertrans.MAW200722.

[44] A. Hasegawa, M. Fukuda, S. Nogami, K. Yabuuchi, Neutron irradiation effects on tungsten materials, Fusion Engineering and Design. 89 (2014) 1568–1572. https://doi.org/10.1016/j.fusengdes.2014.04.035.

[45] Y. Wang, J. Zhao, Understanding the thermal conductivity of pristine W and W–Re alloys from a physics-based model, Journal of Nuclear Materials. 529 (2020) 151931. https://doi.org/10.1016/j.jnucmat.2019.151931.

[46] M. Akiyoshi, L.M. Garrison, J.W. Geringer, H. Wang, A. Hasegawa, S. Nogami, Y. Katoh, Thermal diffusivity of irradiated tungsten and tungsten-rhenium alloys, Journal of Nuclear Materials. 543 (2021) 152594. https://doi.org/10.1016/j.jnucmat.2020.152594.

[47] J. Matolich, H. Nahm, J. Moteff, Swelling in neutron irradiated tungsten and tungsten-25 percent rhenium, Scripta Metallurgica. 8 (1974) 837–841. https://doi.org/10.1016/0036-9748(74)90304-4.

[48] F. A. Garner, Chapter 6: "Irradiation Performance of Cladding and Structural Steels in Liquid Metal Reactors," Vol. 10A of Materials Science and Technology: A Comprehensive Treatment, VCH Publishers, 1994, pp. 419-543., in: 1994: pp. 419–543.

[49] M. Dürrschnabel, M. Klimenkov, U. Jäntsch, M. Rieth, H.C. Schneider, D. Terentyev, New insights into microstructure of neutron-irradiated tungsten, Scientific Reports. 11 (2021) 7572. https://doi.org/10.1038/s41598-021-86746-6.

[50] M.R. Gilbert, J.-Ch. Sublet, Neutron-induced transmutation effects in W and W-alloys in a fusion environment, Nucl. Fusion. 51 (2011) 043005. https://doi.org/10.1088/0029-5515/51/4/043005.

[51] X. Hu, T. Koyanagi, M. Fukuda, N.A.P.K. Kumar, L.L. Snead, B.D. Wirth, Y. Katoh, Irradiation hardening of pure tungsten exposed to neutron irradiation, Journal of Nuclear Materials. 480 (2016) 235–243. https://doi.org/10.1016/j.jnucmat.2016.08.024.

[52] A. Hasegawa, Property change mechanism in tungsten under neutron irradiation in various reactors, Journal of Nuclear Materials. (2011) 4.

[53] M. Fukuda, T. Tanno, S. Nogami, A. Hasegawa, Effects of Re Content and Fabrication Process on Microstructural Changes and Hardening in Neutron Irradiated Tungsten, Mater. Trans. 53 (2012) 2145–2150. https://doi.org/10.2320/matertrans.MBW201110.

[54] M. Fukuda, K. Yabuuchi, S. Nogami, A. Hasegawa, T. Tanaka, Microstructural development of tungsten and tungsten–rhenium alloys due to neutron irradiation in HFIR, Journal of Nuclear Materials. 455 (2014) 460–463. https://doi.org/10.1016/j.jnucmat.2014.08.002.

[55] M. Fukuda, A. Hasegawa, S. Nogami, K. Yabuuchi, Microstructure development of dispersion-strengthened tungsten due to neutron irradiation, Journal of Nuclear Materials. 449 (2014) 213–218. https://doi.org/10.1016/j.jnucmat.2013.10.012.

[56] G.S. Was, Fundamentals of radiation materials science: metals and alloys, Springer, Berlin ; New York, 2007.

[57] G.H. Kinchin, THE DISPLACEMENT OF ATOMS IN SOLIDS BY RADIATION, (n.d.) 52.

[58] M.J. Norgett, M.T. Robinson, I.M. Torrens, A proposed method of calculating displacement dose rates, Nuclear Engineering and Design. 33 (1975) 50–54. https://doi.org/10.1016/0029-5493(75)90035-7.

[59] X. Yi, W. College, Electron Microscopy Study of Radiation Damage in Tungsten and Alloys, (n.d.) 260.

[60] D.R. Mason, X. Yi, M.A. Kirk, S.L. Dudarev, Elastic trapping of dislocation loops in cascades in ion-irradiated tungsten foils, J. Phys.: Condens. Matter. 26 (2014) 375701. https://doi.org/10.1088/0953-8984/26/37/375701.

[61] F. Maury, M. Biget, P. Vajda, A. Lucasson, P. Lucasson, Frenkel pair creation and stage I recovery in W crystals irradiated near threshold, Radiation Effects. 38 (1978) 53–65. https://doi.org/10.1080/00337577808233209.

[62] L. Bukonte, F. Djurabekova, J. Samela, K. Nordlund, S.A. Norris, M.J. Aziz, Comparison of molecular dynamics and binary collision approximation simulations for atom displacement analysis, Nuclear Instruments and Methods in Physics Research Section B: Beam Interactions with Materials and Atoms. 297 (2013) 23–28. https://doi.org/10.1016/j.nimb.2012.12.014.

[63] S.L. Dudarev, DPA definition and estimates, (n.d.) 10.

[64] R.M. Scanlan, D.L. Styris, D.N. Seidman, An in-situ field ion microscope study of irradiated tungsten: II. Analysis and interpretation, The Philosophical Magazine: A Journal of Theoretical Experimental and Applied Physics. 23 (1971) 1459–1478. https://doi.org/10.1080/14786437108217014.

[65] C.S. Becquart, A. De Backer, P. Olsson, C. Domain, Modelling the primary damage in Fe and W: Influence of the short range interactions on the cascade properties: Part 1 – Energy transfer, Journal of Nuclear Materials. 547 (2021) 152816. https://doi.org/10.1016/j.jnucmat.2021.152816.

[66] A. De Backer, C.S. Becquart, P. Olsson, C. Domain, Modelling the primary damage in Fe and W: influence of the short-range interactions on the cascade properties: Part 2 – multivariate multiple linear regression analysis of displacement cascades, Journal of Nuclear Materials. 549 (2021) 152887. https://doi.org/10.1016/j.jnucmat.2021.152887.

[67] J. Knaster, A. Moeslang, T. Muroga, Materials research for fusion, Nature Phys. 12 (2016) 424–434. https://doi.org/10.1038/nphys3735.

[68] J.A. Brinkman, Production of Atomic Displacements by High-Energy Particles, American Journal of Physics. 24 (1956) 246–267. https://doi.org/10.1119/1.1934201.

[69] A.E. Sand, K. Nordlund, S.L. Dudarev, Radiation damage production in massive cascades initiated by fusion neutrons in tungsten, Journal of Nuclear Materials. 455 (2014) 207–211. https://doi.org/10.1016/j.jnucmat.2014.06.007.

[70] R.E. Stoller, G.R. Odette, B.D. Wirth, Primary damage formation in bcc iron, Journal of Nuclear Materials. 251 (1997) 49–60. https://doi.org/10.1016/S0022-3115(97)00256-0.

[71] A. De Backer, A.E. Sand, K. Nordlund, L. Luneville, D. Simeone, S.L. Dudarev, Subcascade formation and defect cluster size scaling in high-energy collision events in metals, EPL. 115 (2016) 26001. https://doi.org/10.1209/0295-5075/115/26001.

[72] A.E. Sand, D.R. Mason, A.D. Backer, X. Yi, S.L. Dudarev, K. Nordlund, Cascade fragmentation: deviation from power law in primary radiation damage, Materials Research Letters. 5 (2017) 357–363. https://doi.org/10.1080/21663831.2017.1294117.

[73] A.D. Backer, C. Domain, C.S. Becquart, L. Luneville, D. Simeone, A.E. Sand, K. Nordlund, A model of defect cluster creation in fragmented cascades in metals based on morphological analysis, J. Phys.: Condens. Matter. 30 (2018) 405701. https://doi.org/10.1088/1361-648X/aadb4e.

[74] P.E. Lhuillier, M.F. Barthe, P. Desgardin, W. Egger, P. Sperr, Positron annihilation studies on the nature and thermal behaviour of irradiation induced defects in tungsten, Phys. Status Solidi (c). 6 (2009) 2329–2332. https://doi.org/10.1002/pssc.200982114.

[75] O.V. Ogorodnikova, L.Y. Dubov, S.V. Stepanov, D. Terentyev, Yu.V. Funtikov, Yu.V. Shtotsky, V.S. Stolbunov, V. Efimov, K. Gutorov, Annealing of radiation-induced defects in tungsten: Positron annihilation spectroscopy study, Journal of Nuclear Materials. 517 (2019) 148–151. https://doi.org/10.1016/j.jnucmat.2019.02.010.

[76] J. Amano, D.N. Seidman, Diffusivity of 3 He atoms in perfect tungsten crystals, Journal of Applied Physics. 56 (1984) 983–992. https://doi.org/10.1063/1.334039.

[77] J. Fikar, R. Schäublin, Molecular dynamics simulation of radiation damage in bcc tungsten, Journal of Nuclear Materials. 386–388 (2009) 97–101. https://doi.org/10.1016/j.jnucmat.2008.12.068.

[78] H. Tanimoto, H. Mizubayashi, H. Nishimura, S. Okuda, A Study of Self-Interstitial Atom in W by Means of Low-Temperature Irradiations, J. Phys. IV France. 06 (1996) C8-285-C8-288. https://doi.org/10.1051/jp4:1996861.

[79] S. long Wen, J. ming Chen, X. Liu, H. Zhu, H. yan Chang, Z. Huang, M. Pan, Y. Zhao, First-principles study on mono-vacancy self diffusion and recovery in tungsten crystal, Fusion Engineering and Design. 109–111 (2016) 569–573. https://doi.org/10.1016/j.fusengdes.2016.02.044.

[80] T. Amino, K. Arakawa, H. Mori, Detection of one-dimensional migration of single self-interstitial atoms in tungsten using high-voltage electron microscopy, Sci Rep. 6 (2016) 26099. https://doi.org/10.1038/srep26099.

[81] C.S. Becquart, C. Domain, Ab initio calculations about intrinsic point defects and He in W, Nuclear Instruments and Methods in Physics Research Section B: Beam Interactions with Materials and Atoms. 255 (2007) 23–26. https://doi.org/10.1016/j.nimb.2006.11.006.

[82] Y.-L. Liu, H.-B. Zhou, Y. Zhang, G.-H. Lu, G.-N. Luo, Interaction of C with vacancy in W: A first-principles study, Computational Materials Science. 50 (2011) 3213–3217. https://doi.org/10.1016/j.commatsci.2011.06.003.

[83] D. Nguyen-Manh, A.P. Horsfield, S.L. Dudarev, Self-interstitial atom defects in bcc transition metals: Group-specific trends, Phys. Rev. B. 73 (2006) 020101. https://doi.org/10.1103/PhysRevB.73.020101.

[84] R.W. Balluffi, Vacancy defect mobilities and binding energies obtained from annealing studies, Journal of Nuclear Materials. 69–70 (1978) 240–263. https://doi.org/10.1016/0022-3115(78)90247-7.

[85] M.W. Thompson, The damage and recovery of neutron irradiated tungsten, Philosophical Magazine. 5 (1960) 278–296. https://doi.org/10.1080/14786436008235842.

[86] L.K. Keys, J. Moteff, Neutron irradiation and defect recovery of tungsten, Journal of Nuclear Materials. 34 (1970) 260–280. https://doi.org/10.1016/0022-3115(70)90193-5.

[87] K.-D. Rasch, R.W. Siegel, H. Schultz, Quenching and recovery investigations of vacancies in tungsten, Philosophical Magazine A. 41 (1980) 91–117. https://doi.org/10.1080/01418618008241833.

[88] G.H. Kinchin, M.W. Thompson, Irradiation damage and recovery in molybdenum and tungsten, Journal of Nuclear Energy (1954). 6 (1958) 275–284. https://doi.org/10.1016/0891-3919(58)90054-8.

[89] W.H. Zhou, Y.G. Li, L.F. Huang, Z. Zeng, X. Ju, Dynamical behaviors of self-interstitial atoms in tungsten, Journal of Nuclear Materials. 437 (2013) 438–444. https://doi.org/10.1016/j.jnucmat.2013.02.075.

[90] F. Dausinger, H. Schultz, Long-Range Migration of Self-Interstitial Atoms in Tungsten, Phys. Rev. Lett. 35 (1975) 1773–1775. https://doi.org/10.1103/PhysRevLett.35.1773.

[91] T. Ahlgren, K. Heinola, N. Juslin, A. Kuronen, Bond-order potential for point and extended defect simulations in tungsten, Journal of Applied Physics. 107 (2010) 033516. https://doi.org/10.1063/1.3298466.

[92] S.P. Fitzgerald, D. Nguyen-Manh, Peierls Potential for Crowdions in the bcc Transition Metals, Phys. Rev. Lett. 101 (2008) 115504. https://doi.org/10.1103/PhysRevLett.101.115504.

[93] J. Heikinheimo, K. Mizohata, J. Räisänen, T. Ahlgren, P. Jalkanen, A. Lahtinen, N. Catarino, E. Alves, F. Tuomisto, Direct observation of mono-vacancy and self-interstitial recovery in tungsten, APL Materials. 7 (2019) 021103. https://doi.org/10.1063/1.5082150.

[94] J.Y. Park, H.C.W. Huang, R.W. Siegel, R.W. Balluffi, A quantitative study of vacancy defects in quenched tungsten by combined field-ion microscopy and electrical resistometry, Philosophical Magazine A. 48 (1983) 397–419. https://doi.org/10.1080/01418618308234901.

[95] W. Xu, J.A. Moriarty, Atomistic simulation of ideal shear strength, point defects, and screw dislocations in bcc transition metals: Mo as a prototype, Phys. Rev. B. 54 (1996) 6941–6951. https://doi.org/10.1103/PhysRevB.54.6941.

[96] H.R. Paneth, The Mechanism of Self-Diffusion in Alkali Metals, Phys. Rev. 80 (1950) 708–711. https://doi.org/10.1103/PhysRev.80.708.

[97] S. Okuda, H. Mizubayashi, Free Migration of Interstitials in Tungsten, Phys. Rev. Lett. 34 (1975) 815–817. https://doi.org/10.1103/PhysRevLett.34.815.

[98] J.A. DiCARLO, C.L. Snead, A.N. Goland, Stage-I Interstitials in Electron-Irradiated Tungsten, Phys. Rev. 178 (1969) 1059–1072. https://doi.org/10.1103/PhysRev.178.1059.

[99] M.J. Attardo, J.M. Galligan, J.G.Y. Chow, Interstitial Removal in Stage-III Recovery of Neutron-Irradiated W, Phys. Rev. Lett. 19 (1967) 73–74. https://doi.org/10.1103/PhysRevLett.19.73.

[100] C. Domain, C.S. Becquart, Ab initio calculations of defects in Fe and dilute Fe-Cu alloys, Phys. Rev. B. 65 (2001) 024103. https://doi.org/10.1103/PhysRevB.65.024103.

[101] C.-C. Fu, F. Willaime, P. Ordejón, Stability and Mobility of Mono- and Di-Interstitials in a-Fe, Phys. Rev. Lett. 92 (2004) 175503. https://doi.org/10.1103/PhysRevLett.92.175503.

[102] P.M. Derlet, D. Nguyen-Manh, S.L. Dudarev, Multiscale modeling of crowdion and vacancy defects in body-centered-cubic transition metals, Phys. Rev. B. 76 (2007) 054107. https://doi.org/10.1103/PhysRevB.76.054107.

[103] K. Heinola, F. Djurabekova, T. Ahlgren, On the stability and mobility of di-vacancies in tungsten, Nucl. Fusion. 58 (2018) 026004. https://doi.org/10.1088/1741-4326/aa99ee.

[104] C.S. Becquart, C. Domain, U. Sarkar, A. DeBacker, M. Hou, Microstructural evolution of irradiated tungsten: Ab initio parameterisation of an OKMC model, Journal of Nuclear Materials. 403 (2010) 75–88. https://doi.org/10.1016/j.jnucmat.2010.06.003.

[105] D. Mason, D. Nguyen-Manh, C. Becquart, An empirical potential for simulating vacancy clusters in tungsten, Journal of Physics: Condensed Matter. 29 (2017). https://doi.org/10.1088/1361-648X/aa9776.

[106] J. Hou, Y.-W. You, X.-S. Kong, J. Song, C.S. Liu, Accurate prediction of vacancy cluster structures and energetics in bcc transition metals, Acta Materialia. 211 (2021) 116860. https://doi.org/10.1016/j.actamat.2021.116860.

[107] R.H.J. Fastenau, L.M. Caspers, A. van Veen, Small clusters of vacancies and helium in molybdenum, Phys. Stat. Sol. (a). 34 (1976) 277–289. https://doi.org/10.1002/pssa.2210340124.

[108] Z.-Z. Li, Y.-H. Li, D. Terentyev, N. Castin, A. Bakaev, G. Bonny, Z. Yang, L. Liang, H.-B. Zhou, F. Gao, G.-H. Lu, Investigating the formation mechanism of void lattice in tungsten under neutron irradiation: from collision cascades to ordered nanovoids, Acta Materialia. 219 (2021) 117239. https://doi.org/10.1016/j.actamat.2021.117239.

[109] N. Castin, A. Dubinko, G. Bonny, A. Bakaev, J. Likonen, A. De Backer, A.E. Sand, K. Heinola, D. Terentyev, The influence of carbon impurities on the formation of loops in tungsten irradiated with self-ions, Journal of Nuclear Materials. 527 (2019) 151808. https://doi.org/10.1016/j.jnucmat.2019.151808.

[110] Y.-W. You, X.-S. Kong, X.-B. Wu, C.S. Liu, Q.F. Fang, J.L. Chen, G.-N. Luo, Interaction of carbon, nitrogen and oxygen with vacancies and solutes in tungsten, RSC Adv. 5 (2015) 23261–23270. https://doi.org/10.1039/C4RA13854F.

[111] A. Alkhamees, H.-B. Zhou, Y.-L. Liu, S. Jin, Y. Zhang, G.-H. Lu, Vacancy trapping behaviors of oxygen in tungsten: A first-principles study, Journal of Nuclear Materials. 437 (2013) 6–10. https://doi.org/10.1016/j.jnucmat.2013.01.317.

[112] L. Yang, B.D. Wirth, Carbon clustering and effect on hydrogen trapping in tungsten: A first-principles study, Computational Materials Science. (n.d.). https://doi.org/10.1016/j.commatsci.2020.109932.

[113] K. Ohsawa, T. Toyama, Y. Hatano, M. Yamaguchi, H. Watanabe, Stable structure of hydrogen atoms trapped in tungsten divacancy, Journal of Nuclear Materials. 527 (2019) 151825. https://doi.org/10.1016/j.jnucmat.2019.151825.

[114] D. Kato, H. Iwakiri, K. Morishita, Formation of vacancy clusters in tungsten crystals under hydrogen-rich condition, Journal of Nuclear Materials. 417 (2011) 1115–1118. https://doi.org/10.1016/j.jnucmat.2010.12.211.

[115] C. Meng, L. Wang, K. Xu, J. Hao, H. Zhou, X. Shu, S. Jin, L. Liang, G.-H. Lu, C.S. Becquart, Object Kinetic Monte Carlo simulation of hydrogen clustering behaviour with vacancies in tungsten, Journal of Nuclear Materials. 526 (2019) 151768. https://doi.org/10.1016/j.jnucmat.2019.151768.

[116] M. Wei, X. Wang, P. Zhang, J. Zhao, P. Zheng, J. Chen, First-principles calculations of transition elements interaction with hydrogen in vanadium, Journal of Nuclear Materials. 564 (2022) 153710. https://doi.org/10.1016/j.jnucmat.2022.153710.

[117] G.-H. Lu, H.-B. Zhou, C.S. Becquart, A review of modelling and simulation of hydrogen behaviour in tungsten at different scales, Nucl. Fusion. 54 (2014) 086001. https://doi.org/10.1088/0029-5515/54/8/086001.

[118] K. Heinola, T. Ahlgren, Diffusion of hydrogen in bcc tungsten studied with first principle calculations, Journal of Applied Physics. 107 (2010) 113531. https://doi.org/10.1063/1.3386515.

[119] Y.-L. Liu, H.-B. Zhou, S. Jin, Y. Zhang, G.-H. Lu, Dissolution and diffusion properties of carbon in tungsten, J. Phys.: Condens. Matter. 22 (2010) 445504. https://doi.org/10.1088/0953-8984/22/44/445504.

[120] Y.-L. Liu, Z.-H. Dai, W.-T. Wang, Influence of carbon–vacancy interaction on carbon and vacancy diffusivity in tungsten, Computational Materials Science. 83 (2014) 1–4. https://doi.org/10.1016/j.commatsci.2013.10.034.

[121] X.-S. Kong, Y.-W. You, C. Song, Q.F. Fang, J.-L. Chen, G.-N. Luo, C.S. Liu, First principles study of foreign interstitial atom (carbon, nitrogen) interactions with intrinsic defects in tungsten, Journal of Nuclear Materials. 430 (2012) 270–278. https://doi.org/10.1016/j.jnucmat.2012.07.008.

[122] A. Vehanen, P. Hautojärvi, J. Johansson, J. Yli-Kauppila, P. Moser, Vacancies and carbon impurities in a - iron: Electron irradiation, Phys. Rev. B. 25 (1982) 762–780. https://doi.org/10.1103/PhysRevB.25.762.

[123] G. Amarendra, R. Rajaraman, S. Rajagopalan, R. Suzuki, T. Ohdaira, Influence of defect-impurity complexes on slow positron yield of a tungsten moderator: Positron annihilation, Auger, and SIMS study, Phys. Rev. B. 69 (2004) 094105. https://doi.org/10.1103/PhysRevB.69.094105.

[124] A. Yabuuchi, M. Tanaka, A. Kinomura, Short positron lifetime at vacancies observed in electron-irradiated tungsten: Experiments and first-principles calculations, Journal of Nuclear Materials. 542 (2020) 152473. https://doi.org/10.1016/j.jnucmat.2020.152473.

[125] A. Alkhamees, Y.-L. Liu, H.-B. Zhou, S. Jin, Y. Zhang, G.-H. Lu, First-principles investigation on dissolution and diffusion of oxygen in tungsten, Journal of Nuclear Materials. 393 (2009) 508–512. https://doi.org/10.1016/j.jnucmat.2009.07.012.

[126] M. Sidibe, Etude du comportement du tungstene sous irradiation : applications aux reacteurs de fusion, phdthesis, Universite d'Orleans, 2014. https://tel.archives-ouvertes.fr/tel-01068634 (accessed January 7, 2021).

[127] X. Yi, M.L. Jenkins, M.A. Kirk, Z. Zhou, S.G. Roberts, In-situ TEM studies of 150 keV W+ ion irradiated W and W-alloys: Damage production and microstructural evolution, Acta Materialia. 112 (2016) 105–120. https://doi.org/10.1016/j.actamat.2016.03.051.

[128] X. Yi, M.L. Jenkins, K. Hattar, P.D. Edmondson, S.G. Roberts, Characterisation of radiation damage in W and W-based alloys from 2 MeV self-ion near-bulk implantations, Acta Materialia. 92 (2015) 163–177. https://doi.org/10.1016/j.actamat.2015.04.015.

[129] The annealing of radiation damage in tungsten investigated by field-ion microscopy, Proc. R. Soc. Lond. A. 312 (1969) 51–63. https://doi.org/10.1098/rspa.1969.0141.

[130] H. Eleveld, A. van Veen, Void growth and thermal desorption of deuterium from voids in tungsten, Journal of Nuclear Materials. 212–215 (1994) 1421–1425. https://doi.org/10.1016/0022-3115(94)91062-6.

[131] A. Debelle, M.F. Barthe, T. Sauvage, First temperature stage evolution of irradiation-induced defects in tungsten studied by positron annihilation spectroscopy, Journal of Nuclear Materials. 376 (2008) 216–221. https://doi.org/10.1016/j.jnucmat.2008.03.002.

[132] F. Ferroni, X. Yi, K. Arakawa, S.P. Fitzgerald, P.D. Edmondson, S.G. Roberts, High temperature annealing of ion irradiated tungsten, Acta Materialia. 90 (2015) 380–393. https://doi.org/10.1016/j.actamat.2015.01.067.

[133] T. Troev, E. Popov, P. Staikov, N. Nankov, T. Yoshiie, Positron simulations of defects in tungsten containing hydrogen and helium, Nuclear Instruments and Methods in Physics Research Section B: Beam Interactions with Materials and Atoms. 267 (2009) 535–541. https://doi.org/10.1016/j.nimb.2008.11.045.

[134] J.M. Campillo Robles, F. Plazaola, Positron Lifetime Calculation of the Elements of the Periodic Table, MSF. 363–365 (2001) 594–596. https://doi.org/10.4028/www.scientific.net/MSF.363-365.594.

[135] P.M.G. Nambissan, P. Sen, Positron annihilation study of the annealing behaviour of alpha induced defects in tungsten, Radiation Effects and Defects in Solids. 124 (1992) 215–221. https://doi.org/10.1080/10420159208220193.

[136] P. Staikov, N. Djourelov, Simulations of 〈100〉 edge and 1/2〈111〉 screw dislocations in a-iron and tungsten and positron lifetime calculations, Physica B: Condensed Matter. 413 (2013) 59–63. https://doi.org/10.1016/j.physb.2012.12.026.

[137] T. Toyama, K. Ami, K. Inoue, Y. Nagai, K. Sato, Q. Xu, Y. Hatano, Deuterium trapping at vacancy clusters in electron/neutron-irradiated tungsten studied by positron annihilation spectroscopy, Journal of Nuclear Materials. 499 (2018) 464–470. https://doi.org/10.1016/j.jnucmat.2017.11.022.

[138] R. Ziegler, H.E. Schaefer, Vacancy Formation in Molybdenum and Tungsten Investigated by Positron Lifetime Measurements, MSF. 15–18 (1987) 145–148. https://doi.org/10.4028/www.scientific.net/MSF.15-18.145.

[139] Y. Xu, Z. Wang, J. Zhu, T. Minamisono, K. Matsuta, Y. Zheng, D. Zhou, G. Xu, E. Du, Y. Fu, M. Fukuda, M. Mihara, S. Zhu, RADIATION EFFECTS IN STAINLESS STEEL AND TUNGSTEN FOR USE IN THE ADS SPALLATION NEUTRON SOURCE SYSTEM, Mod. Phys. Lett. B. 17 (2003) 147–151. https://doi.org/10.1142/S0217984903004981.

[140] S. Zhu, Y. Xu, Z. Wang, Y. Zheng, D. Zhou, E. Du, D. Yuan, M. Fukuda, M. Mihara, K. Matsuta, T. Minamisono, Positron annihilation lifetime spectroscopy on heavy ion irradiated stainless steels and tungsten, Journal of Nuclear Materials. 343 (2005) 330–332. https://doi.org/10.1016/j.jnucmat.2004.11.024.

[141] K. Sato, R. Tamiya, Q. Xu, H. Tsuchida, T. Yoshiie, Detection of deuterium trapping sites in tungsten by thermal desorption spectroscopy and positron annihilation spectroscopy, Nuclear Materials and Energy. 9 (2016) 554–559. https://doi.org/10.1016/j.nme.2016.09.014.

[142] H.-E. Schaefer, Investigation of Thermal Equilibrium Vacancies in Metals by Positron Annihilation, Phys. Stat. Sol. (a). 102 (1987) 47–65. https://doi.org/10.1002/pssa.2211020104.

[143] T.E.M. Staab, R. Krause-Rehberg, B. Vetter, B. Kieback, G. Lange, P. Klimanek, The influence of microstructure on the sintering process in crystalline metal powders investigated by positron lifetime spectroscopy: II. Tungsten powders with different powder-particle sizes, J. Phys.: Condens. Matter. 11 (1999) 1787–1806. https://doi.org/10.1088/0953-8984/11/7/010.

[144] J. de Vries, Positron lifetime technique with applications in materials science, (1987). http://inis.iaea.org/Search/search.aspx?orig_q=RN:20035496 (accessed February 23, 2021).

[145] O.V. Ogorodnikova, M. Majerle, J. Čížek, S. Simakov, V.V. Gann, P. Hruška, J. Kameník, J. Pospíšil, M. Štefánik, M. Vinš, Positron annihilation spectroscopy study of radiation-induced defects in W and Fe irradiated with neutrons with different spectra, Scientific Reports. 10 (2020) 18898. https://doi.org/10.1038/s41598-020-75737-8.

[146] O.V. Ogorodnikova, M. Majerle, V.V. Gann, J. Čížek, P. Hruška, S. Simakov, M. Štefánik, V. Zach, Verification of the theory of primary radiation damage by comparison with experimental data, Journal of Nuclear Materials. 525 (2019) 22–31. https://doi.org/10.1016/j.jnucmat.2019.07.019.

[147] H.A. Filius, Defects in nuclear fusion reactor materials studied by thermal gas desorption spectrometry, (1992). https://repository.tudelft.nl/islandora/object/uuid%3A0b511f6f-4199-43be-b76b-0d31bf49e4b1 (accessed April 13, 2022).

[148] K. Sato, A. Hirosako, K. Ishibashi, Y. Miura, Q. Xu, M. Onoue, Y. Fukutoku, T. Onitsuka, M. Hatakeyama, S. Sunada, T. Yoshiie, Quantitative evaluation of hydrogen atoms trapped at single vacancies in tungsten using positron annihilation lifetime measurements: Experiments and theoretical calculations, Journal of Nuclear Materials. 496 (2017) 9–17. https://doi.org/10.1016/j.jnucmat.2017.09.002.

[149] M. Zibrov, W. Egger, J. Heikinheimo, M. Mayer, F. Tuomisto, Vacancy cluster growth and thermal recovery in hydrogen-irradiated tungsten, Journal of Nuclear Materials. (n.d.). https://doi.org/10.1016/j.jnucmat.2020.152017.

[150] F. Tuomisto, I. Makkonen, Defect identification in semiconductors with positron annihilation: Experiment and theory, Rev. Mod. Phys. 85 (2013) 1583–1631. https://doi.org/10.1103/RevModPhys.85.1583.

[151] Molybdenum, (n.d.). https://www.plansee.com/en/materials/www.plansee.com/en/materials/molybdenum.html (accessed January 22, 2022).

[152] M. Minissale, G.T. Zeweldi, R. Bisson, L. Gallais, The effect of surface temperature on optical properties of molybdenum mirrors in the visible and near-infrared domains, Nucl. Fusion. 58 (2018) 096012. https://doi.org/10.1088/1741-4326/aaca03.

[153] G. Ciraolo, S. Di Genova, H. Yang, A. Gallo, N. Fedorczak, H. Bufferand, J.P. Gunn, P. Tamain, R. Guirlet, C. Guillemaut, C. Desgranges, C. Bourdelle, E. Tsitrone, J.B. Bucalossi, M. Scotto D'Abusco, E. Serre, Y. Marandet, M. Raghunathan, A. Sepetys, J. Romazanov, A. Kirschner, S. Brezinsek, Interpretative modeling of impurity transport and tungsten sources in WEST boundary plasma, Nucl. Fusion. (2021). https://doi.org/10.1088/1741-4326/ac2439.

[154] A. Hakola, J. Likonen, A. Lahtinen, T. Vuoriheimo, M. Groth, H.A. Kumpulainen, M. Balden, K. Krieger, M. Mayer, T. Schwarz-Selinger, S. Brezinsek, M. Kelemen, S. Markelj, M. Barac, S. Gouasmia, I. Bogdanović Radović, A. Uccello, E. Vassallo, D. Dellasega, M. Passoni, M. Sala, E. Bernard, M. Diez, C. Guillemaut, E. Tsitrone, Gross and net erosion balance of plasma-facing materials in full-W tokamaks, Nucl. Fusion. (2021). https://doi.org/10.1088/1741-4326/ac22d2.

[155] R.E. Stoller, M.B. Toloczko, G.S. Was, A.G. Certain, S. Dwaraknath, F.A. Garner, On the use of SRIM for computing radiation damage exposure, Nuclear Instruments and Methods in Physics Research Section B: Beam Interactions with Materials and Atoms. 310 (2013) 75–80. https://doi.org/10.1016/j.nimb.2013.05.008.

[156] W.A. McKinley, H. Feshbach, The Coulomb Scattering of Relativistic Electrons by Nuclei, Phys. Rev. 74 (1948) 1759–1763. https://doi.org/10.1103/PhysRev.74.1759.

[157] P.D. Lesueur, Cascades de deplacement dam les solides polyatomiques, Philosophical Magazine A. 44 (1981) 905–929. https://doi.org/10.1080/01418618108239557.

[158] A. Dunlop, D. Lesueur, J. Dural, Damage production in iron during high-energy ion irradiation: Experimental and theoretical determinations, Nuclear Instruments and Methods in Physics Research Section B: Beam Interactions with Materials and Atoms. 42 (1989) 182–192. https://doi.org/10.1016/0168-583X(89)90705-2.

[159] HAUTOJÄRVI, CORBEL C., POSITRON SPECTROSCOPY OF DEFECTS IN METALS AND SEMICONDUCTORS, ENFI. 125 (1995) 491–532. HTTPS://DOI.ORG/10.3254/978-1-61499-211-0-491.

[160] R. KRAUSE-REHBERG, H.S. LEIPNER, POSITRON ANNIHILATION IN SEMICONDUCTORS: DEFECT STUDIES, SPRINGER-VERLAG, BERLIN HEIDELBERG, 1999. HTTP://WWW.SPRINGER.COM/GP/BOOK/9783540643715 (ACCESSED OCTOBER 19, 2021).

[161] J. ČÍŽEK, CHARACTERIZATION OF LATTICE DEFECTS IN METALLIC MATERIALS BY POSITRON ANNIHILATION SPECTROSCOPY: A REVIEW, JOURNAL OF MATERIALS SCIENCE & TECHNOLOGY. 34 (2018) 577–598. HTTPS://DOI.ORG/10.1016/J.JMST.2017.11.050.

[162] M. FORSTER, W. CLAUDY, H. HERMES, M. KOCH, K. MAIER, J. MAJOR, H. STOLL, H.E. SCHAEFER, HIGH-TEMPERATURE EQUILIBRIUM VACANCY FORMATION IN CERAMIC MATERIALS STUDIED BY POSITRON ANNIHILATION, MSF. 105–110 (1992) 1005–1012. HTTPS://DOI.ORG/10.4028/WWW.SCIENTIFIC.NET/MSF.105-110.1005.

[163] R. CHEHAB, POSITRON SOURCES, IN: EUROPEAN ORGANIZATION FOR NUCLEAR RESEARCH (CERN), 1994: P. 537.

[164] M.F. L'ANNUNZIATA, TABLE OF RADIOACTIVE ISOTOPES, IN: HANDBOOK OF RADIOACTIVITY ANALYSIS, ELSEVIER, 2012: PP. 1305–1360. HTTPS://DOI.ORG/10.1016/B978-0-12-384873-4.15001-7.

[165] J. DRYZEK, D. SINGLETON, IMPLANTATION PROFILE AND LINEAR ABSORPTION COEFFICIENTS FOR POSITRONS INJECTED IN SOLIDS FROM RADIOACTIVE SOURCES 22NA AND 68GE \ 68GA, NUCLEAR INSTRUMENTS AND METHODS IN PHYSICS RESEARCH SECTION B: BEAM INTERACTIONS WITH MATERIALS AND ATOMS. 252 (2006) 197–204. HTTPS://DOI.ORG/10.1016/J.NIMB.2006.08.017.

[166] E. SOININEN, J. MÄKINEN, D. BEYER, P. HAUTOJÄRVI, HIGH-TEMPERATURE POSITRON DIFFUSION IN SI, GAAS, AND GE, PHYS. REV. B. 46 (1992) 13104–13118. HTTPS://DOI.ORG/10.1103/PHYSREVB.46.13104.

[167] P. ASOKA-KUMAR, K.G. LYNN, IMPLANTATION PROFILE OF LOW-ENERGY POSITRONS IN SOLIDS, APPL. PHYS. LETT. 57 (1990) 1634–1636. HTTPS://DOI.ORG/10.1063/1.104071.

[168] X. NING, X. CAO, C. LI, D. LI, P. ZHANG, Y. GONG, R. XIA, B. WANG, L. WEI, MODIFICATION OF SOURCE CONTRIBUTION IN PALS BY SIMULATION USING GEANT4 CODE, NUCLEAR INSTRUMENTS AND METHODS IN PHYSICS RESEARCH SECTION B: BEAM INTERACTIONS WITH MATERIALS AND ATOMS. 397 (2017) 75–81. HTTPS://DOI.ORG/10.1016/J.NIMB.2017.02.038.

[169] J.A. BAKER, N.B. CHILTON, K.O. JENSEN, A.B. WALKER, P.G. COLEMAN, MATERIAL DEPENDENCE OF POSITRON IMPLANTATION DEPTHS, APPL. PHYS. LETT. 59 (1991) 2962–2964. HTTPS://DOI.ORG/10.1063/1.105812.

[170] A. VEHANEN, K. SAARINEN, P. HAUTOJÄRVI, H. HUOMO, PROFILING MULTILAYER STRUCTURES WITH MONOENERGETIC POSITRONS, PHYS. REV. B. 35 (1987) 4606–4610. HTTPS://DOI.ORG/10.1103/PHYSREVB.35.4606.

[171] C. HE, EXPERIMENTAL STUDY OF THE INTERACTION OF VACANCY DEFECTS WITH Y, O AND TI SOLUTES TO BETTER UNDERSTAND THEIR ROLES IN THE NANOPARTICLES FORMATION IN ODS STEELS, THESE DE DOCTORAT, ORLÉANS, 2014. HTTP://WWW.THESES.FR/2014ORLE2057 (ACCESSED JANUARY 17, 2021).

[172] W. ASPLET, ETUDE DES INTERACTIONS ENTRE LES DEFAUTS LACUNAIRES ET LES SOLUTES Y,O, TI POUR MIEUX COMPRENDRE LEUR ROLE DANS LA FORMATION DES NANOPARTICULES D'OXYDES DANS LES ACIERS ODS, (N.D.) 269.

[173] J. DRYZEK, P. HORODEK, GEANT4 SIMULATION OF SLOW POSITRON BEAM IMPLANTATION PROFILES, NUCLEAR INSTRUMENTS AND METHODS IN PHYSICS RESEARCH SECTION B: BEAM INTERACTIONS WITH MATERIALS AND ATOMS. 266 (2008) 4000–4009. HTTPS://DOI.ORG/10.1016/J.NIMB.2008.06.033.

[174] P.J. SCHULTZ, K.G. LYNN, INTERACTION OF POSITRON BEAMS WITH SURFACES, THIN FILMS, AND INTERFACES, REV. MOD. PHYS. 60 (1988) 701–779. HTTPS://DOI.ORG/10.1103/REVMODPHYS.60.701.

[175] N.G.H. MEYENDORF, P.B. NAGY, S.I. ROKHLIN, EDS., NONDESTRUCTIVE MATERIALS CHARACTERIZATION: WITH APPLICATIONS TO AEROSPACE MATERIALS, SPRINGER BERLIN HEIDELBERG, BERLIN, HEIDELBERG, 2004. HTTPS://DOI.ORG/10.1007/978-3-662-08988-0.

[176] M.-F. BARTHE, C. CORBEL, G. BLONDIAUX, CARACTERISATION DE DEFAUTS LACUNAIRES PAR ANNIHILATION DE POSITONS, (2003) 26.

[177] P.A.M. DIRAC, ON THE ANNIHILATION OF ELECTRONS AND PROTONS, MATH. PROC. CAMB. PHIL. SOC. 26 (1930) 361–375. HTTPS://DOI.ORG/10.1017/S0305004100016091.

[178] S. TANG, A. ILDERTON, B. KING, ONE-PHOTON PAIR ANNIHILATION IN PULSED PLANE-WAVE BACKGROUNDS, PHYS. REV. A. 100 (2019) 062119. HTTPS://DOI.ORG/10.1103/PHYSREVA.100.062119.

[179] N.P. Kalashnikov, E.I. Mulyarchik, A.S. Olchak, Single-photon Annihilation of the Channeled Positrons, Physics Procedia. 74 (2015) 165–168. https://doi.org/10.1016/j.phpro.2015.09.180.

[180] M.J. Puska, R.M. Nieminent, Defect spectroscopy with positrons: a general calculational method, (n.d.) 15.

[181] P. Kirkegaard, M. Eldrup, The least-squares fitting programme POSITRONFIT: principles and formulas, Riso. (1971).

[182] T.E.M. Staab, B. Somieski, R. Krause-Rehberg, The data treatment influence on the spectra decomposition in positron lifetime spectroscopy Part 2: The effect of source corrections, Nuclear Instruments and Methods in Physics Research Section A: Accelerators, Spectrometers, Detectors and Associated Equipment. 381 (1996) 141–151. https://doi.org/10.1016/0168-9002(96)00585-2.

[183] S. McGuire, D.J. Keeble, Positron lifetimes of polycrystalline metals: A positron source correction study, Journal of Applied Physics. 100 (2006) 103504. https://doi.org/10.1063/1.2384794.

[184] M. Bertolaccini, L. Zappa, Source-supporting foil effect on the shape of positron time annihilation spectra, Nuov Cim B. 52 (1967) 487–494. https://doi.org/10.1007/BF02711092.

[185] M. Hakala, M.J. Puska, R.M. Nieminen, Momentum distributions of electron-positron pairs annihilating at vacancy clusters in Si, Phys. Rev. B. 57 (1998) 7621–7627. https://doi.org/10.1103/PhysRevB.57.7621.

[186] P. Asoka-Kumar, M. Alatalo, V.J. Ghosh, A.C. Kruseman, B. Nielsen, K.G. Lynn, Increased Elemental Specificity of Positron Annihilation Spectra, Phys. Rev. Lett. 77 (1996) 2097–2100. https://doi.org/10.1103/PhysRevLett.77.2097.

[187] S. Szpala, P. Asoka-Kumar, B. Nielsen, J.P. Peng, S. Hayakawa, K.G. Lynn, H.-J. Gossmann, Defect identification using the core-electron contribution in Doppler-broadening spectroscopy of positron-annihilation radiation, Phys. Rev. B. 54 (1996) 4722–4731. https://doi.org/10.1103/PhysRevB.54.4722.

[188] R. Rementeria, R. Domínguez-Reyes, C. Capdevila, C. Garcia-Mateo, F.G. Caballero, Positron Annihilation Spectroscopy Study of Carbon-Vacancy Interaction in Low-Temperature Bainite, Sci Rep. 10 (2020) 487. https://doi.org/10.1038/s41598-020-57469-x.

[189] C. He, T. Yoshiie, Q. Xu, K. Sato, S. Peneva, T.D. Troev, Detection of hydrogen in neutron-irradiated nickel using positron lifetime spectroscopy, Phil. Mag. 89 (2009) 1183–1195. https://doi.org/10.1080/14786430902915404.

[190] H.D. Smyth, Primary and Secondary Products of Ionization in Hydrogen, Phys. Rev. 25 (1925) 452–468. https://doi.org/10.1103/PhysRev.25.452.

[191] J.J. Mitchell, R.H. Perkins, F.F. Coleman, Secondary Processes of Ion Production in the Mass Spectrometer, The Journal of Chemical Physics. 16 (1948) 835–836. https://doi.org/10.1063/1.1747005.

[192] Dynamic Secondary Ion Mass Spectrometry, (n.d.) 43.

[193] Brochure IMS 7f 21x28 BAT, (n.d.) 8.

[194] F. Chamssedine, T. Sauvage, S. Peuget, DIADDHEM set-up: New IBA facility for studying the helium behavior in nuclear glasses, Nuclear Instruments and Methods in Physics Research Section B: Beam Interactions with Materials and Atoms. 268 (2010) 1862–1866. https://doi.org/10.1016/j.nimb.2010.02.031.

[195] E. Kashy, R.R. Perry, J.R. Risser, Excited States in N 14 from C 12 (d , d) C 12 , C 12 (d , p 0) C 13 , and C 12 (d , p 1) C 1 3 *, Phys. Rev. 117 (1960) 1289–1296. https://doi.org/10.1103/PhysRev.117.1289.

[196] G. Martin, T. Sauvage, P. Desgardin, P. Garcia, G. Carlot, M.F. Barthe, Accurate automated non-resonant NRA depth profiling: Application to the low 3He concentration detection in UO2 and SiC, Nuclear Instruments and Methods in Physics Research Section B: Beam Interactions with Materials and Atoms. 258 (2007) 471–478. https://doi.org/10.1016/j.nimb.2007.01.288.

[197] A. Hasegawa, M. Fukuda, K. Yabuuchi, S. Nogami, Neutron irradiation effects on the microstructural development of tungsten and tungsten alloys, Journal of Nuclear Materials. 471 (2016) 175–183. https://doi.org/10.1016/j.jnucmat.2015.10.047.

[198] M.L. Jenkins, M.A. Kirk, Characterization of Radiation Damage by Transmission Electron Microscopy, IOP Publishing Ltd, 2001. https://doi.org/10.1887/075030748X.

[199] B. Yao, D.J. Edwards, R.J. Kurtz, G.R. Odette, T. Yamamoto, Multislice simulation of transmission electron microscopy imaging of helium bubbles in Fe, Journal of Electron Microscopy. 61 (2012) 393–400. https://doi.org/10.1093/jmicro/dfs065.

[200] A.V. Michel, G. Carlot, C. Onofri, C. Sabathier, M. Cabié, M. Dumont, TEM characterisation of helium platelets in implanted uranium dioxide, Journal of Nuclear Materials. 528 (2020) 151832. https://doi.org/10.1016/j.jnucmat.2019.151832.

[201] Z. Hu, P. Desgardin, C. Genevois, J. Joseph, B. Décamps, R. Schäublin, M.-F. Barthe, Effect of purity on the vacancy defects induced in self–irradiated tungsten: A combination of PAS and TEM, Journal of Nuclear Materials. 556 (2021) 153175. https://doi.org/10.1016/j.jnucmat.2021.153175.

[202] A. Vehanen, K.G. Lynn, P.J. Schultz, M. Eldrup, Improved slow-positron yield using a single crystal tungsten moderator, Appl. Phys. A. 32 (1983) 163–167. https://doi.org/10.1007/BF00616613.

[203] E. Lassner, W.-D. Schubert, Tungsten: Properties, Chemistry, Technology of the Element, Alloys, and Chemical Compounds, Springer US, Boston, MA, 1999. https://doi.org/10.1007/978-1-4615-4907-9.

[204] F.A. Stevie, R.G. Wilson, D.S. Simons, M.I. Current, P.C. Zalm, Review of secondary ion mass spectrometry characterization of contamination associated with ion implantation, Journal of Vacuum Science & Technology B: Microelectronics and Nanometer Structures Processing, Measurement, and Phenomena. 12 (1994) 2263–2279. https://doi.org/10.1116/1.587753.

[205] M.Y. Tsai, B.G. Streetman, R.J. Blattner, C.A. Evans, Study of Surface Contamination Produced during High Dose Ion Implantation, J. Electrochem. Soc. 126 (1979) 98. https://doi.org/10.1149/1.2128999.

[206] S. Hasanzadeh, R. Schäublin, B. Décamps, V. Rousson, E. Autissier, M.F. Barthe, C. Hébert, Three-dimensional scanning transmission electron microscopy of dislocation loops in tungsten, Micron. 113 (2018) 24–33. https://doi.org/10.1016/j.micron.2018.05.010.

[207] Z. Zhou, S.L. Dudarev, M.L. Jenkins, A.P. Sutton, M.A. Kirk, Diffraction imaging and diffuse scattering by small dislocation loops, Journal of Nuclear Materials. 367–370 (2007) 305–310. https://doi.org/10.1016/j.jnucmat.2007.03.135.

[208] K. Arakawa, M.-C. Marinica, S. Fitzgerald, L. Proville, D. Nguyen-Manh, S.L. Dudarev, P.-W. Ma, T.D. Swinburne, A.M. Goryaeva, T. Yamada, T. Amino, S. Arai, Y. Yamamoto, K. Higuchi, N. Tanaka, H. Yasuda, T. Yasuda, H. Mori, Quantum de-trapping and transport of heavy defects in tungsten, Condensed Matter Physics. (n.d.). https://doi.org/10.1038/s41563-019-0584-0.

[209] T. Amino, K. Arakawa, H. Mori, Activation energy for long-range migration of self-interstitial atoms in tungsten obtained by direct measurement of radiation-induced point-defect clusters, Philosophical Magazine Letters. 91 (2011) 86–96. https://doi.org/10.1080/09500839.2010.533133.

[210] G.S. Was, T. Allen, Intercomparison of microchemical evolution under various types of particle irradiation, Journal of Nuclear Materials. 205 (1993) 332–338. https://doi.org/10.1016/0022-3115(93)90097-I.

[211] C.J. Ortiz, M.J. Caturla, Cascade damage evolution: rate theory versus kinetic Monte Carlo simulations, J Computer-Aided Mater Des. 14 (2007) 171–181. https://doi.org/10.1007/s10820-007-9082-9.

[212] R.A. Johnson, Point-defect calculations for tungsten, Phys. Rev. B. 27 (1983) 2014–2018. https://doi.org/10.1103/PhysRevB.27.2014.

[213] K. Heinola, T. Ahlgren, K. Nordlund, J. Keinonen, Hydrogen interaction with point defects in tungsten, Phys. Rev. B. 82 (2010) 094102. https://doi.org/10.1103/PhysRevB.82.094102.

[214] A. De Backer, P.E. Lhuillier, C.S. Becquart, M.F. Barthe, Modelling of the implantation and the annealing stages of 800keV 3He implanted tungsten: Formation of nanovoids in the near surface region, Journal of Nuclear Materials. 429 (2012) 78–91. https://doi.org/10.1016/j.jnucmat.2012.05.024.

[215] H.H. Neely, D.W. Keefer, A. Sosin, Electron Irradiation and Recovery of Tungsten, Phys. Stat. Sol. (b). 28 (1968) 675–682. https://doi.org/10.1002/pssb.19680280225.

[216] O.S. Oen, CROSS SECTIONS FOR ATOMIC DISPLACEMENTS IN SOLIDS BY FAST ELECTRONS, Oak Ridge National Lab., Tenn., 1965. https://doi.org/10.2172/4600067.

[217] N. Igata, S. Sato, FIM observation of point defect clusters in ion-implanted tungsten surfaces, Nanotechnology. 4 (1993) 213–217. https://doi.org/10.1088/0957-4484/4/4/006.

[218] Y. Kamimura, T. Tsutsumi, E. Kuramoto, Influence of Dislocations on Positron Lifetime in Iron, J. Phys. Soc. Jpn. 66 (1997) 3090–3096. https://doi.org/10.1143/JPSJ.66.3090.

[219] F. Wan, Q. Zhan, Y. Long, S. Yang, G. Zhang, Y. Du, Z. Jiao, S. Ohnuki, The behavior of vacancy-type dislocation loops under electron irradiation in iron, Journal of Nuclear Materials. 455 (2014) 253–257. https://doi.org/10.1016/j.jnucmat.2014.05.048.

[220] B. Somieski, T.E.M. Staab, R. Krause-Rehberg, The data treatment influence on the spectra decomposition in positron lifetime spectroscopy Part 1: On the interpretation of multi-component analysis studied by Monte Carlo simulated model spectra, Nuclear Instruments and Methods in Physics Research Section A: Accelerators, Spectrometers, Detectors and Associated Equipment. 381 (1996) 128–140. https://doi.org/10.1016/0168-9002(96)00584-0.

[221] A. Hollingsworth, M.-F. Barthe, M.Y. Lavrentiev, P.M. Derlet, S.L. Dudarev, D.R. Mason, Z. Hu, P. Desgardin, J. Hess, S. Davies, B. Thomas, H. Salter, E.F.J. Shelton, K. Heinola, K. Mizohata, A. De Backer, A. Baron-Wiechec, I. Jepu, Y. Zayachuk, A. Widdowson, E. Meslin, A. Morellec, Comparative study of deuterium retention and vacancy content of self-ion irradiated tungsten, Journal of Nuclear Materials. 558 (2022) 153373. https://doi.org/10.1016/j.jnucmat.2021.153373.

[222] Q. Yang, P. Olsson, Full energy range primary radiation damage model, Phys. Rev. Materials. 5 (2021) 073602. https://doi.org/10.1103/PhysRevMaterials.5.073602.

[223] R.E. Stoller, Primary Radiation Damage Formation, in: Comprehensive Nuclear Materials, Elsevier, 2012: pp. 293–332. https://doi.org/10.1016/B978-0-08-056033-5.00027-6.

[224] C.S. Becquart, A. De Backer, C. Domain, Atomistic Modeling of Radiation Damage in Metallic Alloys, in: S. Schmauder, C.-S. Chen, K.K. Chawla, N. Chawla, W. Chen, Y. Kagawa, C.-H. Hsueh (Eds.), Handbook of Mechanics of Materials, Springer, Singapore, 2018: pp. 1–30. https://doi.org/10.1007/978-981-10-6855-3_21-1.

[225] O.V. Ogorodnikova, V.V. Gann, M.S. Zibrov, Yu.M. Gasparyan, Comparison of Deuterium Retention in Tungsten Pre-damaged with Energetic Electrons, Self-ions and Neutrons, Physics Procedia. 71 (2015) 41–46. https://doi.org/10.1016/j.phpro.2015.08.309.

[226] A. Reza, H. Yu, K. Mizohata, F. Hofmann, Thermal diffusivity degradation and point defect density in self-ion implanted tungsten, Acta Materialia. 193 (2020) 270–279. https://doi.org/10.1016/j.actamat.2020.03.034.

[227] R. t Hoen, B. Tyburska-Püschel, K. Ertl, M. Mayer, J. Rapp, A. Kleyn, P.A. Zeijlmans van Emmichoven, Saturation of deuterium retention in self-damaged tungsten exposed to high-flux plasmas, Nuclear Fusion. 52 (2012) 023008. https://doi.org/10.1088/0029-5515/52/2/023008.

[228] P.M. Derlet, S.L. Dudarev, Microscopic structure of a heavily irradiated material, Phys. Rev. Materials. 4 (2020) 023605. https://doi.org/10.1103/PhysRevMaterials.4.023605.

[229] M.-C. Marinica, L. Ventelon, M.R. Gilbert, L. Proville, S.L. Dudarev, J. Marian, G. Bencteux, F. Willaime, Interatomic potentials for modelling radiation defects and dislocations in tungsten, J. Phys.: Condens. Matter. 25 (2013) 395502. https://doi.org/10.1088/0953-8984/25/39/395502.

[230] D.R. Mason, S. Das, P.M. Derlet, S.L. Dudarev, A.J. London, H. Yu, N.W. Phillips, D. Yang, K. Mizohata, R. Xu, F. Hofmann, Observation of Transient and Asymptotic Driven Structural States of Tungsten Exposed to Radiation, Phys. Rev. Lett. 125 (2020) 225503. https://doi.org/10.1103/PhysRevLett.125.225503.

[231] O.V. Ogorodnikova, Z. Zhou, K. Sugiyama, M. Balden, G. Pintsuk, Y. Gasparyan, V. Efimov, Surface modification and deuterium retention in reduced-activation steels under low-energy deuterium plasma exposure. Part II: steels pre-damaged with 20 MeV W ions and high heat flux, Nucl. Fusion. 57 (2016) 036011. https://doi.org/10.1088/1741-4326/57/3/036011.

[232] A. Hollingsworth, M.Yu. Lavrentiev, R. Watkins, A.C. Davies, S. Davies, R. Smith, D.R. Mason, A. Baron-Wiechec, Z. Kollo, J. Hess, I. Jepu, J. Likonen, K. Heinola, K. Mizohata, E. Meslin, M.-F. Barthe, A. Widdowson, I.S. Grech, K. Abraham, E. Pender, A. McShee, Y. Martynova, M. Freisinger, A. De Backer, Comparative study

OF DEUTERIUM RETENTION IN IRRADIATED EUROFER AND FE–CR FROM A NEW ION IMPLANTATION MATERIALS FACILITY, NUCL. FUSION. 60 (2020) 016024. HTTPS://DOI.ORG/10.1088/1741-4326/AB546E.

[233] Y. KANZAKI, N. SEKIMURA, S. ISHINO, ACCUMULATION PROCESSES OF CASCADE DAMAGE UNDER HEAVY ION IRRADIATION, JOURNAL OF NUCLEAR MATERIALS. 191–194 (1992) 1119–1122. HTTPS://DOI.ORG/10.1016/0022-3115(92)90649-6.

[234] S.J. ZINKLE, B.N. SINGH, ANALYSIS OF DISPLACEMENT DAMAGE AND DEFECT PRODUCTION UNDER CASCADE DAMAGE CONDITIONS, JOURNAL OF NUCLEAR MATERIALS. 199 (1993) 173–191. HTTPS://DOI.ORG/10.1016/0022-3115(93)90140-T.

[235] S. AGARWAL, M.O. LIEDKE, A.C.L. JONES, E. REED, A.A. KOHNERT, B.P. UBERUAGA, Y.Q. WANG, J. COOPER, D. KAOUMI, N. LI, R. AUGUSTE, P. HOSEMANN, L. CAPOLUNGO, D.J. EDWARDS, M. BUTTERLING, E. HIRSCHMANN, A. WAGNER, F.A. SELIM, A NEW MECHANISM FOR VOID-CASCADE INTERACTION FROM NONDESTRUCTIVE DEPTH-RESOLVED ATOMIC-SCALE MEASUREMENTS OF ION IRRADIATION–INDUCED DEFECTS IN FE, SCIENCE ADVANCES. 6 (2020) EABA8437. HTTPS://DOI.ORG/10.1126/SCIADV.ABA8437.

[236] A.F. CALDER, D.J. BACON, A.V. BARASHEV, Y.N. OSETSKY, COMPUTER SIMULATION OF CASCADE DAMAGE IN A-IRON WITH CARBON IN SOLUTION, JOURNAL OF NUCLEAR MATERIALS. 382 (2008) 91–95. HTTPS://DOI.ORG/10.1016/J.JNUCMAT.2008.08.016.

[237] L. YANG, Z. J. BERGSTROM, B. D. WIRTH, EFFECT OF INTERATOMIC POTENTIAL ON THE ENERGETICS OF HYDROGEN AND HELIUM-VACANCY COMPLEXES IN BULK, OR NEAR SURFACES OF TUNGSTEN, JOURNAL OF NUCLEAR MATERIALS. (N.D.). HTTPS://DOI.ORG/S0022311518310766.

[238] P. ASOKA-KUMAR, J.H. HARTLEY, R.H. HOWELL, P.A. STERNE, D. AKERS, V. SHAH, A. DENISON, DIRECT OBSERVATION OF CARBON-DECORATED DEFECTS IN FATIGUED TYPE 304 STAINLESS STEEL USING POSITRON ANNIHILATION SPECTROSCOPY, ACTA MATERIALIA. 50 (2002) 1761–1770. HTTPS://DOI.ORG/10.1016/S1359-6454(02)00027-7.

[239] X.-Z. TANG, Z. GUO, PLASMA POWER RECYCLING AT THE DIVERTOR SURFACE, FUSION SCIENCE AND TECHNOLOGY. 71 (2017) 110–121. HTTPS://DOI.ORG/10.13182/FST16-119.

[240] H.Q. WANG, H.Y. GUO, T.W. PETRIE, A.W. LEONARD, D.M. THOMAS, J.G. WATKINS, EFFECTS OF LOW-Z AND HIGH-Z IMPURITIES ON DIVERTOR DETACHMENT AND PLASMA CONFINEMENT, NUCLEAR MATERIALS AND ENERGY. 12 (2017) 942–947. HTTPS://DOI.ORG/10.1016/J.NME.2017.01.027.

[241] M. WEI, X. WANG, P. ZHANG, J. ZHAO, P. ZHENG, J. CHEN, FIRST-PRINCIPLES CALCULATIONS OF TRANSITION ELEMENTS INTERACTION WITH HYDROGEN IN VANADIUM, JOURNAL OF NUCLEAR MATERIALS. 564 (2022) 153710. HTTPS://DOI.ORG/10.1016/J.JNUCMAT.2022.153710.

Presentations at conferences

Oral Presentations

- *Oct/2020* **The Nuclear Material Conference NuMAT 2020**

  Combination of PAS and TEM to characterize defects in self–irradiated tungsten for fusion application
  ***Z. Hu**, M-F. Barthe, P. Desgardin, C. Genevois J.Joseph B. Decamps, R. Schaublin*

  ------***Selected paper for JNM***

- *Jan/2021* **EMIR&A** users' meeting

  Combination of PAS and TEM to characterize defects in self–irradiated tungsten for fusion application
  ***Z. Hu**, M-F. Barthe, P. Desgardin, C. Genevois J.Joseph B. Decamps, R. Schaublin*

- *Mar/2021* **GDR SciNEE doctorant**

  Caractérisation des défauts lacunaires dans le tungstène sous irradiation pour l'application de la fusion
  Z.Hu

- *June/2021* European Materials Research Society spring meeting **E-MRS 2021**

  Combination of PAS and TEM to characterize defects in self–irradiated tungsten for fusion application
  ***Z. Hu**, M-F. Barthe, P. Desgardin, C. Genevois J.Joseph B. Decamps, R. Schaublin*

Poster

- *Oct/2021* 20th international conference on Fusion Reactor Materials **ICFRM-20**

  Experimental investigations on the light-element impurities (Carbon, Oxygen) in irradiated tungsten
  ***Z. Hu**, F. Jomard, M-F. Barthe, P. Desgardin, J. Joseph*

  ------***Best poster prize***

List of publications

Published

- Z. Hu, P. Desgardin, C. Genevois, J. Joseph, B. Décamps, R. Schäublin, M.-F. Barthe, '*Effect of purity on the vacancy defects induced in self–irradiated tungsten: A combination of PAS and TEM'*, Journal of Nuclear Materials. 556 (2021) 153175. https://doi.org/10.1016/j.jnucmat.2021.153175.

- Hollingsworth, M.-F. Barthe, M.Y. Lavrentiev, P.M. Derlet, S.L. Dudarev, D.R. Mason, Z. Hu, P. Desgardin, J. Hess, S. Davies, B. Thomas, H. Salter, E.F.J. Shelton, K. Heinola, K. Mizohata, A. De Backer, A. Baron-Wiechec, I. Jepu, Y. Zayachuk, A. Widdowson, E. Meslin, A. Morellec, '*Comparative study of deuterium retention and vacancy content of self-ion irradiated tungsten, Journal of Nuclear Materials'*. 558 (2022) 153373. https://doi.org/10.1016/j.jnucmat.2021.153373.

Under review

- Qigui Yang, Zhiwei Hu, Ilja Makkonenc, Pierre Desgardin, Werner Egger, Marie-France Barthe, Pär Olsson '*A combined experimental and theoretical study of small and large vacancy clusters in tungsten'* submitted to Journal of Nuclear Materials

In preparation

- Hollingsworth, M.-F. Barthe, Z. Hu, A. Wohlers, M.Yu. Lavrentiev, P. Desgardin, Y. Zayachuk, R. Brown, A. Mansourian, H. Smith, E. Garciadiego-Ortega, A. Cooper, A. Widdowson, N. Peng, J. Likonen, K. Mizohata, K. Heinola, E. Meslin, A. Morellec, A. De Backer '*New results from a study of hydrogen isotope retention as a function of vacancy content of self-ion irradiated reactor materials'*

- A. De Backer, A. Baron-Wiechec, M.F. Barthe, C.S. Becquart, B. Butler, A. Davies, K. Heinola, J. Hess, A. Hollingsworth, I. Jepu, Z. Kollo, J. Likonen, M. Laventriev, E. Meslin,A. Morellec, S. Van Boxel, A. Widdowson, and Z.Hu *Deuterium decoration of defects in damaged tungsten seen by Positron Annihilation Spectroscopy, Thermal Desorption Spectroscopy and Second Ion Mass Spectroscopy*

Chapitre V: Résumé du manuscrit

V.1 Introduction

Dans le contexte actuel de besoin de développer des solutions alternatives pour répondre à la demande énergétique croissante, la production d'énergie par la fusion thermonucléaire est envisagée comme une des meilleures solutions eu égard à la disponibilité du combustible et au faible impact sur l'environnement de cette technologie. Cependant, la mise au point de réacteurs fusion capables de produire de l'énergie passe par des études préliminaires. Parmi les verrous encore présents, la prévision du comportement des matériaux dans les conditions extrêmes (haute température, irradiation avec des particules de haute énergie et exposition au plasma de fusion) qu'ils subiront dans les tokamaks est une question clé. Elle passe par une meilleure connaissance de l'évolution de la microstructure (ou comportement des défauts) des matériaux sous irradiation.

Le tungstène, un des matériaux les plus prometteurs, a été sélectionné pour couvrir le composant critique du TOKAMAK, le « divertor », afin de faire face aux conditions extrêmes. L'irradiation dans le TOKAMAK génère divers types de défauts -lacunes, interstitiels, dislocations…- qui modifient la microstructure des matériaux et leurs propriétés macroscopiques. Des irradiations avec des neutrons de fission ont montré la formation de boucles de dislocation, d'amas lacunaires et de précipités dans le tungstène dont les proportions dépendent des conditions d'irradiation [44,132]. Des défauts similaires ont été aussi observés dans le tungstène auto-irradié (irradié avec des ions de tungstène). Donc, l'auto-irradiation est souvent utilisée pour simuler l'irradiation aux neutrons.

En dehors des défauts intrinsèques, les atomes d'impuretés ont aussi des incidences sur l'évolution de la microstructure du tungstène, par exemple, les éléments Rhénium et Osmium générés par la transmutation induite par les neutrons, forment des précipités [49]. Ces précipités diminuent le gonflement mais augmentent la dureté du matériau. En parallèle de l'irradiation aux neutrons, l'exposition au plasmas composé d'hélium (produit de la réaction de fusion) et d'hydrogène (combustible) provoque la formation de bulles et d'une mousse (« fuzz ») à la surface du tungstène [18,27]. De plus, à part ces deux sources d'impuretés, les éléments légers ne doivent pas être ignorés. En effet divers résultats théoriques prévoient une interaction forte entre l'oxygène, le carbone et l'azote et les défauts lacunaires [239,240]. Pourtant peu de résultats expérimentaux ont été publiés sur ce sujet [24,124].

Sur le plan théorique, la position d'occupation la plus favorable dans la matrice de tungstène est en site interstitiel octaédrique OIS pour le carbone et l'azote, et en site interstitiel tétraédrique TIS pour l'hydrogène et l'oxygène, vu que l'énergie de formation est relativement plus faible. De nombreux résultats théoriques prédisent des interactions entre les LEs et les défauts ponctuels (DP). Par exemple,

Castin et al. [109] ont démontré l'effet du carbone sur l'évolution des boucles du type interstitiel dans le tungstène auto-irradié, en combinant la simulation OKMC et les techniques de caractérisation (SIMS et TEM). La Table 3 résume les propriétés des atomes LE (H, C, N, O) prédits par les simulations dans la matrice de tungstène [22–30]. Ces résultats indiquent que les atomes LEs préfèrent occuper le site interstitiel octaédrique (OIS) ou tétraédrique TIS à proximité des monolacunes (V_1) dans la matrice de tungstène. En outre, les énergies de liaison entre les atomes LE et V_1 sont élevées, ce qui suggèrent que les LEs ont tendance à être piégés dans des monolacunes. Une monolacune peut piéger plusieurs atomes LEs. Par exemple, une seule V_1 peut piéger jusqu'à 12 atomes d'hydrogène [33], 4 atomes de carbone [82], 6 atomes d'azote [110] et 6 atomes d'oxygène [111]. Becquart et *al.* [104] et Heinola et *al.* [103] ont démontré que la présence de carbone dans la lacune stabilise la formation de bilacunes 2NN dans le tungstène en accord avec [112], et la présence d'atomes de H augmente également la stabilité des bilacunes [113] avec une énergie de liaison supérieure à celle du complexe V_1-H [114]. Le nombre d'atomes H piégés dans V_1 diminue avec l'augmentation de la température, le nombre maximum recommandé est de douze [115]. Parallèlement, les complexes LE-lacunes ont également été étudiés dans d'autres métaux BCC. Barouh et *al.* [64] ont prédit que le complexe de trilacunes (V_3) décoré par un atome LE (X), c'est-à-dire V_3X, est le soluté le plus mobile dans le fer BCC [64]. Il a également été découvert que les complexes lacune-oxygène interagissent avec les atomes d'hydrogène dans le vanadium [241]. Par ailleurs, les atomes de H piégés dans une monolacune diminuent avec l'augmentation des atomes de C piégés [112], c'est-à-dire que V_1, et les complexes V_1-C_1, V_1-C_2 et V_1-C_3 peuvent piéger 12, 8, 5 et 3 atomes de H, respectivement.

Sur le plan expérimental, Vehanen et *al.* [122] ont utilisé la spectroscopie d'annihilation de positons pour caractériser les défauts lacunaires dans du fer (BCC) dopés au carbone irradié aux électrons. Ils ont démontré que des complexes carbone-lacune (V-C) sont formés au stade III (200 K, lié à la migration de V) en raison du piégeage des lacunes par les atomes de carbone. Ces complexes V-C empêchent la migration et/ou agglomération des lacunes jusqu'à environ 450 K quand la dissociation du complexe V-C a été observée. Ils ont également montré qu'à ~350 K, les atomes de carbone deviennent mobiles et peuvent être piégés dans les complexes V-C. Plus le nombre d'atomes de carbone est élevé dans le complexe, V-C_n plus le piégeage des positons dans le défaut devient difficile. Cependant, dans le tungstène, seuls Amarendra et *al.* [123] ont supposé la formation de complexes carbone-lacune dans le tungstène recuit. Et Yabuuchi et *al.* [124] ont évoqué la formation de complexes hydrogène-lacunes dans le tungstène irradié aux électrons, sans réussir à quantifier les atomes de C et H. Par conséquent, d'autres études expérimentales sont nécessaires pour mieux comprendre la formation des complexes LEs-lacunes et leur effet sur l'évolution des défauts.

Par conséquent, l'objectif de ce travail est d'étudier l'effet des conditions d'irradiation et l'impact des interactions avec les atomes LEs sur la distribution des défauts lacunaires. Pour cela des irradiations dans différentes conditions ont été effectuées. Des irradiations aux électrons ont été utilisées afin de

produire des défauts simples. Des irradiations aux ions W^+ (auto-irradiations) ont été réalisées afin de simuler l'endommagement généré par les particules produites par la fusion dans le TOKAMAK. Cette étude combine plusieurs techniques de caractérisation : la microscopie électronique à transmission (TEM) pour les défauts les plus gros, la spectroscopie d'annihilation de positons (PAS), spécialement adaptée pour caractériser les petits défauts lacunaires, et la spectrométrie de masse des ions secondaires (SIMS) pour analyser les éléments légers. Ces études ont mis en évidence certains effets des conditions d'irradiation (particule incidente, dose d'endommagement, température) et des éléments légers sur l'évolution de la microstructure du tungstène sous irradiation.

V.2 Matériaux et Méthode

Des échantillons de tungstène de pureté différente (3N-HP : 99,95 wt. % et 6N-XHP : 99,9999 wt. %) polis et recuits à haute température ont été irradiés dans diverses conditions : **i/** irradiations aux électrons de 2.5 MeV pour introduire des défauts ponctuels quantifiables sur de grandes profondeurs (>100µm), **ii/** auto-irradiations avec des ions de différentes énergies de 1.2, 2 et 20 MeV pour créer des défauts similaires à ceux induits par les neutrons sur de faibles profondeurs entre environ 100 et 1600 nm respectivement. La nature et la distribution des défauts induits par irradiations (RID) ont été caractérisées par PAS et TEM. Pour sonder les défauts par PAS plusieurs techniques ont été utilisées : **i/** un accélérateur de positons lents (0.5-25 keV) couplé à un spectromètre d'élargissement Doppler (SPB-DB) qui permet de sonder les défauts près de la surface (0-700 nm dans W) et plus adapté pour caractériser les zones endommagées près de la surface, **ii/** un spectromètre de temps de vie (PALS) couplé à des sources de positons rapides pour caractériser les 50 premiers µm sous la surface. En outre, des techniques d'analyse chimique quantitative (SIMS, NRA) ont été utilisées pour révéler la distribution et quantifier les atomes LEs (ex : C et O). L'analyse SIMS des éléments carbone et oxygène dans le tungstène a été calibrée sur des échantillons W implantés avec des ions C et O à plusieurs fluences. Les distributions de C et O ont été corrélées avec les comportements des défauts obtenus par PAS et TEM.

V.3 Irradiation aux electrons

Des échantillons (3N-HP, carrés (Neyco) et disques (Goodfellow)) de tungstène irradiés aux électrons de 2.5 MeV avec deux fluences (FF : 1×10^{19} $e^-.cm^{-2}$, et HF : 2×10^{19} $e^-.cm^{-2}$ correspondant aux doses d'endommagement de 3.74×10^{-4} et 7.47×10^{-4} dpa respectivement telles que calculées avec les codes POLY&SMOTT) à RT, ont été caractérisés par SPB-DB, PALS, TEM et SIMS.

Tout d'abord, l'analyse SIMS a détecté une distribution hétérogène de l'oxygène en contraste avec celle du carbone jusqu'à 2 µm sous la surface des échantillons irradiés et vierges. Pour l'échantillon irradié (PS#3) et vierge (PS#6), la concentration de carbone ne dépassait pas la limite de détection inférieure d'environ 50 at. ppm, tandis que la concentration d'oxygène fluctuait entre 100 et 400 at. ppm

dans la plupart des cas. La collection des ions secondaires chargés positivement ou négativement avec une masse de 0 à 250 a.m.u. a confirmé que l'oxygène est la principale impureté dans les échantillons 3N-Neyco. De plus, il est intéressant de noter que les masses (200, 216, et 232 a.m.u.) qui présentent les signaux les plus intenses coïncident avec les espèces contenant l'élément de matrice (W) et l'impureté principale (O) (WO, WO_2, et WO_3). De ce fait, la présence de nanoparticules d'oxydes dans le matériau vierge a été spéculée.

Deuxièmement, les mesures SPB-DB ont indiqué que les défauts détectés sont principalement des monolacunes, et que leur concentration augmente avec la fluence, mais pour les deux fluences, la concentration des monolacunes est inférieure à la celle estimée par les codes POLY& SMOTT. En parallèle, les mesures PALS ont confirmé l'annihilation de positons dans les monolacunes pour les deux fluences, avec une concentration d'environ 21 et 37 at. ppm estimée en utilisant un modèle à deux pièges profonds pour FF et HF, respectivement. Ce facteur environ deux est en accord avec le rapport des fluences. Néanmoins, une composante de temps de vie d'environ 135 à 147 ps (pour FF et HF respectivement) correspondant à un défaut X non identifié, avec une intensité supérieure à 50 %, a été extraite du spectre PALS pour les deux fluences. En outre, le taux de piégeage des défauts X semble dépendre de la température, car une seule composante de temps de vie a été extraite des spectres PALS acquis à 25 K et 60 K, ce qui indique que les défauts X pourraient être un piège à positons peu profond. De plus, le temps de vie de référence calculée τ_{mod} indique que les spectres expérimentaux correspondent à un nombre de composantes plus grand (> 3) que celui qui peut être extrait. Les observations TEM montrent que dans les conditions d'irradiation utilisées dans ce travail (faible flux d'électrons) aucun défaut de type boucle de dislocation n'est visible. Cela écarte la possibilité d'attribuer les défauts X à ce type de piège peu profond. Les résultats de temps de vie et d'élargissement Doppler ont été comparés avec des caractéristiques d'annihilation théoriques calculées par DFT pour différents types de défauts lacunaires y compris des complexes lacune-oxygène[14]. La corrélation entre les résultats PAS et l'analyse SIMS nous a permis de conclure que la nature la plus probable des défauts X est le mélange de plusieurs types de complexes lacune-oxygène.

V.4 Auto-irradiations (ions W)

V.4.1 2 et 20 MeV-W^+ à RT

Les échantillons (3N fournis par Goodfellow et Plansee et 6N par FZJ) de tungstène ont été irradiés aux ions W^+ à RT avec deux énergies différentes (2 MeV, 20 MeV) et une série de fluences allant de 10^{12} à 2×10^{14} cm^{-2} ce qui correspond aux doses d'endommagement (calculées avec le code SRIM, l'option « Kinchin-Pease» et l'énergie de déplacement E_d = 55. 3 eV) comprises entre 0.0085 et 0.318

[14] A co-authored paper submitted to Journal of Nuclear Materials

dpa (Table 7). Les mesures SPB-DB des échantillons irradiés à deux énergies montrent une évolution équivalente des fractions d'annihilation de faible moment ***S*** et de fort moment ***W*** dans les régions endommagées. i.e. ***S*** augmente et ***W*** diminue lorsque le niveau d'endommagement augmente, avant d'arriver à une saturation. Cette saturation est atteinte, lorsque le niveau d'endommagement est compris entre 0,425 et 0,85 dpa. Les valeurs de ***S*** et ***W*** montrent que des défauts lacunaires ont été générés par l'irradiation et que leur distribution en taille varie en fonction du niveau d'endommagement jusqu'à la saturation. Au plus faible endommagement (~0,0085 dpa), principalement des monolacunes V_1 ont été détectées par les positons dans les 100 premiers nm sous la surface, avec une concentration d'environ $9,4 \times 10^{25}$ m^{-3}. Lorsque le niveau d'endommagement augmente jusqu'à ~0,085 dpa, de petits amas lacunaires V_n contenant environ 5 à 7 monolacunes ont été détectés et la concentration totale minimale de lacunes (V_1 et celles dans les amas V_n) a été estimée à 5×10^{26} m^{-3}. Ces résultats confirment les simulations MD (Dynamique Moléculaire) [69] qui montrent que dans les cascades de collisions générées par des PKA de 150 keV, ce sont principalement des monolacunes (environ 70 %) qui sont créées, ainsi que quelques petits clusters (environ 28 % avec 2 à 5 lacunes) et une fraction très faible de cavités qui dépend du potentiel empirique utilisé.

Ces résultats ont été comparés à d'autres études expérimentales qui confirment la saturation de la densité de défauts pour une dose d'endommagement comprise entre 0,1 et 0,8 dpa. Cette valeur seuil dépend de la technique utilisée pour la caractérisation des dommages (TGS [226] exposition D et TDS [225]). La modélisation (CRA, Creation-Relaxation Algorithm [228]) a également prédit une telle saturation pour un seuil d'endommagement d'environ 0,5 dpa. Ces simulations ont montré qu'une microstructure "d'équilibre" se forme lorsque la dose d'endommagement atteint cette saturation. Cet équilibre serait le résultat de la compétition entre la recombinaison des défauts ponctuels et le chevauchement des cascades et l'agglomération des boucles d'auto-interstitiels. Cette microstructure "d'équilibre" est constituée de défauts lacunaires (monolacune (V_1) et amas lacunaires (Vn)) dispersés dans un réseau de dislocations de type interstitiel[15].

De plus, il faut noter que cette saturation ne dépend pas de l'énergie d'irradiation. Le spectre en énergie des PKA –Primay Knocked Atoms ou premier atome choqué- générés par collisions entre les ions incidents et les atomes de la cible irradiée (Figure 89), a été calculé avec le code SRIM-2008, et l'option 'full-cascades' pour une énergie seuil de déplacement fixée à E_d = 55,3 eV. Il faut noter que ces spectres sont proches pour les deux énergies d'irradiation.

[15] Un papier a été soumis à Journal of Nuclear Materials

V.4.2 1,2 et 20 MeV-W^+ à 500 °C et 700 °C

Les échantillons (3N-Goodfellow, et 6N-FZJ Plansee) de tungstène ont été irradiés aux ions W de 1.2 et 20 MeV à 500 et 700 °C avec une série de fluences allant de 10^{12} à 10^{14} cm^{-2} (Table 7). Les mesures SPB-DB ont mis en évidence que la distribution des défauts détectés dépend de i/ ***la température*** d'irradiation et ii/ de ***la pureté*** des échantillons pour les irradiations à haute température (HT, 500 et 700°C).

V.I.1 Effet de la température

Les mesures SPB-DB sur les échantillons 3N ont révélé la formation de défauts lacunaires dans le tungstène auto-irradié avec de faibles doses d'endommagement 0,02 dpa. Pour les échantillons irradiés à haute température HT, (500, 700 °C), les caractéristiques ***S-W*** montrent que les positons s'annihilent dans de gros amas lacunaires dont la taille semble proche de celle des V_N les plus gros détectés dans le tungstène (S_{VN}, W_{VN}), contenant environ 20 - 30 lacunes ou plus -soit un diamètre ≥ 0,8 nm-. Leur taille est même supérieure à celle induite par un niveau d'endommagement 16 fois plus élevé à RT. Des caractéristiques d'annihilation très proches ont été trouvées pour l'irradiation à 500 et 700 °C, montrant que des amas lacunaires de taille proche ont été générés aux deux températures, même si une légère différence des valeurs ***S*** et ***W*** pourrait être due à la présence de quelques plus gros amas lacunaires à 700 °C.

De plus, les observations TEM ont confirmé que des cavités sont formées à ces hautes températures et leur distribution en taille dépend de la température. Des cavités légèrement plus grandes ont été observées pour l'irradiation à 700 °C. Leur diamètre varie de 0.5 à 1.45 nm pour les irradiations à 500°C pour une taille moyenne de 0.97 ± 0.19 nm. Ces tailles de cavités correspondent à des clusters de lacunes V_N (dont le diamètre est supérieur ou égal à 0,8 nm) ou plus gros. Cependant il est intéressant de noter que les caractéristiques ***S-W*** mesurées à haute température n'atteignent pas le point (S_{VN}, W_{VN}). Cela suggère que les positons détectent des défauts plus petits que V_N. Nous avons vu plus haut que les calculs MD prédisent la formation de clusters lacunaires dans les cascades de collisions. Cependant la fraction des grosses cavités dans ces calculs reste très faible par rapport aux densités obtenues en TEM. Mason et *al.* [105] ont calculé, par DFT, l'énergie de migration E_m pour les petits clusters de lacunes : E_m est de 1.76 eV pour la monolacune V_1, proche de la valeur de 1.66 eV [81]. Il est intéressant de noter que E_m est encore plus faible pour la tri-lacunes V_3 ($E_m(V_3)$ = 1.14 eV). Il s'ensuit que ces petits défauts lacunaires, V_1 et V_3 sont mobiles à 500 °C, comme il a déjà été montré (523 K) [131]. Cela signifie que certaines lacunes peuvent interagir et s'agglomérer pour former des amas lacunaires et faire croître les clusters avec la fluence des ions (ou l'endommagement). C'est ce que nous avons observé dans la mesure SPB-DB : les positons ont détecté une fraction de grosses cavités plus importante lorsque le niveau d'endommagement est augmentée d'un facteur 2 (à 0,04 dpa). Par conséquent, la migration des petits

défauts lacunaires (V_1 et V_3) devrait être à l'origine de la formation des plus grosses cavités pendant les irradiations à HT.

V.I.2 Effet de la pureté

Différentes distributions de défauts ont été observées après auto-irradiations à HT (500 et 700°C) dans les échantillons 6N-XHP et 3N-HP. Les mesures de SPB-DB et TEM ont détecté les plus gros amas lacunaires dans les échantillons 6N-XHP. Nous avons vu plus haut que les caractéristiques ***S-W*** obtenues dans les échantillons irradiés à HT correspondent très probablement à l'annihilation de positons dans différents pièges : les plus gros amas lacunaires V_N tels qu'observés en TEM et un défaut inconnu Dx. Nous pouvons conclure que les positons sont sensibles à un défaut Dx qui ne peut être détecté en TEM. Ce résultat peut être interprété par une fraction d'annihilation plus faible dans les plus grosses cavités V_N dans les échantillons 3N-HP que dans les échantillons 6N-XHP. En d'autres termes, une fraction d'annihilation plus importante dans les Dx a été révélée dans les échantillons 3N-HP. La nature de ces défauts Dx est discutée dans la suite.

Tout d'abord, étant donné que les deux techniques SPB-DB et TEM montrent que l'agglomération de petites lacunes a été entravée dans les échantillons les moins purs (3N-HP), il est raisonnable de s'intéresser aux impuretés de type éléments légers LEs tels que H, C, N et O, étant données leurs propriétés dans le tungstène et leurs fortes interactions avec les défauts lacunaires (voir la section I.3.4). Comme le montre la Table 28. La quantité de LEs n'a pas pu être détectée dans les analyses par LA-ICP-MS effectuées dans les 6N-XHP par FZJ. Nos analyses SIMS indiquent une faible concentration de C et O dans les échantillons auto-irradiés J11 et J01. Une concentration moyenne d'environ 65 at. ppm proche de la limite de détection pour le carbone et d'environ 100 at. ppm pour l'oxygène a été détectée dans la profondeur sondée par les positrons lents (~700 nm).

En ce qui concerne les échantillons 3N-HP, leur fournisseur a suggéré une concentration plus élevée de LEs, variant entre 130 et 910 at. ppm, avec en particulier 460 at. ppm de carbone et 345 at. ppm d'oxygène considérés comme une valeur maximale. La concentration obtenue par SIMS reste faible et est d'environ 100 at. ppm pour le C, dans G-05 et 75 at. ppm dans G-01. Cependant celle de l'oxygène est beaucoup plus hétérogène et plus élevée variant de 100 à 3000 at. ppm. Il s'ensuit que la concentration en C et en O est plus élevée dans les échantillons les moins purs (3N-HP) que dans les plus purs (6N-XHP).

De plus, ces LEs ont une énergie de migration assez faible dans le tungstène, ils sont donc mobiles aux températures d'irradiation utilisées dans ce travail (500 et 700°C). De plus, ils peuvent être fortement liés à des lacunes simples et former les complexes V-LE en raison de leur énergie de liaison élevée comme nous l'avons vu dans nos études d'irradiations aux électrons. Ainsi, nous pouvons supposer que de tels complexes V-LE se forment sous irradiation dans le tungstène lorsque la température d'irradiation

est suffisamment élevée pour faciliter la migration des LEs ou des monolacunes, ce qui est le cas pour les deux espèces à partir de 500 °C. Selon les travaux de simulation, le site d'occupation le plus favorable pour les atomes de C, N et O se trouve à proximité d'une monolacune, à une distance d'environ 1,3 Å du centre de la lacune, près d'un site octaédrique [111,121,241]. Les énergies de dissociation E_{diss} des complexes V-LE ont été calculées en sommant l'énergie de liaison du complexe avec l'énergie de migration de l'espèce la plus mobile (voir les valeurs E_{diss} dans la Table 28). Une valeur relativement élevée a été obtenue pour les complexes lacune-carbone V-C (3,39 eV), lacune-azote, V-N (3,21 eV) et lacune-oxygène, V-O (3,22 eV), contrairement au complexe lacune-hydrogène, uniquement 1,4 eV. Par conséquent, les complexes lacune-C, O et N, devraient être stables même à haute température (500 et 700 °C) alors que les complexes V-H devraient être dissociés. Ces complexes ne peuvent pas être détectés par TEM en raison de leur taille alors que les positons devraient y être sensibles. En effet les atomes LE ne devraient pas être piégés au centre des lacunes et devraient ainsi laisser des volumes libres dans la structure cristalline où la densité électronique devrait être plus faible que dans le réseau (***Lattice***) et ainsi permettre aux positons de s'y piéger et de s'y annihiler.

Nous avons constaté que le point $\boldsymbol{S_{Dx}, W_{Dx}}$ devrait être situé sur la ligne L_3 qui rejoint le point S_{VN}, W_{VN} correspondant à l'annihilation dans les plus gros amas lacunaires détectés dans le tungstène (20-30 monolacunes) et qui tend vers les deux tiers de la ligne L_1 - caractéristique de l'annihilation dans une monolacune. Les caractéristiques d'annihilation $\boldsymbol{S_{Dx}}$ et $\boldsymbol{W_{Dx}}$ de ces défauts devraient être différentes de celles de la lacune pure et se manifester par un ***S*** plus faible et un ***W*** plus élevé avec une densité électronique plus élevée par rapport à la monolacune pure.

De plus, la formation de ces complexes V-LE pourrait être plus efficace dans le matériau le moins pur (3N-HP) que dans le plus pur (6N-XHP). Ces complexes pourraient empêcher la migration d'une partie des monolacunes qui auraient migré et rejoint les autres lacunes, contribuant à leur agglomération dans les échantillons 3N-HP, comme cela qui a été montré dans le Fe dopé au carbone pour le complexe V-C [122].

La nature des complexes ne peut être déterminée dans la présente étude, et la détermination du nombre d'atomes LE dans les complexes est encore un défi. En comparaison avec les travaux théoriques, ils pourraient être $V\text{-}C_n$, $V\text{-}N_n$, $V\text{-}O_n$, ou V-C-H sans exclure certains amas lacunaires plus complexes composés de plusieurs lacunes dont les propriétés ne sont pas encore connues. Néanmoins, le nombre de LEs liés dans les complexes devrait être suffisamment faible pour que le piégeage des positons dans ces complexes soit possible. Considérant que la densité des cavités observées en TEM d'environ $1.6 \pm 0.5 \times 10^{24}$ m^{-3} correspondant au plus grosses cavités détectés par SPB-DB, c'est-à-dire V_N, le taux de piégeage K_{VN} peut donc être estimé à environ 1×10^{11} s^{-1} dans des échantillons irradiés à 0.02 dpa comme indiqué dans [159]. Connaissant le taux de piégeage total estimé à partir de la longueur de diffusion effective des positons, le taux de piégeage dans les défauts D_x est d'environ 5×10^{11} s^{-1}. Si l'on

considère que le coefficient de piégeage des défauts D_x reste proche de celui des lacunes pures ($\mu_V = 6 \pm 3 \times 10^{-15}$ $m^{-3}.s^{-1}$ [159]), la concentration de D_x peut être estimée grossièrement à environ 7×10^{25} m^{-3} (c'est-à-dire environ 1105 at. ppm). Il est intéressant de noter que ces valeurs approximatives sont du même ordre de grandeur que la concentration totale d'O dans les échantillons 3N-HP.

II. Conclusion générale

Des échantillons de tungstène de puretés différentes (99,95 à 99,9999 % en poids) ont été irradiés dans diverses conditions : ***i/*** irradiation aux électrons pour introduire des défauts ponctuels quantifiables, ***ii/*** auto-irradiations pour créer des défauts similaires à ceux induits par les neutrons. En tenant compte de la complémentarité de leur limite de détection en termes de taille des défauts, les techniques PAS et TEM ont été utilisées pour caractériser les défauts de type lacunaire, de la monolacune aux plus gros amas lacunaires détectables (~2 nm). En outre, les techniques SIMS et NRA ont été utilisées pour quantifier les éléments légers (LEs) dans les échantillons. Les distributions de défauts et chimiques ont été corrélées pour mettre en évidence différents effets sur la distribution des défauts induits par les irradiations.

La qualité des échantillons préparés a été vérifiée par des mesures SPB-DB et PALS. La majorité des échantillons présentent des caractéristiques d'annihilation proches de celles du réseau parfait (***Lattice***), ce qui suggère qu'ils contiennent une faible concentration de défauts. Par conséquent, ils sont adaptés à l'étude des défauts induits par des irradiations. Cependant, l'analyse quantitative (SIMS, et NRA) a indiqué qu'une partie des échantillons préparés présente une couche enrichie en carbone dont l'épaisseur et la concentration peuvent atteindre jusqu'à ~2 µm et ~20 at. % respectivement. Cette couche enrichie en C peut être identifiée par une morphologie particulière de la surface, qui contient d'innombrables petits points sombres, lorsqu'on l'observe au microscope optique. Des analyses SIMS et NRA systématiques ont été réalisées sur des échantillons recuits à haute température (1700 °C) avec des durées de recuit différent (de 1 à 4 h). Il est à noter que la contamination provient d'une source externe aux échantillons. Lors d'un nouveau recuit effectué après le remplacement du porte-échantillon (pour une plaque de tungstène plus pure) et le nettoyage des composants du four, la surface " cotonneuse " a disparu, ce qui indique que la contamination a été réduite. De plus, il semble que la couche enrichie en C ait un effet sur les caractéristiques d'annihilation.

Les défauts induits sous diverses conditions d'irradiation ont été étudiés dans les échantillons de pureté différente. Les résultats principaux de ces études se déclinent en deux branches principales.

D'une part, dans les échantillons irradiés aux électrons avec deux fluences à RT, les mesures PALS ont révélé qu'entre la surface de l'échantillon et une profondeur d'environ 50 µm, la concentration des monolacunes induits par l'irradiation est environ deux fois plus élevée dans l'échantillon irradié à haute fluence (HF) par rapport à celle détectée dans les échantillons irradiés à faible fluence (FF). Ces résultats

sont en accord avec le profil d'endommagement calculé (voir Chap. II.2.1). Néanmoins, une composante de temps de vie de positons plus longue que celle du réseau (***Lattice***) et plus courte que celle de la monolacune est détectée. Ceci montre que les positons ont été piégés dans un défaut inconnu X dans lequel l'annihilation est dominante contrairement aux deux autres états d'annihilation (***Lattice*** et monolacune pure). De plus, le taux de piégeage des positons dans ce défaut X semble être favorisé à la température cryogénique (25 et 60 K), à laquelle une seule composante de temps de vie peut être extraite des spectres de temps de vie avec une valeur d'environ 131 ps (25 K) et 147 ps (60 K). Ni des boucles de dislocation ni des petites cavités n'ont été observées en TEM. En outre, l'analyse SIMS a détecté une concentration non négligeable d'oxygène avec une distribution hétérogène dans ces échantillons. Cet élément léger est très mobile même à la température ambiante dans le tungstène selon les données théoriques (Figure 27). De plus, les caractéristiques d'annihilation estimées pour le défaut X sont proches de celles calculées pour des monolacunes décorées avec un nombre variable d'atomes d'oxygène. Enfin, en utilisant le modèle de piégeage à deux pièges, nous avons confirmé que les spectres du temps de vie contiennent plus de trois états d'annihilation lorsqu'ils sont mesurés à température ambiante. Par conséquent, la nature la plus probable du défaut X est le mélange de plusieurs types de complexes de lacunes-oxygène.

D'autre part, l'évolution de la distribution des défauts lacunaires a été étudiée dans des échantillons de tungstène de différentes puretés (99,95 % en poids et 99,9999 % en wt.%) auto-irradiés dans différentes conditions (énergie des ions W, température, fluences).

Tout d'abord, les échantillons auto-irradiés avec des ions de 2 MeV et 20MeV à la température ambiante ont été étudiés à l'aide de SPB-DB. La taille des défauts lacunaires induits augmente avec le niveau d'endommagement, et atteint une saturation à environ 0,5 dpa. Ceci est en corrélation avec les résultats récents de modélisation. Il est également intéressant de noter que la distribution des défauts induits par des ions W^+ de 2 et 20 MeV à RT est très proche, ceci est probablement dû à la distribution en énergie des atomes de reculs qui reste très proches pour les deux énergies.

Deuxièmement, dans les échantillons auto-irradiés à 20 MeV à haute température (HT, 500 et 700 °C) pour une dose d'endommagement moyen d'environ 0,02 dpa dans la région entre 0 et 700 nm, les mesures SPB-DB ont montré que, par rapport aux irradiations à RT, des plus gros amas lacunaires se sont formés à HT, et que leur taille est proche pour 500 et 700 °C. Cela peut être expliqué par l'agglomération de petits défauts lacunaires (V_1 et V_3), qui deviennent mobiles lorsque la température augmente. De plus, la pureté des échantillons impacte la distribution des défauts lacunaires. Pour des échantillons qui ont été irradiés en même temps, des plus petits amas lacunaires ont été révélés dans les échantillons 3N-HP par rapport à ceux induits dans les échantillons 6N-XHP. Un résultat similaire a également été obtenu pour les échantillons irradiés à 500 °C à 0,04 dpa. De plus, les observations TEM ont confirmé les résultats PAS : pour les mêmes conditions d'irradiation (une dose d'endommagement

de 0.02 dpa, à HT -500, et 700 °C-), les plus grosses cavités ont été observées dans les lames minces 6N-XHP par rapport aux échantillons 3N-HP. L'analyse SIMS des échantillons irradiés a révélé une distribution hétérogène du carbone et de l'oxygène pour tous les échantillons analysés, en particulier pour l'oxygène. La concentration mesurée de C et en particulier celle de l'O sont plus élevées dans les échantillons 3N-HP que dans les échantillons 6N-XHP dans la région sensible aux positons (0-700 nm). De plus, le PAS a révélé une distribution hétérogène des défauts dans un échantillon 6N-XHP contaminé en carbone par rapport à l'échantillon non contaminé du même lot irradié dans les mêmes conditions. Une forte concentration d'oxygène a également été détectée dans les premiers 600 nm sous la surface dans cet échantillon contaminé. En résumé, il semble que la présence des LEs (C et O) ait empêché l'agglomération des lacunes. En se basant sur les caractéristiques d'annihilation trouvées dans ces échantillons moins purs, et sur les propriétés théoriques de l'oxygène et du carbone qui prédisent de fortes interactions entre les LEs et les lacunes, nous proposons que les défauts de lacunes décorées par l'oxygène empêchent l'agglomération des lacunes dans les matériaux moins purs.

III. Perspectives

Différentes perspectives peuvent être proposées à la suite de ce travail, tant sur le plan expérimental que sur celui de la simulation.

Du point de vue expérimental, les investigations suivantes nous semblent intéressantes pour compléter ce travail :

Les résultats PAS et SIMS sur les échantillons irradiés aux électrons et celles aux ions W, suggèrent que les atomes d'oxygène ont une influence majeure sur la distribution des défauts lacunaires induits par les irradiations à haute température. Probablement, des complexes lacunaires décorés avec des atomes d'oxygène sont formés, empêchant l'agglomération des amas lacunaires. Pour approfondir l'investigation de ce type de défauts, d'autres techniques de caractérisation présentant une plus haute résolution doivent être réalisées.

- En particulier la sonde atomique tomographique devrait permettre d'obtenir la distribution en 3D des atomes d'oxygène, et ainsi de vérifier la concentration d'oxygène dissous dans le tungstène irradié à 500 ou 700 °C, et aussi de déterminer la nature des hétérogénéités locales, qui pourraient être liées aux nanoparticules d'oxyde dans les échantillons vierges.
- La microscopie électronique à transmission à balayage (STEM) pourrait permettre directement d'observer les cavités décorées ou les petits amas lacunaires.

Il serait également intéressant de réaliser des recuits après irradiation électronique dans des échantillons contenant une concentration contrôlée d'oxygène pour vérifier la dissociation des défauts lacunaires décorés.

Comme l'évolution des propriétés macroscopiques du tungstène est une des questions majeures pour les applications TOKAMAK, il serait également important d'étendre ces études sur l'évolution de la microstructure du tungstène à des doses d'endommagement plus élevées. Il serait nécessaire d'étudier *Comment la température d'irradiation impacte la saturation des dommages que nous avons mis en évidence à RT*. De plus, ces études de la microstructure devraient être combinées avec des techniques de caractérisation qui sont capables de donner des informations macroscopiques, le gonflement par exemple.

En parallèle de ces études expérimentales, des études théoriques devraient également être réalisées pour mieux comprendre l'effet des impuretés et de la température d'irradiation sur les défauts induits par l'irradiation :

- Le calcul des caractéristiques d'annihilation et des coefficients de piégeage de divers défauts lacunaires décorées V_n-LEs_m pourrait aider à mieux identifier et quantifier ces défauts.
- Le calcul des propriétés de migration de tels complexes devrait permettre de vérifier s'ils sont immobiles à température ambiante, comme le V-C l'est dans le fer.

De plus, les calculs des caractéristiques d'annihilation de $\boldsymbol{S}$ et $\boldsymbol{W}$ de divers amas lacunaires en combinaison avec la méthode d'ajustement basée sur le modèle de piégeage, et des observations microscopiques (TEM), pourraient permettre de mieux quantifier les différentes tailles d'amas lacunaires, notamment les plus petits amas dans les échantillons auto-irradiés.

Appendix

A. SIMS craters

- 2.5 MeV electron irradaition

Ps#3	Total crater depth	Total sputtering time	Sputtering rate	
			V_1	V_2
	nm	s	$nm.s^{-1}$	$nm.s^{-1}$
C1	1572 1163 1355	1000	1.3	-
C2	1449 1855 1798	1400	1.04	2.23
C3	804 946 978	1600	0.57	-
C5	558 1406 1376	1398	0.80	-

Ps#6	Total crater depth	Total sputtering time	Sputtering rate	
			V_1	V_2
	nm	s	$nm.s^{-1}$	$nm.s^{-1}$
C1	2732 1085 1805	1000	0.86	2.12
C2	1340 1294 1297	1200	1.09	
C3	639 594 663	1000	0.63	

PS3	PS6
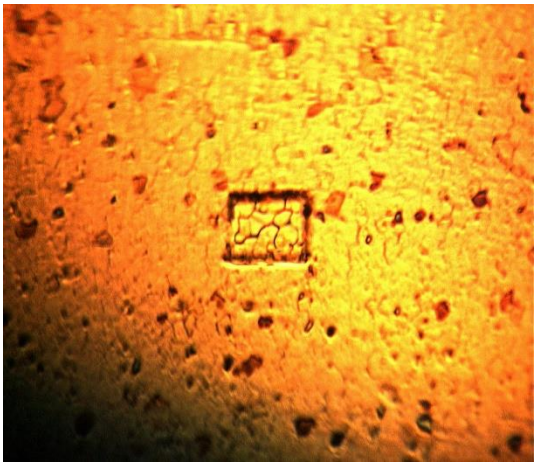	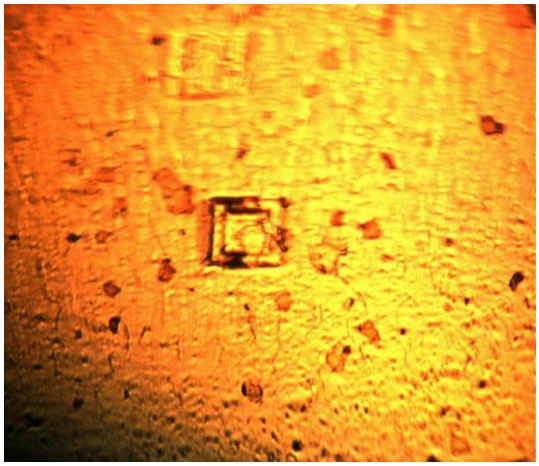
Crater 1 (1.5 × 10^{-9} mbar)	Crater 1 (1.4 × 10^{-9} mbar)
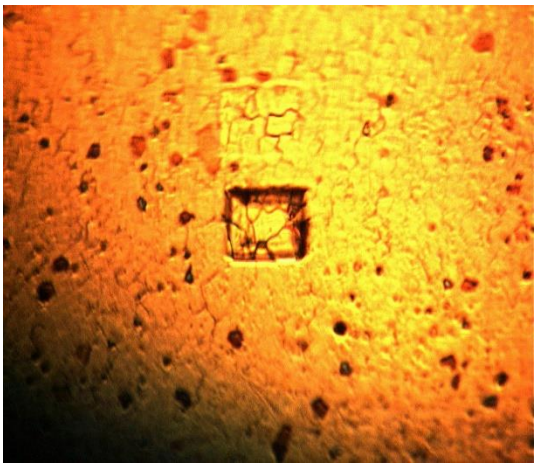	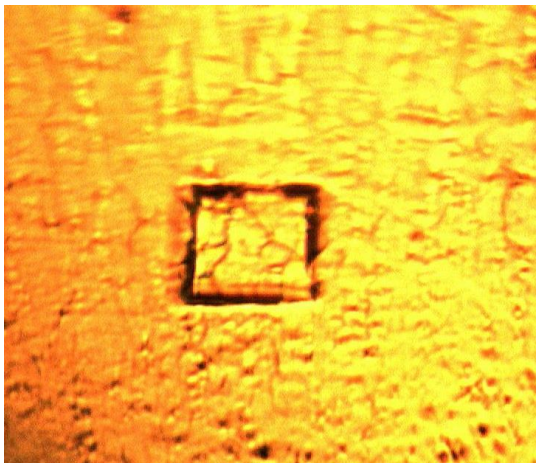
Crater 2 (1.4 × 10^{-9} mbar)	Crater 2 (1.4 × 10^{-9} mbar)
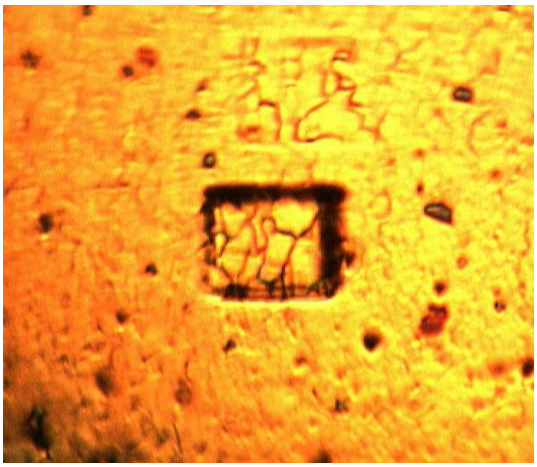	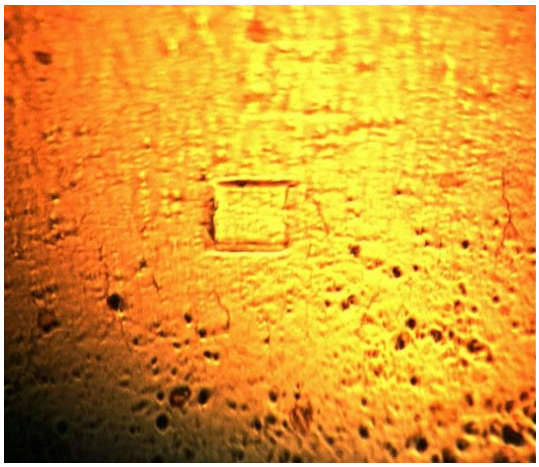
Crater 3 (1.4 × 10^{-9} mbar)	Crater 3 (1.4 × 10^{-9} mbar)

Figure 104: Craters (150 × 150 µm²) of SIMS analysis on the sample irradiated to 2.5MeV with a fluence of 2.10^{19} cm^{-2} (Ps3) at RT and a pristine one (Ps6) in of the same batch.

- 20MeV self-ion irradaition **<u>0.02 dpa 500°C</u>**

J1-C11 XHP	Crater depth (nm)	Sputtering time	Sputtering rate
	nm	s	nm/s
O1	3227 3179 3182	2004	1.59
O2	2895 3054 3035	2004	1.49
O6	4463 4628 4554	3204	1.42

J2-C16 XHP enriched in carbon	Crater depth (nm)	Sputtering time	Sputtering rate
	nm	s	nm/s
O1	3991 3964 3758	2408	1.59
O2	5065 5137 5122	3408	1.49
O6	5691 5675 5821	1418	1.42

G-C05 HP	Crater depth (nm)	Sputtering time	Sputtering rate
	nm	s	nm/s
O1	3227 3179 3182	2004	1.59
O2	2895 3054 3035	2004	1.49
O6	4463 4628 4554	3204	1.42

J1-C11	J2-C16	G-C05
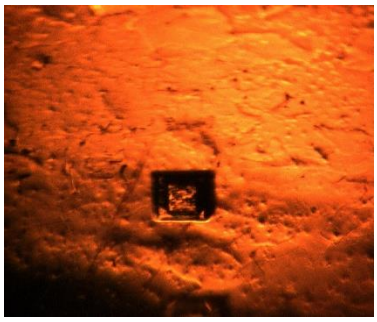	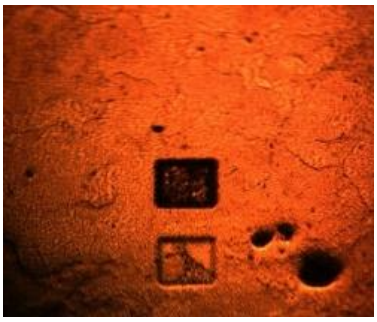	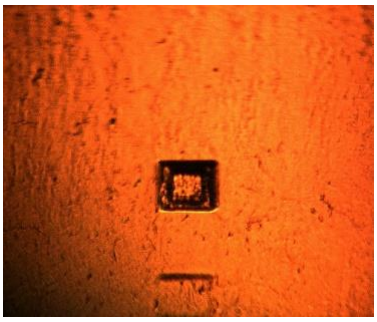
Crater 1 (7.40 × 10^{-10} mbar)	Crater 1 (6.60 × 10^{-10} mbar)	Crater 1 (7.10 × 10^{-10} mbar)
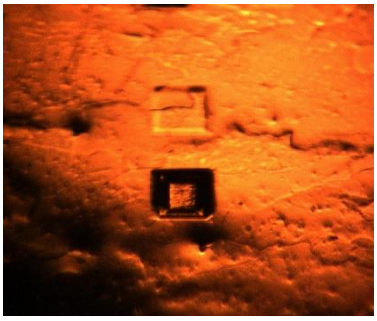	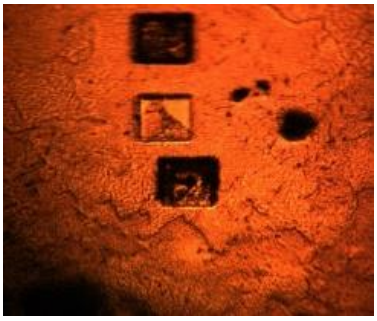	
Crater 2 (7.50 × 10^{-10} mbar)	Crater 2 (6.60 × 10^{-10} mbar)	Crater 2 (7.00 × 10^{-10} mbar)
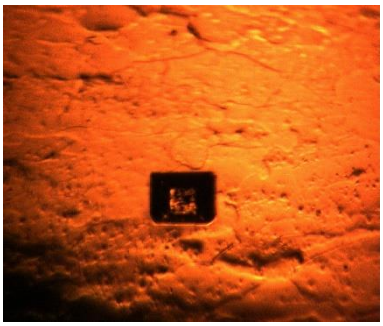	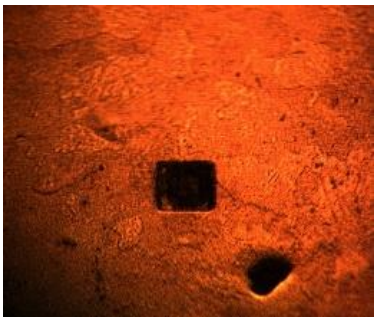	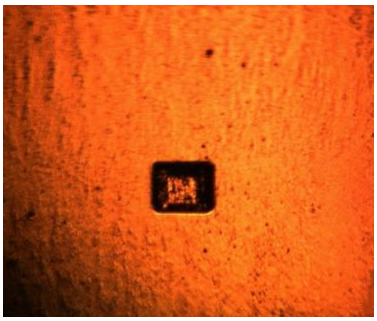
Crater 3 (7.60 × 10^{-10} mbar)	Crater 3 (7.20 × 10^{-10} mbar)	Crater 3 (7.10 × 10^{-10} mbar)

Figure 105 : Craters (150 × 150 µm^2) of SIMS analysis on the sample self-irradiated to 20MeV at 500°C 0.02 dpa

- 20MeV self-ion irradaition **<u>0.04 dpa 500°C</u>**

G-C01	J-C01
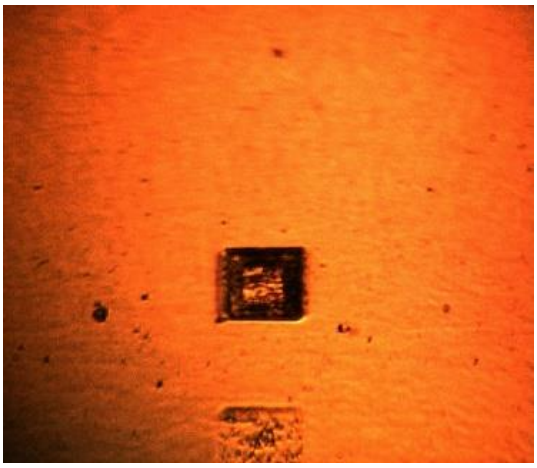	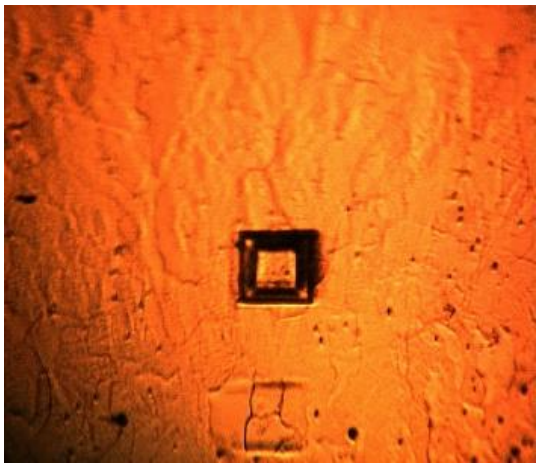
Crater 1 (7.20 × 10^{-10} mbar)	Crater 1 (7.50 × 10^{-10} mbar)
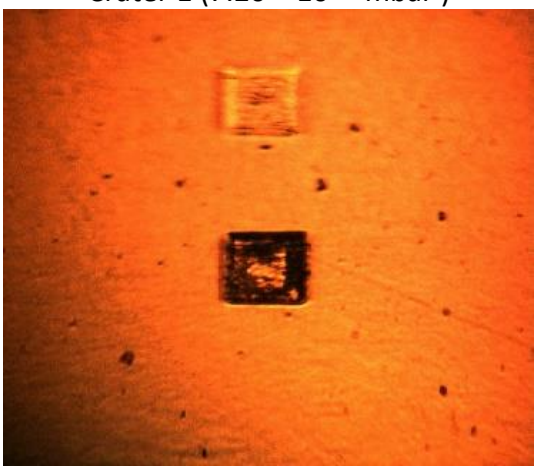	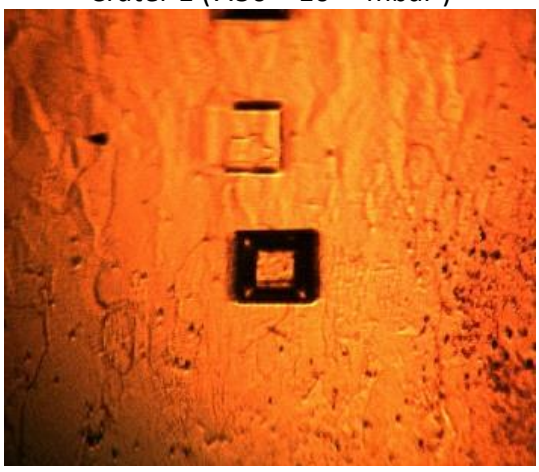
Crater 2 (7.40 × 10^{-10} mbar)	Crater 2 (7.30 × 10^{-10} mbar)
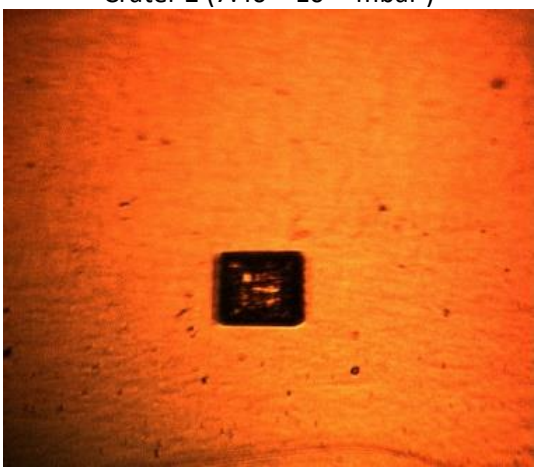	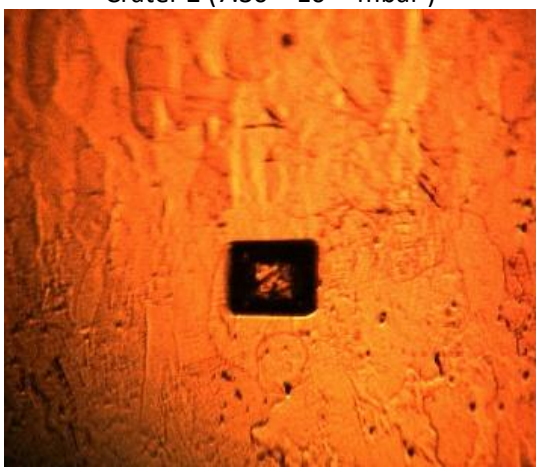
Crater 3 (7.30 × 10^{-10} mbar)	Crater 3 (7.80 × 10^{-10} mbar)

Figure 106 : Craters (150 × 150 µm²) of SIMS analysis on the sample self-irradiated to 20MeV at 500°C 0.04 dpa

B. Demonstration of $\tau_{mod} = \tau_L$

Trapping model of One deep trap:

If annihilation occurs 100 % in the ***Lattice*** and at **one deep trap** defect denoted d_1. In other word the sum of the annihilation fraction in both states equals to1: $\eta_L + \eta_d = 1$.

$$\begin{cases} \dfrac{dn_L(t)}{dt} = -(\lambda_L + k_d)n_L(t) \\ \dfrac{dn_d(t)}{dt} = -\lambda_d n_d(t) + k_d n_L(t) \end{cases} \xrightarrow{n_L(0)=1 \text{ and } n_d(0)=0} \begin{cases} n_L(t) = n_L(0)e^{-\frac{t}{\tau_1}} \\ n_d(t) = I_2(e^{-\frac{t}{\tau_1}} + e^{-\frac{t}{\tau_2}}) \end{cases}$$

With $\tau_1 = \frac{1}{\lambda_L + k_d}$, $\tau_2 = \frac{1}{\lambda_d}$ and $I_1 = 1 - I_2$, $I_2 = \frac{k_d}{\lambda_L - \lambda_d + k_d}$

$$\frac{I}{\tau_{mod}} = \frac{I_1}{\tau_1} + \frac{I_2}{\tau_2}$$

$$= \frac{(\lambda_L - \lambda_d)(\lambda_L + k_d) + k_d\lambda_d}{\lambda_L - \lambda_d + k_d}$$

$$= \frac{{\lambda_L}^2 + \lambda_L k_d - \lambda_L\lambda_d - k_d\lambda_d + k_d\lambda_d}{\lambda_L - \lambda_d + k_d}$$

$$= \frac{\lambda_L(\lambda_L - \lambda_d + k_d)}{\lambda_L - \lambda_d + k_d}$$

$$\frac{I}{\tau_{mod}} = \lambda_L = \frac{1}{\tau_L}$$

Trapping model of two independent deep-traps:

If annihilation occurs 100 % in the ***Lattice*** and at **two deep traps**, defect 1 denoted d_1, and defect 2 denoted d_1. In other word the sum of the annihilation fraction in both states equals to1:

$$\eta_L + \eta_{d1} + \eta_{d2} = 1.$$

$$\begin{cases} \dfrac{dn_b(t)}{dt} = -(\lambda_L + k_{d1} + k_{d2})n_L(t) \\ \dfrac{dn_{d1}(t)}{dt} = -\lambda_{d1} n_{d1}(t) + k_{d1} n_L(t) \\ \dfrac{dn_{d2}(t)}{dt} = -\lambda_{d2} n_{d2}(t) + k_{d2} n_L(t) \end{cases} \xrightarrow{n_L(0)=1 \text{ and } n_{d1,2}(0)=0} \begin{cases} n_L(t) = e^{-\frac{t}{\tau_1}} \\ n_{d1}(t) = I_2(e^{-\frac{t}{\tau_1}} + e^{-\frac{t}{\tau_2}}) \\ n_{d2}(t) = I_3(e^{-\frac{t}{\tau_1}} + e^{-\frac{t}{\tau_3}}) \end{cases}$$

with three lifetime components $\tau_1 = \frac{1}{\lambda_L + k_{d1} + k_{d2}}$, $\tau_2 = \frac{1}{\lambda_{d1}}$ and $\tau_3 = \frac{1}{\lambda_{d2}}$ and their intensities $I_1 = 1 - I_2 - I_3$, $I_2 = \frac{k_{d1}}{\lambda_L + k_{d1} + k_{d2} - \lambda_{d1}}$ and $I_3 = \frac{k_{d2}}{\lambda_L + k_{d1} + k_{d2} - \lambda_{d2}}$

$$\frac{I}{\tau_{mod}} = \frac{I_1}{\tau_1} + \frac{I_2}{\tau_2} + \frac{I_3}{\tau_3}$$

To simplify the calculation, we put $\lambda_1 = \lambda_L + k_{d1} + k_{d2}$

$$\frac{I}{\tau_{mod}} = \frac{I_1}{\tau_1} + \frac{I_2}{\tau_2} + \frac{I_3}{\tau_3}$$

$$\frac{I}{\tau_{mod}} = \frac{\lambda_1(\lambda_1 - \lambda_{d1})(\lambda_1 - \lambda_{d2}) - \lambda_1 k_{d1}(\lambda_1 - \lambda_{d2}) - \lambda_1 k_{d2}(\lambda_1 - \lambda_{d1})}{(\lambda_1 - \lambda_{d1})(\lambda_1 - \lambda_{d2})} + \frac{\lambda_{d1} k_{d1}}{(\lambda_1 - \lambda_{d1})} + \frac{\lambda_{d2} k_{d2}}{(\lambda_1 - \lambda_{d2})}$$

$$= \frac{\lambda_1(\lambda_1-\lambda_{d1})(\lambda_1-\lambda_{d2})-\lambda_1 k_{d1}(\lambda_1-\lambda_{d2})-\lambda_1 k_{d2}(\lambda_1-\lambda_{d1})}{(\lambda_1-\lambda_{d1})(\lambda_1-\lambda_{d2})} + \frac{\lambda_{d1}k_{d1}}{(\lambda_1-\lambda_{d1})} + \frac{\lambda_{d2}k_{d2}}{(\lambda_1-\lambda_{d2})}$$

$$= \frac{\lambda_1(\lambda_1-\lambda_{d1})(\lambda_1-\lambda_{d2})-\lambda_1 k_{d1}(\lambda_1-\lambda_{d2})-\lambda_1 k_{d2}(\lambda_1-\lambda_{d1})+\lambda_{d1}k_{d1}(\lambda_1-\lambda_{d2})+\lambda_{d2}k_{d2}(\lambda_1-\lambda_{d1})}{(\lambda_1-\lambda_{d1})(\lambda_1-\lambda_{d2})}$$

$$= \frac{\lambda_1(\lambda_1-\lambda_{d1})(\lambda_1-\lambda_{d2})-(\lambda_1-\lambda_{d1})(\lambda_1-\lambda_{d2})k_{d1}-(\lambda_1-\lambda_{d2})(\lambda_1-\lambda_{d1})k_{d2}}{(\lambda_1-\lambda_{d1})(\lambda_1-\lambda_{d2})}$$

$$= \lambda_1 - k_{d1} - k_{d2}$$

$$= \lambda_L = \frac{1}{\tau_L}$$

Trapping model of n independent deep-traps:

$$\begin{cases} \frac{dn_b(t)}{dt} = -(\lambda_L + k_{d1} + \cdots + k_{dn})n_L(t) \\ \frac{dn_{d1}(t)}{dt} = -\lambda_{d1}n_{d1}(t) + \cdots k_{d1}n_L(t) \\ \cdots \\ \frac{dn_{dn}(t)}{dt} = -\lambda_{dn}n_{dn}(t) + k_{dn}n_L(t) \end{cases} \xrightarrow{n_L(0)=1 \text{ and } n_{d1,2}(0)=0} \begin{cases} n_L(t) = e^{-\frac{t}{\tau_1}} \\ n_{d1}(t) = I_2(e^{-\frac{t}{\tau_1}} + e^{-\frac{t}{\tau_2}}) \\ \cdots \\ n_{dn}(t) = I_{n+1}(e^{-\frac{t}{\tau_1}} + e^{-\frac{t}{\tau_n}}) \end{cases}$$

with three lifetime components $\tau_1 = \frac{1}{\lambda_L + k_{d1} + k_{d2}}$, $\tau_2 = \frac{1}{\lambda_{d1}}$ and $\tau_3 = \frac{1}{\lambda_{d2}}$ and their intensities $I_1 = 1 - \sum_2^{N+1} I_i$, $I_2 = \frac{k_{d1}}{\lambda_L + k_{d1} + \cdots + k_{dn} - \lambda_{d1}}$ and $I_{n+1} = \frac{k_{dn}}{\lambda_L + k_{d1} + \cdots + k_{dn} - \lambda_{dn}}$

According to the recurrence method, the relation of $\frac{I}{\tau_{mod}} = \frac{1}{\tau_L}$ until n independent deep-traps.

C. SIMS profile of ^{12}C in samples J33 and J34

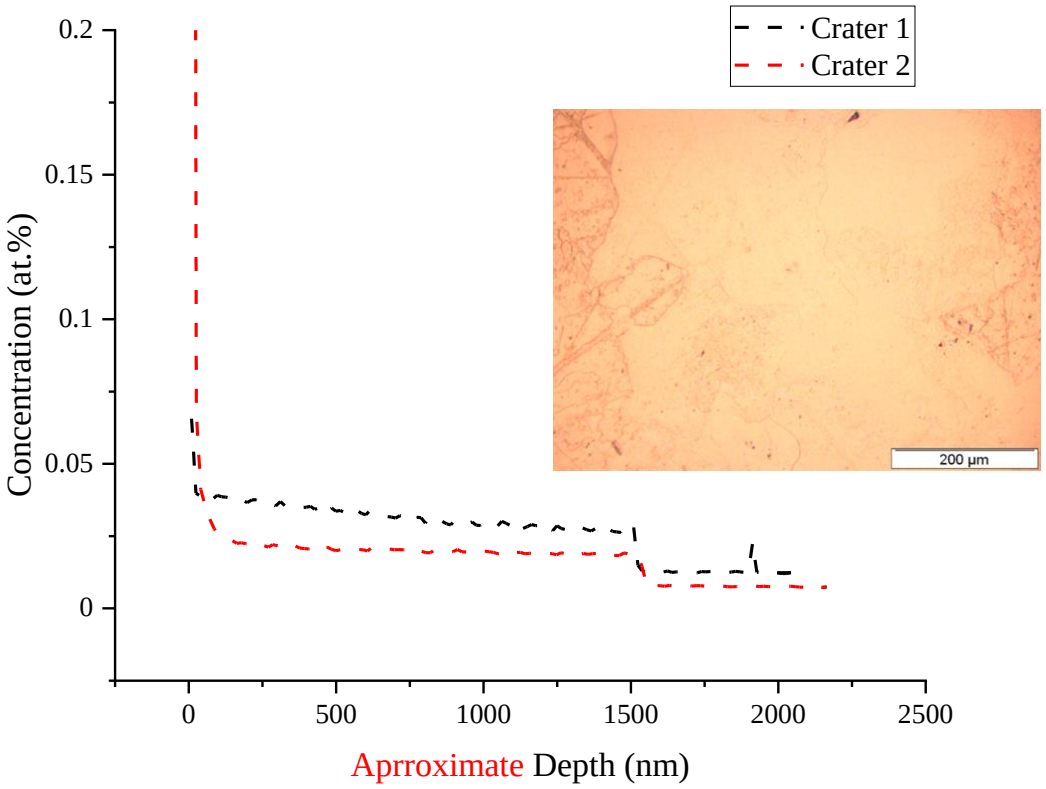

*Figure 107: SIMS profile of ^{12}C of the samples **J33** obtained by two random craters and the surface aspect acquired by using optical microscope before annealing experiment with various exposure times*

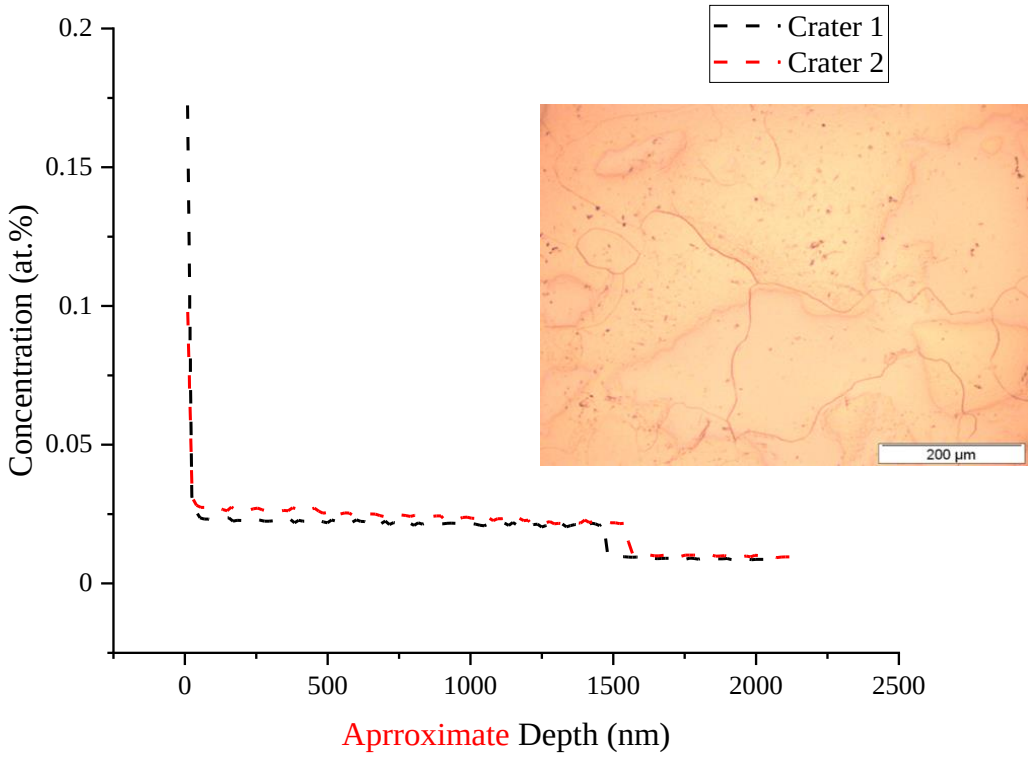

*Figure 108: SIMS profile of ^{12}C of the samples **J34** obtained by two random craters and the surface aspect acquired by using optical microscope before annealing experiment with various exposure times*

D. SIMS profie of ^{12}C and ^{16}O in 3N-HP and 6N-XHP samples

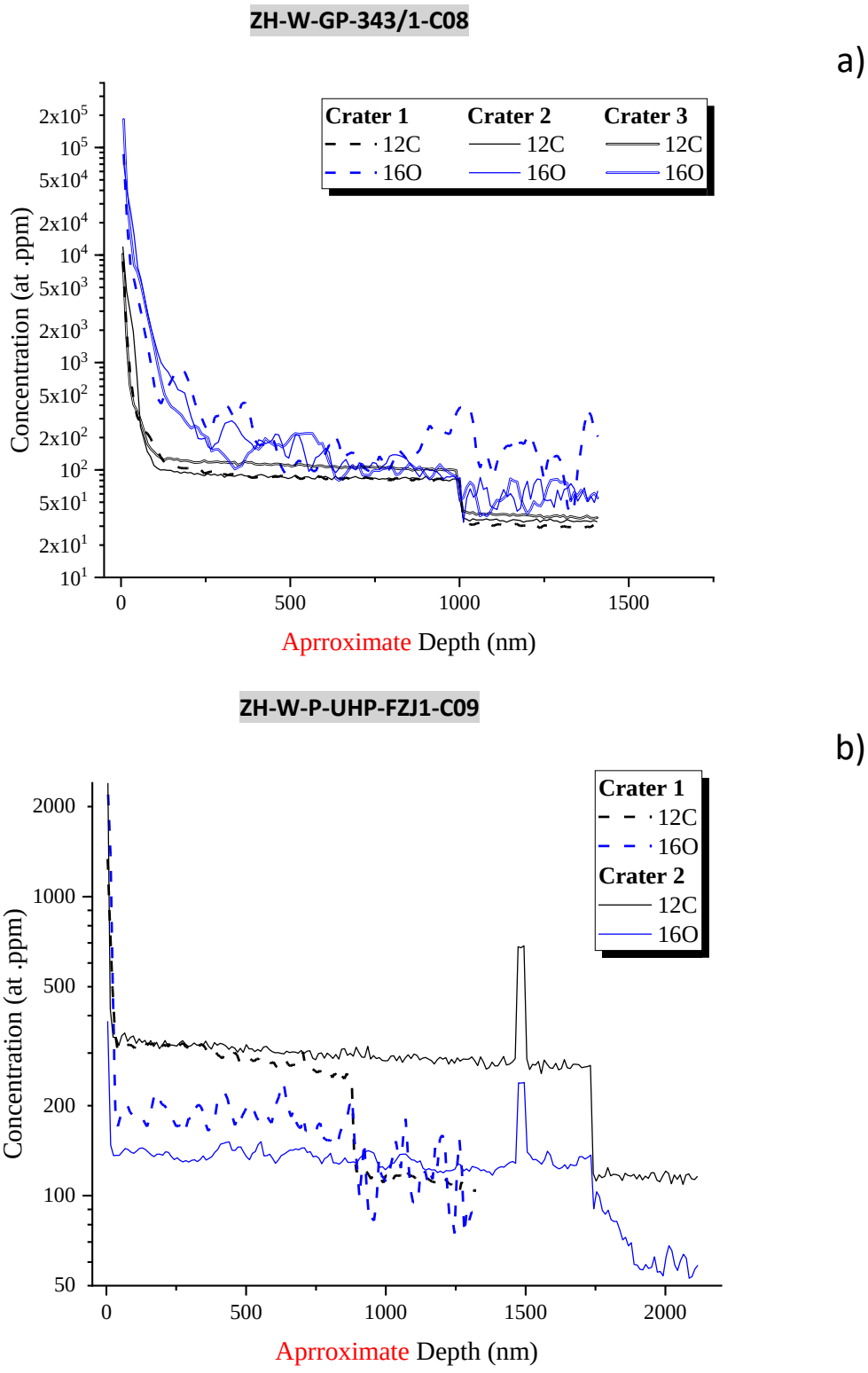

*Figure 109: SIMS profile of ^{12}C and ^{16}O of the samples **irradiated to 20 MeV-W 0.32 dpa at RT GP-08 (annealed to 600 °C, from 100 °C with a step of 50 °C/1h) and J1-C09 (as-damaged).**obtained by different random craters*

Zhiwei Hu

Effet de la pureté sur l'évolution de la microstructure du tungstène sous irradiation

Le réacteur thermonucléaire expérimental international (ITER) est une étape essentielle dans le développement de la technologie de fusion pour la production d'énergie. Le tungstène (W) est l'un des matériaux les plus adaptés pour recouvrir le divertor, composante critique d'ITER et la première paroi de DEMO (réacteur démonstrateur). Il devra résister à l'exposition au plasma et à l'irradiation des particules produits lors de la fusion (neutrons de 14,1 MeV et particules alpha de 3,5 MeV), qui génèrent des défauts à l'échelle atomique. L'évolution de ces défauts conduit à la dégradation des propriétés du tungstène, ce qui peut avoir un impact sur le fonctionnement du réacteur. L'objectif de ce travail est d'étudier l'évolution des défauts lacunaires induits par l'irradiation d'électrons et d'ions de tungstène (atomes de reculs générés par les interactions du tungstène avec les produits de la fusion). En utilisant la spectroscopie d'annihilation de positrons (PAS), un nouveau défaut lacunaire X avec une fraction prédominante a été révélé après irradiation aux électrons avec deux fluences (1 et 2×10^{19} cm^{-2}) à température ambiante (T_{amb}). En combinant la microscopie électronique à transmission (TEM) et la spectroscopie de masse des ions secondaires (SIMS), il apparait que ces défauts X pourraient être des lacunes décorées avec des atomes d'oxygène. Des échantillons de tungstène irradiés avec des ions W de 2 MeV et 20 MeV à T_{amb} ont été caractérisés par PAS. Lorsque l'endommagement atteint 0,5 dpa, la taille des défauts n'évolue plus pour les deux énergies. Des irradiations avec des faibles doses d'endommagement (0,01 à 0,04 dpa) ont été réalisées à différentes températures (RT, 500 °C, et 700 °C). À 500 °C ou plus, la combinaison de PAS, TEM et SIMS montre que l'agglomération des petites lacunes a été limitée dans les échantillons les moins purs (99,95 wt.%) par rapport aux ultra-purs (99,9999 wt.%), très probablement par les impuretés d'éléments légers (C et O).

Mots clés : tungstène, irradiation, défauts lacunaires, PAS, TEM, SIMS

The effect of the purity on the microstructural evolution of the tungsten under irradiation

The International Thermonuclear Experimental Reactor (ITER) is an essential step in the development of fusion technology for energy production. Tungsten (W) is one of the most suitable materials to cover the divertor, a critical component of ITER and the first wall of DEMO (Demonstrator Reactor). It will have to withstand exposure to the plasma and irradiation by the particles produced during fusion (14.1 MeV neutrons and 3.5 MeV alpha particles), which generate defects on an atomic scale. The evolution of these defects leads to the degradation of the tungsten properties, which can have an impact on the operation of the reactor. The objective of this work is to study the evolution of vacancy defects induced by the irradiation with electrons and tungsten ions (recoil atoms generated by the interactions of tungsten with the fusion products). Using positron annihilation spectroscopy (PAS), a new vacancy defect X with a predominant fraction was revealed after electron irradiation with two fluences (1 and 2×10^{19} cm^{-2}) at room temperature (RT). Combining transmission electron microscopy (TEM) and secondary ion mass spectroscopy (SIMS), it appears that these X defects could be vacancies decorated with oxygen atoms. Tungsten samples irradiated with 2 MeV and 20 MeV W ions at RT were characterized by PAS. When the damage reaches 0.5 dpa, the size of the defects no longer changes for both energies. Irradiations with low damage doses (0.01 to 0.04 dpa) were performed at different temperatures (RT, 500 °C, and 700 °C). At 500 °C or higher, the combination of PAS, TEM, and SIMS shows that the agglomeration of small vacancies was limited in the less pure samples (99.95 wt.%) compared to the ultrapure ones (99.9999 wt.%), most likely by the light element impurities (C and O).

Keywords: tungsten, irradiation, vacancy-type defect, PAS, TEM, SIMS

[Conditions Extrêmes et Matériaux : Haute Température et Irradiation
CEMHTI - UPR3079 CNRS]